Experimental and Numerical Study of Submerged Arc Welding Induced Thermal History, Residual Stresses, Distortion and Weldment Characterization

A Thesis Submitted in
Partial Fulfillment of the Requirements
for the Degree of

DOCTOR OF PHILOSOPHY

by

ARPAN KUMAR MONDAL
(Roll No. 11610318)

DEPARTMENT OF MECHANICAL ENGINEERING
INDIAN INSTITUTE OF TECHNOLOGY GUWAHATI
GUWAHATI-781039, INDIA

June 2018

DEPARTMENT OF MECHANICAL ENGINEERING

INDIAN INSTITUTE OF TECHNOLOGY GUWAHATI

GUWAHATI–781039, ASSAM, INDIA

CERTIFICATE

This is to certify that the thesis entitled **"Experimental and Numerical Study of Submerged Arc Welding Induced Thermal History, Residual Stresses, Distortion and Weldment Characterization"** submitted by **Mr. Arpan Kumar Mondal (Reg. No. 11610318)** to the Department of Mechanical Engineering, Indian Institute of Technology Guwahati, is a record of original research work carried out under our supervision and it has not been submitted elsewhere for the award of any other degree or diploma.

The thesis in our opinion, has reached the standard fulfilling the requirements for the award of degree of Doctor of Philosophy in accordance with the regulations of the institute.

Prof. Pankaj Biswas
Department of Mechanical Engineering,
Indian Institute of Technology Guwahati,
Guwahati – 781039, India

Prof. Swarup Bag
Department of Mechanical Engineering,
Indian Institute of Technology Guwahati,
Guwahati – 781039, India

6th June, 2018

Dedicated

To

My Family

ACKNOWLEDGEMENTS

I would like to express my heartfelt gratitude towards all those who have immensely helped me during this long arduous journey and eventually assisted me to emerge as an experienced researcher and a mature individual.

First and foremost, I must express my deepest sense of appreciation and respect for my thesis supervisors, Prof. Pankaj Biswas and Prof. Swarup Bag for providing me the opportunity to work under their supervision. Their persistent patience and friendliness in the moments of difficulties have always been remembered and also his constant encouragement have played a crucial role in writing the thesis and bringing it to its present form.

I would like to thank my doctoral committee members, Prof. P S Robi, Prof. S. Pal, and Prof. S. K. Majumder for carefully reading the reports at various stages of evaluation and providing many useful comments, which have helped in the development of this thesis.

My sincere gratefulness to past and present departmental heads Prof. D. Chakraborty, Prof. P. Mahanta, Prof. A. K. Dass and Prof. S. K. Dwivedy for their kind permission for enrollment, registration and several important supports at IIT Guwahati. I am also grateful to all the faculty members of Mechanical Engineering Department for giving me a comfortable and friendly environment for pursuing my research. I would also like to acknowledge the contribution of office staff, for helping me with various academic as well as non-academic issues.

I would like to express my sense of gratitude to Dr. D K Sharma and Mr. N K Das, past and present Assistant Workshop Superintendent and all the staffs of the workshop specially Mr. Dilip Chetri, Mr. Dipak K. Deka, Mr. Chandan Banikya, Mr. Minesh Ch. Medhi, Mr. Nidul Saikia and Mr. Amzad Khan for extending their help in fabrication of the different experimental set-ups for this work. I sincerely acknowledge the assistance received from Mr.Sanjib Sarma, Mr. Saiffuddin Ahmed, Mr. Jiten Basumatary, Mr. Nip Borah in various experimental proceedings.

I also wise to express my gratitude to the Central Instrument Facility, IIT Guwahati to providing technical support with SEM, and FESEM.

The financial support of this research, which was provided by the Department of Mechanical Engineering, Indian Institute of Technology Guwahati, is gratefully acknowledged.

The most important support for this work came from my parents, Sri. Amiya Kumar Mondal and Smt. Sumita Mondal, for encouraging me to go still further at every points of life. I would like to thank my extended family for all of their love and support through the years, especially at peak of the economy encouraged me to pursue Ph.D on a modest stipend.

Finally the friends form an important part of this long and enduring journey, and without their constant support and encouragement, the completion of this thesis perhaps would have been an impossible task. I would therefore be forever be grateful to all my friends and well-wishers.

I consider myself privileged and fortunate to work in the Indian Institute of Technology Guwahati.

Above all, I am thankful to the Almighty.

6th June, 2018 Arpan Kumar Mondal

ABSTRACT

Submerged arc welding is a fusion welding process which is characterized by its high deposition, deep penetration, high productivity and smooth finish especially for down-hand position welding. It is generally used in fabrication of large structures, which involves the formation of residual stresses and distortion. The purpose of the present work is to study the thermo-mechanical behaviour and weldment characterization of the submerged arc welded joints and development of suitable mitigation technique for controlling the weld induced residual stresses and angular deformation. For this purpose, numerical analysis and numerous experimental investigation of submerged arc welded mild steel plates were carried out in this present study. 3-D transient, nonlinear, elasto-plastic finite element models were developed to estimate the thermal history, the residual stresses and distortion of the welded plates. To eliminate the time for edge preparation, welding were carried out for square butt joint with top and bottom reinforcement. A comparative study between single and double sided fillet joints was carried out. Effect of tacking sequences and welding sequences were studied for the development of sustainable mitigation techniques. Angular distortion in large structures also estimated by using an equivalent technic, which eliminated huge computation time and resources. Results obtained from the numerical analysis were compared with the experimental one. Estimation of correct heat source parameters is quite a challenging task. A new volumetric heat source model was developed which can be used in the simulations of fusion welding. Thermal profiles as well as weld bead dimensions were estimated by the application of the new heat source. Effect of weld parameters, joint geometry on weld bead geometry as well as mechanical property was studied. The addition of surface active elements enhances the weld penetration, effect of the same was studied. Single and multi-response optimizations were carried out to determine the best parameter combination.

Keywords: Transient thermal analysis, structural analysis, 3-D finite element analysis, residual stresses, angular deformation, inherent strain, plastic strain, elastic strain, large structure, heat source, welding sequence, tacking sequence, surface active element, included angle, welding process parameter, optimization.

CONTENTS

LIST OF FIGURES

LIST OF TABLES

NOMENCLATURE

Symbol	Description
C_p	Specific heat
$[C]$	Specific heat capacity matrix
E	Young's modulus
$[K]$	Thermal conductivity matrix
M_r, M_f	Fraction of heat deposited in rear and front parts of avocado-configuration heat source model
Q	Heat input
$\dot{Q}$	Volumetric heat source
q	Heat flux on to the surface
q_f	Power density distribution for front
q_r	Power density distribution for rear
q_s	Surface heat flux
$Q_{max.}$	Maximum value of the heat intensity
$\{Q\}$	Heat flow vector
T	Temperature
t	Time variable
$\{T\}$	Temperature vector
(x, y, z)	Cartesian coordinate system
$\{d\epsilon\}$, $\{d\varepsilon^p\}$, $\{d\epsilon^t\}$ and $\{d\epsilon^e\}$	Total strain, plastic strain, thermal strain and elastic strain
μ	Poisson's ratio
σ	Stefan-Boltzmann constant
$\sigma_1, \sigma_2, \sigma_3$	Principal stresses
ρ	Density

CHAPTER 1

Introduction

1.1 General background

Welding is the most widely used joining process in the fabrication of structures, which includes the conventional industrial applications to modern engineering applications like the fabrication of aerospace structures, nuclear application, high-pressure vessels, marine structures etc. [1]. Welding is known as one of the most complex manufacturing processes, as a large number of variables and factors controls the welding process towards the determination characteristics of the final weld joint [2]. Even though welding is recognized as one of the most significant fabrication processes used in engineering industries, there is little scientific understanding present in productivity measurement and evaluation of welding processes [2]. As a widely used manufacturing technique, welding offers a number of technical challenges to the welding community specially shop floor engineers engaged in integrated structures through welding [1]. Compared to conventional mechanical joining methods welding offers some significant advantages including flexibility of design, improved structural integrity and weight & cost savings [1, 3]. However, during joining of components of a structure, highly localized thermal gradients induces thermal strains in the weld joint and base metal regions resulting in generation of high magnitude of residual stresses within and around the weld region. Which in turn combine and react to produce internal forces and results in bending, buckling, and rotation. These displacements are termed as welding distortions [1, 4]. Both weld residual stress and distortion can significantly impair the performance and reliability of the welded structures [5]. Therefore, they must be critically dealt with design and manufacturing phases to ensure intended in-service use of the welded structures. Over several fusion welding processes, one of the established techniques for welding big structure is submerged arc welding (SAW). The quantitate assessment of distortion and residual stress of an integrated structure is of paramount interest to the researchers. Therefore the present work is focused on thermomechanical analysis of submerged welded structure through experimental investigation and by the development of numerical model.

1.2 Submerged arc welding (SAW) process

Submerged arc welding is a fusion welding process which fuses the parts to be joined by heating them with an arc or arcs between a bare electrode or electrodes and the base metal. The process is normally semi-automatic or fully automatic [6]. It is used to weld medium-to-thick steels in a flat or down hand position. It has become popular for heavy plate welding because it produces high-quality weld metal at a minimum cost. It is normally used for welding steels and is not applied to nonferrous metals [9].

SAW process uses a blanket of granular fusible flux, beneath which both the weld and the arc zone, are protected or “submerged.” This flux blanket guards against atmospheric contamination, stabilizes the arc during welding, prevents splatter and sparks from flying about, and suppresses radiation and fumes that are typical of the shielded metal arc welding process. The arc is flat and the same is maintained between the end of a bare wire electrode and the weld. After initiation of the arc, the consumable electrode is continuously fed by a wire feeding mechanism towards the weld line at a controlled rate and the welding torch is moved automatically along the weld seam. A schematic representation of submerged arc welding process and equipment is shown in Figure 1.1. The heat generated by the arc progressively melts the electrode tip, the adjacent edges of base metal and some of the flux, which is continuously fed in front and around the electrode from a hopper. The molten slag thus formed, floats on the molten metal and thus completely shields the molten pool from atmosphere. As the welding arc advances along the seam, the deposited weld metal and the liquid slag cools down and solidifies, forming the weld bead and the protective slag shield over it. This slag shield results in a slower cooling rate for the deposited weld metal thus providing an annealing effect to the weld deposit.

There are some key parameters of the submerged arc welding process. These variables includes the arc voltage, the wire feed speed, travel speed, contact tip to work or electrode stick-out, polarity and current type (may be either AC or DC), as well as variable balance AC current. The submerged arc welding process is one of the efficient electrical arc welding technologies using in the construction of ship and civilian vessels due to its various advantages over manual metal arc welding such as high efficiency [10], high deposition rate [11], high current density [11] and good weld shape [10].

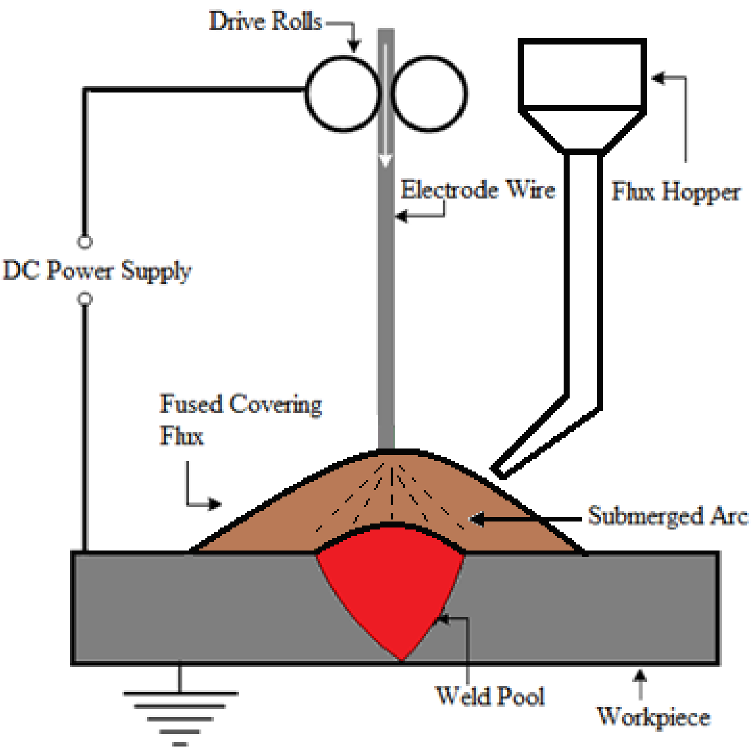

Figure 1.1 Schematic illustration of submerged arc welding process and equipment

SAW is most widely used method for welding thick section in down hand position being a highly economical method for fabrication [12], especially in restoration of worn parts [11]. It is commonly used due to its easy applicability, its ability to deposit a large amount of weld metal while using more than one wire at the same time [11] and at least half or more of the flux is recoverable. Recent researchers are trying to reuse the most of the fluxes [7] to improve the cost effectiveness. Optimization process parameters to achieve the best weld joint is going on for steels of various thickness as well as other advanced materials. Residual stress and angular deformation is one of the area where some researchers are concentrating. Fluid flow based modes for tandem SAW is quite successful one. Nearly 100% joint efficiency with high deposition rate is possible in SAW that is why it has got extensive industrial applications in the field of pressure vessel, manufacturing, structural engineering, shipbuilding industries, chemical plants, commercial vessels, pipe welding (very large diameter and high thickness pipes), railway industry , bridge building, rebuilding and surfacing, motor industry, general fabrication, nuclear, power generation plants, land transportation (beam, boom, tractor, and multi-head type rigs) etc.

1.3 Welding as a multi-physics problem

Modelling of welding is a multi-physics problem, starting from the arc initiation to the cooling of the welded joints there are involvement of several physical fields along with coupling between different physical fields which are of very complex nature.

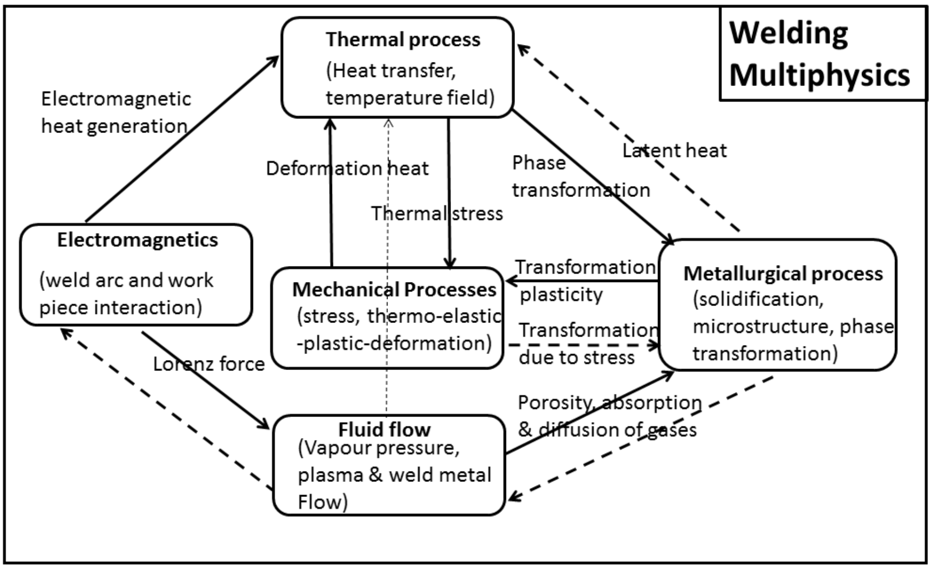

Figure 1.2 Welding as a multi-physics problem

Figure 1.2 shows the schematic diagram of welding-multi-physics. It can be clearly seen that welding involves the interaction among thermal, electrical, electromagnetic fields, metallurgical transformation, fluid flow, mechanical processes etc. The arc initiation where there is an electron flow between the electrode and the work piece due to the electrical process and generates intense heat. The arc itself influenced by the electromagnetic forces like Lorentz force which influences the droplet shape and eventually have influence on the heat transfer. If shielding gas is used the magnetic field influences the shielding gas flow and molten pool behaviour, a plasma column forms between the cathode and anode drop zones which is responsible for the droplet transfer from the electrode to the work piece.

Non-uniform heating and cooling occurs in a small area which is responsible for the metallurgical changes i.e. the phase transformation of the base material as the temperature due to welding raises to well above the melting point. Followed by heating, cooling occurs and the formation of new microstructures like austenite or martensite (in steel) etc. take place depending upon the cooling rate and type (whether it's a controlled or air cooling). Though the phase transformation effect is not significant for residual stress & distortion of low carbon steels [13]. Again due to the non-uniform heating and cooling volumetric change occurs in the fusion zone and thermal stress develops which leads to the development of residual stress and the deformation of the weld structure after cooling.

Therefore the residual stress and deformation in welded structure depends upon thermal as well as microstructural changes in the weld metal. The plastic deformation also has a contribution in it by affecting the microstructure and heat generation. The microstructural variation is also affected by the use of shielding gases, and the porosity, diffusion and absorption of the gases is dependent on the microstructure of the weld metal. Therefore it is well understood that welding is a multiphysics problem, to model a welding process effectively we have to consider thermal properties, electrical, electromagnetic properties, weld metal flow, flow of gases, filler material, residual stress, deformation, microstructure etc. But considering each and every parameter will make the model extremely complex therefore the parameters which has influences the most is generally considered during the modelling and simulation of a welding process.

1.4 Residual stress and distortion in SAW process

Residual stress is the type of stress which remains in a body which is stationary and at equilibrium with its surroundings [14, 15]. During the welding process locally rapid melting and solidification occurs in specific zones of the base plate (FZ and HAZ), the existence of high temperature gradient in the weld zone creates a very high stress concentration in the weld zone and nearby HAZ [16, 17], which generally exceeds the yield strength of the material. If the stresses generated from thermal expansion/contraction exceed the yield strength of the parent metal, localized plastic deformation of the metal occurs. Plastic deformation causes a permanent reduction in the component dimensions and distorts the structure [18].

Initially when the weld pool is formed upon the base metal, heat is transferred rapidly and heat affected zone is formed but due to this extreme heating the metal at HAZ gets expanded and compressive stresses are formed in the surrounding cold base metal to counter this expansion. But, tensile stresses arises upon cooling when the contraction of the weld metal as well as the HAZ takes place and which is resisted by the adjacent cold base metal. Presence of large amount of residual stresses in the welded structure can evidently reduce the fatigue strength, cause crack generation and shorten the lifetime of the welded part [19, 17]. In a nutshell the principle of the distortion can be assumed as the material shrinkage during heating and cooling cycle of the welding process.

The change in temperature and stresses during welding are studied by many researchers. The formation of residual stresses during welding is explained in the Figure 1.3 [20]. A welding plate with a moving arc and the corresponding temperature and stress distribution (σ_x) at four different cross sections are shown. The egg-shaped region (cross section 2-2') is the present location of the heat source and this is the area where melting took place, cross section 3-3' is the cooled down region, the melted region is denoted by cross section 4-4' and the zone yet to welded is shown by cross section 1-1'.

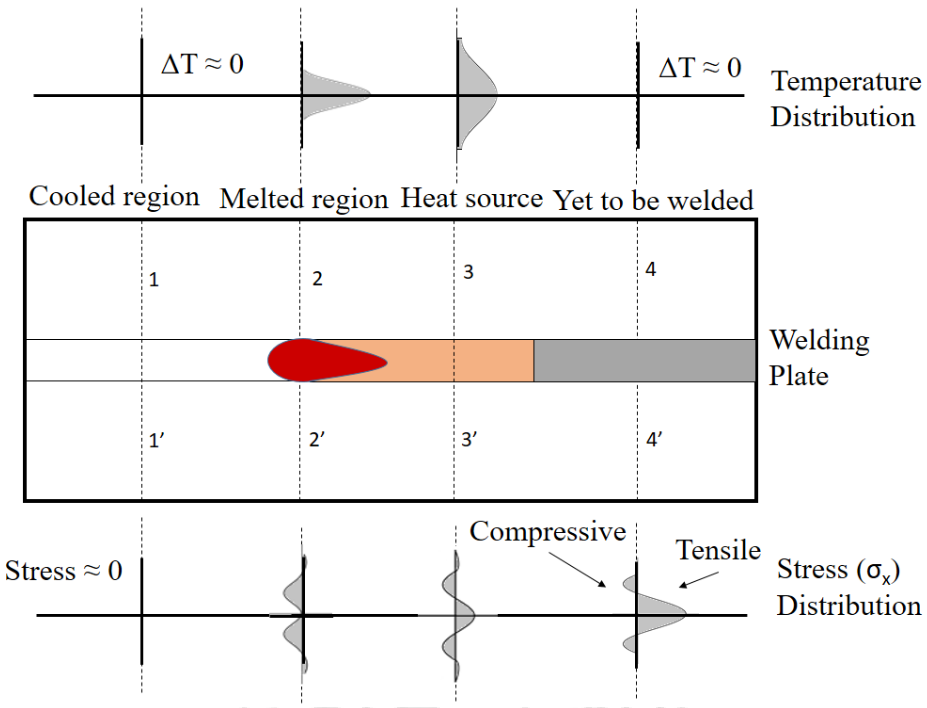

Figure 1.3 Schematic diagram of changes in temperature and stresses during welding [20]

Now from the temperature distributions it can be seen that Section 1-1' is located at some distance ahead of the welding torch/heat source therefore the temperature gradient, ΔT due to the welding is almost zero. Along the section 2-2', which is located just at the welding arc where the change in temperature is very high and it follows an uneven distribution. Section 3-3', which is located at some distance behind the welding arc where the change in temperature is less steep and the distribution is more even. Finally the last section 4-4, which is located far away from the welding arc and as the due to this the metal already cools down and again the temperature gradient due to welding is zero.

The stress distribution due to the temperature gradients at the same cross sections i.e. 1-1’, 2-2’, 3-3’, and 4-4’ are shown. Only σx is considered as shearing and normal stresses in y-direction are much smaller value. In the section 4-4’, the welding thermal stresses are zero. As the molten metal in the weld pool region at section 4-4’ cannot support a load, the stresses in the region are also almost zero. The stresses in the heat affected zone (HAZ) at section 3-3’ are compressive due to the expansion of these areas is restrained by surrounding colder metal. In section 3-3’, weld metal and HAZ is cooled enough, the resulting stress is tensile in nature in this region as they try to shrink. The stresses are compressive in nature further away from the weld line. Finally, section 1-1’ represents the cooled down region, where higher tensile stresses are present in the HAZ zone and compressive stresses exist away from the weld line.

During welding, heat is applied from the weld torch in localized manner therefore thermal gradients are produced. Due to localized non-uniform heating and cooling cycles in the weld and adjacent base metal, complex thermal strains are developed. The stresses resulting from the thermal strains produce internal forces leading to shrinkage of the material. The stresses that would exist in a weldment after all external loads are removed are called residual stresses. The residual stresses are internal stresses of self-equilibrating nature i.e. it can be tensile and compressive in different locations but both types will balance each other. The development of residual stress with temperature distribution in one direction is illustrated in Figure 1.3, it can be seen that both compressive and tensile residual stresses are present after cooling.

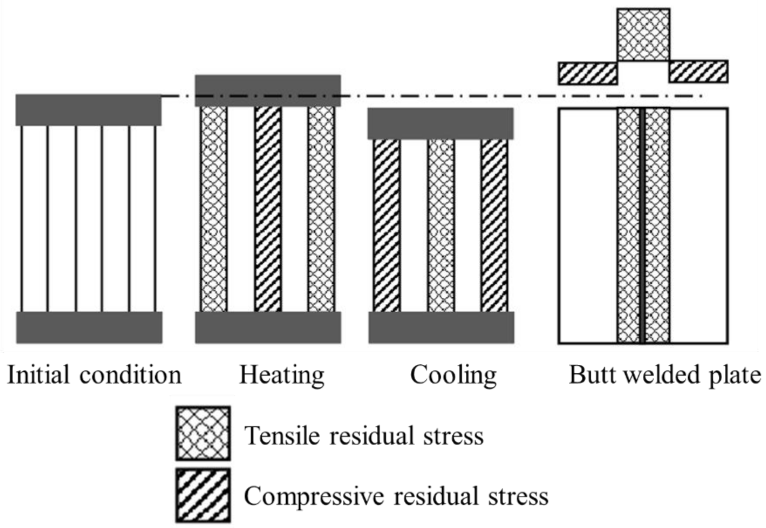

Figure 1.4 Three bar analogy for residual stresses [21]

If we consider the three bar analogy as shown in the Figure 1.4, where the weld zone is thought of the middle bar and the surrounding sides are two other bars fixed together at both ends. While heating the middle bar i.e. the weld zone will try to expand but the attached colder bars (surrounding) will resist therefore compressive residual stress will develop in the weld zone but tensile residual stress will develop in the surroundings. But during cooling the molten weld zone will try to shrink. Due to this tensile stress will develop in the longitudinal as well as in the transverse direction in the weld zone. Both compressive and tensile stresses are complementary in nature and balance each other. The stress distribution in transverse and longitudinal direction is shown in Figure 1.5. As the transverse thermal gradient is much larger the longitudinal one, the plastic strain and shrinkage in transverse direction will be around 10 times more than the longitudinal strain and shrinkage, thus the magnitude of the transverse stresses will be much smaller that the longitudinal one.

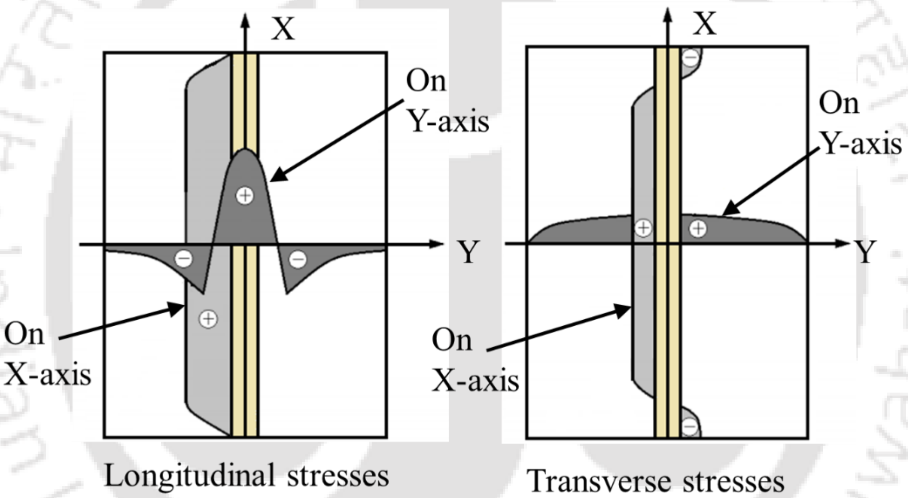

Figure 1.5 Residual stress distribution in butt welded joint **[190]**

Residual stress magnitude depends upon various factors like the amount and rate of heat input, preheat and post weld heat treatment of the sample, material properties, any calculated welding or tacking sequence, use of fasteners or any mechanical treatments etc. Depending upon application (location & orientation) residual stress can have positive and negative effects on the stability of the weld structure. Tensile residual stresses are detrimental for the structure under tensile loading as it will enhance the failure but compressive residual stresses does the opposite. Sometimes residual stress are incorporated into the structures by operations like shot peening to get the benefit of it. The fatigue strength of welded structure is highly influenced by residual stresses, presence of tensile residual stress reduces the fatigue strength but compressive one enhances the same. The residual stresses can be relieved from the weld by relieving the locked in strains. From a metallurgical point of view, three different types of residual stress are identified, based on the scale of the observed material [22]. The macroscopic stresses (stresses of the first kind) are defined on the level of several metal grains; micro stresses of the second kind are defined over one single grain, while micro stresses of the third kind are defined on a part of the grain.

Residual stresses due to thermal gradient produces deformations of the structure. During cooling stage, molten weld zone and the adjacent base metal shrinks, due to the shrinkage forces distortions develops in the welded structure. As a rule of thumb residual stress and angular deformation are inversely related, if residual stress increases the amount of distortion decreases and vice versa. The plot of residual stress and distortion is shown in the Figure 1.6. It can be observed from the Figure 1.6, with the increase in degree of restraint, the magnitude of residual stress increases but distortion decreases & vice versa.

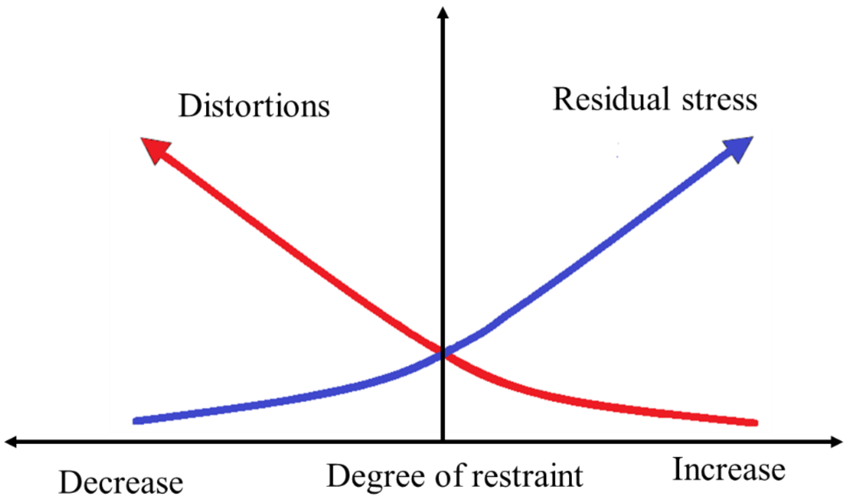

Figure 1.6 Relation between residual stress and distortion [23]

During welding, thermal gradients are produced. Due to non-uniform heating and cooling cycles in the weld and adjacent base metal, complex thermal strains are developed. The stresses resulting from the thermal strains produce internal forces leading to shrinkage of the material. The stresses that would exist in a weldment after all external loads are removed are called residual stresses. Depending on the shrinkage pattern and the shape of the structure welded, various deformations take place. Generally there four fundamental types of weld distortion viz. transverse shrinkage, longitudinal shrinkage and angular deformation in two directions. Figure 1.7 shows various types of weld distortions like transverse and longitudinal shrinkage, bending, buckling, rotational distortion, angular distortion etc. for but welded joints. Angular deformations for fillet welded joints are also shown in the Figure 1.8.

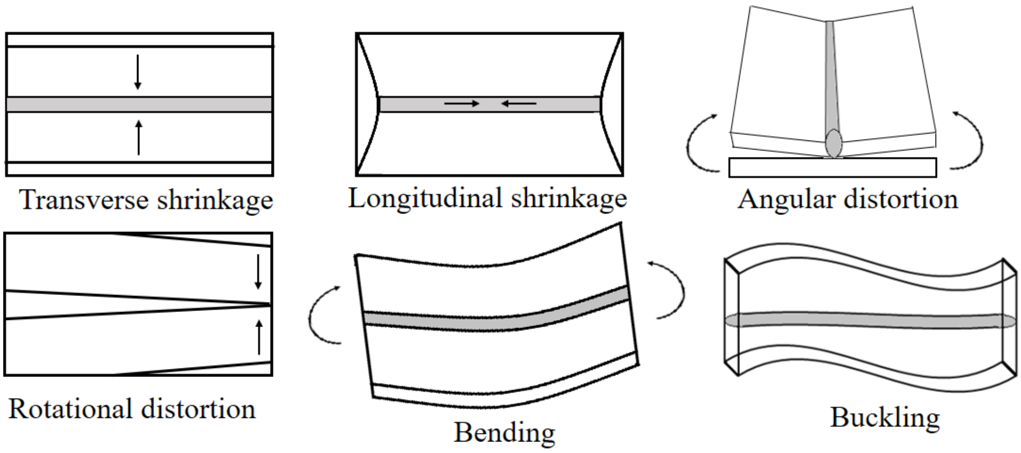

Figure 1.7 Types of welding deformations for butt joints

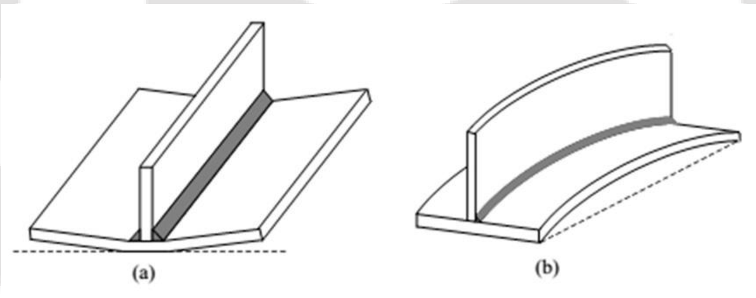

Figure 1.8 Various types of welding distortions in fillet joints (a) angular deformation (b) Longitudinal distortion

Shrinkage force dring cooling of the welds causes the distortions in the welded structure. Post welding residual stress and distortion are the major problems to get a sound weld joint. Residual stresses are more difficult to predict than the in-service stresses on which they superimpose. For this reason, it is important to have reliable methods for the prediction & control and measurement of these stresses and distortions. Understanding & developing proper methods is necessary to address the challenging issues for mitigation of residual stress and distortion in real life welded structures.

In a nutshell, development of techniques for reducing the angular deformation for various joint configurations as well as large structures is the main objective of the present work. Numerical simulation of heat transfer as well as structural analysis of submerged arc welding process for prediction of the residual stress and angular deformation are among the other major contribution of the present work. Emphasis was given towards the development of a new heat source to predict the weld bead geometry of submerged arc welding. Thereafter, experimental investigation was performed for studying the mechanical properties of the submerged arc welded mild steel joints. Optimization techniques were applied for predicting best weld parameter combination for getting a sound weld joint. It is understood that the developed thermo-mechanical model of submerged arc welding has scope for utilization for real life problems in industries for practicing engineers.

1.5 Research Objectives

The overall objective of the thesis is understanding the physics of submerged arc welding while efforts have been given to quantify the residual stress and deformation in submerged arc welds. In this effect, some work is done in the direction of developing suitable mitigation techniques for controlling resdual stress and deformation. The influence of activated flux on weld bead geometry as well as mechanical properties have been studied. Optimization process parameters in different weld conditions were given some importance. Development of appropriate heat source for fusion welds is a challenging task, so efforts have been made in that direction. Finally some works are reported to predict angular deformation in large structures using equivalent loading techniques. Finally to achieve the research objectives the following segments were accomplished either separately or simulteneously, which are developed over the whole duration of the research work.

- Prediction of thermal history and residual deformation of single pass single sided butt joints and single & double sided fillet joints.
- Development of FE transient elasto-plastic thermo-mechanical model to compute the influence of tacking sequence on residual stress and distortion
- Development of a FE thermo-mechanical model to study the effect of welding sequence on thermal history, residual stresses and distortion in fillet welds.

- Comparative study of residual stresses and angular deformation between single and double sided fillet welded joints.
- Estimation of weld induced distortion of large structures using an equivalent loading technique.
- Development of a new heat source model i.e. avocado-configuration volumetric heat source model with more accurate consideration of the shape of the moving heat source. Prediction of the temperature distribution and the weld-pool dimensions using the newly developed avocado-configuration heat source model.
- Study of the effect of activated flux on weld bead geometry and mechanical properties.
- Study of the influence of edge process parameters on weld mechanical properties
- Optimization of the welding process parameters using Taguchi method and Grey relational analysis for getting the best weld mechanical property.

1.6 Layout of thesis

- Introduction to the subject, main objective and the layout of the report is included in Chapter 1. It also describes the working principle of submerged arc welding and types of welding deformations.

- Chapter 2 presents a critical literature review of the work of previous researchers. A brief description of different heat source models proposed from past to till date is given in Chapter 2. It also includes the past works on FEM prediction of residual stress analysis as well as experimental analysis. The works on the effect of flux composition on SAW joints and the metallurgical aspects of SAW is described briefly. The use of several optimization techniques applied on SAW has explained here in Chapter 2.

- The beginning of Chapter 3 outlines the theory of the heat transfer, then the highly temperature dependent thermal properties are introduced. A brief theory of residual stress analysis, theoretical background of the numerical analysis and the detail procedure of the coupled thermo-mechanical analysis and theory of soft computing techniques has been discussed in chapter 3. It also includes the mathematical background for the development of a volumetric new heat source model.

- The detail plan of work and experimental investigation procedure has been described in the chapter 4. Submegred arc welding was used to weld mild steel plates. Welding were carried out in different joint configurations. Mechanical properties as well as microstructural properties have been studied. Angular deformatoon and residual sresses were also measured.

- The results and discussion of the experimental investigation and the numerical analysis is represented in Chapter 5. The results are validated with experimental and published literature. The study of the effect of tacking and welding sequences on residual stress and angular distortion of single sided fillet weld is done and validated with conducted experiments. A study on comparison of residual stresses induced in a single vs. double sided fillet welding structure is presented here. An analysis is made to find out the influence of welding parameters on weld induced residual stresses in a butt joint. An equivalent loading technique is applied to find out the angular deformation in large structure. Furthermore, this chapter presents the influence of surface active elements on weld bead geometry and mechanical properties. Effect of edge preparation on mechanical properties also presented here. Finally optimization modules were used to find out the optimum process parameters.

- The conclusions of present research work are described in Chapter 6. The outline of the future works are also included in this chapter.

- The thesis ends with appendix-1, author's resume and a list of references cited in different chapters.

CHAPTER 2

Literature Review

2.1 General Introduction

Fusion welding process uses a suitable heat source to melt and join the parent metal locally with or without filler metal deposition followed by solidification of the joint. A number of aspects involved in this complete process are namely heat generation, heat transfer, thermal expansion, thermal contraction & solidification etc. The heat applied from the fusion welding heat source creates a huge temperature gradient in a localized manner, followed by thermal expansion and contraction of the joint materials. Therefore after the weld joint cools down to the ambient temperature it possesses residual stress and angular distortion, thus affecting quality of the final part.

To understand the thermo-mechanical behaviour of the fusion welding process, the research work of the previous researchers in the field of computational welding mechanics was surveyed. The complexity of the welding process makes the prediction of weld thermal cycle a difficult task but by the application of finite element (FE) modelling and simulation helps in the prediction of thermal history, residual stress & distortion, weld bead geometry, heat affected zones and weld metal flow pattern etc. beforehand. Some of which cannot be well understood using the conventional experimental techniques alone. Tools are being developed to simulate the welding process so that the methods of controlling and mitigating the residual stresses and angular deformations can be controlled to increase the life of the welded structure. Finding a proper combination of welding parameters is a critical issue, as the optimal welding parameter setting plays a crucial role to achieve a sound weld joint, various optimization tools have been developed to predict the optimum process parameters. A good understanding of the recent research works is necessary, so the quality of the weld joint as well as the end product can be improved as well as failures of the same can be reduced. Therefore this chapter presents a brief literature survey on the recent developments in the numerical and experimental studies of thermo-mechanical analysis of fusion welding followed by optimization of the process parameters and developments in the field of weld induced residual stress and distortion analysis.

2.2 Modelling of heat sources in welding

One of the major problems in the welding industries is to tackle with problems of the weld induced residual stresses and distortions. If weld induced residual stresses and distortions are not treated by post weld heat treatment or by any preventive measures, then it will eventually cause reduced strength of a welded structure and early failure of the weld joint. These problems result directly from the localized differential heating and cooling due to the instance heat input from welding arc. Thermal stresses are the sole reason for the development of residual stress and distortion in the welded structures therefore precise prediction of these stresses, distortions, and strength requires precise prediction of the thermal history. The primary objective of the weld heat source modelling is to represent the distribution of true source of heat mathematically. Weld parameters like welding current, voltage, diameter of the electrode, welding speed, wire feed rate & length of electrode stick out etc. are involved in arc welding process. Thermal history patterns depend upon the weld parameters as these are the functions of heat input. Therefore, as heat distribution shape is a function of the input weld parameters and the shape changes with the variation in input parameters of welding process. Therefore, to successfully design an accurate weld joint, study of temperature distribution of the weld is essential.

Rosenthal [25] implemented Fourier's [24] basic theory of heat conduction in moving coordinate system to develop solutions for point and line heat sources. Linear two-dimensional and three-dimensional heat flow in solid of infinite size or bounded by planes was established. To validate the model, experiments were conducted and agreement was seen in between the predicted and experimentally measured temperature distributions during plate welding of different geometries (length, width, and thickness). The effect of welding parameters was taken into consideration into Rosenthal's model. Welding current, welding voltage, welding speed, and weld geometry were considered in Rosenthal's model. Rosenthal simplified the welding heat source into three types as per the heat transfer patterns, which are point heat source, line heat source and area heat source. The temperature distribution by a point heat source which can be used for surfacing thick plates can be found from the following formula.

$$T = \frac{2Q}{c\rho(4\pi\alpha t)^{3/2}} \exp\left(-\frac{D^2}{4\alpha t}\right) \tag{2.1}$$

where Q is the instantaneous heat energy offered by the heat source, $Q = \eta IV$, η = efficiency of the heat source, I = welding current and V = welding voltage, α = thermal diffusivity, D = distance away from the center of the heat source such that:

$$D = (x^2 + y^2 + z^2)^{1/2} \tag{2.2}$$

In the case of infinite thin plate, a line heat source is considered along the plate thickness, the temperature field can be expressed as:

$$T = \frac{Q}{4\pi\lambda ht} \exp\left(-\frac{d^2}{4\alpha t}\right) \tag{2.3}$$

where d is the distance away from the line source, $d = (x^2 + y^2)^{1/2}$

In the case of butt-welding the heat source is considered as area source, and the temperature field can be found as:

$$T = \frac{Q}{c\rho A(4\pi\alpha t)^{1/2}} \exp\left(-\frac{d^2}{4\alpha t}\right) \tag{2.4}$$

where A is the area of the section and x is the distance away from the area source.

As per the study of Eager et al. [26] and subsequent researchers, Rosenthal models have the limitation of not able to predict temperature in and near the weld joint as he considered point heat source and temperature at the heat source is infinity. There was limitation to consider temperature dependent material properties, phase change, and latent heat. Therefore, the accuracy of prediction of the HAZ is relatively low. However Rosenthal's model gave good approximation of temperature in the extended field. Due to the simplicity of the model and acceptable accuracy in the low temperature zone Rosenthal's model is one of the most widely accepted models.

Followed by Rosenthal's work, researchers developed several other heat source models to predict the weld temperature distribution. Some notable works like multiple point heat sources by Rybicki et al. [27]. Debicarri [28] produced better estimation of transient temperature distribution. Line heat source was used by Seo et al. [29] to model heat input from the welding torch. Gaussian distributed heat source was proposed by Friedman [30] to approximate the heat flux in the heating spot, as shown in Figure 2.1. The distributed heat flux *q(r)* can be expressed as:

$$q(r) = q_{\max} \exp(-\frac{3r^2}{R^2}) = \frac{3Q}{\pi R^2} \exp(-\frac{3r^2}{R^2}) \tag{2.5}$$

where q_{max} is the maximum heat flux at the center of the heat source; r is the distance from the heat source center; Q is the heat input energy of the arc; and R is the radius of the heating spot. The Gaussian distributed heat source modal is widely used for the welding processes like SAW, GTAW, SMAW and proved to provide accurate enough results.

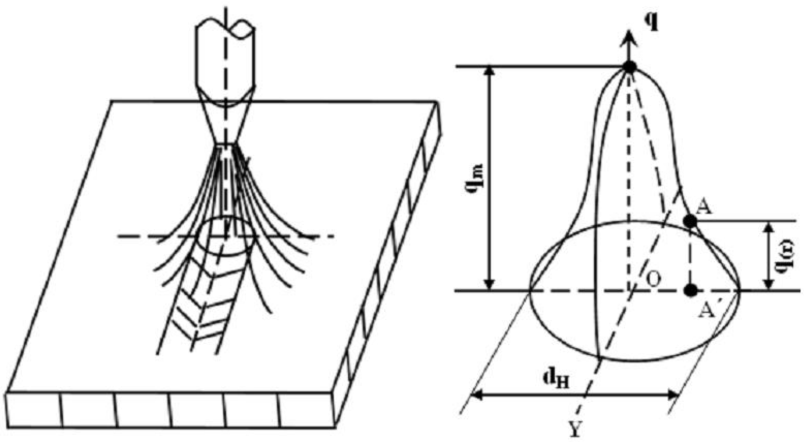

Figure 2.1 The Gaussian distributed heat source [30]

Due to the welding speed, the momentum effect of arc is considerably large which was not addresses by the previous researchers therefore accuracy of the models were poor. Goldak et al. [32] suggested a Gaussian distributed semi-ellipsoidal heat source model, where the shape of the models looks like an ellipse and the heat flux is distributed in a Gaussian manner throughout the heat source's volume as shown in the Figure 2.2. It can be seen from the figure that a_h, b_h and c_h are the semi-axes of the ellipsoid. At the center of the heat source heat flux reaches the maximum value.

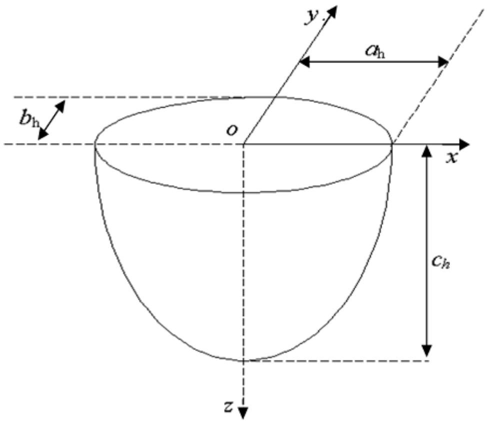

Figure 2.2 Goldak's semi-ellipsoidal distributed heat source [32]

The heat flux *Q(x, y, z)* at a point *(x, y, z)* within the semi-ellipsoid is expressed by:

$$q(x,y,z)=\frac{6\sqrt{3}Q}{a_h b_h c_h \pi\sqrt{\pi}}\exp(-\frac{3x^2}{a_h{}^2}-\frac{3y^2}{b_h{}^2}-\frac{3z^2}{c_h{}^2}) \tag{2.6}$$

While comparing the predicted data by the semi-ellipsoidal model with experimental ones, it has been found that the estimated temperature gradients in front of the weld arc were less steep than the experimental ones. Whereas the estimated temperature gradients behind the arc were steeper than the experimental ones. To overcome this issue appeared in the semi-ellipsoidal model, Goldak et al. [32, 33] proposed the double ellipsoidal model with Gaussian heat source distribution which is shown in Figure 2.3. This model is one of the most widely used model at the present day.

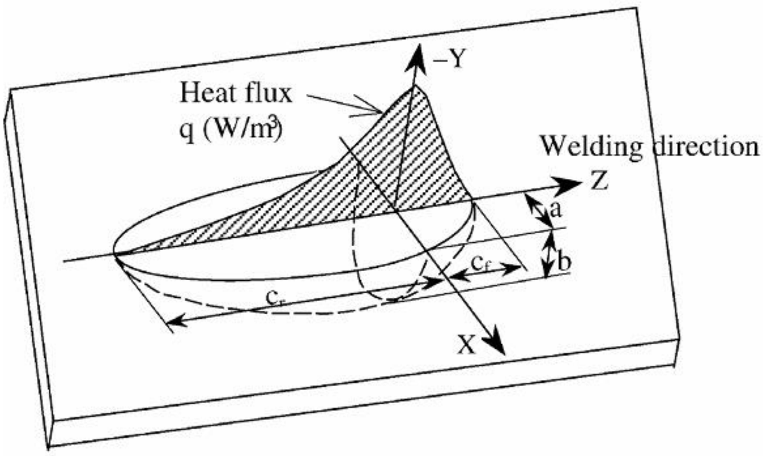

Figure 2.3 Double-ellipsoidal distributed heat source [33]

To develop the double ellipsoid model, Goldak combined two separate semi-ellipsoids, the heat flux within each semi-ellipsoid are expressed by two separate equations.

The heat flux for a point within the first semi-ellipsoid located in front of the welding arc is expressed by the following equation:

$$q_f(x,y,z)=\frac{6\sqrt{3}f_fQ}{abc_f\pi^{3/2}}\exp(-\frac{3x^2}{a^2}-\frac{3y^2}{b^2}-\frac{3z^2}{c_f{}^2})\text{, } x\geq 0 \tag{2.7}$$

Similarly the equation of the heat flux for the rear part is expressed as:

$$q_r(x,y,z)=\frac{6\sqrt{3}f_rQ}{abc_r\pi^{3/2}}\exp(-\frac{3x^2}{a^2}-\frac{3y^2}{b^2}-\frac{3z^2}{c_r{}^2}) \tag{2.8}$$

where f_f and f_r are the heat inputs fractions in the front and rear sections of the heat source respectively. a, b, c_r and c_f are the ellipsoidal heat source parameters as shown in Figure 2.3. As the double ellipsoidal model provides a realistic shape and good approximations of the arc welds using a simple elliptical curve, this model is most widely used and it is widely called as double ellipsoidal heat source model.

In the past years, considerable interest in the thermal aspects of welding was expressed by many researchers, such as Michaleris and DeBiccari [34], Wahab et al. [35], and Gery et al. [36] and others. Keeping in view the requirements, certain other heat source models such as those, which were presented, by Sabapathy et al. [37] and Ravichandran et al. [38] are also in practice. As welding is a multi-physics problem, models backed by fluid flow is capable of predicting the weld pool shape most appropriately, where weld metal flow characteristics are also taken into conversation during modelling. Most prominent among the few researchers who have significant contribution in the flow based models are Zhang et al. [42], Rai et al. [43], Wang et al. [44] and Hel et al. [45]. A three-dimensional numerical model based on transport phenomena to analyse heat transfer and fluid flow in fusion welding process is developed using finite element method (FEM) to estimate the temperature profile during fusion welding process by Bag et al. [36]. Though, these models can predict the weld pool shape more accurately but on the other hand it increases the computational complexity.

The recent heat source models used in estimation of fusion welding temperature distributions are analytically estimated in various geometric shapes, which follow Gaussian distribution. However, more accurate estimation of the shape and size of volumetric heat source is established based on the experimentally measured weld dimensions. Prediction of the unknown parameters of heat source is estimated by following inverse approach combining experimental data and numerical data within a kernel of multivariable optimization algorithm [46-49]. Bag et al. [46] applied genetic optimization to predict the uncertain weld parameters of adaptive volumetric heat source models. A differential evolution (DE) based optimization tool was established to find the uncertain weld parameters in inverse analysis. It was followed by 3D finite element (FE) based fluid flow and heat transfer model to predict the thermal history of laser welding [49]. Figure 2.4 shows the dimensions of different parts of a heat source moving at a certain velocity. a_1, a_2 denotes the heat source length, b is the width and c is the depth of the heat source.

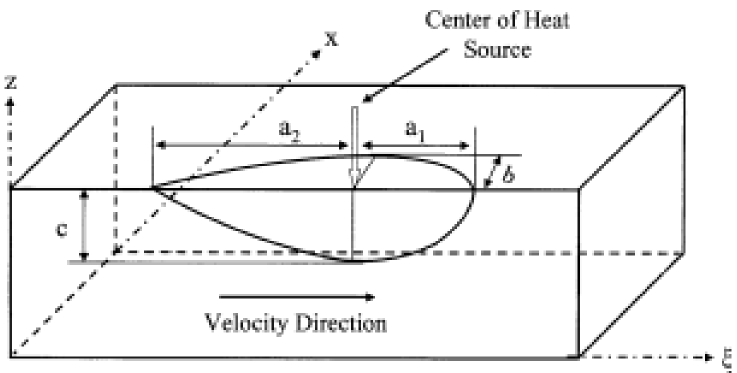

Figure 2.4 Schematic representations of the dimensions of the heat source [46]

A 2D finite element model of the thermal cycle during SAW multi-pass butt welding is developed by Perez et al. [50]. The results of the 2D model are compared against the results of a 3D model showing that it is reliable to use 2D models in engineering applications. Ghosh et al. [51] has presented a heat transfer model considering a moving heat source with Gaussian distribution to predict the thermal history related to submerged arc welded plates. The analytical solutions for a dynamic heat source (such as semi and double ellipsoidal) was developed by Nyguyen et al. [52] but the prediction results of the semi ellipsoidal 3-D heat source was less accurate then the double ellipsoidal one.

Ghosh et al. [53, 54] developed some analytical models, they developed the analytical solutions for a double central conicoidal heat source model. It is reported that the developed model [54] is providing less error than the double ellipsoidal heat source model. By choosing suitable heat source parameter values the double central conicoidal heat source can be applied for any welding process. It can also be reduced to 2-D Gaussian distributed heat source and point heat source; therefore it is a more generalized model. The heat source model was used to estimate the temperature distributions of submerged arc welded thick plates [53], the heat input that is applied on the plate is considered exactly as same amount of heat lost for electric arc. The heat density *q(x, y, z)* at a point *(x, y, z)* with in semi-central conicoid is expressed as follows:

$$q(x,y,z)=\frac{2\sqrt{abc}}{\pi^{3/2}}Q_0\,\mathrm{e}^{-(ax^2+by^2+cz^2)} \tag{2.9}$$

As it is quite challenging to experimentally measure the front and rear ellipsoid length of the heat source accurately, in practice, some approximate value is assumed. The dimensions of the heat source changes while moving at different speeds as per the requirements of the welding process. Yadaiah et al. [55] proposed a 3D model to determine the optimum value of the ratio of front and rear length of the ellipsoids of the double ellipsoidal heat source model. The ratio is assumed on the basis of the weld speed and a suitable functional form is calculated over a range of welding speed and welding current.

Over the years researchers have tried to modify the existing heat source model to get better approximation, some novel models were also proposed. Works in the direction of identifying model parameters and development of composite heat source models by merging different existed models was also reported. Wu et al. [56] have proposed a combined heat source model for the estimation of thermal profile of keyhole plasma arc welding process. One double ellipsoidal and one cylindrical heat source models were combined together to account the heat source configuration in keyhole mode plasma arc welding process. Figure 2.5 shows the comparison between the predicted and measured weld cross-section using the hybrid heat source, a good agreement can be observed.

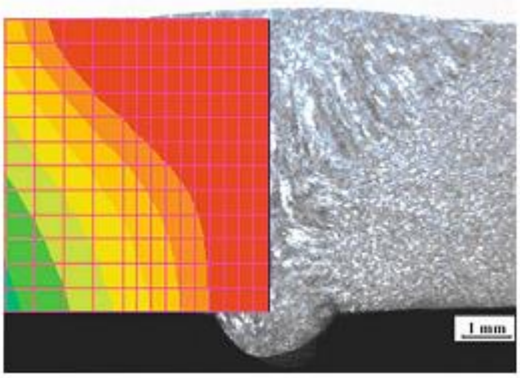

Figure 2.5 Comparison between the predicted and measured weld cross-section [56]

Luo et al. [57] have reported another use of combined heat source model, they studied the thermal effects of electron beam welded magnesium alloy. Gaussian distributed heat flux is considered on top surface and volumetric conical heat source model was applied through thickness of the plate. Li et al. [58] developed combined heat source model for the study of the tandem submerged arc welding (T-SAW) process. Due to the self-induced magnetic field the arc is deflected in T-SAW, because of which the authors developed the heat source model by taking the reflection angle into account. Gaussian distributed surface flux was used along with double ellipsoidal heat source models. The model parameters were obtained by PSM (pattern search method) and predicted by ANN (Artificial Neural Network) and SVM (Support Vector Machine).

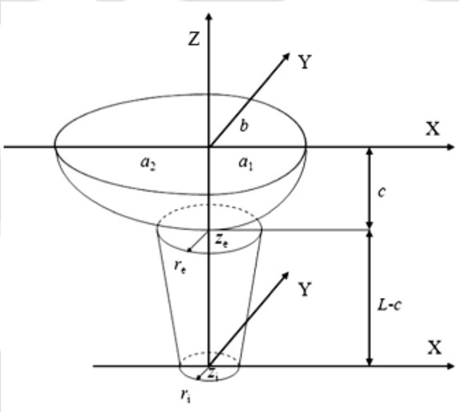

Figure 2.6 Combined volumetric heat source model [59]

Li et al. [59] proposed a combined heat source model to analyse the heat transfer and fluid flow patterns in plasma arc welding process (Figure 2.6). Two existing heat sources are combined together to get the new volumetric heat source model, a double-ellipsoidal heat source is used at the upper part and a conical volumetric heat source at the lower part to get the approximation of the key-hole mode plasma arc. Azer et al. [60] estimated the dimensions of a heat source based upon experimentally observed weld pool sizes. An analytical approach named ‘discretely distributed point heat source model’ is used as an intermediate stage between the experiments and the numerical model. In the numerical model, the heat source is splitted into two perpendicular 2-D ellipsoidal heat sources which correspond to the double ellipsoidal heat source model. To approximate the moving heat source accurately, the third dimension of the heat source is measured from end crater as shown in the following Figure 2.7.

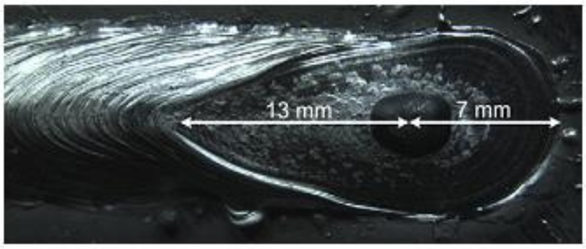

Figure 2.7 Calibration of front and rear sections based on the end crated geometry [60]

Podder et al. [61] proposed a heat source model to estimate weld bead geometry of submerged arc welded mils steel joints. They combined three ellipsoids, where the heat source parameters of the double ellipsoidal model are determined through regression analysis. Temperature dependent material properties like thermal conductivity of the molten weld metal was found to provide a realistic picture of heat flow for submerged arc welding of plates with plate thicknesses ranging from 6 to 16 mm. The heat source model is shown in the Figure 2.8 and the corresponding weld bead geometry from experiments is shown in Figure 2.9. The weld beads *(A)*, horizontal penetration depth *(B)*, and finger formation *(C)* were considered as separate ellipsoids. Ellipsoids *A* and *B* contribute to the heat content of the horizontal portion, and ellipsoid *C* will contribute to the heat content of the vertical portion. The overlap portion is also considered as the heat content of the horizontal portion. The ellipsoids *A* and *B* were jointly taken as one ellipsoid.

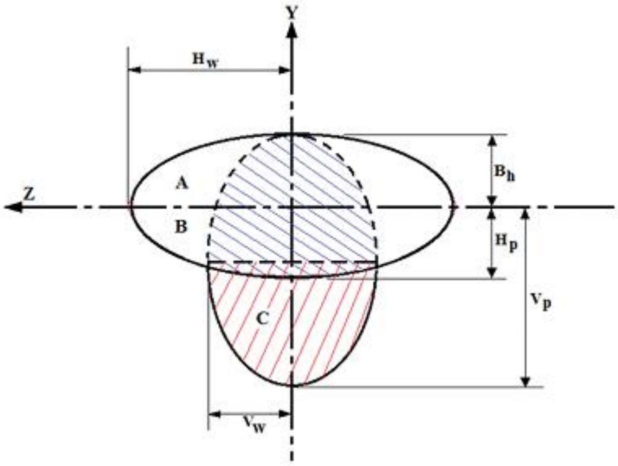

Figure 2.8 Assumption of the realistic weld pool shape [61]

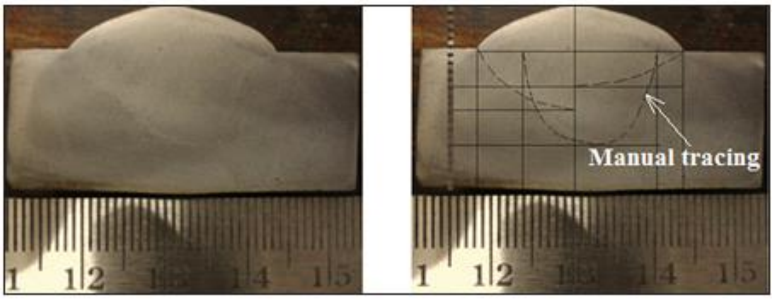

Figure 2.9 A typical weld pool showing the vertical and horizontal ellipsoids [61]

Yadaiah et al. [62] developed a new egg shaped heat source model in the direction of minimizing the model parameters with geometric shape of an egg for the simulation of fusion welding processes without violating the non-symmetry heat density distribution. The effect of welding speed on volumetric heat is taken into account with changes in measurable weld dimensions and the parameter '*m*'. The authors reported to develop generalized form of heat source, while the present available distributed heat source models are mapped with regular geometric shapes like disc, semi-ellipse, double ellipsoidal, conical, spherical, or combinations of these existing configurations. The 2-D comparison of the egg shape model with an ellipse of same semi axis is shown in the Figure 2.10.

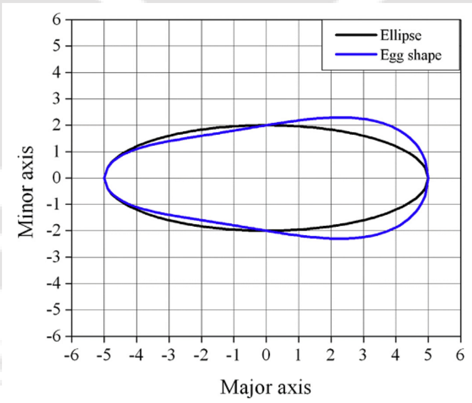

Figure 2.10 Comparison of 2D egg shape and ellipse with same semi-axes: ellipse and egg shape [62]

The heat density distribution inside the front part and rear part of the egg shape model is expressed as:

$$q_f(x,y,z) = \frac{36\sqrt{3}QN_f}{\pi\sqrt{\pi}\times abc(6+m^2b^2)} e^{-[\frac{3y^2}{b^2}+(\frac{3x^2}{a^2}+\frac{3z^2}{c^2})\times(\frac{1}{my+m^2y^2+1})]} \quad (2.10)$$

$$q_r(x,y,z)=\frac{36\sqrt{3}QN_r}{\pi\sqrt{\pi}\times abc(6+m^2b^2)}\mathrm{e}^{-[\frac{3y^2}{b^2}+(\frac{3x^2}{a^2}+\frac{3z^2}{c^2})\times(\frac{1}{-my+m^2y^2+1})]} \tag{2.11}$$

where N_f and N_r are the front and rear fraction of the heat deposition respectively. *a, b, c* are the semi-axes of the egg-shape model in the *x, y, z* directions respectively. The term '*m*' is the prime factor for deciding the shape of egg.

It is well understood from the literatures that the heat conduction based models are not sufficient to predict the thermal history precisely; volumetric heat source can do the job more effectively. However, Gaussian distributed heat flux is used for simplicity of the analysis. It can also be agreed that accurate estimation of the heat source shape is quite a challenging task, therefore researchers considered some near neat heat source shapes for the prediction of the thermal history.

2.3 Thermo-mechanical analysis in fusion welding

The transient thermo-mechanical history of welding involves a lots of sub-processes viz. heat transfer, fluid flow, structural changes, micro-structural changes etc. therefore accurate measurement of the thermo-mechanical history is necessary for critical understanding of the thermo-mechanical behavior of the welds. Experimental measurement procedures of the thermo-mechanical behavior of the welds always comprises of critical measurement steppes, significant amount of time and resources. Mathematical modelling provides a platform to analyze the thermo-mechanical behavior of the welds in a resource effective way followed by an experimental validation. Over the years researchers are trying to model the thermo-mechanical behavior using various analytical and numerical tools. With the development of powerful computational facilities, the FE methods are extensively being more useful to solve the problems in the field of welding technology. The works done by the previous researchers in the field of computational welding mechanics are presented as follows.

Published literature reveals significant computational work related to the modelling and simulation of single or multi-pass welds. The emphasis was to successfully model the nonlinear transient heat flow during welding with the introduction of moving heat source. A number of literature reviews on welding simulation research are already published, one of the prominent work among them is the inclusive review by Lindgren in three parts [63-65]. As the heat flow determines the final mechanical property of the welded joints therefore understanding the theory of heat flow is necessary to study the welding process. The first research was done by Rosenthal [25], who developed a conduction mode analytical model for studying the welding heat flow and estimated the shape of weld pool for two and three dimensional welds. To find precise estimation he introduced the concept of moving coordinate system in welding simulation using point and line heat sources. This model took the effect of welding parameters like current, voltage, welding speed and weld geometry into consideration. Watanabe and Satoh [66] used analytical models for predicting the thermal deformations in welding as well as in line heating. They considered the theory of elasticity for prediction of thermal deformations but due to the limited availability of the elastic solutions, there is limited application of this proposed method.

Ueda and Yamakawa [39] were the first among those who analyze the transient thermal stresses by using thermal elasto-plastic finite element model in a butt joint configuration with considering material deposition from a moving electrode. Figure 2.11 shows the computed longitudinal residual stresses. To determine the weld induced residual stress they used the thermal stress strain relationship, total increment in strain determined by the Equation 2.12.

$$\{d\varepsilon\} = \{d\varepsilon^{e}\} + \{d\varepsilon^{T}\} \qquad (2.12)$$

where $\{d\varepsilon^{T}\} = \{\alpha\}dT$; ε^{e} is elastic strain increment, ε^{T} is elastic strain increment, α is the thermal expansion coefficient

Ueda and Yamakawa [39] & Hibbitt and Marcal [4] pioneered the application of finite element techniques in simulation of welding. While carrying out the non-linear uncoupled thermo-mechanical finite element analysis they considered the material nonlinearity and thermal boundary conditions. They predicted the temperature field and residual stress in solids undergoing fusion transformation to a reasonable accuracy but there was no agreement with the experimentally measure results. They had shown that the rate of heat input has a significant effect on the peak temperatures. The complications and intricacies presented by these researchers, restrained the following researchers to explore this complex phenomenon. Later, Friedman [30], Rybicki et al. [27] and Andersson [41] showed some interest in this domain and their contribution helped in clarifying the methodologies involved in welding simulations.

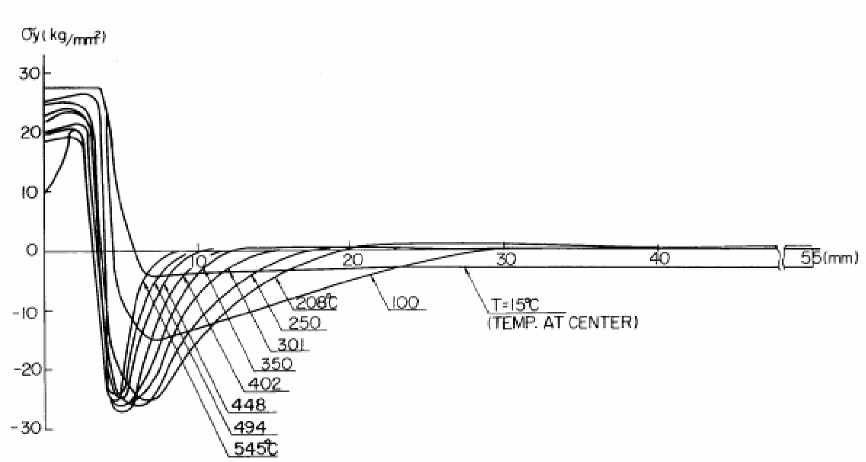

Figure 2.11 Computed Residual stresses [39]

Following this pioneering work, researchers have successfully developed various numerical models [4, 27, 40, 67-70] based on finite element method to predict temperature distribution, analyze the welding residual stress and distortion both in 2-D and 3-D problems. Tekriwal [71] and Bonifaz [72] developed thermal FE simulations to investigate the temperature distribution of metals. Over a sustained period of time FEA is used by many researchers to predict the temperature distribution, residual stresses, and distortion of welded joints. Noticeable among them are Friedman [30], Brown and Song [73], and Michaleris and Debiccari [34]. Use of FEA has been successful in predicting temperature distribution, distortion, and also in tackling of complex phenomena like crack propagation in welded joints. Many researchers used 2D FEA of Friedman [30] to verify their 3D computational model of welding process.

Several researchers [74-75] has carried out experiments to determine the temperature distribution of multi-pass welding. Murugan et al. [75] investigated the temperature distribution during multi-pass welding of carbon steel plates of 6, 8 and 12 mm thicknesses. Figure 2.12 shows the temperature distribution of the multi-pass weld pad. Malik et al. [76] presented a numerical simulation backed with experimental validation to study the thermal history and estimate different weld zone sizes viz. fusion zone (FZ), heat affected zone (HAZ) in TIG welding of mild steel. A simple demonstration of heat effects from welding has presented by Englund et al. [77]. An approximate finite element analysis of the heat applied during welding, and the material changes that considered as a result of the welding operation are included.

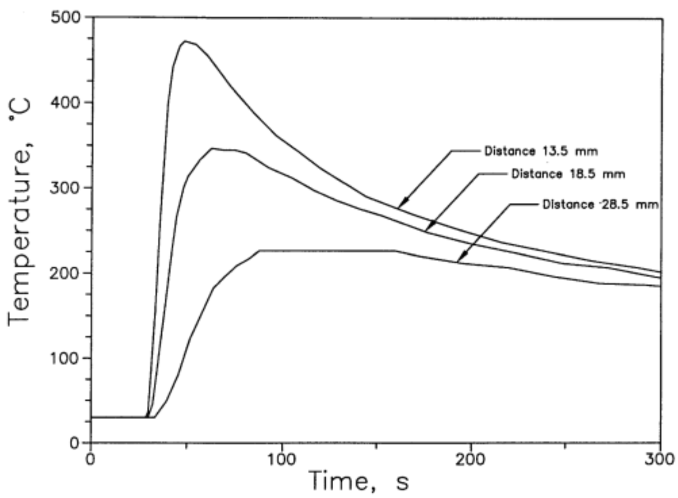

Figure 2.12 Thermal history of multi-pass (second pass) stainless steel weld pad [75]

The arc welding process is a very complex phenomenon which involves very high temperature gradients, rapid heating and cooling, leading to micro-structural changes and formation of thermal stresses. These welding heat induced thermal stresses can cause residual stress extremely high magnitude and angular deformations after the cooling of the weld metal. As a result the strength of the structure may reduce and it may become vulnerable to fracture, buckling, fatigue and enhanced corrosion. Welding distortion causes dimensional inaccuracies and misalignments of structural members, corrective measures or rework may be necessary if tolerance limit is exceeded. This in turn, lengthens the production cycle leading to increase in the cost of production. Hence, the problem of residual stress and distortion are always of great concern in shipbuilding industries. To deal with this problem, suitable mitigation techniques are to be developed. However, prior to that, it is necessary to have a reliable prediction tool to assess the extent of possible distortion and residual stresses that may form during fabrication. During welding, there are various factors like welding parameters, welding sequence, heating and rate of cooling, level of constraints and joint geometry etc. which influence the extent of residual stress and distortion.

Most of the research in the field of thermo-mechanical analysis of welding in recent past was carried out to study the distribution of residual stress and distortion of the welded metal. Michaleris and Debiccari [34] conducted thermo-elasto-plastic FEA to predict weld induced angular deformation by using temperature dependent material properties of the steel. Mandal and Sundar [78] estimated the welding shrinkage in a butt welded joint by applying a near field-far field approach. Puchaicela [79] reviewed and analyzed several formulae in an attempt to provide a practical guide to control and reduce distortion.

Cho et al. [109] has reported detailed analysis on the determination of residual stress after welding and after a post weld heat treatment by using a finite element transient heat flow analysis in conjunction with a coupled thermo-mechanical analysis. A 3-D FEA was developed by Mahapatra et al. [83] to predict the effect of SAW process parameters on temperature distribution and angular distortions in single-pass butt joints with top and bottom reinforcements (to minimize angular distortions). The process was modeled considering a distributed moving heat source, reinforcements, filler material deposition in each pass of welding, and temperature dependent material properties. Figure 2.13 shows the comparison of the predicted and experimentally measured angular distortion.

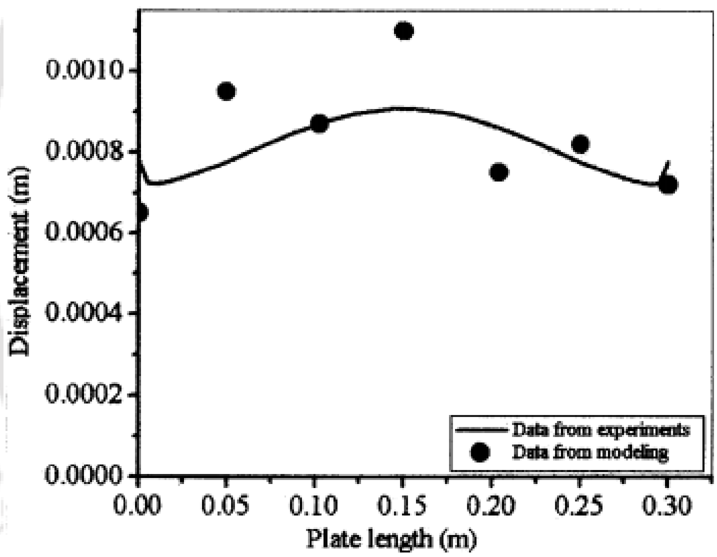

Figure 2.13 Comparison of measured and predicted displacements [83]

Teng et al. [84] have estimated the residual stresses and distortion of fillet welds using 2D FE analysis. Similar work was reported by Tsai et al. [85], they modelled the angular distortion of T-joints using plasticity based distortion analysis. Tack welding is performed to hold the plates in position before the actual welding, which may alter the residual stress distribution of the final part, Mahapatra et al. [86] analysed the effect of tack weld positions on angular deformation in single sided submerged arc welded fillet joints. Tsai and Cheng [80] studied the distortion mechanism and the effects of welding sequence on thin panel distortion using finite element analysis. The works of the above researchers indicates that angular deformation in a welded joint is a matter of great concern which strongly affects the performance of the final structure.

In addition to residual stresses and distortion, researchers have also studied the effect of welding parameters, viz. welding sequences, welding joint geometry, and root opening in the past. A FE analysis of residual stresses of butt weld is reported by Hong et al. [68]. Tsai et al. [80] studied the effect of welding sequence on buckling and warping behavior of a thin plate panel structure. Tsai et al. [81] have also investigated the effect of welding parameters and joint geometry on the magnitude and distribution of residual stresses on thick section butt joint. Jang et al. [82] studied the effect of root opening on the mechanical properties, deformations, and residual stress of the weld joint, Figure 2.14 (a & b) shows the thermal profile of multi-pass welds with 0 mm and 6 mm root opening respectively.

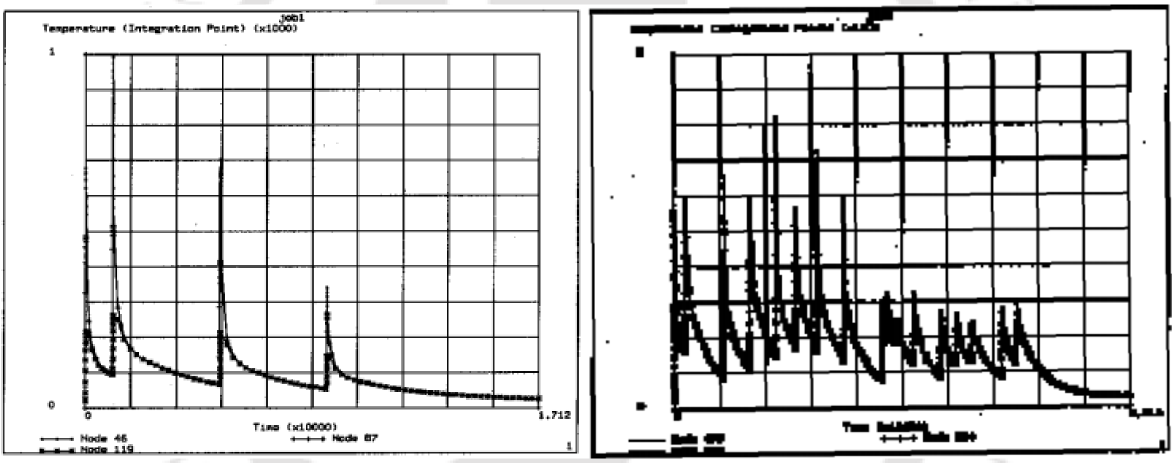

(a) (b)

Figure 2.14 Thermal cycles of multi-pass weld (a) at 0 mm root opening (b) at 6 mm root opening [82]

Biswas et al. [83-88, 127] had performed several investigations to predict the effects of SAW process parameters on temperature distribution and angular distortions in submerged arc welded plates. A 3D FE analysis was developed [83] to predict the effects of weld parameters on temperature distribution and angular distortions in single-pass submerged arc welded butt joints with top and bottom reinforcements to minimize angular distortions. Modelling and prediction of angular distortion [87] of double-pass butt-welded plate was also reported. The process was modelled using 3D FE analysis considering a distributed moving heat source, reinforcements, filler material deposition in each pass of welding, and temperature dependent material properties. Biswas et al. [128] developed a numerical elasto-plastic thermo-mechanical model for predicting the thermal history and resulting angular distortions of submerged arc welded double-sided fillet joints. Biswas et al. [127] also presented another thermo-mechanical finite element analysis and experimental investigation of single-pass single-sided submerged arc welding of C-Mn steel plates. It can be understood from the literatures that distortions occur almost in every type of welded joint, it depends upon various welding parameters, i.e. welding speed, plate thickness, welding current and voltage, restraints applied to the job while welding and thermal history, etc. Welding of large strictures involves multiple welding passes as well as numerous welding sequences. Welding sequence has a significant effect on distortion pattern, proper control of the welding sequences can reduce the weld induced angular deformations. Large orthogonally stiffened panels are generally used in ships and offshore structures, a study on the effect of welding sequence in angular distortions of large stiffened plate panels was also reported by Biswas et al. [88].

But one concern with these models is the huge time consumption for structural analysis. Some researchers tried to develop various equivalent techniques to minimize the analysis time. Souloumiac et al. [89] developed a local/global approach in order to determine the welding residual distortions of large structures. They assumed that plastic strains induced during welding process were located close to the welding path and depend on local thermal and mechanical conditions. The plastic strains obtained by the local approach were then projected to a complete shell of whole structure as initial strain. The final distortions were computed using an elastic simulation. Ueda et al. [90] proposed the experiment-based, equivalent-mechanical-loading method to obtain the final deformation quickly. It assumes that the assigned mechanical forces and moments adjacent to weld-joints generate welding deformation. A critical limitation of this method was that the applied loads should be calculated only from experiments.

To overcome this limitation, inherent strain based equivalent mechanical loading method was proposed by Murakawa et al. [91]. Many researchers further developed this methodology to predict welding distortions [92, 191]. The concept of inherent strain can be understood from the following formula (2.13) and (2.14).

$$\varepsilon = \varepsilon^{e} + \varepsilon^{p} + \varepsilon^{c} + \varepsilon^{T} + \varepsilon^{tr} \tag{2.13}$$

where ε is total strain, ε^{e} is elastic strain, ε^{p} is plastic strain, ε^{c} is creep strain, ε^{T} is thermal strain, ε^{tr} is the strain produced through phase transformation, then inherent strain ε^{*} is defined as follows.

$$\varepsilon - \varepsilon^{e} = \varepsilon^{p} + \varepsilon^{c} + \varepsilon^{T} + \varepsilon^{tr} = \varepsilon^{*} \tag{2.14}$$

However, this methodology had the limitation to be applied for the curved welding joints as the imposed forces might induce welding shrinkage, as well as undesirable angular deformation in case of a curved weld line. Some other researchers like Ha et al. [93, 94] also tried to estimate the angular deformation using the inherent strain method. They suggested that an inherent strain based, equivalent thermal loading method in combination with the nodal temperatures and thermal expansion coefficient could induce welding deformation. They assumed that the positive temperature values are assigned into certain weld line nodes, and others are zero. Also, the imaginary, negative thermal expansion coefficient values equivalent to the inherent strain for the joint of concern, are mapped only onto the weld line elements. The philosophy of this simplified analysis methodology is that the final welding deformation can be produced by finite element analysis, after thermally loaded elements close to the weld line are subject to elasto-plastic behavior by surrounding a stiffened region with no temperature change. The finite element analysis of welding problems is generally performed using commercially available software and standard reference books can be followed [95-97] for the basic formulations of thermo-mechanical analysis.

It can be understood from the literatures that study of the residual stress and distortion in welded structure is quite important to design a stable welded structure. Researchers used finite element analysis to estimate the temperature history followed by thermal strains and residual stresses. Research work to study the effect of welding sequence & process parameters were conducted, some researchers developed residual stress mitigation technics. Though the FE simulation is quite time consuming, it is difficult to analyze the large structures, because of which researchers used some equivalent technic to predict the distortion in large structure.

2.4 Characterization of residual stress

According to Withers and Bhadeshia [14, 15] residual stress is that which remains in a body that is stationary and at equilibrium with its surroundings. It can be very detrimental to the performance of a material or the life of a component. Alternatively, beneficial residual stresses can be introduced deliberately. Residual stresses are more difficult to predict than the in-service stresses on which they superimpose. For this reason, it is important to have reliable methods for the measurement of these stresses and to understand the level of information they can provide. From a metallurgical point of view, three different types of residual stress are recognised [22]. The first kind is macroscopic stresses, which are defined on the level of several metal grains; the second kind is micro stresses which are defined over one single grain, while the third one, micro stresses are defined on a part of a grain. The residual stress measuring techniques can be divided into three categories [98] namely non-destructive, semi-destructive, and destructive.

Commonly used non-destructive techniques are X-ray diffraction (XRD) and neutron diffraction testing. X-ray diffraction [22, 99, 100] is having the ability to measure residual stress in crystalline materials to a maximum depth of about 0.05 mm. Subsurface measurement of the residual stress using XRD technique requires removal of layers using electrolytic polishing which in turn makes the measurement to some extent a destructive one. Neutron diffraction testing can be used to measure residual stresses to depths up to 10 cm. According to references [22, 99, 101-104] the neutron diffraction method has the capability to determine the full residual stress tensor deep below the surface. The major limitations of this technique are the cost of using a neutron diffraction facility, size and weight of the component which can be investigated etc. Smith et al. [102] and Ripley [105] uses neutron diffraction technique and discussed briefly why neutrons are most suitable for measuring residual stresses and the principles that lie behind the measurements. Colegrove et al. [106] measured the residual stresses of each of the SAW samples by neutron diffraction technique.

Other non-destructive techniques commonly in practice are the ultrasonic method [107] and the magnetic method. The application of magnetic method is limited to ferromagnetic materials only. Uzun and Bilge [108] and Bray et al. [107] investigates the total welding residual stress by using ultrasonic wave velocity variations. According to the principle that Ultrasonic wave speed is constant for a material, these waves in turn are used to detect variations in the crystal structure of materials. The source of welding residual stress is welding heat. The relation between thermal stress and ultrasonic wave velocity variations are investigated. By using this relation and ultrasonic wave velocity changes between two samples, residual stress distribution throughout the welded sample is determined. Among the other non-traditional & non-destructive techniques positron annihilation spectroscopy (PAS) [99] have been used to measure residual stresses in austenitic and martensitic stainless steels that were subjected to either cold-deformation or welding operations.

The hole drilling method Cho et al. [109], Centre-hole drilling, ring-coring [99] and deep-hole (DH) drilling [100,102] surface hole Bouchard et al. [103] are considered to be semi-destructive techniques for the measurement of residual stresses. It is performed by making a hole in the test specimen at the centre of a strain gauge rosette [76]. The measurements are performed at various depths, measuring the residual stress values along the thickness of the test specimen. The deep hole drilling method has been applied by various researchers [102, 103, 111-113]. The measurements have been made in butt-welded steel plates 100 mm and 50 mm thick [114] The method has also been applied to obtain through-thickness residual stress distributions in butt-welded ferrite steel pipes of wall thickness 85 mm [112, 113]. These methods are considered to be semi-destructive if the measurements are limited to only few points of the structure that can be repaired easily.

Fully destructive methods include crack compliance [22], slotting, block removal, splitting and layering (BRSL) technique, Sach's boring method [112], Contour method (using WEDM) and Sectioning method [98] These methods are sensitive to the macroscopic residual stresses only. The BRSL method [115] can be used to measure residual stresses to sufficient depths of welded steel plates 50 mm thick [116-118], but essentially destroys the sample. Contour method and sectioning method has been discussed. Ivetic et al. [22] studied the residual stress in welded panels using a destructive sectioning method, using electric strain gauges. Hodgson et al. [119] examines the application of the incremental slitting technique (using WEDM) for residual stress measurement to plastically deformed four-point bent beams and autogenously edge welded steel beams. In their research work Hosseinzadeh and Bouchard [120] illustrates how the contour method of measuring residual stress can be applied to various weldments in order to provide high quality experimental data. In particular they demonstrated the accuracy of the contour method by comparing its results with those obtained from independent measurement techniques, namely neutron diffraction and the slitting method.

2.5 Measurement of angular deformation

Welding stresses and deformations are connected to each other. Thermal stresses disappears after the thermal gradient becomes zero. Though stresses due to phase-transformation may develop during welding of some alloy steels but they do not have any significant effect in the stress development process. Stresses caused by the plastic deformation always exists in the area closer to the weld bead area [121]. During heating and cooling, thermal strains occur in the weld and adjacent area. The strains produced during the heating stage of welding are always associated with plastic deformations of metals. The stresses resulting from these strains combine and react to produce internal forces that cause a variety of welding distortions which can be described as mainly of four types, namely longitudinal shrinkage, transverse shrinkage, angular distortion and bowing. Residual deformations introduce severe problems in the assembly of welded structures and reduce their quality. In some cases mechanical and thermal post-welding treatment is required to correct the deformations. Distorted shape and incorrect dimensions of the structures may render them useless. Welding stresses and deformations have various effects on the welded structures. Mostly, they have negative influence [21, 111-114].

Welding shrinkage and deformations are measured using several methods. Authors like Deng et al. [122-124] used Vernier calliper to measure the transverse shrinkage of a fillet welded joint. Readings were taken before and after the welding at predefined locations. Measuring lines were drawn perpendicular to the weld direction on the back side of the weld joint then a gap ruler was used to measure the initial and final deformation, though the initial deformations were neglected [123]. Instruments like dial gauge was also used to measure the angular deformation [121] where fixtures used to hold the sample. Some researchers [125, 127-129] used linear variable displacement transducer (LVDT) to measure angular deformation at predefined location where the LVDTs are fixed. Matsuoka et al. [131] used laser irradiation experiment where a laser beam is used to measure the positive and negative angles of the deformed weld plate. Some researchers reported the use of Co-ordinate measuring machine (CMM) [132] to measure the angular deformation. In this method a grid line is drawn before welding, then pre and post weld angular deformations of those locations are measured. In an attempt to measure the variation of angular deformation of butt weld, Njiraini et al. [170] used a Vernier height gauge, dial test indicator (DTI) and the time was observed using a stop watch. Various methods of distortion control was applied and the angular deformation at each case was recorded by taking data at predefined multiple locations.

2.6 Mechanical and metallurgical characterization of weld joint

Characterization of mechanical properties is performed to check if the weld is sound enough for the specific application. Generally tensile, hardness, impact and fatigue test of the welds along with some microstructure are popular. Submerged arc welding of thick ferritic martensitic 12Cr stainless steel was performed by Taban et al. [133]. They varied the consumable electrodes and compared the joint strength for different cases. The strength of the weld joints for different cases were characterized by measuring hardness and toughness. Microshear test is a characterization method to estimate the mechanical properties and fracture toughness of pressure vessels. Zhang et al. [134] performed narrow gap submerged arc welding of nuclear pressure vessel steel, A508CL3 and the joints were characterized by the microshear test method. To know the weld joint strength comparison of the yield strength (YS) and ultimate tensile strength (UTS) with the base metal is very much essential, researchers [135] estimates the local tensile strength, YS and UTS of welded joints. Study on double sided single pass submerged arc welding is also reported for high thickness metals [136]. SAW welded 2205 duplex stainless steel and the joint strength was characterized by determining the micro-hardness of the different weld zones. The data was recorded at distance perpendicular to the weld line to know the hardness distribution over fusion zone, heat affect zone and the base metal. It will generally increase towards to the weld center i.e. the fusion zone due to the melting of the metal. Impact test shows the ductile mode fracture in the weld zone, a mixture fracture feature appears with a shear lip and tears in the fusion zone near the fusion line. Ramakrishnan et al. [137] studied fracture toughness of cold wire addition in narrow groove submerged arc welding process. The improvement in toughness in cold wire narrow gap SAW is demonstrated through different tests such as impact energy test, fracture toughness tests, plane strain fracture toughness test, and crack tip opening displacement test.

Over the years researchers has worked to study the mechanical properties as well as the microstructural developments of submerged arc welded work pieces. Welding microstructure can provide adequate information about the effect of welding parameters on the mechanical and tribological behaviour so it is very essential to investigate the welding microstructure. A schematic diagram of various microstructure zones of a butt bead-on-plate weld is presented in Figure 2.15, where BH is the bead height, BW is the bead width, DP is depth of penetration, DH is depth of HAZ and HW is the HAZ width.

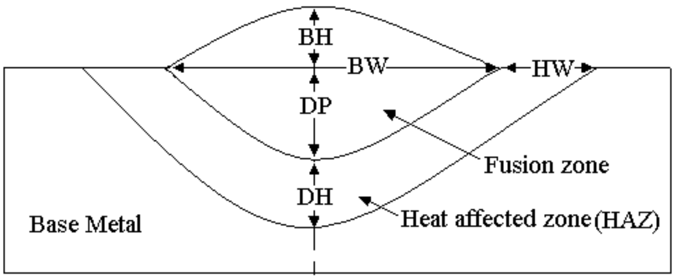

Figure 2.15 Microstructure zones of a butt bead-on-plate

Kolhe and Datta [138] have investigated and correlate the relationship between the various parameters; mechanical properties and microstructure of single "V" butt joint of mild steel plate, and performed the phase analysis of the multipass welded joint to get defect free welded structures. They presented the experimental results of hardness, fracture toughness, HAZ width from top and bottom of the weld joint and the theoretical analysis of phases of the steel at different heat input of multipass submerged arc welding from the top of welded joint by using image analysis software and correlated the same to the microstructures of fusion zone as well as the heat-affected zone of mild steel. Lu et al. [139] has determined the microstructure and wear property of Fe-Mn-Cr-Mo-V alloy cladding by submerged arc welding.

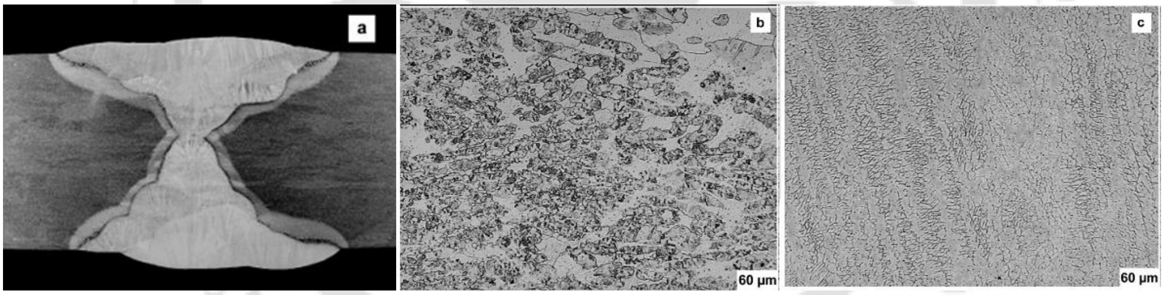

Figure 2.16 (a) Macrograph, (b) micrograph of HAZ, (c) micrograph of fusion zone [133]

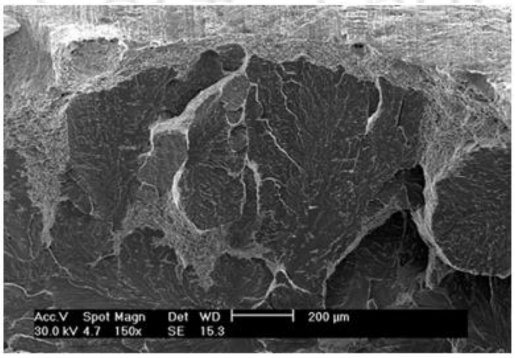

Figure 2.17 SEM fractograph [133]

Microstructural characterization was performed by Taban et al. [133], Figure 2.16 (a) shows the cross section of the weld joint, welded by 21 multi-passes using submerged arc welding. Figures 2.12 (b and c) shows the micrographs of the heat affected zone (HAZ) and the fusion zone. Few samples of the face and root bend testing were failed, which implies decent joint strength of the welds. The fractograph using scanning electron microscope (SEM) is shown in the Figure 2.17. Prasad and Dwivedi [140] investigates the influence of the submerged arc welding process parameters (welding current and welding speed) on the microstructure, hardness, and toughness of HSLA steel weld joints. Attempts have also been made to analyse the results on the basis of the heat input. High heat input increases the deposition rate and lowers the welding time. Paniagua-Mercado et al. [141] presents a study of the effect of TiO_2 additions in fluxes on the mechanical properties and microstructure of the weld metal formed during Submerged-Arc Welding (SAW) of ASTM A-36 steel plates.

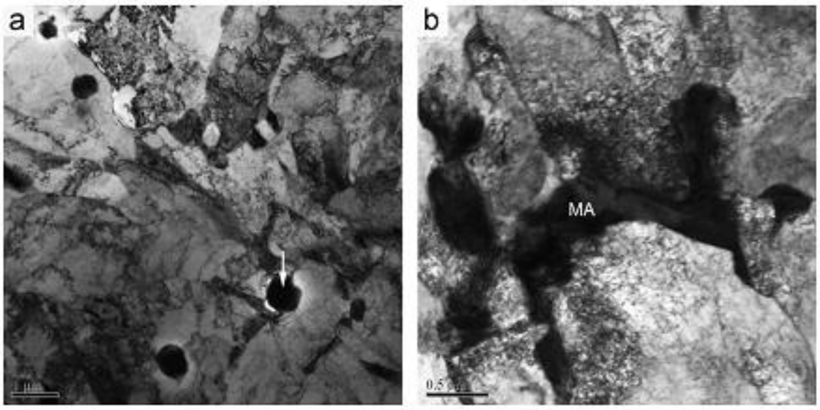

Figure 2.18 TEM micrographs showing (a) acicular ferrite plates and inclusion distribution, (b) irregular MA constituent distributed along the acicular ferrite plate boundary [142]

In depth study of the microstructural variation in high strength bainitic low carbon steel weld was carried by Lan et al. [142] by means of optical microscope, transmission electron microscope (TEM) and scanning electron microscope (SEM). The results displayed (Figure 2.18) confirmed the presence of acicular ferrite, coarse granular ferrite and fine polygonal ferrite in the weld microstructure. The martensite-austenite (MA) constituent has a variable structure in each sub-zone, which includes fully martensite and fully retained austenite. Meanwhile, the fine grained heat affected zone has higher content of retained austenite than the welded metal (WM) and coarse grained heat affected zone (CGHAZ).

2.7 Effect of surface active flux

DuPont [143] reported that there are several theories that attempt to explain the physics due to which surface-active fluxes increase penetration. The effect of Marangoni flow, or surface tension driven flow is the most recognised theory, which states that the surface-active oxide and sulphide fluxes alters the surface tension, reversing the flow of the liquid in the weld pool. Therefore liquid weld metal, flows from the edges of the weld pool to inward and downward towards the pool bottom rather than the typical outward flow (Figure 2.19) which results in deeper, narrower welds due to the heat transfer in the inward and downward to the pool bottom.

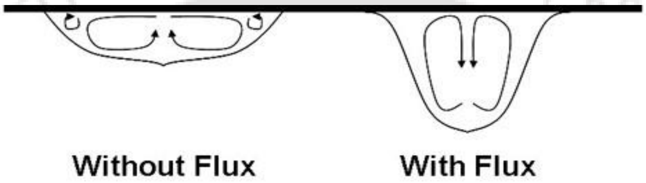

Figure 2.19 Schematic diagram of fluid flow direction in molten weld pool with the use of surface-active flux [143]

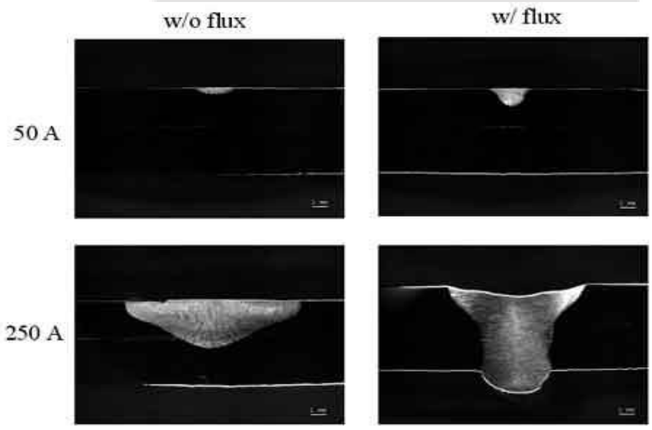

Figure 2.20 Effect of surface active flux on depth of Penetration of GTA welds [143]

Effect of surface active flux on depth of Penetration GTA welds at two different weld currents is shown in Figure 2.20. Other welding parameters were kept constant for this comparison. Regardless of the mechanism, it has been shown that surface fluxes increase the penetration of GTA welds. In their study Tseng & Chuang [144] and Tseng [145] investigates the influences of specific oxide and sulphide flux powders, including FeF_2, FeO, and FeS on weld bead geometry, surface appearance and angular deformation. TIG welds produced with FeF_2 powder had a satisfactory surface appearance, whereas the FeO and FeS welds produced slag and spatter. TIG welding with FeS powder resulted in undercut. TIG welding with FeO and FeS powders increases both the joint penetration and weld aspect ratio, reducing the angular distortion.

Her-Yueh Huang [146] investigated the effects of shielding gas composition and activating flux on weld morphology, angular distortion, retained delta-ferrite content, mechanical properties and hot cracking susceptibility. Activating flux materials consisted of manganese oxide powder and zinc oxide powder mixture. The results showed that the penetration and cross-sectional area of the weld increased. In his another work Her-Yueh Huang [147] used three kinds of oxides, Fe_2O_3, SiO_2, and $MgCO_3$ to study the effect of activating flux assisted MIG welding on weld bead geometry, angular deformation and mechanical properties in low carbon steel.

Modenesi et al. [148] presented that the use of a thin layer of an active flux that results in a great increase in weld penetration. The results of the experiment conducted by Qing-ming et al. [149] indicate that the SiO_2 flux can increase the arc voltage, while TiO_2 has no this effect on arc voltage. Liu et al. [150] used a new type filler wire (flux-coated wire) and reported its advantages in increasing the weld penetration and improving appearance of the weld seam surface are introduced. Lowke et al. [151] reported that the weld depth can be increased by a factor of two or more if a thin layer of flux powder is initially coated on the steel. Snow [152] has shown that the use of a surface active flux (several oxides) during GTA welding has greatly increase penetration. Bag et al. [153] studied the possible role of surface active elements in weld pool modelling of fusion welding process. In this work, the influence of surface active elements is analysed through the nature of flow pattern in autogeneous gas tungsten arc welding process. 3D finite element based heat transfer and fluid flow model is developed to illustrate the transport phenomena of liquid metal within small weld pool. Various researchers have investigated the effect of surface active elements to increase the depth of penetration to find economic alternatives for achieving deep narrow penetration. There is also substantial research [154] to find the possibility of achieving desired penetration in a single pass using surface active elements, which saves the expenses for joint preparation for multiple pass welding.

2.8 Optimization of welding process parameters

The submerged arc welding process finds wide industrial application due to its easy applicability, high current density and ability to deposit a large amount of weld metal using more than one wire at the same time. Weld quality plays an important role in the stability of the final structure [155, 156], an improper welding may leads to failure. Quality of a welded product can be assessed by different parameters like strength, toughness, impact strength, hardness, weld bead geometry & deposition rate etc. These characteristics are controlled by a number of welding parameters like welding current, welding voltage, welding speed & length of electrode stick out etc. therefore, to achieve a sound weld, it is important to set up the appropriate welding process parameters [155-156]. These welding process parameters influences the weld quality characteristics deposition rate, percent dilution, weld bead geometry, metallurgical and mechanical characteristics etc. [155-157]. Proper selection and precise control of process parameters can provide desired weld quality. As the weld quality is assessed by multiple parameters, the optimization of weld quality characteristics is a multi-response problem.

Tsai et al. [158] presented a feedforward neural network to model submerged arc welding processes in hardfacing. The relationships between the process parameters (welding current, voltage, welding speed, electrode stick out, and preheat temperature) and the weld quality (deposition rate, hardness, and dilution) are established. A simulated annealing (SA) optimisation algorithm with a performance index is then applied to the neural network for searching the optimal process parameters. Back-propagation artificial neural networks are used to predict the bead geometry and penetration of shielded metal-arc welding process by Nagesh et al. [159]. The use of fuzzy logic in the Taguchi method to optimise the submerged arc welding process with multiple performance characteristics is reported by Tarng et al. [160]. The process parameters, namely arc current, arc voltage, welding speed, electrode protrusion, and preheat temperature are optimised with considerations of the performance characteristics, including deposition rate and dilution [159] highlights application of Taguchi's robust design coupled with fuzzy based desirability function approach for optimizing multiple bead geometry parameters of submerged arc weldment.

Tarng [161] has reported the use of grey-based Taguchi methods for the optimization of the submerged arc welding process parameters in hardfacing with considerations of multiple weld qualities. As Taguchi method alone can't solve a multi-response problem, the grey relational analysis is adopted to find the optimal parameter settings with multiple weld qualities. A grey relational grade obtained from the grey relational analysis is used as the performance characteristic in the Taguchi method. Then, optimal process parameters are determined by using the parameter design proposed by the Taguchi method. Kumanan et al. [156] presented the details related to the application of Taguchi technique and regression analysis to determine the optimal process parameters for submerged arc welding. The optimization of process parameters was done using Taguchi method and Regression analysis.

Bag et al. [154] presents a novel mathematical framework where the values of a set of uncertain input parameters for mathematical modelling are identified inherently by integrating a finite element based heat transfer simulation using adaptive volumetric heat source and a multivariate optimization algorithm. To obtain the prevalent value of the absorption coefficient as a part of the modelling calculation itself, the present work has integrated a multivariate optimization algorithm with the numerical heat transfer model. In their another work, Bag et al. [162] has performed the error analysis of forward and reverse heat conduction and convection calculations considering uncertainties in welding. A genetic algorithm (GA) assisted integrated numerical model, following either convection or conduction based calculations, can identify the suitable values of the uncertain model input parameters and in turn provides reliable computed results for the prediction of the weld pool dimensions. Bag et al. [163] also have applied the GTA in the development of efficient numerical heat transfer model coupled with genetic algorithm based optimisation for prediction of process variables in GTA spot welding.

Dutta et al. [164] adopted Taguchi philosophy to obtain optimal parametric combinations for achieving desired weld bead geometry and dimensions related to the heat-affected zone (HAZ), such as HAZ width in submerged arc welding. Submerged arc welding is characterized by multiple process parameters and influences multiple output or responses such as deposition rate, percent dilution, features of bead geometry, and mechanical-metallurgical characteristics of weldment [157]. Taguchi method alone cannot handle the multi-response problems, therefore a multi-response Grey-based Taguchi approach for process optimization has been carried out to solve this multi-response optimization problem [164]. In their other works [165, 166] the authors performed Grey-based-Taguchi optimization to determine the maximum amount of slag-flux mixture that can be used without sacrificing any negative effect on bead geometry, compared to the conventional SAW process. All the data have been utilized to develop mathematical models between predictors and responses. Response surface methodology (RSM), followed by the multiple linear regression method.

As the selection of process parameters has a great influence on the quality of a welded connection based on three level factorial design of experiments of three process parameters a mathematical model is constructed by using multiple curvilinear regression analysis by Karaoglu and Secgin [167]. Sensitivity analysis of parameters and fine tuning requirements of the parameters has also been performed for getting optimum weld bead geometry. An attempt has been made to solve the correlated multiple criteria optimization problem of submerged arc welding [168]. Principal component analysis (PCA) has been adapted to covert multiple objectives of the optimization problem into a single objective function. Taguchi's robust optimization technique has been applied to determine the optimal setting. Same type of word of using nonconventional optimization techniques has been reported by Dhas and Kumanan [155]. Taguchi's design of experiment was followed to carry out the experiments, regression analysis was carried out to establish a relationship between the input and output parameters of the welding process. By this relationship, an attempt was made to minimize weld bead width. Optimization process based on the concept of genetic algorithm (GA) [169] and particle swarm optimization (PSO) algorithm were reported to be used to determine optimal weld parameters.

2.9 Summary

Over the years researchers are studying various welding processes, in this section an attempt has been made to understand the contributions of the previous researchers. Heat source models developed by previous researchers were extensively studied. The use of finite element method has made possible the prediction of transient thermal history, residual stress, and distortion. This helps to understand the complex heat transfer and fluid flow mechanism in welds with the direction to successfully estimate the bead geometry, thermal profile, residual stress, and deformation. To find the weld joint strength and determine the amount of residual stress and distortion experiments have been performed by several researchers. Some efforts have been made by previous researchers to find the optimal parameter to get a sound weld joint using various optimization techniques.

2.10 Scope of the thesis

Fusion welding has got a wide application as a joining method. Submerged arc welding is one of the most prominent fusion welding processes having the ability to weld thin to very thick metal pieces. It is used extensively in heavy industries like shipbuilding, bridge structures etc. But before welding, if the process is not studied properly, the defects due to the weld cannot be prevented in advance. Dimensional inaccuracies is a common concern due to the weld induced distortion., Thermal stresses generates as a result of the temperature gradient during welding and these stresses finally settle down as residual stresses. Selection of the proper weld parameters controls the penetration which determines the joint strength. It is not always feasible to carryout prototype testing in case of large structural application due to time and resource constraints. Therefore, always there is a need of proper prediction method which can accurately model the fusion welding process and predict the desired properties.

Welding heat source is the most critical part of any welding process, researchers tried to accurately model the welding heat source. Here an attempt has been made to model the heat source of fusion welding by considering the asymmetricity of the moving heat source. Methods have been developed to analyse the effect of process parameters on residual stress distribution of submerged arc welded butt joint. Influence of tacking sequence and welding sequence on thermal history, residual stresses, and distortion has been studied. A comparison of residual stress and deformation has been made between the single and double sided fillet joints welded by submerged arc welding. Weld reinforcement also has some influence on angular distortion of the structure which has been studied here. Generally, modelling and simulation of large structure takes huge time and computational resource. Here an attempt has been made to estimate the angular deformation in a large structure using inherent strain technique. Mechanical characterization was performed to check the joint strength of the weld. Use of surface active element enhances the weld penetration. Experiments were performed to study the influence of surface active elements on the weld pool dimension. Generally, V-groove joint configuration is used in high thickness welds, so here a comparative study was done to analyse the effect of different included angles and square butt configuration on the mechanical property of the weld. Finally, optimization techniques were employed to determine the optimum parameter combination.

CHAPTER 3

Theoretical Background & Modelling Methodology

3.1 General introduction

Welding is a widely used joining process, which in turn is also a very complex physical phenomenon, involving heat transfer, fluid flow, development of residual stresses and distortion after solidification in the welded structure. In this present research work, submerged arc welding process (SAW) was used which is a fusion welding process where intense heat is generated from the arc between consumable electrode & work piece, is applied locally to melt & join the work pieces.

Here a 3-D transient, elasto-plastic, thermo-mechanical analysis was carried out considering temperature dependent material properties. Transient elasto-plastic thermo-mechanical phenomena consisting of uneven heating & cooling which leads to uneven expansion & contraction, which is responsible for the formation of thermal elasto-plastic strains. After cooling, the thermal strain gets locked into the welded structure which precipitates the formation of residual stress & distortions in the welded structure.

In this chapter the theoretical basis of the heat transfer, residual stresses and distortions are presented. Finite element (FE) heat transfer model based upon the Gaussian distributed heat flux was considered to analyze the transient thermal history of SAW process, however a new volumetric heat source model was also developed to overcome the shortcomings of the previous developed models. The transient thermal analysis temperature data was used in structural model for carrying out the nonlinear elasto-plastic thermo-mechanical analysis to predict the residual stresses and distortions. Though the prediction capability of these models is close enough to the experimental results but it was observed that these models require a huge amount of computational time for large structure simulation. Therefore an equivalent loading technique was introduced to predict the residual deformation of large welded structures within a very short time.

Optimal process condition evaluation for welding low carbon steels using submerged arc welding is an important aspect. To evaluate the effect of various process parameters on weld quality i.e. mechanical properties, bead geometry, distortions etc. different techniques i.e. Taguchi method, Utility Theory etc. was used to find out the optimal parameter setting for best weld quality. First trial and error method was used to determine the range of parameters then Grey-based Taguchi approach has been carried out for the multi-response optimization of process parameters. Finally the confirmation test was carried out to verify the optimal results.

3.2 Thermal modelling

A three dimensional Finite Element (FE) thermal model was developed in the present work to analyze the transient thermal history in submerged arc welding. From the literature survey it is clear that heat transfer mechanism in molten pool is extremely complex and understanding the physics is essential. Heat transfer mechanisms can be grouped into 3 broad categories i.e. (i) conduction (ii) convection & (iii) radiation

3.2.1 Conduction: Regions with greater molecular kinetic energy will pass their thermal energy to regions with less molecular energy through direct molecular collisions, a process known as conduction. In metals, a significant portion of the transported thermal energy is also carried by conduction-band electrons.

In general, the rate of the heat transfer through conduction is given by the Fourier’s law heat conduction.

$$q'' = -k\nabla T \tag{3.1}$$

where q'' is the heat flux, k is the thermal conductivity of the material, T is temperature and $\nabla = (\frac{\partial}{\partial x}, \frac{\partial}{\partial y}, \frac{\partial}{\partial z})$.

The conservation of energy in a differential form can be written as follows:

$$c\rho\frac{\partial T}{\partial t} = \frac{\partial}{\partial x}(k_x\frac{\partial T}{\partial x}) + \frac{\partial}{\partial y}(k_y\frac{\partial T}{\partial y}) + \frac{\partial}{\partial z}(k_z\frac{\partial T}{\partial z}) + \dot{Q} \tag{3.2}$$

where ρ is the density of the material, c is specific heat, $\dot{Q}$ is heat generated inside the element and t is time. If the thermal conductivity of the material, k is assumed constant, then Equation 3.2 becomes:

$$\frac{\partial T}{\partial t} = \alpha(\frac{\partial^2 T}{\partial x^2} + \frac{\partial^2 T}{\partial y^2} + \frac{\partial^2 T}{\partial z^2}) + \dot{Q} \tag{3.3}$$

where $\alpha = \dfrac{k}{c\rho}$ is thermal diffusivity.

Equation 3.3 is the differential equation of heat conduction for a stationary, homogeneous, isotropic solid with constant thermal conductivity, *k.* The solution to this equation is strongly dependent on the initial conditions and boundary conditions.

3.2.2 Convection: When heat conducts into a static fluid it leads to a local volumetric expansion. As a result of gravity-induced pressure gradients, the expanded fluid parcel becomes buoyant and displaces, thereby transporting heat by fluid motion (i.e. convection) in addition to conduction [126]. Such heat-induced fluid motion in static fluids is known as free convection.

The convective heat transfer equation can be represented as shown in the Equation 3.4.

$$q''_{con} = -h_f (T - T_\infty) \tag{3.4}$$

where h_f is convection heat transfer coefficient, T is body temperature, T_∞ is surrounding temperature.

3.2.3 Radiation: All materials radiate thermal energy in amounts determined by their temperature, where the energy is carried by photons of light in the infrared and visible portions of the electromagnetic spectrum [126]. When temperatures are uniform, the radioactive flux between objects is in equilibrium and no net thermal energy is exchanged. The balance is upset when temperatures are not uniform, and thermal energy is transported from surfaces of higher to surfaces of lower temperature. The radiation heat transfer formula is:

$$q''_{rad} = \sigma\varepsilon(T^4 - T^4_\infty) \tag{3.5}$$

where ε is the emissivity, σ is the Stefan-Boltmann constant, T is body temperature, T_∞ is surrounding temperature. Understanding of the theory of heat flow is essential in order to study the welding process analytically, numerically or experimentally.

3.2.4 Formulation of Finite element (FE) transient thermal analysis

The schematic diagram of butt-welding process with co-ordinate system is shown in Figure 3.1.

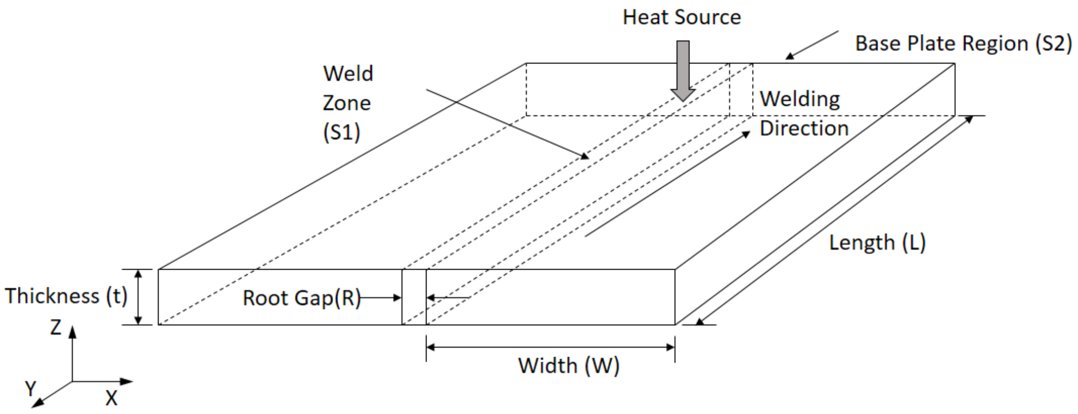

Figure 3.1 Various Regions of welding plate

3.2.4.1 Assumptions made in the FE thermal analysis

To develop the 3-D FE thermal model it is tried to accommodate the actual welding condition as far as possible. Following were the assumptions made to develop the thermal model of the welding process.

- All the thermal properties were considered as a function of temperature.
- Linear Newtonian convection cooling was considered on all the surfaces except the weld zone.
- No forced convection was considered.
- As the arc is fully submerged inside the granulated flux that's why radiation loss is small, hence the same was neglected.
- Arc efficiency was incorporated to account for other losses.
- Heat flux was considered as a load.
- Liquid metal flow was not considered.
- Phase transformation induced stresses were not considered.
- Heat of fusion on melting and solidification were not considered.
- Natural cooling was considered.

- Forced convection was not considered, however in submerged as the weld bead is submerged under the flux, there might be some effect of the same which was ignored.

The governing differential equation for heat conduction for a homogenous, isotropic solid without heat generation in the rectangular coordinate system (*x*,*y*,*z*) as shown in Equation 3.6.

$$\frac{\partial}{\partial x}[k\frac{\partial T}{\partial x}]+\frac{\partial}{\partial y}[k\frac{\partial T}{\partial y}]+\frac{\partial}{\partial z}[k\frac{\partial T}{\partial z}]=\rho c\frac{\partial T}{\partial t} \tag{3.6}$$

where ρ (kg/m^3) is the density, C (J/kg$^{\circ}$C) is specific heat capacity, T ($^{\circ}$C) is temperature, t (s) is time, k (W/m$^{\circ}$C) are the thermal conductivity which are considered equal in all directions. Equation 3.6 can be written as

$$\rho c\frac{\partial T}{\partial t}=-\{L\}^T\{q\} \tag{3.7}$$

where $\{L\}=\left\{\frac{\partial}{\partial x}\frac{\partial}{\partial y}\frac{\partial}{\partial z}\right\}^T$ is a vector operator, $\{q\}$ is heat flux vector.

From Fourier's law of heat conduction the heat flux vector can be correlated to the thermal gradient. Therefore,

$$\{q\}=-[D]\{L\}T \tag{3.8}$$

where $[D]=\begin{bmatrix}k & 0 & 0\\ 0 & k & 0\\ 0 & 0 & k\end{bmatrix}=$ Conductivity matrix, the negative sign indicating the heat is occurring in the direction of decreasing temperature. After substituting the value of $\{q\}$ the Equation 3.7 can be written as,

$$\rho c\frac{\partial T}{\partial t}=\{L\}^T[D]\{L\}T \tag{3.9}$$

To solve Equation 3.9, a set of boundary conditions are required. Figure 3.2 shows the solution domain with all applied boundary conditions.

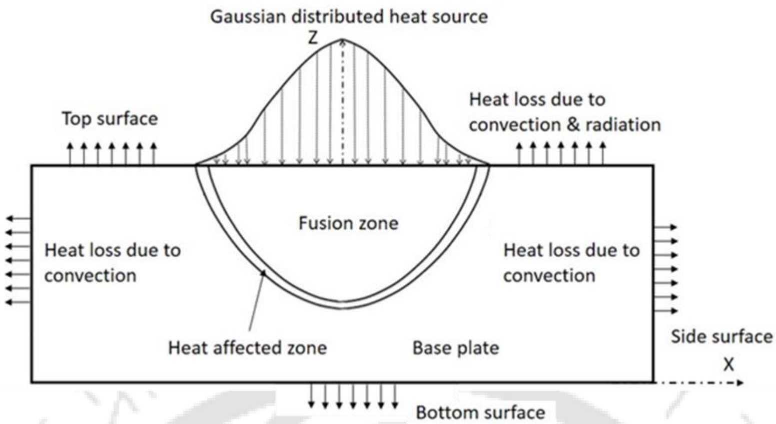

Figure 3.2 Schematic representation of the solution domain with all boundary conditions

3.2.4.2 Boundary conditions

The following boundary conditions were used in this present model.

(i) **Initial condition**: A specified initial temperature for the welding that covers the entire elements of the specimen:

$T = T_{\infty}$ for $t=0$ (3.10)

where T_{∞} is the ambient temperature.

To develop the boundary conditions, energy balance at the work surface is considered as,

Heat supply = Heat loss

(ii) **First boundary condition**: A specific heat flow acting over surface S_1 (as shown in Figure 3.1) as given in Equation 3.11,

$$q_n = -q_{\sup} \qquad (3.11)$$

$$or - k\frac{\partial T}{\partial n} = -q_{\sup}$$

The quantity q_n represents the component of the conduction heat flux vector normal to the work surface. The quantity $q_{\sup}$ represents the heat flux supplied to the work surface in, from an external heat source.

$$q_n = \{q\}^T \{n\} \text{ on the surface } S_1 \text{ for } t > 0 \tag{3.12}$$

where $\{n\}$ = unit outward normal vector.

(iii) **Second boundary condition**: Considering heat loss q_{conv} due to convection over surface S_2 (Base plate; Newton's law of cooling as shown in Figure 3.2) as given in Equation 3.12.

$$q_n = q_{conv}$$

or

$$q_n = q_{conv} - k\frac{\partial T}{\partial n} = h_f\left(T - T_\infty\right)$$

or

$$-k\frac{\partial T}{\partial n} = -h_f\left(T_\infty - T\right) \text{ on surface } S_2 \text{ for } t > 0$$

or

$$\{q\}^T \{n\} = h_f\left(T - T_\infty\right) \text{ on surface } S_2 \text{ for } t > 0 \tag{3.13}$$

It should be noted that positive specified heat flow is into the boundary (i.e. in the direction opposite of $\vec{n}$). Pre multiplying Equation 3.9 by a virtual change in temperature, integrating over the volume of the element, and combining with Equation 3.12 and 3.13 and with some algebraic manipulation yield the following:

$$\int_{vol}\left(\rho c\delta T\left(\frac{\partial T}{\partial t}\right) + \{L\}^T(\delta T)\left([D]\{L\}T\right)\right)d(vol) = \int_{S_1}\delta T q_{\sup} d(S_1) + \int_{S_2}\delta T h_f\left(T_\infty - T\right)d(S_2)$$

(3.14)

where vol = volume of element

δT = an allowable virtual temperature $\left(=\delta T(x, y, z, t)\right)$

3.2.4.3 Derivation of heat flow matrices

As stated before, the variable T was allowed to vary both in space and time. This dependency is expressed as:

$$T = \{N\}^T \{T_e\} \tag{3.15}$$

where $T = T(x,y,z,t)$ = temperature; $\{N\} = \{N(x,y,z,t)\}$ = element shape function and $\{T_e\} = \{T_e(t)\}$ = nodal temperature vector. Thus, the time derivatives of Equation 3.10 may be written as follows:

$$\dot{T} = \frac{\partial T}{\partial t} = \{N\}^T \{\dot{T}_e(t)\} \tag{3.16}$$

δT has the same form as T:

$$\delta T = \{\delta T_e\}^T \{N\} \tag{3.17}$$

The combination of $\{L\}T$ is written as

$$\{L\}T = [B]\{T_e\}$$

where $[B] = \{L\}\{N\}^T$ (3.18)

Now, the variational statement of Equation 3.16 can be combined with Equations 3.15-3.18 to yield Equation 3.19:

$$\int_{vol} \rho c \{\delta T_e\}^T \{N\}\{N\}^T \{\dot{T}_e\} d(vol) + \int_{vol} \{\delta T_e\}^T [B]^T [D][B]\{T_e\} d(vol) = \int_{S_1} \{\delta T_e\}^T \{N\} q_{\sup} d(S_1) + \int_{S_2} \{\delta T_e\}^T \{N\} h_f \left(T_\infty - \{N\}^T \{T_e\}\right) d(S_2) \tag{3.19}$$

The density ρ is assumed to remain constant and specific heat c may vary over the element. Finally $\{T_e\}, \{\dot{T}_e\}$ and $\{\delta T_e\}$ are nodal quantities and do not vary over the element, so that they also may be removed from the integrals. Now, since all quantities are pre multiplied by $\{\delta T_e\}$ this term may also be dropped from the resulting equation. The solution is obtained using FE ANSYS 12.0 [8] package.

Thus Equation 3.19 may be reduced to Equation 3.20.

$$\rho\int_{vol} c\{N\}\{N\}^T d(vol)\{\dot{T}_e\} + \int_{vol} [B]^T [D][B] d(vol)\{T_e\} = \int_{S_1} \{N\} q_{\sup} d(S_1) + \int_{S_2} T_\infty \{N\} h_f d(S_2) - \int_{S_2} h_f \{N\}\{N\}^T \{T_e\} d(S_2)$$

(3.20)

Equation 3.13 can be rewritten as:

$$[C_e^t]\{\dot{T}_e\} + ([K_e^{tb}] + [K_e^{tc}])\{T_e\} = \{Q_e^{\ f}\} + \{Q_e^{\ c}\} \quad (3.21)$$

where $[C_e^t] = \rho\int_{vol} c\{N\}\{N\}^T d(vol)$ = Element specific heat matrix,

$[K_e^{tb}] = \int_{vol} [B]^T [D][B] d(vol)$ = Element diffusion conductivity matrix,

$[K_e^{tc}] = \int_{S_2} h_f [N][N]^T d(S_2)$ = Eelement convection surface conductivity matrix,

$\{Q_e^f\} = \int_{S_1} \{N\} q_{\sup} d(S_1)$ = Eelement heat flow vector for surface S_1 and

$\{Q_e^c\} = \int_{S_2} T_\infty h_f \{N\} d(S_2)$ = Element convection for surface S_2 heat flow vector.

The Equation 3.22 represents an element level general transient nonlinear heat conduction formulation. The element specific heat matrix $[C_e^t]$ is evaluated from the specific heat of the material. The enthalpy of the material is a function of temperature. Enthalpy H is defined as the integral of heat capacity with respect to temperature.

$$\rho c = \frac{dH}{dT}$$

or

$$H = \int \rho c \, dT \quad (3.22)$$

3.2.5 Heat source model

The distribution of heat applied on the surface of the work-piece or in a volume internal to the weldment has an important effect on the heat distribution pattern in the vicinity of the weld. It is in that region where the weld bead and the HAZ are formed, and it is important to identify how the heat input distribution influences their size and shape. If the weld thermal cycle in the vicinity of the weld metal and heat affected zone is not of interest. The heat input distribution is not important, and the heat input can be treated as a concentrated heat source. The heat input and the weld speed are then sufficient to determine the thermal cycle.

For arc welding processes, the deposition of heat may be characterized as a distribution of heat flux on the weldment surface. Assuming that the heat from the welding arc is applied at any given instant of time as a normally distributed heat flux then the rate of heat generation is given by

$$q_{\text{sup}}(r) = \frac{3\eta Q}{\pi \bar{r}^2} \exp\left[-3\left(\frac{r}{\bar{r}}\right)^2 \right] \tag{3.23}$$

where

r is the distance from the center of the heat source on the surface

$\bar{r}$ is the characteristics radial dimensional distribution parameter that defines the region in which 95% of heat flux is deposited [129].

A heat source of suitable radius moving along the weld line at a particular speed can be used for modelling the welding process. The total arc heat input to the joint can be applied as a moving heat source, as a volumetric heat source and as a surface heat flux input. This heat flux can be also applied as a rectangular or square shape.

3.3 Development of a new heat source model

It is observed that the most widely used double ellipsoidal model is also symmetrical in the front and rear end of the ellipse, which has a limitation for modelling moving heat source. As during welding the heat source moves in a specific velocity, due to this the rear end becomes very narrow in comparison with the front end. Here an attempt has been made to model the shape of the moving heat source during welding. In this present work, the heat source dimensions/ parameters were taken directly from the experimentally measured data to model the heat source more accurately.

In the present study, a shape of the ellipsoid is altered to get an asymmetric avocado like shape which has been used as a volumetric heat source for heat generation in the weld pool. The end crater shape of the weld bead of submerged arc welding is shown in Figure 3.3 which is similar to the cross section of an avocado.

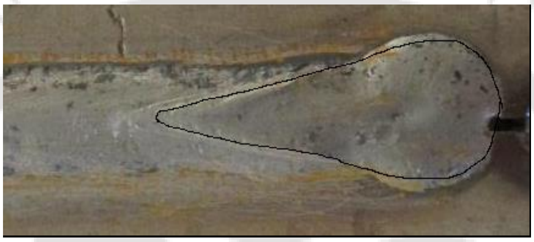

Figure 3.3 End crater shape of a weld bead

The Gaussian distribution of Pavelic's disc [171] heat source model can be expressed as following:

$$q(r) = q(o) \times exp(-Cr^2) \tag{3.24}$$

where $q(r)$ is the surface heat flux in W/m^2 which is a function of radius 'r', $q(o)$ is the heat flux at the centre of the heat source (maximum) in W/m^2, radial distance from the heat source center is denoted by 'r' in (m), and C is the concentration coefficient in m^{-2}. Friedman *et al.* [172] suggested the alternate form of Pavelic's model for moving heat source which can be expressed as

$$q(x,\xi) = \frac{3Q}{\pi c^2} \times exp\{\frac{-3}{c^2}(x^2 + \xi^2) \tag{3.25}$$

where Q is the energy input rate in W, 'c' is the characteristic radius of flux distribution in m. A Cartesian coordinate system (x, y, z) is considered in the work piece and also a lag factor τ

is added to define the position of the heat source with change in time (t), therefore the change involving the fixed and moving coordinate systems is:

$$\xi = y + v(\tau - t) \tag{3.26}$$

where v is the welding velocity in m/s. The equation of ellipse is altered to get the three dimensional non-uniform elliptical shape which is used in the proposed heat source configuration. The three dimensional form of the modified elliptical equation in Cartesian coordinate system is given as below

$$\frac{y^2}{b^2} + \left\{\frac{x^2}{a^2} + \frac{z^2}{c^2}\right\} \times \{t(y)\} = 1 \tag{3.27}$$

Here it is considered that the heat source moves with a local coordinate system (x, y, z) in 'y' direction. Therefore the shape and degree of asymmetry of the avocado-curve is decided by the semi-axes lengths of ellipsoid (i.e. a, b, c) and the function $t(y)$, while the heat source is moving along 'y' direction. But if the heat source moves along 'x' direction the functional form of $t(y)$ need to be revised as $t(x)$ and the adjustment in the equation has to be taken care accordingly. The shape was assumed from the end crater geometry of a weld bead in submerged arc welding. The semi-major axis length of the forward and rear ellipsoid used in this study are taken from experimental study.

In this present study, to get the asymmetrical avocado like shape a multiplication factor, $t\ (y)$ is introduced which can be represented by several functional forms like linear, quadratic, cubic, exponential, logarithmic etc. The selection of specific functional form is based upon the shape of interest and the solution procedure of the same is intended. While the heat source is moving during welding process the heat source power density is non-uniform in nature. Here "$t\ (y)$" provides the necessary non-uniformity in the heat source power density distribution. The functional form, "$t\ (y)$" considered in this present work is shown in Equation 3.28.

$$t(y) = \frac{1}{e^{my}} \tag{3.28}$$

where 'm' is a constant which magnitude decides the shape of the heat source. It is a more generalized way to have a floating value of "$t\ (y)$" rather than setting a fixed numerical value, hence 'm' term is incorporated.

Figure 3.4 shows the comparison of the present development with 2D shape of ellipse, egg shape while considering same semi-axis lengths. It can be observed from the Figure 3.4 that the present avocado shape is more realistic and similar to experimental one as compared to the other earlier developed heat sources. Therefore it would be advantageous to use this present developed model as a moving heat source.

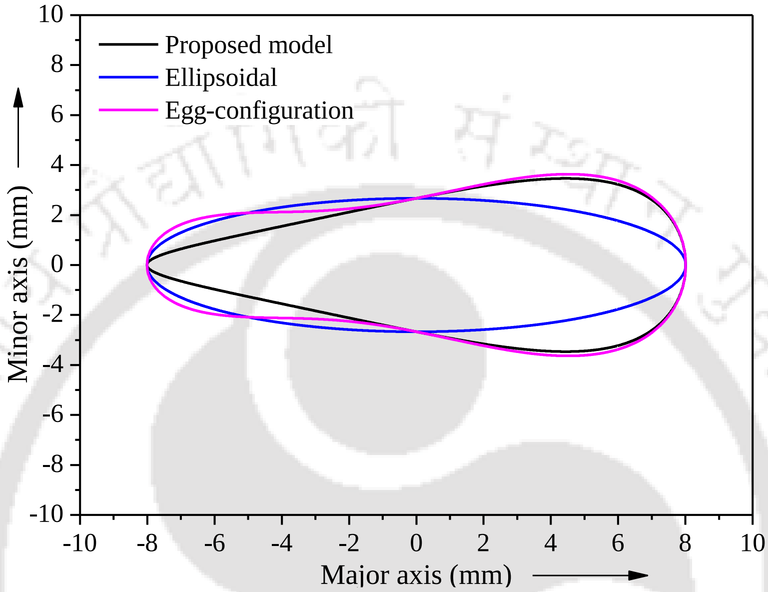

Figure 3.4 Comparison of 2D shape among egg shape, ellipse and avocado shape with same semi-axes with m = 0.1

To get a proper match of the weld heat source shape, a sensitivity analysis was performed. Figure 3.5 shows the sensitivity of the avocado shape with the value of '*m*'. This actually helps to identify the proper value of '*m*' for a specific shape of weld pool. Variation in the semi axis lengths in turn changes of the elliptical shape of the proposed avocado shape model with different values of 'm' with similar semi-axis length. At m = 0, the Equation 3.27 reduces to an ellipse which is a special case for stationary hear source. At this present study the parameter '*m*' is kept constant for all welding conditions.

The value of '*m*' can be selected based on the sensitivity analysis of weld pool shapes for all experimental conditions. The final shape of avocado configuration is shown in the Figure 3.6 with the axis ratio of 1.2 and m=0.1. The ratio of major and minor axis was calculated from the end crater dimensions. Figure 3.7 (a, b) shows the shape and size of the avocado shape with different experimental value of weld bead shapes as shown in the Table 5.19 where the value of ‘*m*’ is kept fixed as 0.1. The value of major axis is taken as the average value of the end crater length.

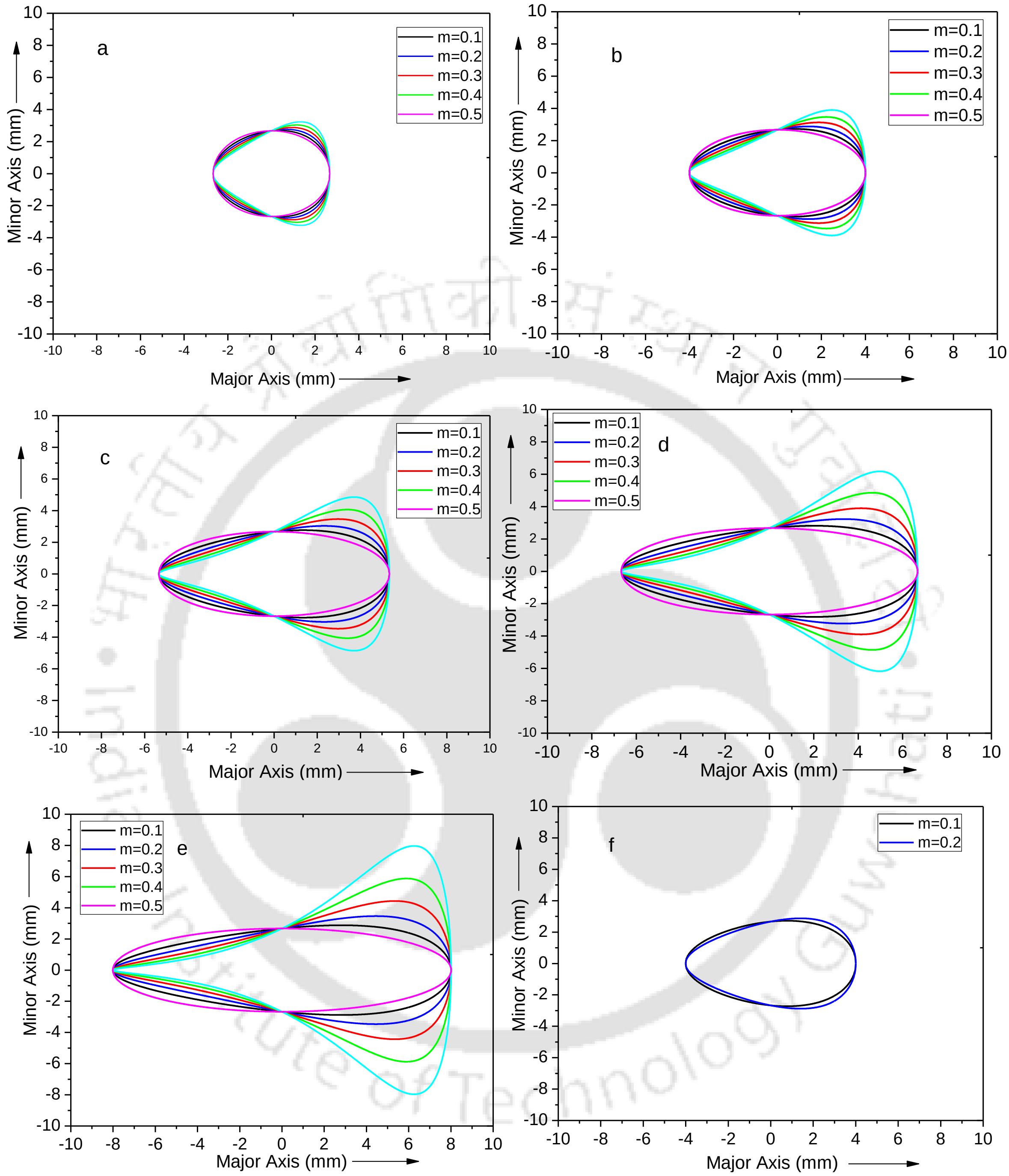

Figure 3.5 Avocado shape configuration at different values of ‘m’ and ratio between major and minor axis length: (a) ratio=1, (b & f) ratio=1.5, (c) ratio=2.0, (d) ratio=2.5, (e) ratio=3.0

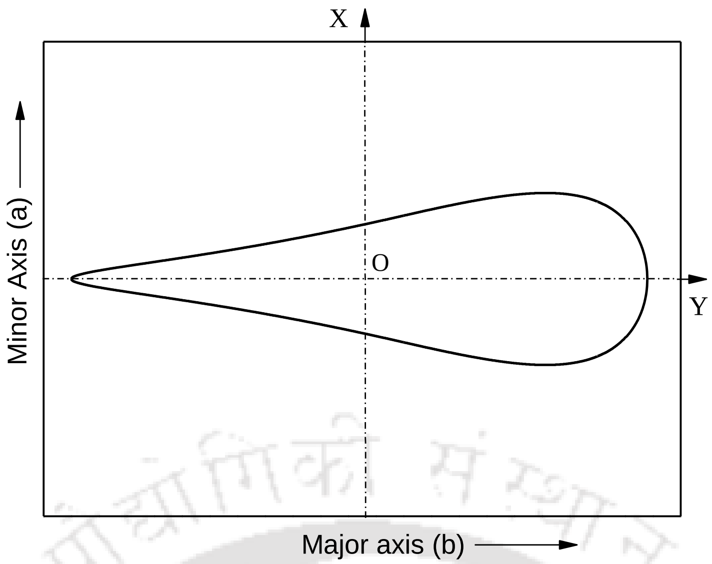

Figure 3.6 Avocado shape configuration with m=0.1 and major and minor axis ratio=1.2

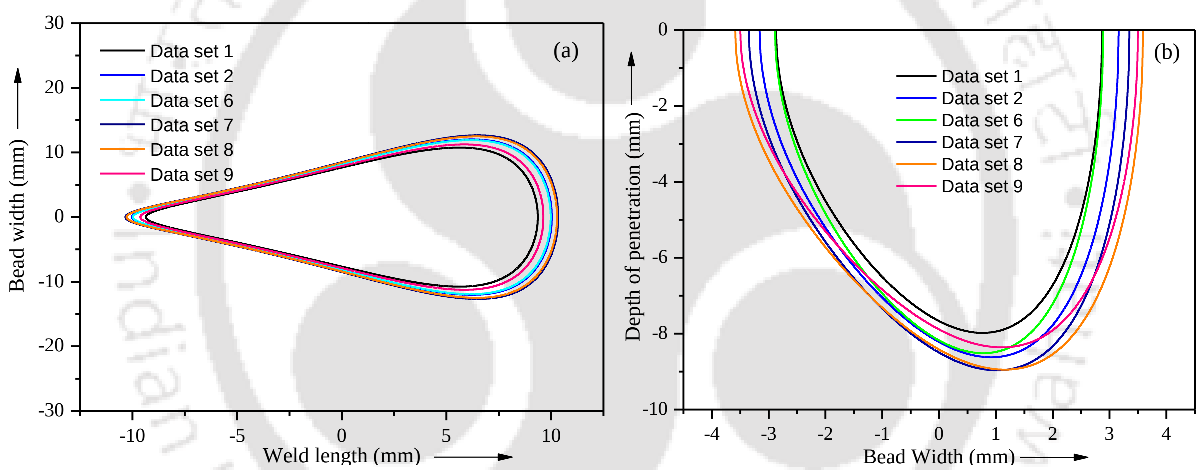

Figure 3.7 (a) XY- plane and (b) YZ plane for m = 0.1 and major & minor axis ratio = 1.2 corresponding to experimental data set as shown in the Table 5.20

The Gaussian distributed power density of the proposed avocado shaped heat source model with centre located at (0, 0, 0) and semi-axes a, b, c parallel to coordinate axes x, y, z can be written as:

$$q(x,y,z) = q_m e^{[-\{By^2 + (Ax^2 + Cz^2).t(y)\}]} \tag{3.29}$$

where A, B, C are the distribution parameters, q_m is the maximum heat flux density at the center.

The total heat input into the system can be expressed as

$$Q = \eta VI \quad \text{or} \quad Q = \eta P \tag{3.30}$$

where η is the arc efficiency, V = arc voltage, I = arc current, P = arc power.

Total volumetric energy distributed over the half of the heat source is expressed as

$$2Q = \int_{-\infty}^{\infty}\int_{-\infty}^{\infty}\int_{-\infty}^{\infty} q(x,y,z)\,dxdydz \tag{3.31}$$

where Q is the net heat input to the solution domain.

To satisfy the conservation of energy principle the following must be true

$$2Q = 2\eta P = \int_{-\infty}^{\infty}\int_{-\infty}^{\infty}\int_{-\infty}^{\infty} q(x,y,z)\,dxdydz \tag{3.32}$$

The value of q_m is calculated by solving the Equation 3.31, the maximum power density is expressed as

$$q_m = \frac{2Q}{\left(\frac{\pi\sqrt{\pi}\, e^{\frac{m^2}{4B}}}{\sqrt{ABC}}\right)} \tag{3.33}$$

To estimate A, B, C, the semi-axes of a proposed avocado-shape a, b, c in the x, y, z directions respectively, are defined such that the heat density falls to $0.05q_m$ at the surface of the heat source. The distribution parameters A, B and C are estimated as (appendix I) follows.

$$A \approx \frac{3}{a^2};\ B \approx \frac{3}{b^2};\ C \approx \frac{3}{c^2} \tag{3.34}$$

The amount of non-symmetry was further enhanced by shifting the ellipsoid center to a new location. The point (0, 0) is the old location and point (p, 0) is the new location of the center of the ellipsoid, which is interpreted in the Figure 3.8.

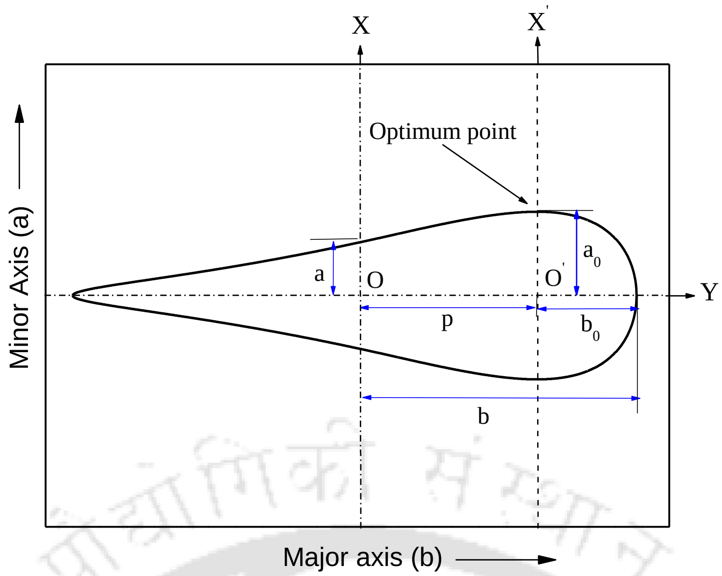

Figure 3.8 New center point of the ellipsoid

The top surface of the non-uniform elliptical heat source is expressed as:

$$\frac{y^2}{b^2}+\frac{x^2}{a^2}.e^{-my}=1 \tag{3.35}$$

$$\Rightarrow 2y.\frac{1}{b^2}.\frac{dy}{dx}+\frac{2x}{a^2}.e^{-my}+\frac{x^2}{a^2}.e^{-my.(-m)}.\frac{dy}{dx}=0$$

$$\Rightarrow \frac{2y}{b^2}=m.\frac{x^2}{a^2}+.e^{-my} \tag{3.36}$$

$$From(12)and(13)\Rightarrow \frac{y^2}{b^2}+\frac{2y}{b^2 m}=1$$

$$\Rightarrow my^2+2y-b^2m=0$$

$$\therefore\ y=\frac{-1+1\sqrt{1+b^2m^2}}{2.m}=p(let)$$

So, the modified equation of the three dimensional non-uniform elliptical-shape in Cartesian coordinate system is:

$$\frac{(y-p)^2}{b^2}+\frac{x^2}{a^2}.e^{-my}=1 \tag{3.37}$$

where $p=\dfrac{-1+1\sqrt{1+b^2m^2}}{2.m}$; p is the amount of offset from the original center of the elliptical shape.

By considering the new center, the volumetric distribution of heat intensity in moving coordinate system (x, y, z) can be expressed as below:

$$q_{(x,y,z)} = q_m \times e^{\left\{-\left[By^2+\left(Ax^2+Cz^2\right)\times\frac{1}{e^{my}}\right]\right\}}$$

$$= \frac{2Q.e^{\left\{-\left[\frac{3}{(b-p)^2}y^2+\left(\frac{3}{a^2}x^2+\frac{3}{c^2}z^2\right)\times\frac{1}{e^{my}}\right]\right\}}}{\left(\frac{\pi\sqrt{\pi}\, e^{\frac{m^2}{4.\frac{3}{(b-p)^2}}}}{\sqrt{\frac{3}{a^2}.\frac{3}{b^2}.\frac{3}{c^2}}}\right)} = \frac{6\sqrt{3}.Q.e^{\left\{-\left[\frac{3}{(b-p)^2}y^2+\left(\frac{3}{a^2}x^2+\frac{3}{c^2}z^2\right)\times\frac{1}{e^{my}}\right]\right\}}}{\pi\sqrt{\pi}.a.b.c.e^{\frac{m^2}{4.\frac{3}{b^2}}}}$$

$$\Rightarrow q_{(x,y,z)} = \frac{6\sqrt{3}.Q.e^{\left\{-\left[\frac{3}{(b-p)^2}y^2+\left(\frac{3}{a^2}x^2+\frac{3}{c^2}z^2\right)\times\frac{1}{e^{my}}\right]\right\}}}{\pi\sqrt{\pi}.a.b.c.e^{\frac{m^2b^2}{12}}} \tag{3.38}$$

As during welding the heat source moves in welding direction with a constant welding velocity so the heat source power density distribution is non-uniform. Therefore, the heat distribution in front and rear part of the avocado-shape should not be the same. It is also evident from the shape of the proposed avocado configuration that heat deposition in front and rear parts are different. To consider the effect of non-uniformity, the heat density distribution in the front and rear parts of the heat source can be expressed as:

$$q_{f(x,y,z)} = q_m \times A_f \times e^{\left\{-\left[By^2+\left(Ax^2+Cz^2\right)\times\frac{1}{e^{my}}\right]\right\}}$$

$$= \frac{6\sqrt{3}.Q.A_f\, e^{\left\{-\left[\frac{3}{(b-p)^2}y^2+\left(\frac{3}{a^2}x^2+\frac{3}{c^2}z^2\right)\times\frac{1}{e^{my}}\right]\right\}}}{\pi\sqrt{\pi}.a.b.c.e^{\frac{m^2b^2}{12}}} \tag{3.39}$$

$$q_{r(x,y,z)} = q_m \times A_r \times e^{\left\{-\left[By^2+\left(Ax^2+Cz^2\right)\times\frac{1}{e^{-my}}\right]\right\}}$$

$$= \frac{6\sqrt{3}.Q.A_r.e^{\left\{-\left[\frac{3}{(b-p)^2}y^2+\left(\frac{3}{a^2}x^2+\frac{3}{c^2}z^2\right)\times\frac{1}{e^{-my}}\right]\right\}}}{\pi\sqrt{\pi}.a.b.c.e^{\frac{m^2b^2}{12}}} \tag{3.40}$$

$$A_f = \frac{4}{(\frac{\pi\sqrt{\pi}\,e^{\frac{m^2}{4B}}}{\sqrt{ABC}})} \times 2 \times \frac{1}{4}(\frac{\pi\, e^{\frac{m^2}{4B}}}{2\sqrt{AC}}.\frac{p}{6}[e^{-\frac{m^2}{4B}} + 4e^{-\frac{B}{4}(p+\frac{m}{B})^2} + e^{-B(p+\frac{m}{2B})^2}] + \frac{\pi\sqrt{\pi}.e^{\frac{m^2}{4B}}}{2\sqrt{ABC}}) \quad (3.41)$$

$$\therefore A_f = \frac{2}{(\frac{\pi\sqrt{\pi}\,e^{\frac{m^2}{4B}}}{\sqrt{ABC}})} \times (\frac{\pi\, e^{\frac{m^2}{4B}}}{2\sqrt{AC}}.\frac{p}{6}[e^{-\frac{m^2}{4B}} + 4e^{-\frac{B}{4}(p+\frac{m}{B})^2} + e^{-B(p+\frac{m}{2B})^2}] + \frac{\pi\sqrt{\pi}.e^{\frac{m^2}{4B}}}{2\sqrt{ABC}}) \quad (3.42)$$

where A_f is the fraction that accounts the amount of heat deposition in front portion and A_r accounts the heat deposition in rear part of the arc. Therefore, the total energy is expressed as

$$Q = \eta VI = \frac{1}{2}(A_f Q) + \frac{1}{2}(A_r Q) \quad (3.43)$$

$$\text{i.e. } A_f + A_r = 2 \quad (3.44)$$

However, the deterministic value of A_r and A_f can be expressed in terms of model parameters (*m* and *b*) which are shown in Appendix I. Since the model parameter '*b*' changes according to the welding conditions, the values of A_f and A_r change accordingly and always satisfy the relation of Equation 3.44. It is noteworthy if '*m*' value is equal to zero then the power density becomes equal to power density of semi-ellipsoidal heat source model. When $b_f = b_r = b$ then the power density becomes equal to power density of avocado-shaped heat source model. When $b_f=b_r=b$ and $m=0$ then the power density becomes ellipsoid heat source. When $m=0$, $c=0$ and $a=b$ then the present model becomes the Pavelic's disk heat source model and when $a=b=c$=constant and $m=0$ then the present model converts to the spherical heat source model.

3.3.1 New heat source for FE thermal model

By using the above developed heat source model, the transient thermal analysis was performed in a mild steel plate of dimension 150×150×8 mm. The welding was carried out along *y*-direction with a welding traverse velocity *u*. For the moving heat source problem, the coordinate system of the moving heat source can be modelled as (*x, y', z*), where $y' = y - u \times t$, *u*

= welding speed, t = welding time. And the corresponding welding heat distribution was represented by the present developed heat source model which is shown in Equation 3.45.

$$q(x,y,z) = \frac{6\sqrt{3}.Q.\mathrm{e}^{\left\{-\left[\frac{3}{(b-p)^2}\mathrm{y}^2 + \left(\frac{3}{a^2}\mathrm{x}^2 + \frac{3}{c^2}\mathrm{z}^2\right)\times\frac{1}{e^{my}}\right]\right\}}}{\pi\sqrt{\pi}.a.b.c.\mathrm{e}^{\frac{m^2b^2}{12}}} \tag{3.45}$$

3.4 Welding thermo-mechanical analysis

The nodal temperatures from the transient thermal analysis were used as the input load in the structural analysis to perform the non-linier elasto-plastic structural analysis to predict the residual stresses and distortions.

3.4.1 Formulation of 3D FE stress-strain relationship

In this analysis, quasi-static equation of equilibrium is given by

$$\nabla\sigma + F = 0 \tag{3.46}$$

where

∇ is differential operator

σ is the stress

F is the body force

The elastic stress strain relationship is defined as follows

$$\{\sigma\} = [D]\{\varepsilon_e\} \tag{3.47}$$

where $\{\sigma\}$ = stress vector = $[\sigma_X\ \sigma_Y\ \sigma_Z\ \sigma_{XY}\ \sigma_{YZ}\ \sigma_{XZ}]^T$, [D] = stress-strain correlation matrix (stiffness matrix), $\{\varepsilon_e\}$ = elastic strain vector. For the deformation of metals the von Mises yield criterion is employed and the elastic strain is given by

$$\varepsilon_e = \varepsilon - \varepsilon_{pl} - \varepsilon_{th} \tag{3.48}$$

where ε_e = the elastic strain vector, ε = total strain vector = $[\varepsilon_X\ \varepsilon_Y\ \varepsilon_Z\ \varepsilon_{XY}\ \varepsilon_{YZ}\ \varepsilon_{XZ}]^T$,
ε_{pl} = plastic strain vector and ε_{th} = thermal strain vector.

After neglecting the plastic strain part the above equation becomes as follows:

$\{\varepsilon^e\} = \{\varepsilon\} - \{\varepsilon^{th}\}$ = elastic strain vector and Equation 3.48 may be written as follows:

$$\{\varepsilon\} = \{\varepsilon^t\} + [D]^{-1}\{\sigma\} \quad (3.49)$$

For three-dimensional cases the thermal strain vector can be represented as following:

$$\{\varepsilon^t\} = \Delta T\,[\alpha_X\ \ \alpha_Y\ \ \alpha_Z\ \ 0\ 0\ 0]^T \quad (3.50)$$

where α_X, α_Y and α_Z = coefficient of thermal expansion in x, y and z directions respectively. The temperature difference is given by, $\Delta T = T - T_\infty$

The compliance matrix for three dimensional case can be written as follows:

$$[D]^{-1} = \begin{bmatrix} \frac{1}{E_X} & \frac{-\nu_{XY}}{E_X} & \frac{-\nu_{XZ}}{E_X} & 0 & 0 & 0 \\ \frac{-\nu_{YX}}{E_Y} & \frac{1}{E_Y} & \frac{-\nu_{YZ}}{E_Y} & 0 & 0 & 0 \\ \frac{-\nu_{ZX}}{E_Z} & \frac{-\nu_{ZY}}{E_Z} & \frac{1}{E_Z} & 0 & 0 & 0 \\ 0 & 0 & 0 & \frac{1}{G_{XY}} & 0 & 0 \\ 0 & 0 & 0 & 0 & \frac{1}{G_{YZ}} & 0 \\ 0 & 0 & 0 & 0 & 0 & \frac{1}{G_{XZ}} \end{bmatrix} \quad (3.51)$$

where ν_{XY} = major Poisson's ratio, ν_{YX} = minor Poisson's ratio, E_X = Young's modulus in x direction and G_{XY} = shear modulus in x-y plane. Since the $[D]^{-1}$ matrix is presumed to be symmetric,

$$\frac{\nu_{YX}}{E_Y} = \frac{\nu_{XY}}{E_X} \tag{3.52}$$

$$\frac{\nu_{ZX}}{E_Z} = \frac{\nu_{XZ}}{E_X} \tag{3.53}$$

and

$$\frac{\nu_{ZY}}{E_Z} = \frac{\nu_{YZ}}{E_Y} \tag{3.54}$$

For isotropic material $E_X = E_Y = E_Z$ and $\nu_{XY} = \nu_{YZ} = \nu_{XZ}$. From the above Equations it can be written that:

$$\varepsilon_X = \alpha_X \Delta T + \frac{\sigma_X}{E_X} - \frac{\nu_{XY}\sigma_Y}{E_X} - \frac{\nu_{XZ}\sigma_Z}{E_X} \tag{3.55}$$

$$\varepsilon_Y = \alpha_Y \Delta T - \frac{\nu_{XY}\sigma_X}{E_X} + \frac{\sigma_Y}{E_Y} - \frac{\nu_{YZ}\sigma_Z}{E_Y} \tag{3.56}$$

$$\varepsilon_Z = \alpha_Z \Delta T - \frac{\nu_{XZ}\sigma_X}{E_X} + \frac{\sigma_Z}{E_Z} - \frac{\nu_{YZ}\sigma_Y}{E_Y} \tag{3.57}$$

$$\varepsilon_{XY} = \frac{\sigma_{XY}}{G_{XY}} \tag{3.58}$$

$$\varepsilon_{YZ} = \frac{\sigma_{YZ}}{G_{YZ}} \tag{3.59}$$

$$\varepsilon_{XZ} = \frac{\sigma_{XZ}}{G_{XZ}} \tag{3.60}$$

where ε_X = direct strain in the x direction, σ_X = direct stress in x direction, ε_{XY} = shear strain in the x-y plane and σ_{XY} = shear stress on the x-y plane.

$$\sigma_X = \frac{E_X}{h}\left(1-(\nu_{YZ})^2\frac{E_Z}{E_Y}\right)(\varepsilon_X - \alpha_X \Delta T) + \frac{E_Y}{h}\left((\nu_{XY}) + \nu_{XZ}\nu_{YZ}\frac{E_Z}{E_Y}\right) (\varepsilon_Y - \alpha_Y \Delta T) + \frac{E_Z}{h}(\nu_{XZ} + \nu_{YZ}\nu_{XY})(\varepsilon_Z - \alpha_Z \Delta T) \tag{3.61}$$

$$\sigma_Y = \frac{E_Y}{h}\left(1-(\nu_{XZ})^2\frac{E_Z}{E_X}\right)(\varepsilon_Y-\alpha_Y\Delta T)+\frac{E_Y}{h}\left(\nu_{XY}+\nu_{XZ}\,\nu_{YZ}\frac{E_Z}{E_Y}\right)$$
$$(\varepsilon_X-\alpha_X\,\Delta T)+\frac{E_Z}{h}\left(\nu_{YZ}+\nu_{XZ}\,\nu_{XY}\frac{E_Y}{E_X}\right)(\varepsilon_Z-\alpha_Z\,\Delta T) \tag{3.62}$$

$$\sigma_Z = \frac{E_Z}{h}(\nu_{XZ}+\nu_{YZ}\,\nu_{XY})(\varepsilon_X-\alpha_X\,\Delta T)+\frac{E_Z}{h}\left(\nu_{YZ}+\nu_{XZ}\,\nu_{XY}\frac{E_Y}{E_X}\right)$$
$$(\varepsilon_Y-\alpha_Y\,\Delta T)+\frac{E_Z}{h}\left(1-(\nu_{XY})^2\frac{E_Y}{E_X}\right)(\varepsilon_Z-\alpha_Z\Delta T) \tag{3.63}$$

$$\sigma_{XY} = G_{XY}\,\varepsilon_{XY} \tag{3.64}$$

$$\sigma_{YZ} = G_{YZ}\,\varepsilon_{YZ} \tag{3.65}$$

$$\sigma_{XZ} = G_{XZ}\,\varepsilon_{XZ} \tag{3.66}$$

where $h = 1-(\nu_{XY})^2\frac{E_Y}{E_X}-(\nu_{YZ})^2\frac{E_Z}{E_Y}-(\nu_{XZ})^2\frac{E_Z}{E_X}-2\nu_{XZ}\nu_{YZ}\,\nu_{XY}\frac{E_Z}{E_X}$

When the shear moduli G_{XY}, G_{YZ}, G_{XZ} are not different for isotropic materials, they reduce to form as: $G_{XY} = G_{YZ} = G_{XZ} = \frac{E_X}{2(1+\nu_{XY})}$.

3.4.2 Derivation of structural matrices

The principle of virtual work states that a virtual (very small) change of the internal strain energy must be offset by an identical change in external work due to the applied loads, which can be stated as shown in Equation 3.67.

$$\delta U = \delta V \tag{3.67}$$

where U = strain energy, V = external work and δ = virtual operator. The virtual strain energy is given in Equation 3.68.

$$\delta U_1 = \int_{vol}\{\delta\varepsilon\}\{\sigma\}\,d(vol)^T \tag{3.68}$$

where $\{\varepsilon\}$ = strain vector, $\{\sigma\}$ = stress vector and vol = volume of the element. Continuing the derivation, Equations 3.67 and 3.68 are combined to give:

$$\delta U_1 = \int_{vol}\left(\{\delta\varepsilon\}^T[D]\{\varepsilon\}-\{\delta\varepsilon\}^T[D]\{\varepsilon^t\}\right)d(vol) \tag{3.69}$$

The strain vector is related to nodal displacements by:

$$\{\varepsilon\} = [B]\{u\} \tag{3.70}$$

where $[B]$ = strain-displacement matrix, based on the element shape functions and $\{u\}$ = nodal displacement vector. Assuming all the effects are in the global Cartesian system, Equation 3.70 can be combined with Equation 3.69, and noting that {u} does not vary over the elemental volume [8], it can be written as shown in Equation 3.71.

$$\delta U_1 = \{\delta u\}^T \int_{vol} [B]^T [D][B] d(vol)\{u\} - \{\delta u\}^T \int_{vol} [B]^T [D]\{\varepsilon^t\} d(vol) \tag{3.71}$$

Another form of virtual strain energy when a surface moves against a distributed resistance may be written as shown in Equation 3.73.

$$\delta U_2 = \int_{arear} \{\delta w_n\}^T \{\sigma\}\, d(arear) \tag{3.72}$$

where $\{w_n\}$ = motion normal to the surface, $\{\sigma\}$ = stress carried by the surface and $arear$ = area of the distributed resistance. Both $\{w_n\}$ and $\{\sigma\}$ have only one non-zero component. The point wise normal displacement is related to the nodal displacements by:

$$\{w_n\} = [N_n]\{u\} \tag{3.73}$$

where $[N_n]$ = matrix of shape functions for normal motions at the surface.

$$\{\sigma\} = k_f \{w_n\} \tag{3.74}$$

where k_f = the foundation stiffness in units of force per length per unit area. Combining Equations 3.72 through Equation 3.74 and assuming that k_f is constant over the area.

$$\delta U_2 = \{\delta u\}^T k_f \int_{arear} [N_n]^T [N_n] d(arear)\{u\} \tag{3.75}$$

By considering principle of virtual work it can be written that

$$\left([K_e]+[K_e^f]\right)\{u\}-\{F_e^t\}=[M_e]\{a\}+\{F_e^p\}+\{F_e^n\} \tag{3.76}$$

where $[K_e]$ is the element stiffness matrix, $[K_e^f]$ is the element foundation stiffness matrix, $\{F_e^t\}$ is the element thermal load vector, $[M_e]$ is the element mass matrix, $\{u\}$ is nodal displacement vector, $\{a\}$ is acceleration vector, $\{F_e^n\}$ is the vector of nodal forces applied to the elements and $\{F_e^p\}$ is the element pressure vector.

3.4.3 Structural analysis with material non-linearities

The structural material non-linearities generally includes nonlinear plasticity having well defined yield point and nonlinear elasticity like in case of aluminum or fibre reinforced composites. In such cases the elastic strain vector is represented as:

$$\{\varepsilon^e\}=\{\varepsilon\}-\{\varepsilon^t\}-\{\varepsilon^p\} \tag{3.77}$$

where

$\{\varepsilon^e\}$= elastic strain vector,

$\{\varepsilon\}$ = total strain vector,

$\{\varepsilon^t\}$= thermal strain vector, and

$\{\varepsilon^p\}$ = plastic strain vector.

Material non-linearities are due to the nonlinear relationship between stress and strain, that is, the stress is a nonlinear function of the strain [173-176]. In case of mild steel the rate independent plasticity, kinematics hardening and bilinear von Mises yield criteria [176-178] are applicable. The above-mentioned formulations are mainly derived with the help of reference books of the software ANSYS 12.0 [8], was used in the analysis and standard text books on finite element analysis [95-97]. The yield criterion, flow rule, hardening rule and plastic strain increment used in the analysis are briefly described below:

Yield Criterion: The yield criterion determines the stress level at which yielding is initiated. For multi-component stresses, this is represented as a function of the individual components, $f(\{\sigma\})$, which can be interpreted as an equivalent stress:

$$\sigma_e = f(\{\sigma\}) \tag{3.78}$$

where $\{\sigma\}$ = stress vector. When the equivalent stress is equal to a material yield parameter σ_y as shown in Equation 3.79,

$$f(\{\sigma\}) = \sigma_y \tag{3.79}$$

The material will develop plastic strains. If σ_e is less than σ_y, the material remains in elastic state and the stresses will develop according to the elastic stress-strain relations. It is to be noted that the equivalent stress can never exceed the material yield since in this case plastic strains would develop instantaneously, thereby reducing the stress to the material yield.

Rate-Independent Plasticity: Rate-independent plasticity is characterized by the irreversible straining that occurs in a material once a certain level of stress is reached. The plastic strains are assumed to develop instantaneously, that is, independent of time.

Flow Rule: The flow rule determines the direction of plastic straining and is given as:

$$\{d\varepsilon^p\} = \lambda \left\{ \frac{\partial Q_P}{\partial \sigma} \right\} \tag{3.80}$$

where λ = plastic multiplier (which determines the amount of plastic straining), and Q_P = function of stress, termed as the plastic potential (which determines the direction of plastic straining).

Assuming Q_P as the yielding function, the flow rule is termed associative and the plastic strains occur in a direction normal to the yield surface.

Hardening Rule: The hardening rule describes the changing of the yield surface with progressive yielding, so that the conditions (i.e. stress states) for subsequent yielding can be established. Kinematic hardening, which is used in the present analysis, assumes that the yield surface remains constant in size and the surface translates in stress space with progressive yielding.

3.5 Materials properties

The thermal and mechanical material properties of metal i.e. the specific heat, thermal conductivity, modulus of elasticity, thermal expansion co-efficient and yield stress etc. vary with the change of temperature. The average values of the material properties can be used in analysis, if the temperature does not vary too much. While in the welding process, the temperature of the weldment varies sharply. Therefore, the temperature-dependent material properties are supposed to be taken into consideration in welding process simulation. Quite a few researchers had addressed this topic namely Tsai & Eagar [179], Guedes Soares *et al.* [180], and Adak & Mandal [121]. Temperature dependent material properties used in this present work are shown in Tables 3.1-3.3.

Table 3.1 Temperature dependent material properties of C-Mn steel [181]

Temperature (^{o}C)	Thermal Conductivity (W/mK)	Specific Heat (J/kgK)	Thermal expansion co-efficient ($10^{-6}/^{o}C$)	Young modulus (GPa)	Poisson ratio
0	51.9	450	10	200	0.2786
100	51.1	499.2	11	200	0.3095
300	46.1	565.5	12	200	0.331
450	41.05	630.5	13	150	0.338
550	37.5	705.5	14	110	0.3575
600	35.6	773.3	14	88	0.3738
720	30.64	1080.4	14	20	0.3738
800	26	931	14	20	0.4238
1450	29.45	437.93	15	2	0.4738
1510	29.7	400	15	0.2	0.499
1580	29.7	735.25	15	0.00002	0.499
3500	42.1	400	15.5	0.00002	0.499

Table 3.2 Temperature dependent Enthalpy for mild steel [73]

Temperature (°C)	0	100	200	300	400	500	600	700	800	900	1000	>2500
Enthalpy (MJ/m^3)	0	360	720	1100	1500	1980	2500	3000	3700	4500	5000	9000

Table 3.3 Temperature dependent Yield stress for mild steel [73]

Temperature (K)	293	373	573	773	973	1073	1273	1473	1673
Yield stress (σ_y) (MPa)	398	379	305	192	41	36	28	20	12

3.6 Overall FE solution strategy

The thermo-mechanical analysis carried out in the present work, for fusion welding is represented by a block diagram as shown in Figure 3.11. First thermal analysis was performed followed by the structural analysis. The significant steps are described as follows.

- First the model was created as per the specimen dimension
- The model was then discretized into finite number of elements (element type: SOLID70)
- The temperature dependent thermal and structural material properties were defined.
- The elements size was taken of non-uniform distribution, the finer mesh was done in weld zone but away from weld zone coarser mesh was done to save the computational time.
- The boundary conditions and process parameters were specified.
- Transient thermal analysis was carried out by considering moving co-ordinate heat source to predict the overall thermal history.
- The transient thermal analysis was switched to non-linear elasto-plastic thermos-mechanical structural analysis.
- For structural analysis the structural element i.e. SOLID45 was taken.
- Structural boundary conditions were applied.
- The computed time temperature history was used as the load for the structural analysis.
- Residual stresses and distortions were computed.

SOLID70 and SOLID45 elements were used during thermal and structural analysis respectively which are shown in Figure 3.9. The boundary conditions applied for mechanical analysis is shown in Figure 3.10. Figure 3.11 shows the overall procedure for the thermo-mechanical analysis, where thermal analysis was performed followed by the structural analysis.

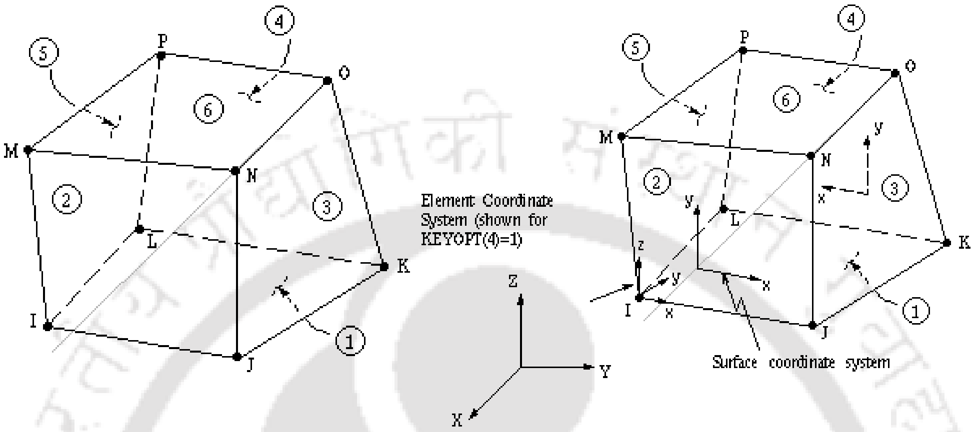

Figure 3.9 Elements for thermo-mechanical analysis (a) SOLID70 (b) SOLID45

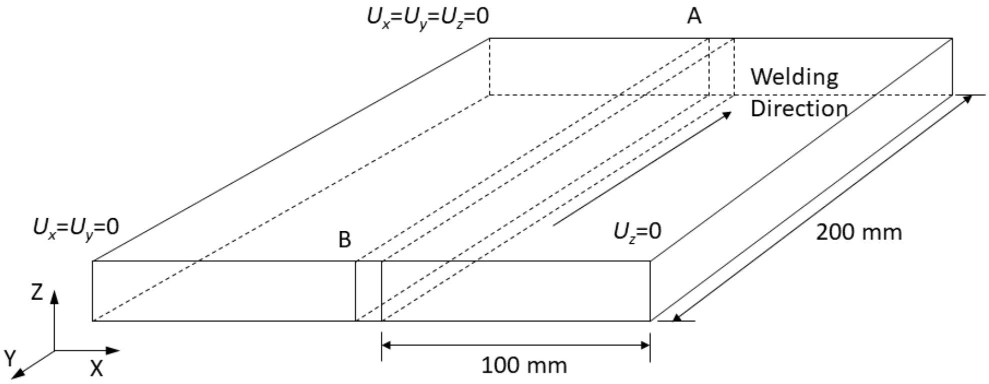

Figure 3.10 Mechanical boundary conditions

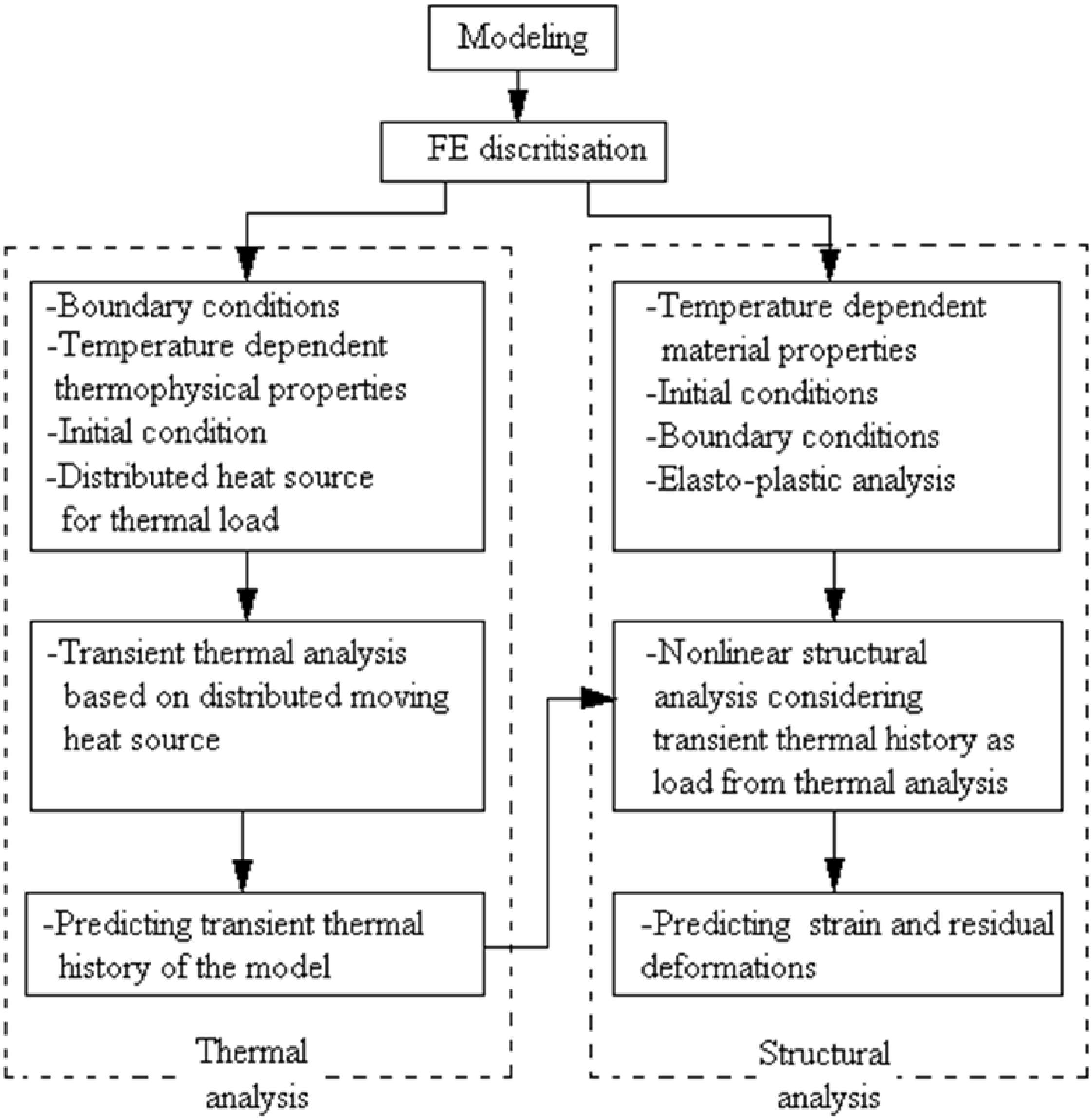

Figure 3.11 Thermo-mechanical analysis of fusion welding problem

3.7 Equivalent loading technique

As the conventional coupled transient, nonlinear, elasto-plastic thermo-mechanical analysis involves huge computational time. Computing a weld sample of small size with single pass itself takes several hours, which will be a huge amount of time in case of large structures consisting of several welding passes thus there is a real need of an efficient alternative technique to predict the post weld distortions. In the present work an attempt was made to determine the deformation in a submerged arc welded structure using equivalent load technique which reduces the total analysis time drastically of the conventional techniques in case of a small weld structure. In this proposed method, the major time consuming part of analysis i.e. the transient nonlinear elasto-plastic structural analysis part was almost eliminated. So, this method can effectively use to predict the weld induced distortion of very large structure with a computation time almost equal to the time required for transient thermal analysis of a small weld structure only. The theoretical details of equivalent loading technique are as follows:

Let us consider a continuous body at different states i.e. (a) standard, (b) stressed and, (c) stress released as shown in Figures 3.2a), (b), and (c), respectively [182]. State (a) is the initial stress-free state where neither external force nor internal stress exists. This state is regarded as the standard state. State (b) is the residual stress. State (c) is the stress released state in which the body is cut into small elements. From state (b) to state (c), each element deforms elastically to completely release the residual stress. The distance between two close particles in the body is ds_0 in state (a), ds in state (b), ds^* in state (c). The strain in the states (b) and (c) can be defined as shown in Equations 3.81 & Equation 3.82, respectively [183].

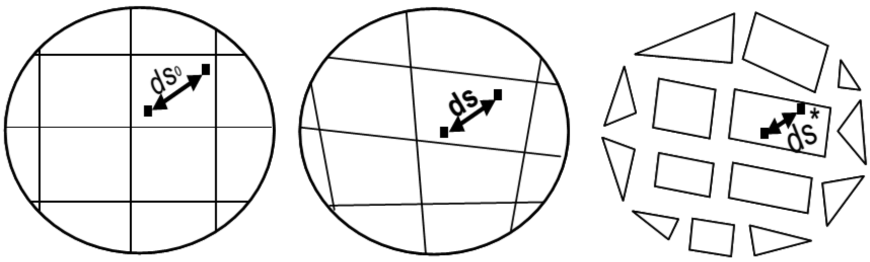

Figure 3.12 Inherent strain (a) standard state, (b) stressed state and, (c) stress released state [182]

$$\varepsilon = (ds - ds_0) / ds_0 \tag{3.81}$$

$$\varepsilon^* = (ds^* - ds_0) / ds_0 \tag{3.82}$$

Similarly, the strain increment between states (b) and (c) can be defined as follows:

$$\varepsilon^e = (ds - ds^*) / ds_0 \tag{3.83}$$

The strain defined in Equation 3.81 is usually called total strain and it satisfies compatibility conditions. The strain defined in Equation 3.82 is inherent strain and it does not follow compatibility conditions. The strain defined in Equation 3.83 is elastic strain. The total strain is composed of elastic and inherent strains as in Equation 3.84.

$$\varepsilon = \varepsilon^{e} + \varepsilon^{*} \qquad (3.84)$$

Since the total strain, ε corresponds to the deformation and the elastic strain, ε^{e} corresponds to the stress, the above equation can be written as follows:

$$\varepsilon^{*} = \varepsilon - \varepsilon^{e} \qquad (3.85)$$

Hence the inherent strain produces both the deformation (inherent deformation) and the residual stress.

3.7.1 Inherent strain

The inherent strain occurs in the welded region and this region can be modeled as a bar. Its adjacent region resists deformation and it can be modeled as a spring as shown in Figure 3.13. The change in temperature in bar is much higher than that in the spring which acts as a restraint on the bar. The co-efficient of restraint (β) can be written as follows:

$$B = k^{*}/(k + k^{*}) \qquad (3.86)$$

where k (= AE/L) is the stiffness of the bar, k^{*} is the stiffness of the spring. A and L are the cross sectional area and the length of the bar respectively.

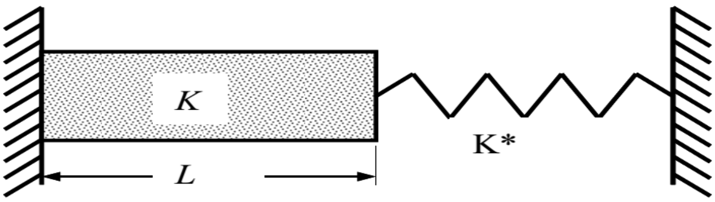

Figure 3.13 Simplified elastic-plastic analysis model [182, 184]

The inherent strain can be calculated as following:

$$\varepsilon^{*} = -\varepsilon_{y}/\beta = -\sigma_{y}/E\beta \qquad (3.87)$$

where σ_y is yield strength of mild steel (2.5×10^8 N/m^2), E is Young's modulus (2.1×10^{11} N/m^2). The restraint force is calculated as shown in Equation 3.88.

$$F = AE\varepsilon^* \tag{3.88}$$

where A is the cross sectional area of the bar and ε^* is the inherent strain. The corresponding moment, M can be calculated as follows:

$$M = \sum (F_1 l_1 + F_2 l_2) \tag{3.89}$$

where F_1 and F_2 are the forces at different nodes and l_1, l_2 are their corresponding distances from the centre of rotation.

3.8 Optimization of welding process parameters

Before conducting the experiment, every experiment has to be planned in proper way, therefore the science behind the observed phenomena can be studied using the obtained data from the experiments. The planning can be possible in certain ways as described below.

3.8.1 Trial-and-error approach: In this approach a series of experiments are required to perform which gives some understanding of the process. This requires making measurements after every experiment so that analysis of observed data will allow deciding the next step. i.e. which parameters should be varied and by how much. The data from trial and error experiments is insufficient to draw any significant conclusions. However, the trial and error experiments can provide a broad view of the range of parameters for getting the desired output, which can further be optimized to get the optimal process parameters for getting the desired output.

3.8.2 Design of experiments: A well planned set of experiments, in which all parameters of interest are varied over a specified range, is a much better approach to obtain systematic data. Mathematically speaking, such a complete set of experiments ought to give desired results. Design of experiments is a systematic method to determine the relationship between factors affecting a process and the output of that process. Usually the number of experiments and resources (materials and time) required are prohibitively large. In many cases, particularly those in which some optimization is required, the method does not point out to the best settings of parameters to carry out the experiments.

3.8.3 Taguchi method: Taguchi's philosophy is an efficient tool for the design of high quality manufacturing system. Dr. Genichi Taguchi, a Japanese quality management consultant, has developed a method based on orthogonal array experiments, which provides much-reduced variance for the experiment with optimum setting of process control parameters. Thus, the integration of design of experiments (DOE) with parametric optimization of process to obtain desired results is achieved in the Taguchi method. Orthogonal array (OA) provides a set of well-balanced (minimum experimental runs) experiments and Taguchi's signal-to-noise ratios (S/N). S/N ratios are logarithmic functions of desired output serve as objective functions for optimization. This technique helps in data analysis and prediction of optimum results.

The S/N ratio takes both the mean and the variability into account. It is the ratio of the mean (signal) to the standard deviation (noise). The ratio depends on the quality characteristics of the product/process to be optimized [187]. The standard S/N ratios are (i) smaller the better (SB), (ii) larger the better (LB) and (iii) nominal is best (NB). The optimal setting is the parameter combination, which has the highest S/N ratio. The three signal-to-noise ratios can be defined as follows.

(i) Smaller-the-better:

$$\eta = -10\log_{10} \frac{1}{n}\sum_{i=1}^{n} y_i^2 \quad (3.90)$$

It can be measured by taking the mean of sum of squares of measured data.

(ii) Larger-the-better:

$$\eta = -10\log_{10} \frac{1}{n}\sum_{i=1}^{n} \frac{1}{y_i^2} \quad (3.91)$$

It can be measured by taking the mean of sum of squares of reciprocal of measured data. It is generally calculated by taking the reciprocals of measured data and then taking the S/N ratio as in the smaller-the-better case.

(iii) Nominal-the-best:

$$\eta = 10\log_{10}\frac{1}{n}\sum_{i=1}^{n}\frac{\mu^2}{\sigma^2} \qquad (3.92)$$

It can be measured by taking the square of mean divided by variance. This case arises when a specified value is most desired i.e. neither a smaller nor a larger value is desirable.

3.8.4 Analysis of variance (ANOVA)

ANOVA is a statistical technique, which can infer some important conclusions based on analysis of the experimental data. The method is very useful to reveal the level of significance of influence of factor(s) or interaction of factors on a particular response. It separates the total variability of the response (sum of squared deviations about the grand mean) into contributions rendered by each of the parameter/factor and the error. Thus

$$SS_T = SS_F + SS_e \qquad (3.93)$$

where

$$SS_T = \sum_{j=1}^{p}(\gamma_j - \gamma_m)^2 \qquad (3.94)$$

and

SS_T = Total sum of squared deviations about the mean

γ_j = Mean response for j^{th} experiment

γ_m = Grand mean of the response

P = Number of experiments in the orthogonal array

SS_F = Sum of squared deviations due to each factor

SS_e = Sum of squared deviations due to error

In ANOVA table, the mean square deviation is defined as:

$$MS = \frac{SS\ Sum\ of\ squared\ deviation)}{DF(Degree\ of\ freedom)} \qquad (3.95)$$

Fisher's F ratio (Variance ratio) is defined as:

$$F = \frac{Mean\ for\ a\ term}{MS\ for\ the\ error\ term} \tag{3.96}$$

Depending on *F*-value, *P*-value (probability of significance) is calculated. If the *P*-value for a term appears less than 0.05 (95% confidence level) then it can be concluded that, the effect of the factor(s)/ interaction of factors is significant on the selected response [185].

3.8.5 Grey relational analysis

In grey relational analysis, experimental data i.e. measured features of quality characteristics of the product are first normalized ranging from zero to one. This process is known as grey relational generation. Next, based on normalized experimental data, grey relational coefficient is calculated to represent the correlation between the desired and actual experimental data. Then overall grey relational grade is determined by averaging the grey relational coefficient corresponding to selected responses. The overall performance characteristic of the multiple response process depends on the calculated grey relational grade. This approach converts a multiple- response- process optimization problem into a single response optimization situation, with the overall grey relational grade as the objective function. The optimal parametric combination is then evaluated by maximizing the overall grey relational grade. In grey relational generation, the normalized data corresponding to Lower-the-Better (LB) criterion can be expressed as:

$$x_i(k) = \frac{\max y_i(k) - y_i(k)}{\max y_i(k) - \min y_i(k)} \tag{3.97}$$

For Higher-the-Better (HB) criterion, the normalized data can be expressed as:

$$x_i(k) = \frac{y_i(k) - \min y_i(k)}{\max y_i(k) - \min y_i(k)} \tag{3.98}$$

where $x_i(k)$ is the is the value after the Grey relational generation, min $y_i(k)$ is the smallest value of $y_i(k)$ for the k^{th} response. An ideal sequence is $\left[x_0(k)\ and\ (k = 1, 2, 3, 4, 5..........)\right]$.

The grey relational coefficient $\xi_i(k)$ can be calculated as

$$\xi_i(k) = \frac{\Delta_{\min} + \psi\Delta_{\max}}{\Delta_{oi}(k) + \psi\Delta_{\max}} \quad (3.99)$$

where $\Delta_{oi} = \| x_0(k) - x_i(k) \|$ = difference of the absolute value $x_o(k)$ and $x_i(k)$; ψ is the distinguishing coefficient $0 \le \psi \le 1$. $\Delta_{\min} = \forall j_{\min} \in i \forall k_{\min} \| x_0(k) - x_j(k) \|$ = the smallest value of Δ_{oi} ; and $\Delta_{\max} = \forall j_{\max} \in i \forall k_{\max} \| x_0(k) - x_j(k) \|$ = largest value of Δ_{oi}. After averaging the grey relational coefficients, the grey relational grade γ_i can be computed as:

$$\gamma_i = \frac{1}{n}\sum_{k=1}^{n} \xi_i(k) \quad (3.100)$$

where n = number of process responses. The higher value of grey relational grade corresponds to intense relational degree between the reference sequence $x_o(k)$ and the given sequence $x_i(k)$. The reference sequence $x_o(k)$ represents the best process sequence. Therefore, higher grey relational grade means that the corresponding parameter combination is closer to the optimal.

However, Equation 3.98 assumes that all response features are equally important. But, in practical case, it may not be so. Therefore, different weightages were assigned to different response features according to their relative priority. In that case, the equation for calculating overall grey relational grade (with different weightages for different responses) is modified as shown below:

$$\gamma_i = \frac{\sum_{k=1}^{n} w_k \xi_i(k)}{\sum_{k=1}^{n} w_k} \quad (3.101)$$

where γ_i is the overall grey relational grade for i^{th} experiment. $\xi_i(k)$ is the grey relational coefficient of k^{th} response in i^{th} experiment and w_k is the weightage assigned to the k_{th} response.

3.8.5 Confirmatory experiment

After evaluating the optimal parameter settings, the next step is to predict and verify the enhancement of quality characteristics using the optimal parametric combination. The estimated Grey relational grade $\hat{\gamma}$ using the optimal level of the design parameters can be calculated as:

$$\hat{\gamma} = \gamma_m + \sum_{i=1}^{o}(\bar{\gamma}_i - \gamma_m) \tag{3.102}$$

where γ_m is the total mean Grey relational grade, $\bar{\gamma}_i$ is the mean Grey relational grade at the optimal level, and "*o*" is the number of the main design parameters that affect the quality characteristics. That means that the predicted or estimated Grey relational grade (optimal) is equal to the mean Grey relational grade plus the summation of the difference between overall mean Grey relational grade and mean Grey relational grade for each of the factors at optimal level.

In Grey-based Taguchi method, the only performance feature is the overall Grey relational grade; and the aim should be to search a parameter setting that can achieve highest overall Grey relational grade. The Grey relational grade is the representative of all individual performance characteristics. In the present study, objective functions was selected in relation to parameters of bead geometry and mechanical properties, and all the responses were given equal weightage.

3.9 Summary

In the present chapter, the theoretical background of all the aspects of thermal and structural analysis of submerged arc welding process is presented. This chapter includes the mathematical background and modelling aspects of thermal as well as structural analysis to predict the welding induced thermal history, residual stresses and distortions of SAW process. This also consists of the development of 3-D transient heat transfer analysis using a newly developed heat source configuration. Moreover, it comprises the theoretical background on prediction of angular deformation in large structure. Finally, the theoretical background behind the optimization techniques has been discussed.

CHAPTER 4

Experimental investigation

4.1 Introduction

In SAW process there are various process parameters e.g. voltage, current, welding speed, wire feed, electrode diameter, flux type, length of stick out etc. which controls the output characteristics i.e. weld quality in terms of mechanical property, weld bead geometry etc. Therefore the optimum parameters combination should be find out to achieve the desired weld quality. Particularly in this study the objective is to find out the optimal parameter conditions to achieve the desired welding quality in a single pass welding without any edge preparation of mild steel samples. The V-groove angle has an influence on the mechanical property of the weld joint, an attempt was made to determine the influence of different groove angles on mechanical property on butt welds. Effect of surface active elements on weld bead geometries as well as mechanical properties were also studied. Butt and fillet welds of different thickness were joined and thermal profile and angular deformations were measured for the validation of the numerical results of thermomechanical analysis.

4.2 Pre-stage of the experiments

In this section the details of pre-requirements of the actual welding are presented briefly.

4.2.1 Trial and error run

Trial and error experiments were performed to get the broad range of the welding parameters. One of the control parameters (viz. voltage, current and speed) was varied at a small increment while other parameters kept. During trial and error run it was found that for higher currents the weld arc was making a through penetration hole in the weld. On the other hand, lower ranges of current was not giving full penetration of the plate. Welding current directly affect the depth of penetration and extends of base metal fusion. The welding arc voltage has a direct influence on the weld bead geometry and external bead appearance. The welding speed has pronounced effect on the weld size and the penetration for a given combination of current and welding voltage. At a given current and voltage, the depth of penetration and hardness are effected by electrode diameter. From trial and error experiments a range of parameters was found and the range of each parameters were divided into sub levels as shown in the Table 4.1. Along with the variable parameters, the SAW setup has some fixed parameters which were kept constant.

Butt joints were welded. The pates were tack welded using shielded metal arc welding (SMAW) before final welding using SAW. A fixture was designed to keep and hold the samples using clamps. A flux filled reusable backing bar was used to provide support to the weld metal from the bottom side of the plate. The Figure 4.1 shows the SAW set up.

4.2.2 Arc initiation

Unlike in manual welding, arc starting can be difficult in SAW, because of the flux cover. Here a rolled ball of steel wool, approximately 10 mm in diameter was placed at the appropriate spot on the joint and the electrode wire is lowered on to it till it is tightly compressed. The flux is then applied and the welding is commenced. The steel conducts the current from wire to the work piece and at the same time melts away rapidly as the arc is formed. After completion of welding for terminating the arc the carriage travel is switched off. The brief pause between the second and third step prevents the wire from moving forward into the molten pool and from sticking to the molten puddle as it solidifies. Is also helps to fill the crater. A constant voltage rectifier type power source, with a 1000A capacity is used to perform the welding process. The polarity used here is the reverse polarity. The arc voltage is established by setting the output voltage on the source. The welding parameters & their levels used in the final experiments are shown in Table 4.1.

Table 4.1 Welding parameters and their levels

Variable Parameters						Fixed Parameters		
Parameters	**Values in each Level**				**Unit**	**Parameters**	**Values**	**Unit**
	L1	**L2**	**L3**	**L4**				
Voltage	27	27.5	28	28.5	V	**Root Gap**	2.5	mm
Current	470	475	480	485	A	**Wire Feed**	Automatic	-
Speed	22	24	26	28	m/h	**Welding Polarity**	-	DCEP
Stick-out	2.2	2.4	2.6	2.8	cm	**Plate Thickness**	8	mm

Figure 4.1 Submerged arc welding set-up

4.2.3 Design of welding fixture

A fixture is a device used to hold the work in the workshop and manufacturing industry. It is used to securely locate (position in a required position or orientation) and give support to the work, ensuring that all parts produced using the fixture will remain fixed. A fixture improves the economy of production by allowing smooth operation and quick transition from part to part, and also reduces the necessity of skilled labor by simplifying the mounting problem of work pieces, and increasing conformity across a production run. Fixtures must always be designed with economics in mind, the purpose of these devices is to reduce costs, and so it must be designed in such a manner that the cost reduction outweighs the cost of implementing the fixture. The top view and front view of fixture with adjustable clamping which was used for the experimentation is shown in Figures 3.2 (a, b & c) respectively.

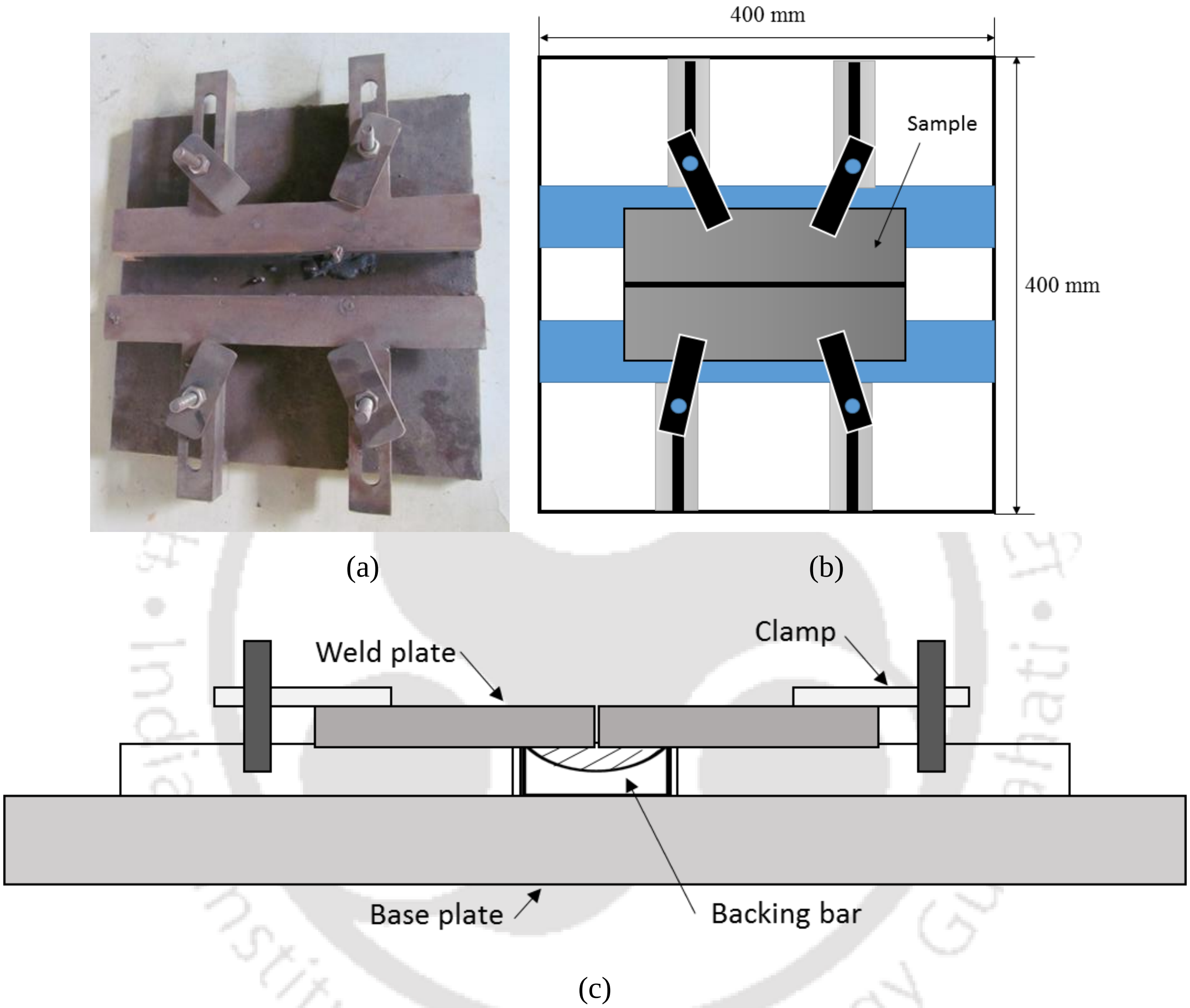

Figure 4.2 (a) Designed fixture to hold the samples, (b) Top view of the fixture (c) Front view of the fixture

4.2.4 Backing bar

It is a metal/ceramic slab placed at the root of a weld joint for the purpose of supporting molten weld metal. Backing bar which is having a deep semicircular groove filled with the same flux as used for SAW is found to be very effective for providing support to the molten metal and to form the required bottom reinforcement. The finer the particle size of the flux used in the backing strip, the better is the formation of bottom reinforcement. The Figure3.3 shows the dimension of the backing bar used in the experiments.

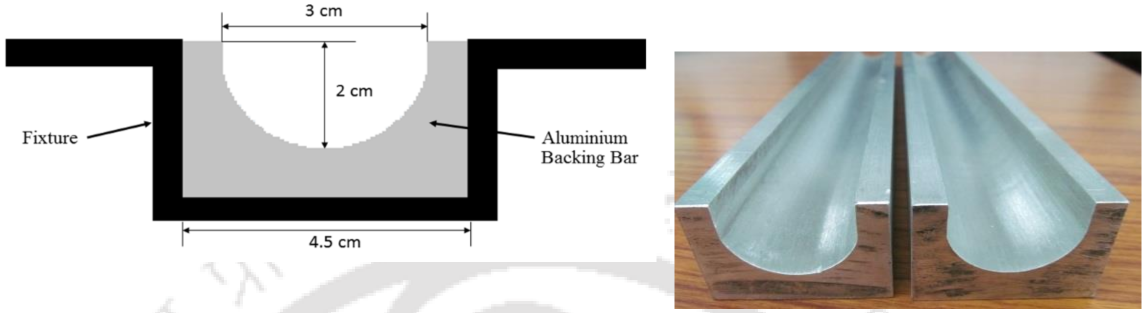

Figure 4.3 Backing bar with dimensions

4.2.5 Materials and job specimen

Mild steel is selected for the work material. Mild steel plate of size 200 mm × 100 mm × 8-10 mm with 1.5-2.5 mm root gap was butt joined by SAW process. 150 mm × 150 mm × 8-10 mm plates with a webb height of 50 mm was used for fillet joints. The work piece dimensions are shown in Figure 4.4.

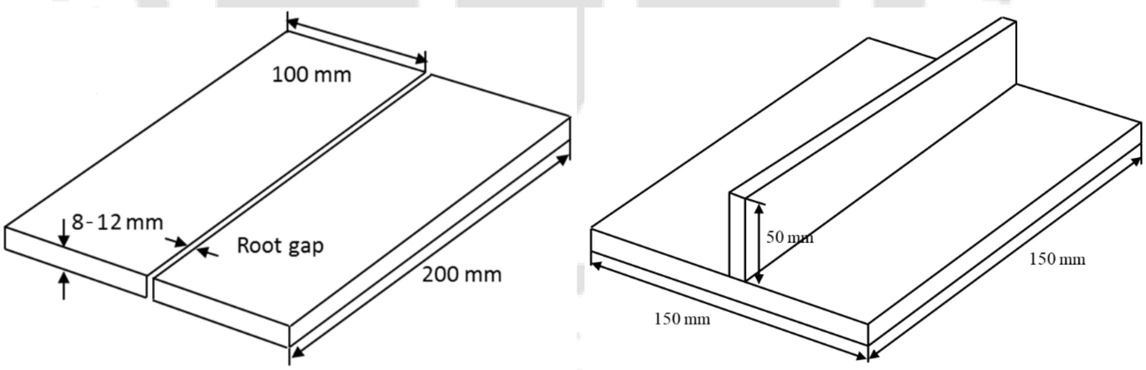

(a) (b)

Figure 4.4 Plate dimensions of (a) butt joint (b) fillet joint

(a) (b)

Figure 4.5 Welded plated (a) butt (b) fillet

Composition of the base metal (IS: 2062, Gr. B mild steel) is shown in Table 4.2. The chemical composition of the work piece is tested in the metal testing laboratory.

Table 4.2 Chemical composition of the base metal

Element	Carbon (C)	Manganese (Mn)	Silicon (Si)	Sulphur (S)	Phosphorus (P)
Percentage (%)	0.15	0.58	0.23	0.020	0.028

Continuous bare wires in the form of coils and dry fluxes in grain form were used for the SAW of mild steel, low alloy steels etc. Auto melt EH-13 copper-coated electrode wire with 3.15 mm diameter in coil form was used for welding. Chemical composition of the electrode wire and fluxes are given in the Table 4.3 & 3.4 respectively.

Table 4.3 Chemical composition of weld metal wire

C	Si	Mn	P	S	Cr	Ni	Mo	Cu	Al
0.06	0.03	1.50	0.03	0.03	0.06	0.03	0.01	0.04	0.046

Table 4.4 Composition of the flux

Composition	SiO_2+TiO_2	CaO+MgO	Al_2O_3+MnO	Ca+F_2
Percentage (%)	25	20	30	35

4.3 Welding without edge preparation and effect on mechanical properties

Edge preparation before welding is performed to weld thick plates which is a time and resource consuming task. Avoiding edge preparation can save both time and manpower but welding without edge preparation is a challenging task, as it involves controlling the weld parameters carefully. Here an attempt was made to control the weld parameters to get a sound weld without edge preparation i.e. square butt joint was used for welding suing SAW. The operating variables associated with SAW are welding current, welding voltage, welding speed, electrode diameter, electrode extension (stick out), type of flux, width and depth of flux layer, polarity and current type (AC or DC).

4.3.1 Design of experiment

Design of experiments is required to properly set the strategy of the experimental investigation. A series of experiments are performed in which purposeful changes are made to the input variables therefore the corresponding changes in the output responses can be observed. At this present study total four variable parameters were considered and varied in four different levels as shown in Table 4.1. If we follow the full factorial design approach, then it is necessary to perform experiments by all possible combination of these four parameters and determine the best out. The total number experiments are supposed to be 256, which is quite time and resource consuming. Therefore here we followed the Taguchi orthogonal arrays to design the experiments, which reduces the number of experiments to 16. Table 4.5 shows the designed experiments using Taguchi L16 orthogonal array.

Table 4.5 Experimental design matrix as per L16 orthogonal array

Weld runs	Current (A)	Voltage (V)	Welding speed (mm/s)	Electrode stick out (mm)
1.	330	28	5.5	23
2.	330	30	6	25
3.	330	32	6.5	27
3.	330	34	7	29
5.	340	28	6	27
6.	340	30	5.5	29
7.	340	32	7	23
8.	340	34	6	25
9.	350	28	6	29
10.	350	30	7	27
11.	350	32	5.5	25
12.	350	34	6	23
13.	360	28	7	25
14.	360	30	6	23
15.	360	32	6	29
16.	360	34	5.5	27

4.4 Comparative study of the effect of V-groove angle on mechanical properties

In the third set of experiments we compare the mechanical properties, hardness and bead geometry of weld. This section deals with the experimental analysis of tensile strength, hardness and bead geometry in square butt, single V-groove butt joints in submerged arc welding using different included angle and keeping the process parameters constant. The two plates are welded by the single V-groove (30°, 60°) butt weld joint with different V-groove angles. The geometry of butt weld joint is as follows. The specimens are fabricated using submerged arc welding process by considering different parameters as given in the Table 4.6.

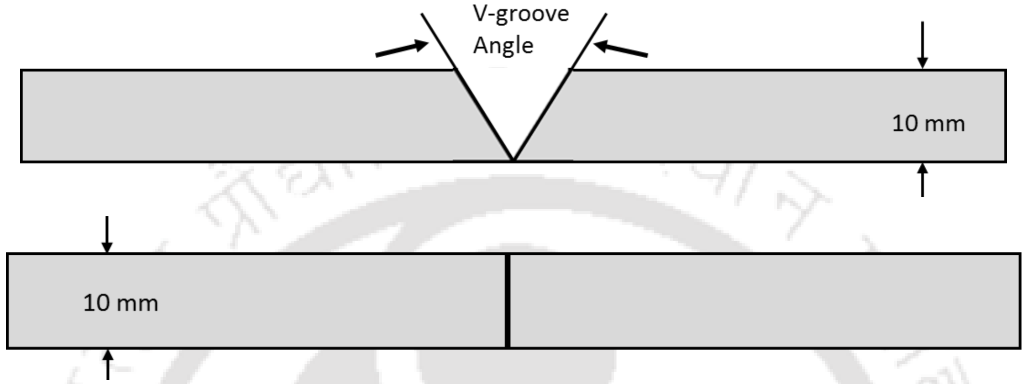

Figure 4.6 Welding geometry (a) with groove angle (b) square butt

Table 4.6 Process parameters and their levels

Process Parameters	Unit	Symbols	Level 1	Level 2	Level 3
Current	A	C	350	400	450
Traverse speed	mm/s	S	5.5	6	6.5
Voltage	V	V	30	30	30
Included Angle	Degree (°)	I	0	30	60

The square butt and Single V-groove butt joints with varying included angle are prepared in single pass by using submerged arc welding process. The size of welded plates used are 200 × 100 × 10 mm (length × width ×thickness). The throat thickness of 7 mm is taken for single V-groove butt joints for different included angles. Using these levels, the experimental matrix is designed as shown in Table 4.7.

Table 4.7 Experimental design matrix for different included angles

Weld runs	Butt Joint / V- Groove	Current (A)		Traverse Speed (mm/s)	
1.		1	350	1	5.5
2.	Flat (Butt joint)	2	400	2	6
3.		3	450	3	6.5
4.		1	350	1	5.5
5.	Included Angle (30^0)	2	400	2	6
6.		3	450	3	6.5
7.		1	350	1	5.5
8.	Included Angle (60^0)	2	400	2	6
9.		3	450	3	6.5

4.5 Experimental study of the effect of surface active elements on mechanical properties

Three types of activated flux namely Titanium oxide, Chromium oxide and Silicon dioxide and its mixtures has been used to study the effect of activating flux on weld geometry in low carbon steel welds. For the simplification of the experiment in each set of experiments (i.e. for one activated elements) current and voltage are taken as variable and keeping the travel speed (5.5 mm/s) and electrode stick out (25 mm) constant. Three experiments have been performed per set using one activated flux. In total there are 15 numbers of experiments with different combinations of the surface activated elements.

Table 4.8 Experimental design matrix for surface active elements

Weld runs	Flux type	Current (A)		Voltage (V)	
1.	SiO_2	1	300	1	30
2.		2	320	2	32
3.		3	350	3	34
3.	TiO_2	1	300	1	30
5.		2	320	2	32
6.		3	350	3	34
7.	Cr_2O_3	1	300	1	30
8.		2	320	2	32
9.		3	350	3	34
10.	SiO_2+ TiO_2+ Cr_2O_3	1	300	1	30
11.		2	320	2	32
12.		3	350	3	34
13.	No flux used	1	300	1	30
13.		2	320	2	32
15.		3	350	3	34

4.5.1 Procedure for applying surface active elements

Mild steel plates of 150 mm length and 150 mm width of 8 mm thickness are used for the study. These plates are first of all, polished with silicon carbide paper which removes surface contamination, and then these are cleaned with acetone. The surface activating elements are prepared by mixing the different oxides with acetone (Figure 4.7).

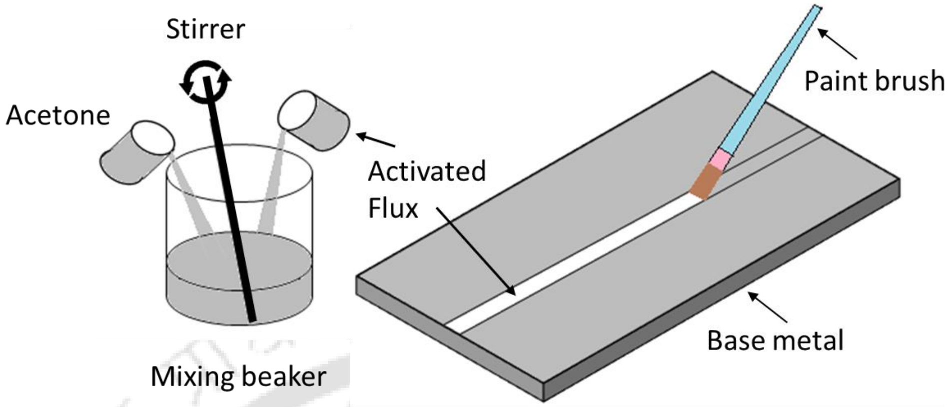

Figure 4.7 Mixing and coating of surface active elements

(a) (b)

Figure 4.8 Plates (a) after application of surface activating elements, (b) after the welding

This mixture is rushed manually on the top surface along the weld line of the specimen before welding. The coating density of flux is maintained approximately. The steps for applying the activated fluxes are described as follows:

- The oxide powder is mixed with acetone in a 1:1 weight ratio, to produce a paint-like consistency (Figure 4.8). The ratio of flux powder to carrier solvent is not critical, although it must be mixed in a consistent manner that can be "painted on**".** Chemical manufacturer's instruction is followed for handling these chemicals.

- The flux mixture has thicken over time as the thinner (acetone) evaporates. More acetone is added according to the requirement to return the mixture to the correct consistency.
- Using the small paint brush, oxide powder is applied to the centre of the plate. The layer has to be sufficiently thick so that the flux appears opaque. The layer should be slightly wider than the expected width of the weld bead. Flux should sufficiently be adhered to the surface to combine in all position.
- During welding, arc length has to be maintained as per welding specification.
- After welding, any unused flux has been removed with ease .Flux that has been consumed by the arc creates a tenacious layer. A residual slag which remains on the surface of the weld pool has been removed by grinding or aggressive wire brushing.

4.5.2 Measurement of temperature profiles

Time temperature history was measured using K-type thermocouples. The Fig 3.9 shows the schematic of the thermocouple arrangements for measuring temperature. Figure 4.10 shows the thermocouple locations during welding. Thermocouples ware attached in both side of the weld line.

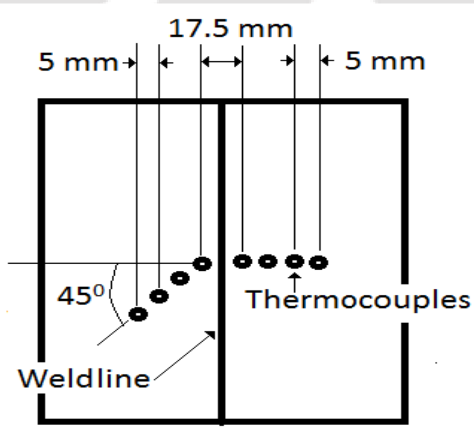

Figure 4.9 Schematic of the thermocouple arrangements

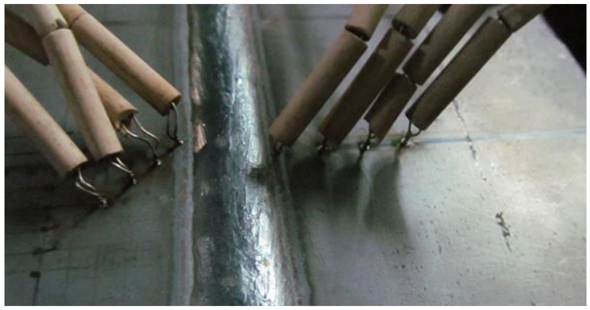

Figure 4.10 Thermocouple locations in a welded plate

4.5.3 Measurement of bead geometry and mechanical properties

Measurements are made for bead penetration and bead width directly and then reinforcement. The measurements of weld bead dimensions are taken by co-ordinate measuring machine (CMM). Figure 4.11 shows the welding plate while measuring the angular deformation using CMM. Tensile samples were prepared using CO_2 laser cutting machine as per ASTM E8 standard. Instron 3382 universal testing machine was used to measure the tensile properties of the welded samples. Figure 4.12 shows the tensile samples and the universal testing machine.

Figure 4.11 Measurement of angular deformation using CMM

(a) (b)

Figure 4.12 Image of the (a) Tensile samples (b) Instron 3382 universal testing machine

After welding each specimen are cut across the weld line to get a cross section of weld pool and were filed using flat file to get a flat surface. After cutting process polishing operations are done on each specimen using sand paper of four different grit sizes 320, 400, 800, 1200 and 2000. The specimens are rubbed on the sand paper in the presence of water. Final polishing has been performed on velvet cloth with alumina powder. After polishing 2% nital solution (mixture of nitric acid and alcohol) was used for etching. The mixture is kept for 20 minutes. Then small cut pieces of the weldment is dipped into that solution. After etching the weld pool and the weld zone, heat affected zone can be clearly be differentiated.

Figure 4.13 Metallurgical microscope

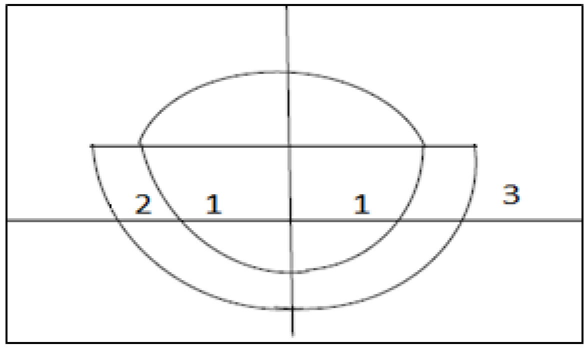

Figure 4.14 Different positions of hardness measurement (1-Weld zone, 2-HAZ zone, 3-parent metal)

Figure 4.13 shows the Zeiss metallurgical microscope used in this study. Vickers micro hardness tester was used to measure the hardness of different weld zones viz. weld bead, HAZ and parent metal. Figure 4.14 shows the locations of hardness measurement. Average of three readings was considered for each measurements.

4.6 Summery

In this section the experimental aspects of all the study were presented, which consists from the preparation of the fixture, backing bar, selection of the welding parameters, design of the experiments. Bead on welding was performed to study the effect of parameter on mechanical properties, welding was performed on mild steel plates of different joint geometries. After welding mechanical and microstructural characterization were conducted. Thermal history was also measured. In a nutshell the overview of the experiments involved in this study were discussed in this section.

CHAPTER 5

Results and discussions

5.1 General introduction

This chapter consists of two sections i.e. results of numerical thermo-mechanical analysis and results of experimental investigations.

A. Results of numerical thermo-mechanical analysis section consists of following subsections:

- Prediction of thermal history and angular deformation of square butt joints
- Prediction of thermal history and angular deformation of double sided fillet joint
- Comparative study of residual stress and angular deformation of single and double sided fillet welds
- Influence of tacking sequence on residual stress and distortion
- Prediction of welding sequence induced thermal history & residual stresses and their effect on welding distortion
- Prediction of weld induced distortion of large structure
- Development of a new heat source model

B. Experimental investigation section consists of following subsections:

- Effect of welding process parameters on weld bead geometry
- Effect of surface active elements on weld bead geometry
- Effect of included angle on mechanical properties of welded joint
- Effect of process parameters on mechanical properties
- Optimization of welding parameters

The numerical modelling of thermo-mechanical analysis of the submerged arc welding is influenced upon the selection of proper material properties, mesh size and other model parameters. In meshing, the smaller is the element size the higher will be the accuracy. So, if very fine mesh size is considered then the accuracy increases but the computational time will also increase. However, this problem can be minimized by selecting an optimum mesh size without losing the accuracy but with less computational time. The details of thermal and mechanical properties of mild steel, model geometry, mesh size selection etc. used in this present study are described below.

5.1.1 Model geometry

Thermal analysis followed by structural analysis was carried out in ASNYS 12.0 software. ANSYS Parametric Design Language (APDL) was used to model and simulate the analysis. The meshed views of the butt and fillet welds are shown in Figures 5.1 & 5.2 respectively. Finer mesh improves the prediction accuracy but increases the computational time therefore a non-uniform meshing scheme was used where finer mesh was done in the weld zone and incrementally coarser mesh was done away from the weld zone, thus it minimizes the computation time as well as improves the prediction accuracy. The mesh density was finalized after mesh sensitivity analysis, keeping a balance between the computation time and prediction accuracy.

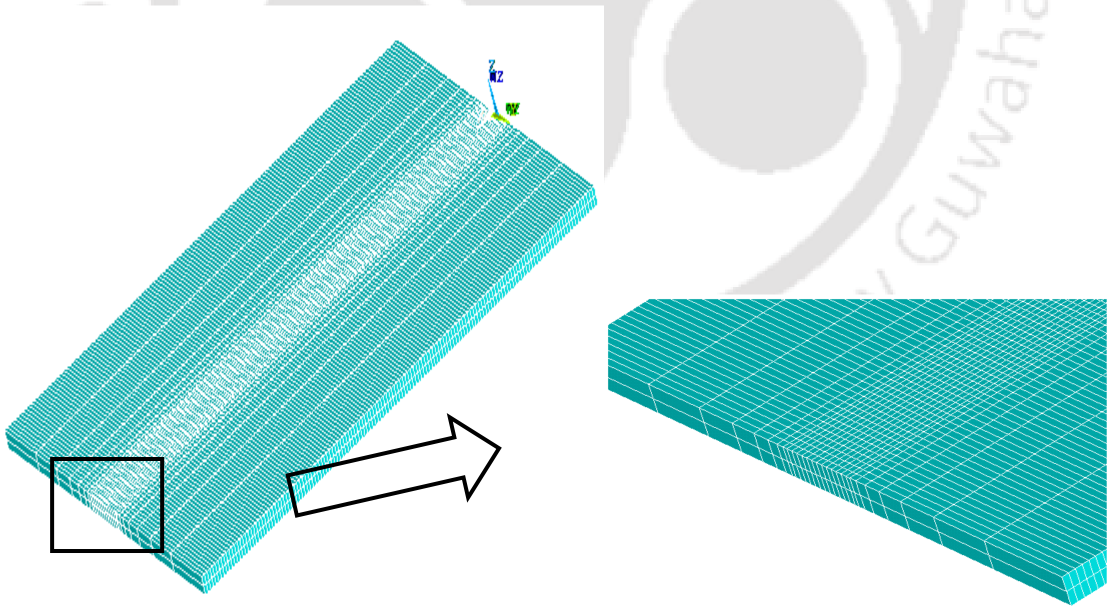

Figure 5.1 FE model and meshed view for butt weld

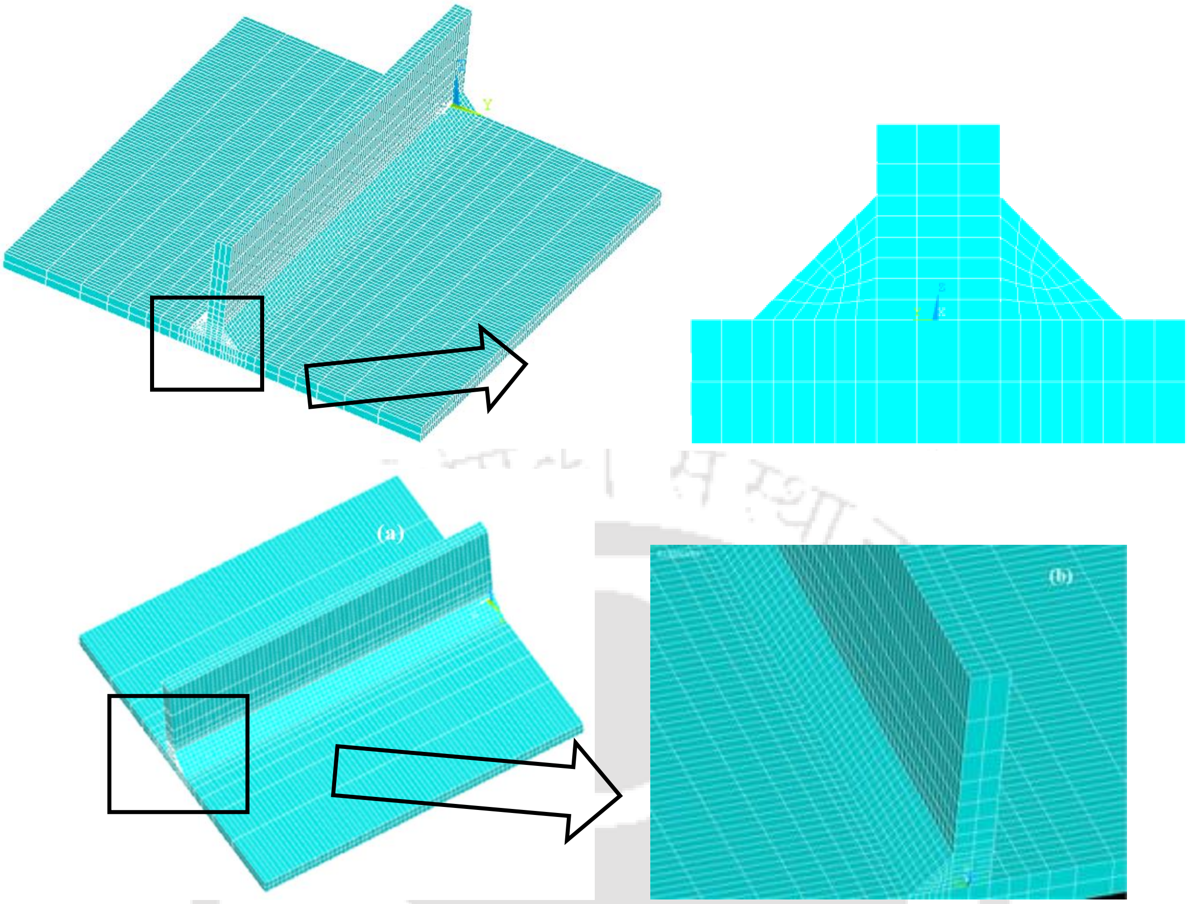

Figure 5.2 FE model with mesh for fillet weld (a) Double sided (b) Single sided

5.1.2 Material properties

The temperature dependent thermal and mechanical properties [73, 192] of the mild steel plates used in this study are shown in the Figures 5.3 (a) to (c). The thermal conductivity, yield stress and Young's modulus decreases with temperature but after 800 ^{o}C the thermal conductivity follows an increasing trend. The temperature dependent yield stress elastic modulus, thermal expansion coefficient and Poisson's ratio of mild steel are shown in the Figure 5.4.

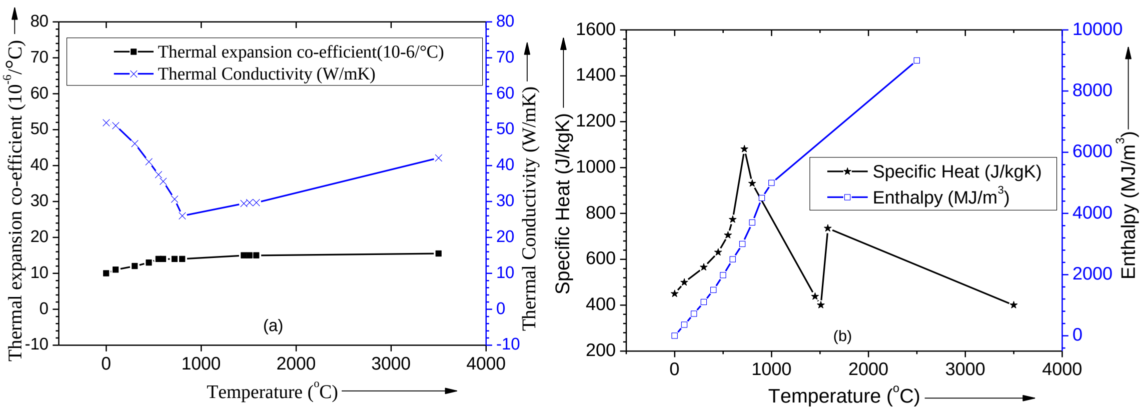

(a) (b)

Figure 5.3 (a) & (b) Temperature dependent thermal properties of mild steel [73, 192]

It is obvious that there are huge variations of material properties with temperature and it challenges to develop a well efficient model.

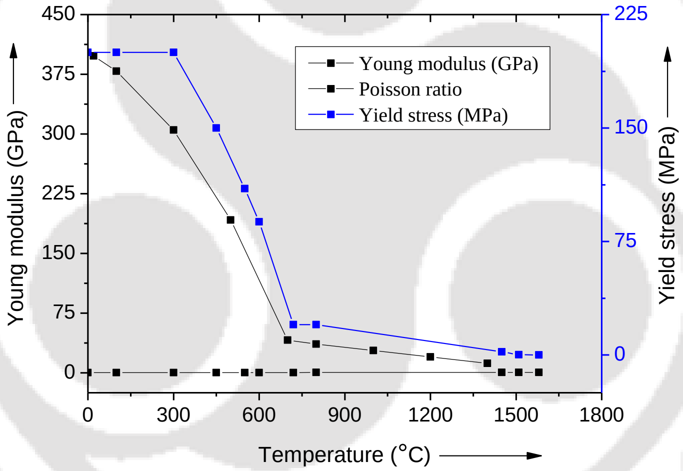

Figure 5.4 Temperature dependent of mechanical properties of mild steel [73, 192]

5.1.3 Experimental details

An ADORE SAW setup was used to perform the welding. Compatible mild steel electrode of 3.1 mm diameter and ESAB OK FLUX 10.17 L granular flux were used for carrying out the experiments. The temperature during welding was measured using K-type thermocouples. The thermocouples were connected to AGILENT 34972A data logger device with 20 channels multiplexer. This data logging device was connected to a PC and the temperature at different locations were measured & recorded with time.

Figure 5.5 (a) shows the welding set up with data logger. Figures 5.5 (b) & (c) show welded sample with thermocouple arrangements and the welded sample submerged under the granulated flux. The angular distortions were measured by using a 3D coordinate measuring machine (CMM), which is shown in the Figure 5.5 (d). Before welding the tack welded samples were marked to measure the coordinates before and after welding with respect to a reference surface. The angular distortion was calculated by subtracting the initial deformation (i.e. before welding data) from the final deformation (i.e. after welding data).

(a)

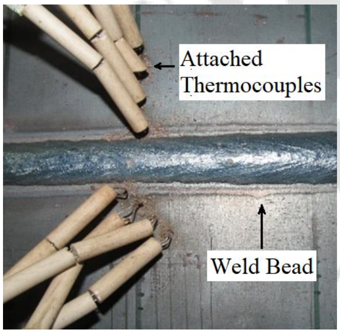

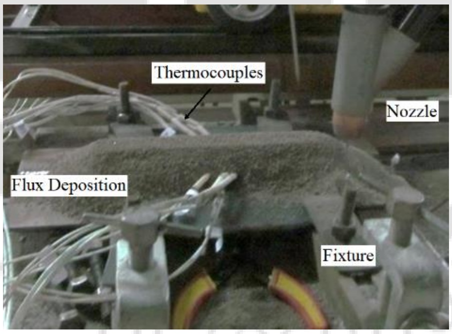

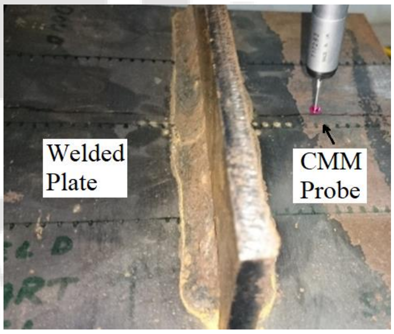

(b) (c) (d)

Figure 5.5 (a) welding set up with data logger, (b), welded plate with thermocouple arrangements (c) weld bead with flux after welding, (d) angular deformation measurement using CMM

A. Numerical thermo-mechanical analysis

Results and discussions of all numerical thermo-mechanical analysis are presented in this section. First, the results and discussions of the butt and fillet weld joints are presented, followed by the analysis of the large structure using an equivalent technique. Finally, a new heat source model was developed and comparative study was done with the existing model.

5.2 Prediction of thermal history and angular deformation of square butt joints

Here, a numerical model was developed for single pass single sided submerged arc welding of square butt joints. Submerged arc welding can be conveniently used to weld a range of plate thicknesses in a single run using a suitable backing strip achieving adequate top and bottom reinforcements. The 3D FE methodology established in the present work can be successfully used to predict the transient thermal history and distortions of square butt welds.

5.2.1 Transient thermal history

3-D modelling was done for welding of 8 mm to 12 mm thick MS plates (melting temperature is 1495^{o}C [188] and A_1 transformation temperature 723^{o}C [188] with square butt. The parameters used for square butt welding are given in Table 5.1. The results of the transient thermal analysis are shown in Figures 5.6 & 5.7.

Table 5.1 Welding parameters for square butt welding

Plate thickness (mm)	Current (A)	Voltage (V)	Welding speed (mm/s)
10	600	29	5.4

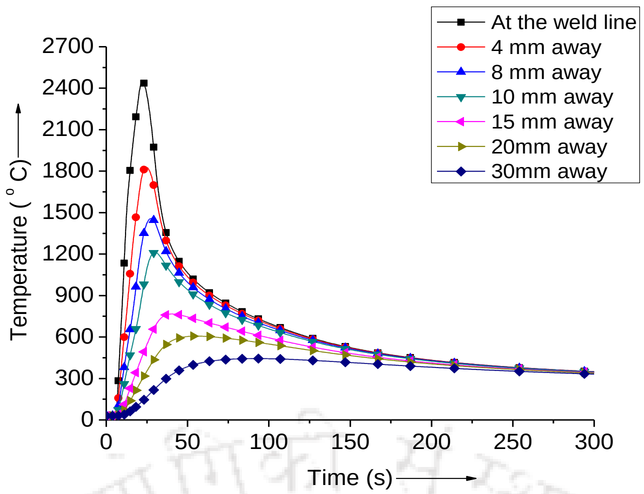

Figure 5.6 Temperature distribution at various points on plate top surface for square butt welding of 10 mm thick MS plate

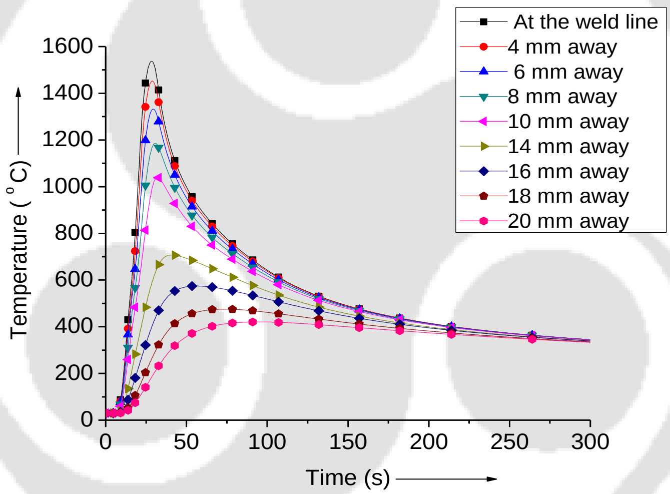

Figure 5.7 Temperature distribution at various points on plate bottom surface for square butt welding of 10 mm thick MS plate

Figure 5.6 & 5.7 represents the transient thermal history from center of weld line to away from the weld line on top & bottom surface respectively. The peak temperature is maximum at the center of weld line & it gradually decreases away from the weld line. Figure 5.8 shows the thermal profile of 8 to 12 mm thick plates along the weld line (mid point) for same welding parameters as shown in Table 5.2. It was seen from the Figure 5.8 that for same welding parameters, the welding temperature increases with decreasing of thicknesses and cooling rate increases with increasing of thicknesses.

Table 5.2 Welding parameters for square butt welding

Thickness (mm)	Root gap (mm)	Current (A)	Voltage (V)	Welding speed (mm/s)
8 to12	3.5	650	27.5	6.46

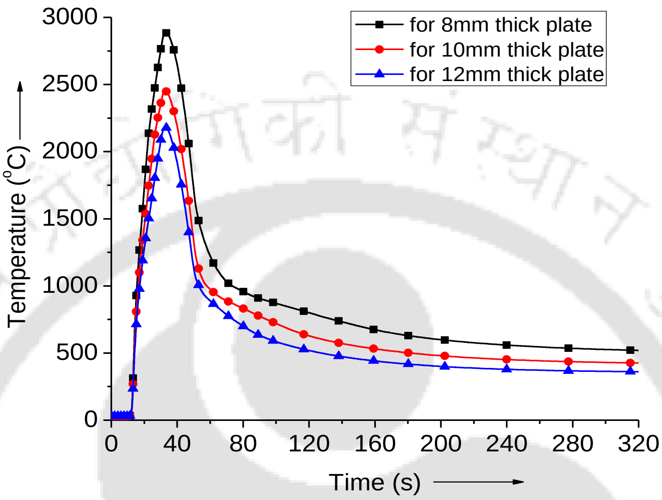

Figure 5.8 Temperature distributions at weld line plate top surface for square butt welding of 8 to 12 mm thick MS plate for same welding parameters

5.2.2 Prediction of angular deformation

Figure 5.9 shows the schematic diagram of a square butt joint, the numbers representing corner points and positions of tacks. Figure 5.10 shows the distortion shapes of 8 to 12 mm thick plate at the edge (parallel to weld line) of the plates with constraints at tack positions (5 and 6) for same welding parameters which is shown in Table 5.2. Figure 5.11 shows the distortion patterns of 8 to 12 mm thick plate at the edge (parallel to weld line) of the plates with constraints at tack positions (5 and 6) and corner points (1, 2, 3 and 4) for same welding parameters and the welding parameters is shown in Table 5.2.

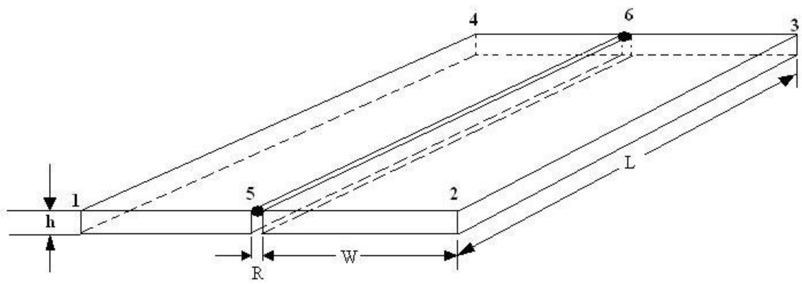

Figure 5.9 Schematic diagram of a square butt joint, the numbers representing corner points and positions of tacks

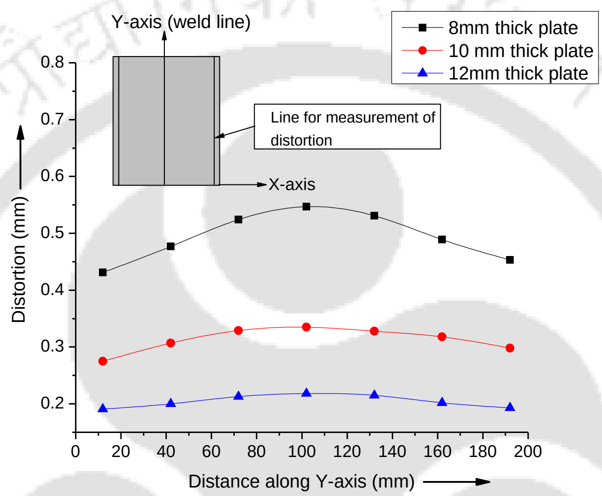

Figure 5.10 Distortion pattern for 8 to12 mm thick plate near the end of welded plate and parallel to the weld line

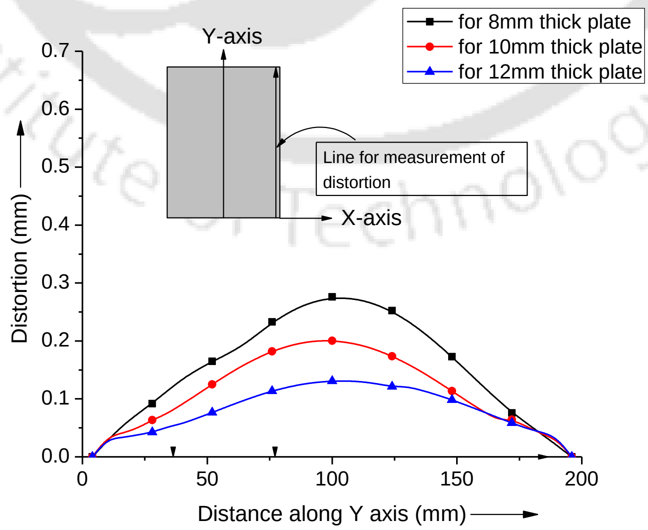

Figure 5.11 Distortion pattern for 8 to 12 mm thick plate near the end of welded plates and parallel to the weld line

From Figures 5.10 & 5.11 it is observed that the maximum magnitude of distortion is more for 8 mm thick plate & it is leas for 12 mm thick plate. From Figure 5.10 & 5.11 it is also observed that positon of constraints also have significant effect on magnitude of deformation.

5.2.3 Validation of numerical results of butt joints

To validate the FE numerical results experiments were conducted. For measuring temperature distribution, K-type thermocouples were used to record temperature history during welding by using temperature data acquisition system. Thermocouples were fixed 10 mm, 30 mm and 35 mm away from the weld line on upper surfaces of the plates during welding. The welding parameters and the joint details are given in Table 5.3. All plates were welded in square butt condition without any edge preparation. Before welding the tack welding were done at tack positions (as shown in Figure 5.9). Schematic diagram of the control points for measuring angular deformation is shown in **Figure** 5.12.

Table 5.3 Welding parameters and joint details

Exp. no.	Thickness (mm)	Root gap (mm)	Current (A)	Voltage (V)	Welding speed (mm/s)	Comments (Reinforcement)
1	10	3.5	635	28	6.67	Top and bottom
2	12	4	665	33	6.67	Top and bottom
3	12	3.6	690	33	7.08	Top and bottom
4	10	3.5	650	27.5	6.46	Top and bottom
5	8	2.6	570	29	6.25	Top and bottom
6	12	3.5	682	33	7.33	Top and bottom
7	10	3.5	635	28	6.67	Top and bottom

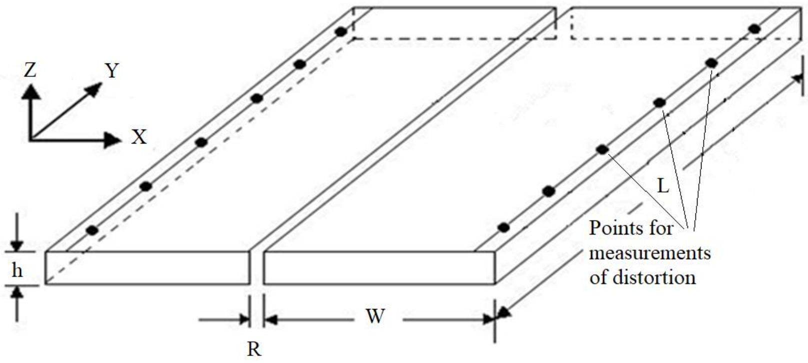

Figure 5.12 Points for measurement of distortions

Figure 5.13 shows the experimental and numerical thermal profiles for 12 mm thick plate. The thermocouple position for Figure 5.13 was 30 mm away from the weld line on top surface of the weld plate. The input welding parameters of this thermal profile (Figure 5.13) is given in Table 5.4, serial number is 1. Figure 5.14 shows the experimental and numerical thermal profiles for 10 mm thick plate. The thermocouple position for Figure 5.14 was 35mm away from the weld line on top surface of the weld plate. The input welding parameters of this thermal profile (Figure 5.14) is given in Table 5.4, serial number is 2.

Table 5.4 Welding parameters for prediction of thermal profiles and distortion

Sl. no.	Thickness (mm)	Root gap (mm)	Current (A)	Voltage (V)	Welding speed (mm/s)
1	12	3.5	682	33	7.33
2	10	3.5	635	28	6.67
3	8	2.6	570	29	6.25

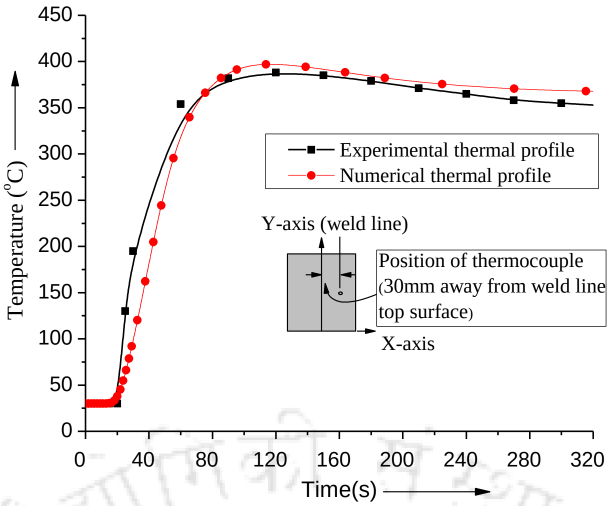

Figure 5.13 Comparison of numerical and experimental thermal profile for 12 mm thick plate

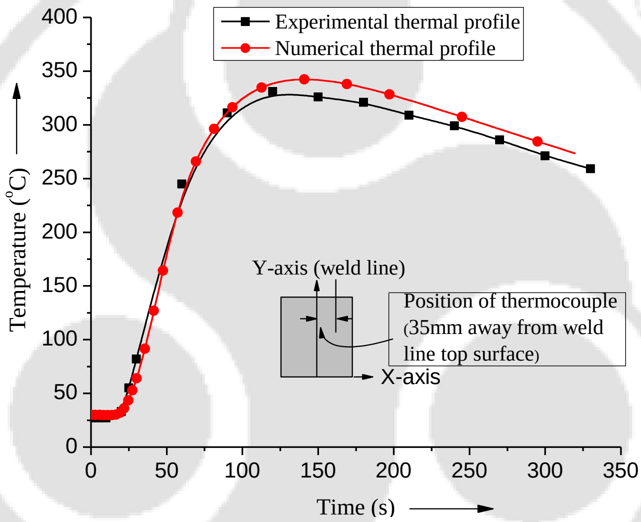

Figure 5.14 Comparison of numerical and experimental thermal profile for 10 mm thick plate

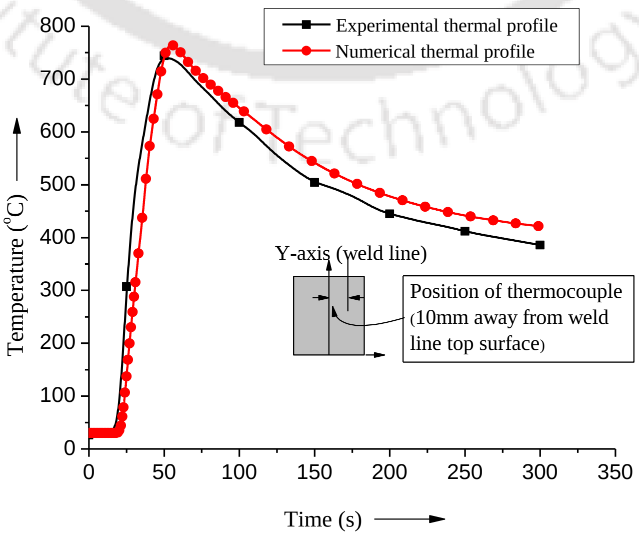

Figure 5.15 Comparison of numerical and experimental thermal profile for 8 mm thick plate

Figure 5.15 shows the experimental and numerical thermal profiles for 8 mm thick plate. The thermocouple position for Figure 5.15 was 10 mm away from the weld line on top surface of the weld plate. The input welding parameters of this thermal profile (Figure 5.15) is given in Table 5.4, serial number is 3. Figure 5.16 shows the experimental and numerical welding distortion patterns for 10 mm thick plate. The input welding parameters of this distortion pattern (Figure 5.16) is given in Table 5.4, serial number is 2.

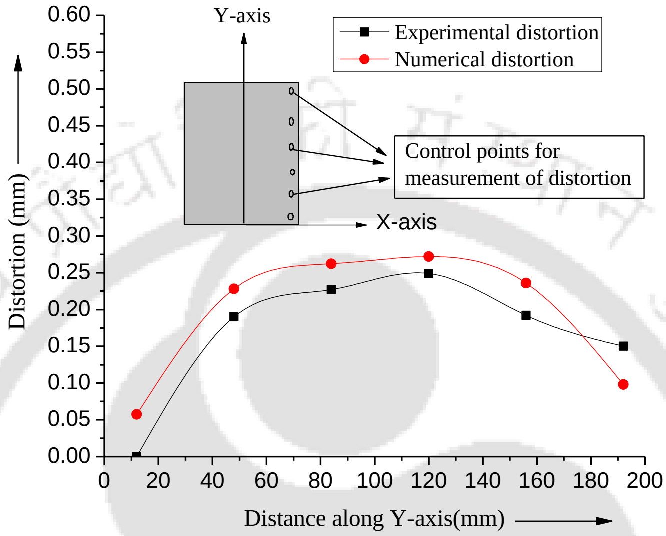

Figure 5.16 Comparison of numerical and experimental distortion for 10 mm thick plate

Figure 5.17 shows the experimental and numerical welding distortions pattern for 12 mm thick plate. The input welding parameters of this distortion pattern (Figure 5.17) is given in Table 5.4, serial number 1.

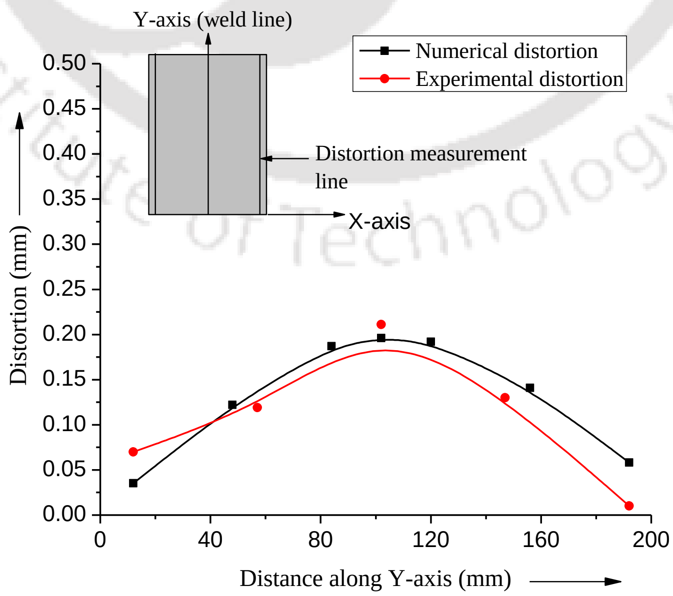

Figure 5.17 Comparison of numerical and experimental distortion for 12 mm thick plate

The resulting distortions matched fairly well with those of the numerically predicted ones. This was achieved by considering the restraining effect of the top and bottom reinforcements. The effect was modeled through the use of element birth technique as described in previous section. As was expected the extent of distortion decreased with increase in plate thickness for a given set of input of welding parameters.

5.2.4 Summary

From the preceding investigation of butt welds, it can be summarized as below:

- Through thickness fusion were achieved in 8 to 12 mm thick plates with square butt edge preparation in a single run of submerged arc weld using flux-filled reusable backing strip and suitable welding process parameters.
- The temperature distributions obtained through analysis and those obtained from experimental measurements compared fairly well with a variation of 3 to 8% only in case of peak temperatures.
- The variation of the predicted distortions and those obtained from experimental measurements was only about 4 to 10%.
- So, the above developed methodology can be successfully utilized to predict transient thermal history & distortions of SAW square butt joint.

5.3 Prediction of thermal history and angular deformation of double sided fillet joint

A three dimensional finite element based thermo-mechanical model was developed to predict the thermal history and distortions of double sided fillet welding by submerged arc welding. Figure 5.18 shows the schematic representation of the axis system of the fillet weld which was used for constructing the FE model. Table 5.5 shows the welding parameters considered for welding the fillet joints.

Table 5.5 Welding Parameters for double sided fillet welding

Plate thickness (mm)	Current (A)	Voltage (V)	Welding speed (mm/s)
10	420	25	5.0

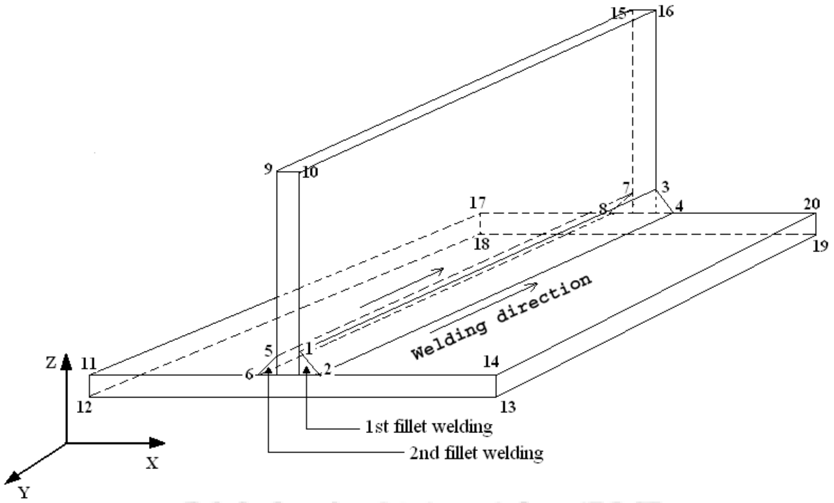

Figure 5.18 Schematic diagram of the fillet weld joint

To weld the double sided fillet weld, welding was performed in two successive passes therefore the transient thermal history was plotted for both the sides. Figures 5.19 and 5.20 shows the transient thermal history for first pass and second pass respectively. Temperature distribution from the center of the weld to away from the weld line was plotted. Second welding was performed after 3 min cooling of the first welding, therefore there is a pre heating effect on the second pass which can be seen from the Figure 5.21. The preheat temperature on the second weld shoot up nearly 420 °C from the first weld. Both heating and cooling of the welds can be observed from the time scale. Due to preheating effect the peak temperature of the second pass (2100 °C) is more than the first pass (1736 °C).

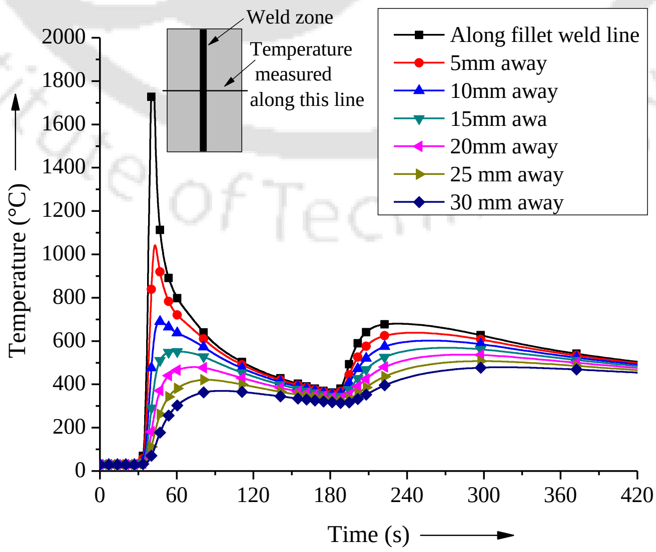

Figure 5.19 Temperature distribution for the first side of double sided fillet welding

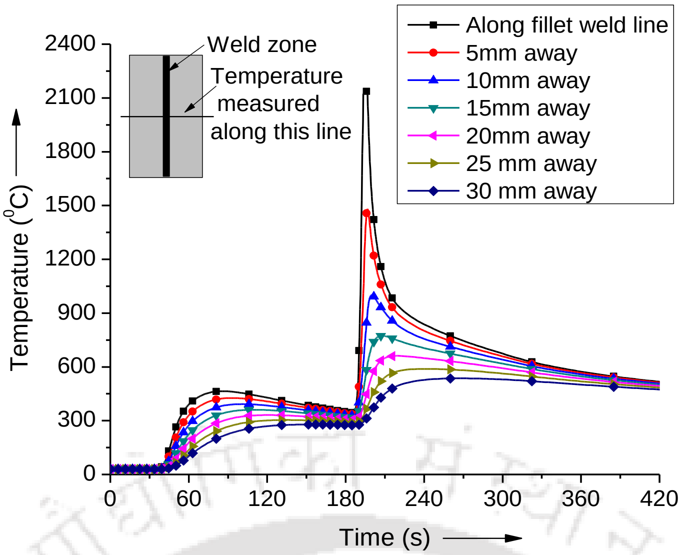

Figure 5.20 Temperature distribution for the second side of double sided fillet welding

Angular deformation was predicted for different welding conditions of double sided fillet welds. The welding parameters are shown in Table 5.6. In the finite element modelling the numerical angular distortions were plotted based on the nodal deflections from the non-linear elasto-plastic analysis at the edges of the plate. **Figure** 5.21 shows the finite element angular distortion comparison (nodal deflections) at the edges of the joint models for the welding parameters as given in Table 5.6.

Table 5.6 Numerical welding parameters for double sided fillet welding

Sl. no.	Thickness (mm)	Current (A)	Voltage (V)	Welding speed (mm/s)
1	10	425	25	5.0
2	10	460	27	5.0

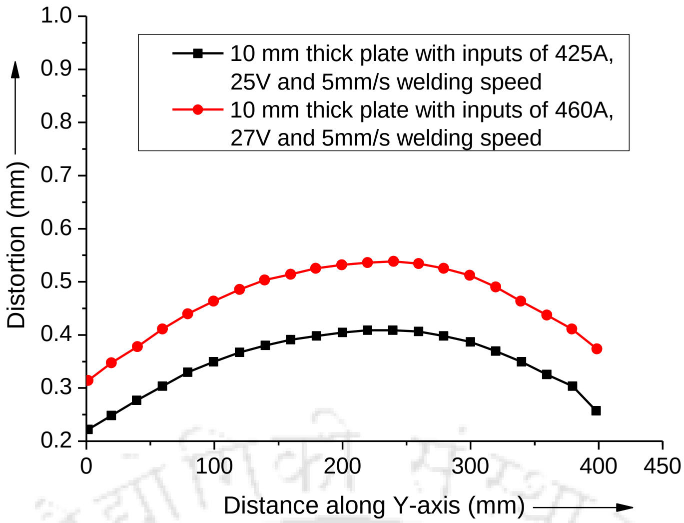

Figure 5.21 Comparison of angular distortion near the end of welded plate and parallel to the weld line (Table 5.6)

5.3.1 Verification of experimental and numerical thermal profile

Figure 5.22 shows the experimental and numerical thermal profiles of 10 mm thick plate for double sided fillet welding. The experimental points (thermocouple position) for the thermal history were located 15 mm away from the (for the first side fillet weld) weld line 2-4 (Figure 5.18) on the top surface of the horizontal plate at a distance of 200 mm from the edge 9-10-11-12-13-14 (Figure 5.18). Figure 5.22 shows the comparison of experimental and numerical thermal profile for the input welding parameters as given in Table 5.7. It can be observed form Figure 5.22 that there is a close agreement between the experimental and numerical thermal profile.

Table 5.7 Experimental welding parameters for double sided fillet welding

Thickness (mm)	Current (A)	Voltage (V)	Welding speed (mm/s)
10	470	27	5.0

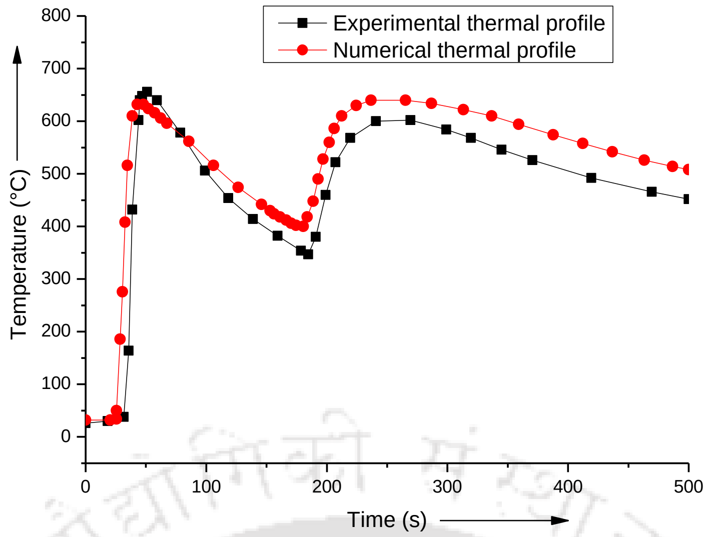

Figure 5.22 Comparison of numerical and experimental thermal profile (Table 5.7)

5.3.2 Verification of experimental and numerical distortion

The methodology developed in the present investigations based on moving distributed SAW heat flux was adequate enough for predicting the temperature distributions and angular distortions. The input experimental parameter of SAW process for two jobs are given in Table 5.8. Figure 5.23 shows the control points of the double sided fillet welding for measurement of distortion.

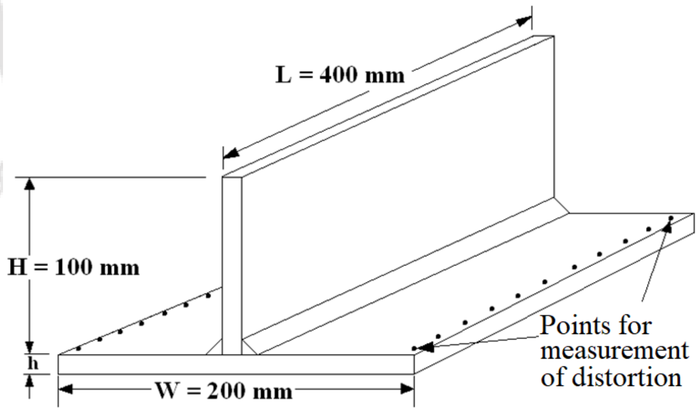

Figure 5.23 Plate dimensions and control points for measurement of distortion

Table 5.8 Experimental welding parameters for double sided fillet welding

Sl. no.	Thickness (mm)	Current (A)	Voltage (V)	Welding speed (mm/s)
1	10	425	25	5.64
2	10	470	27	5.0

Figure 24 shows the experimental and numerical welding distortions patterns for 10 mm thick plate for job 1 as indicated in Table 5.8. Figure 5.25 shows the experimental and numerical welding distortions pattern for 10 mm thick plate of job 2 as indicated in Table 5.8. From Figures 5.24 & 5.25 it can be observed that there is close agreement between the experimental and numerical distortion shape profiles.

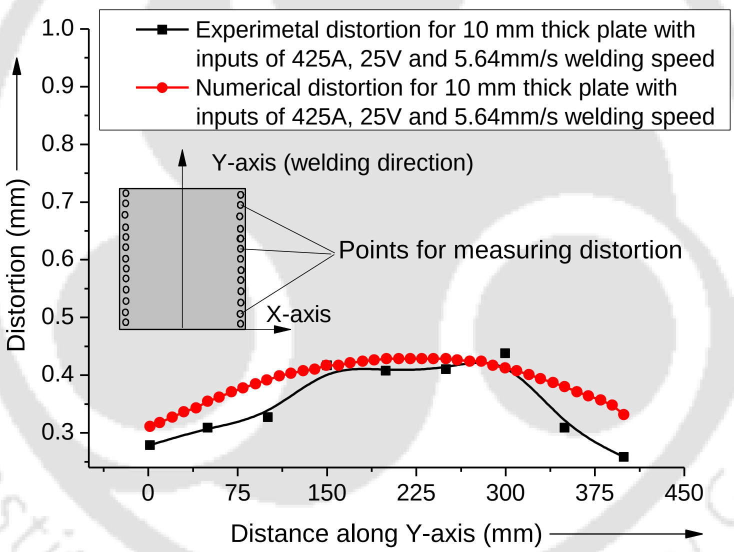

Figure 5.24 Experimental and numerical comparison of angular distortion for welding parameters of job 1 as given in Table 5.8

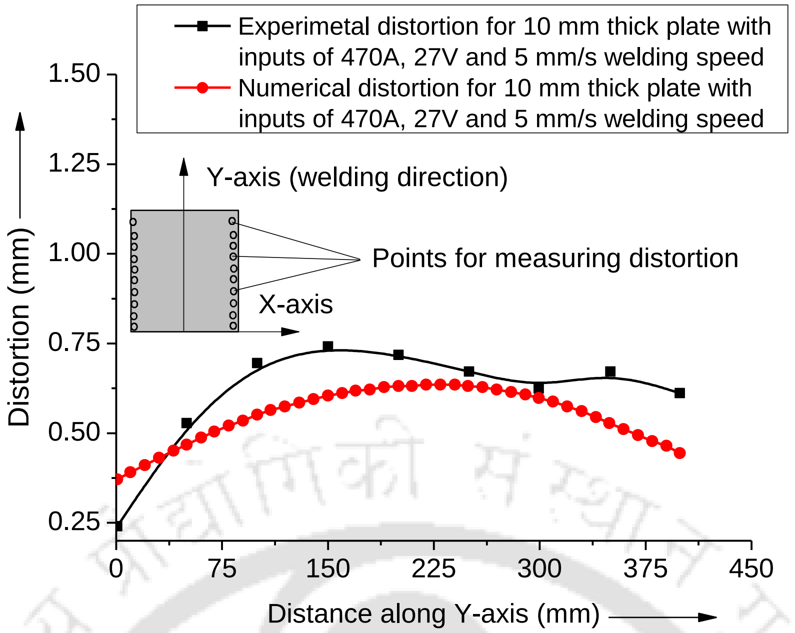

Figure 5.25 Experimental and numerical comparison of angular distortion for welding parameters of job 2 as given in Table 5.8

5.3.3 Summary

From the above investigation of double sided fillet SAW process, it can be summarized as below:

- Temperature distribution for 3-D finite element model for double sided fillet SAW process was developed and compared with the experimental results. It was found from thermo-mechanical modelling that as in the case of experiments the distortion patterns in case of 10 mm plate varied for varying input parameters.
- The temperature distributions obtained through analysis and those obtained from experimental measurements compared fairly well with a variation of 8% only in case of peak temperatures.
- The angular distortions obtained through the finite element analyses and those obtained from experimental measurements compared fairly well with a variation of 5 to 10% only, for maximum value of distortions.

5.4 Comparative study of residual stress and angular deformation of single and double sided fillet joints

Fillet joints are mostly used in structural applications which can be extensively seen in shipbuilding, bridge construction, house buildings, automobile or any other large structures. The aim of the present work is to quantify the amount of residual stresses and angular deformation in a fillet welding joint. An elasto-plastic thermo-mechanical model was developed for predicting residual stresses & distortions in case of single as well as double sided fillet joints. A comparative study of the residual stress and angular deformation between single and double sided fillet weld joint was made.

5.4.1 Experimental investigation of single and double sided fillet joints

Several set of experiments were carried out to study the weld induced residual deformation and thermal history for single and double sided fillet joints. Three welding parameter were taken as variables viz. current, voltage and welding speed where the length of stick out was kept at a constant value of 25 mm. The parameters used in the numerical analysis as shown in the Table 5.9. Figure 5.26 shows the welded samples with the granulated flux. Double and single sided filled welded samples are shown in the Figures 5.27 (a) & (b) respectively. The plate used in this study was 150 mm × 150 mm × 6 mm mild steel plate with a stiffener with a web height of 50 mm and thickness 6 mm.

Table 5.9 Welding parameters used in numerical analysis

Current (A)	Voltage (V)	Welding speed (mm/s)
480	21	6

Figure 5.26 Welded sample with flux and thermocouples attached

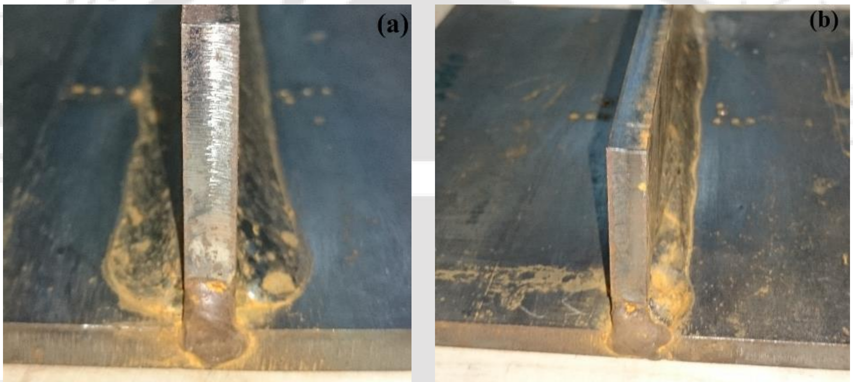

(a) (b)

Figure 5.27 Submerged arc welded fillet joints (a) double sided (b) single sided

5.4.2 Comparison of residual stresses distributions

First of all the residual stresses distribution for fillet welding joints were validated with published literature [186]. The comparison between the estimated results and results from published literatures of longitudinal and transverse residual stress for single sided fillet welded joint are shown in Figures 5.28 and 5.29 respectively. Same parameters were used for the numerical analysis at the present work. A good agreement can be observed in both the cases of longitudinal and transverse residual stresses. After validating the present developed model, it was used to study the residual stresses distribution both in single and double sided fillet welding.

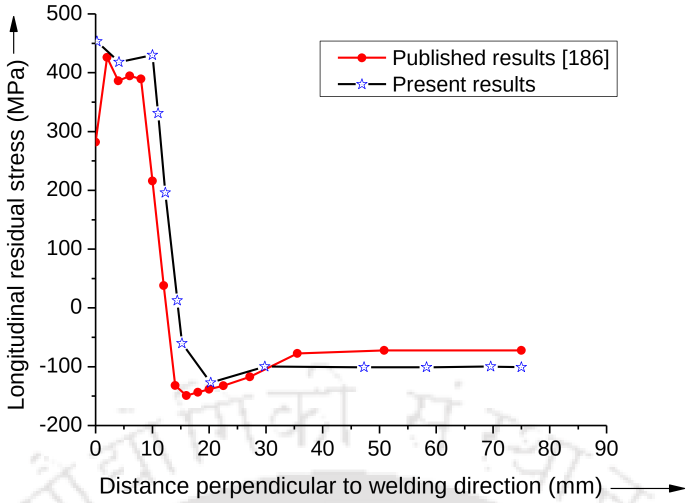

Figure 5.28 Comparison of longitudinal residual stress with published literature [186]

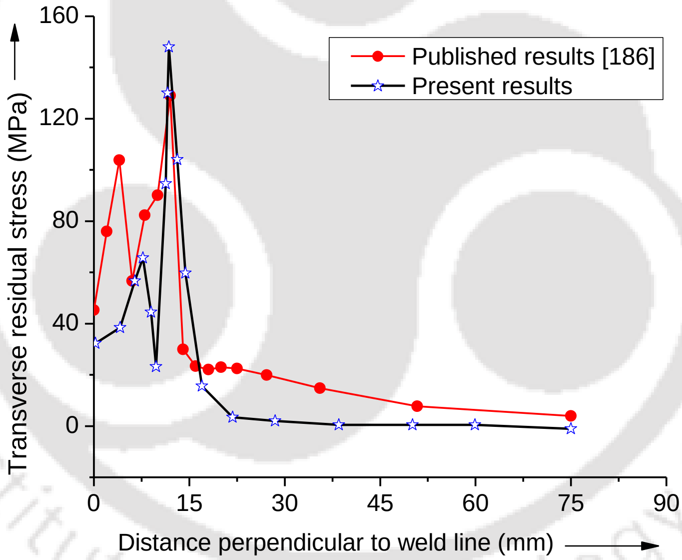

Figure 5.29 Comparison of transverse residual stress with published literature [186]

The contour plots of longitudinal, transverse and von-Misses residual stress distribution for single sided fillet welding are shown in Figure 5.30. Figure 5.31 (a, b & c) represents the longitudinal, transverse & von-Misses residual stress distribution pattern for double sided fillet welding.

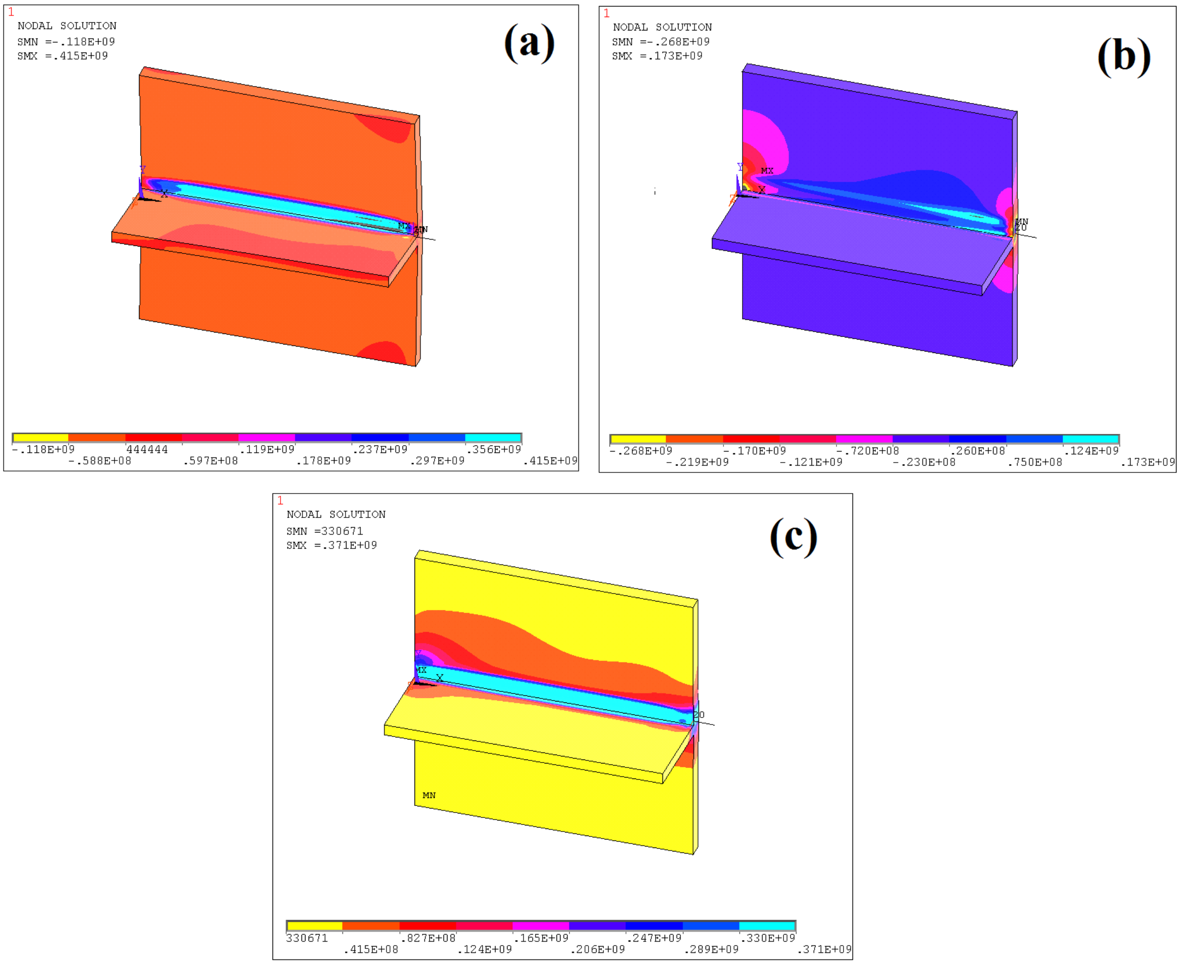

Figure 5.30 (a) Longitudinal, (b) Transverse and (c) von-Misses residual stress distribution for single sided fillet welding

The maximum value of longitudinal and transverse residual stresses are found to be 415 MPa and 173 MPa respectively for single sided fillet welding which is shown in the Figure 5.31 (a & b). It can also be seen from the Figure 5.30 (c) that the maximum magnitude of von-Misses residual stress distribution is 371 MPa. Overall, it is observed that within and proximity to the welding region stress distribution is tensile in nature and away from the weld line it is compressive in nature. As the temperature gradient is maximum at the weld zone, during solidification of the molten metal the weld zone solidifies rapidly thus shrinkage occurs and it pulls the adjacent materials. Therefore the residual stress in the weld zone is always tensile in nature. But away from the weld line i.e. in the heat affected zone the temperature gradient is less and it takes more time to get cooled. To balance the weld shrinkage force induced by the weld zone it applies a counter force. Therefore residual stress is compressive in nature away from the weld line.

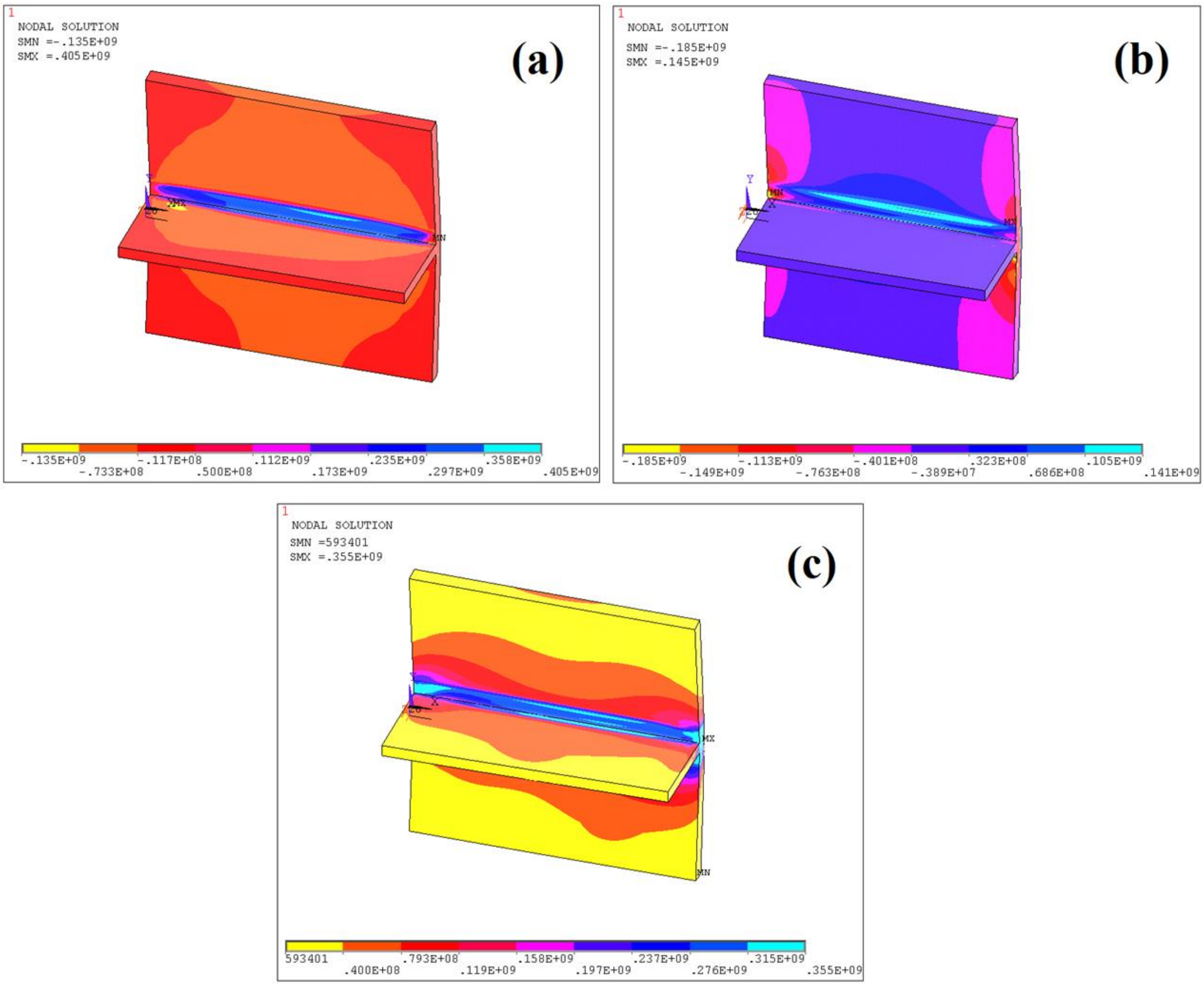

Figure 5.31 (a) Longitudinal, (b) Transverse and (c) von-Misses residual stress distribution for double sided fillet welding

From Figure 5.31, same pattern of residual stress distribution is observed as of the single sided weld. The maximum amount of longitudinal and transverse residual stress is found to be 405 MPa and 145 MPa respectively. The maximum amount of von-Misses residual stress is found to be 355 MPa.

Figure 5.32 shows the comparison of longitudinal residual stress distribution between single and double sided fillet welding from centre of base plate to perpendicular to the welding direction. Comparison of transverse residual stress distribution between single and double sided fillet welding is shown in Figure 5.33. Figure 5.34 shows the comparison of von-Misses residual stress distribution between single and double sided fillet welding. The comparison between the longitudinal & transverse residual stress along the weld line of single and double sided fillet welds are shown in Figures 5.35 & 5.36 respectively.

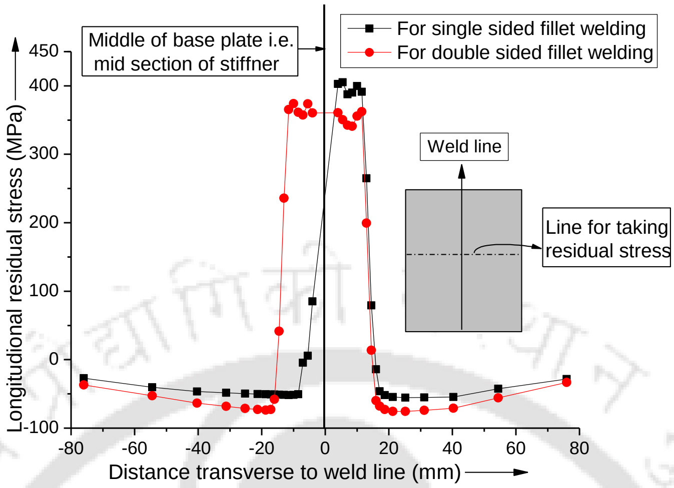

Figure 5.32 Comparison of longitudinal residual stress distribution

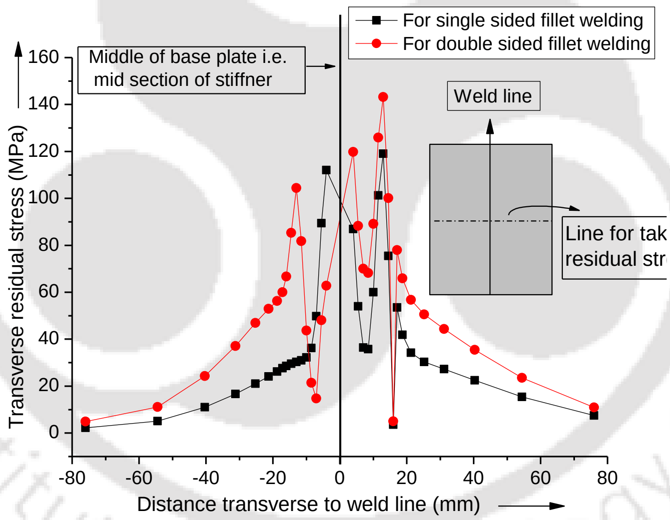

Figure 5.33 Comparison of transverse residual stress distribution

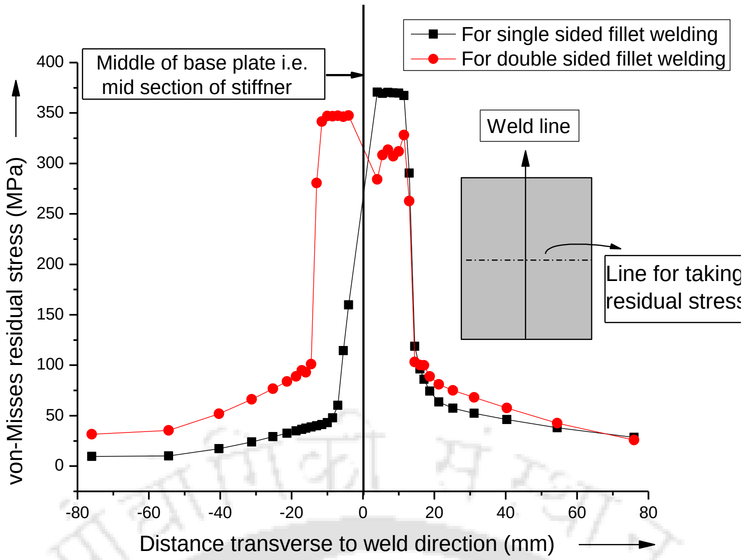

Figure 5.34 Comparison of von-Misses residual stress distribution

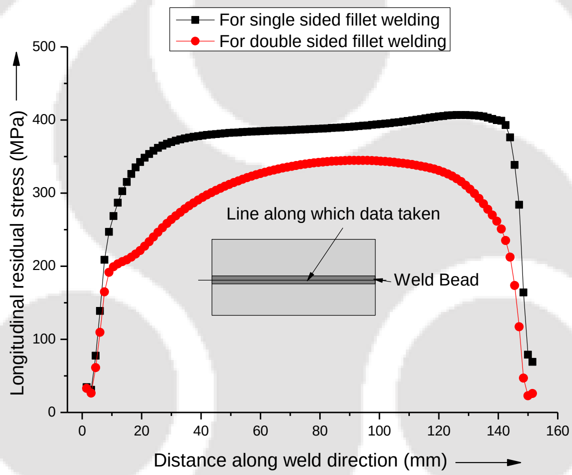

Figure 5.35 Comparison of longitudinal residual stress distribution along weld line

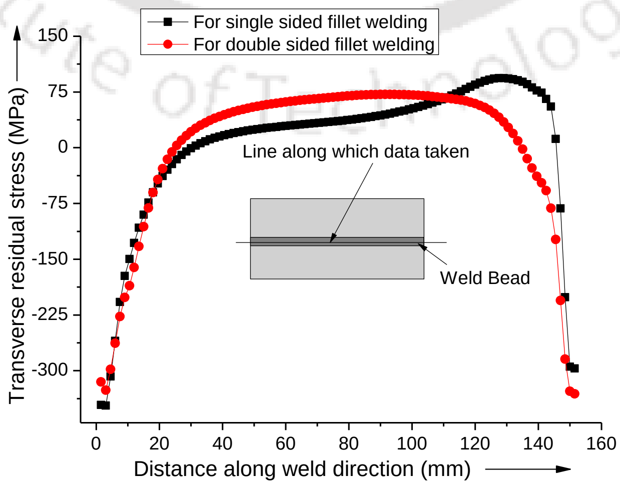

Figure 5.36 Comparison of transverse residual stress distribution along weld line

For same welding parameters the magnitude of both longitudinal and transverse residual stresses are more in case of single sided fillet welding as shown in Figures 5.35 & 5.36. At the beginning of transient stage the residual stress raises to a maximum value and it remains almost constant throughout the entire weld length i.e. along the quasi stationary region. This is because at the initial transient stage the temperature is raising and final transient i.e. at end of the weld length the temperature is decreasing but at the mid region i.e. at the quasi stationary region, the peak temperature remains almost constant. From the above Figures 5.32 to 5.36 it can be observed that the maximum magnitude of the residual stresses for single sided weld is more than the double sided ones.

5.4.3 Comparison of residual deformations

The Maximum value of angular deformation can be seen in the double sided fillet weld joint. Figures 5.37 and 5.38 show the contour plot of angular deformation distribution for double and single sided fillet welds respectively.

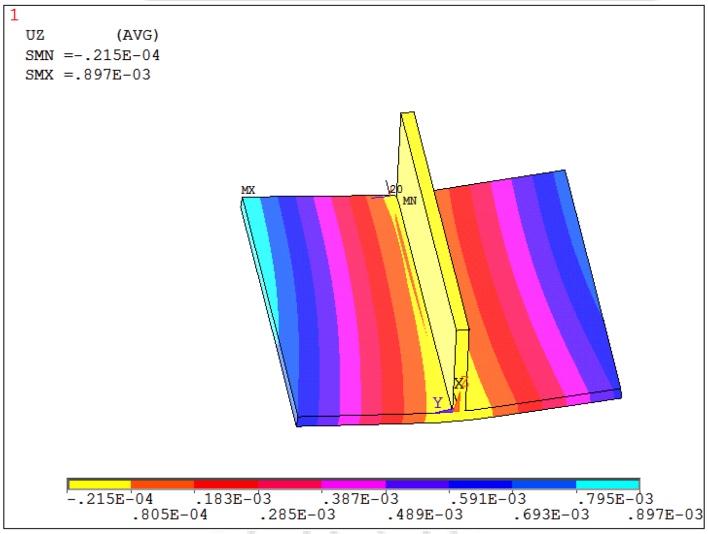

Figure 5.37 Contour plot of angular deformation of double sided fillet weld

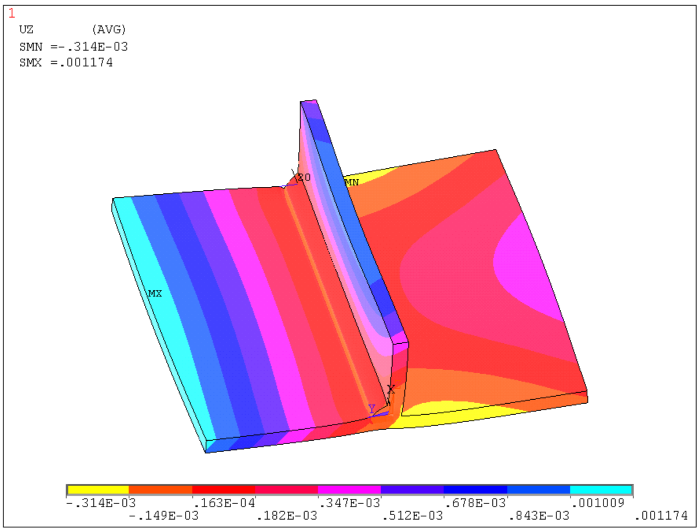

Figure 5.38 Contour plot of angular deformation of single sided fillet weld

Figure 5.39 represents the angular deformation in single and double sided fillet welds, from which it can be clearly concluded that the single sided fillet weld joint is deformed in one side only however it provides the lower angular deformation that the double sided fillet welded joint. A co-ordinate measuring machine (CMM) was used to measure the angular deformation of the welded plates. Figure 5.40 shows the plot of angular deformation from experimental analysis. It can be noted that similar trend is visible in both prediction and experimental analysis thus the developed model is effective in prediction of the angular deformation of fillet welded joints.

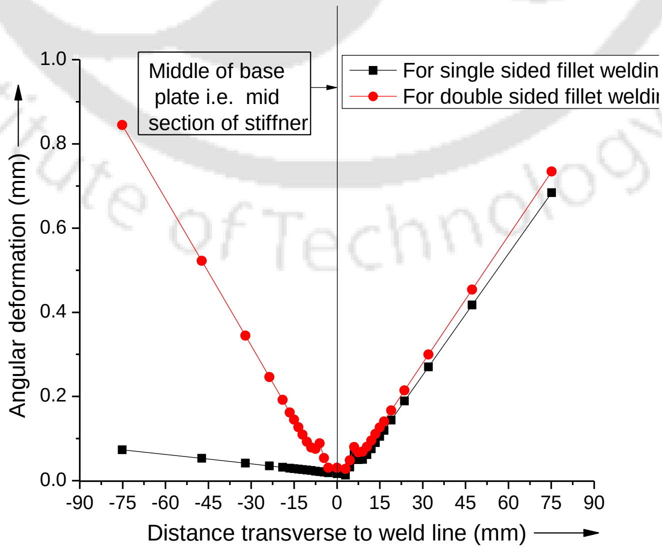

Figure 5.39 Comparison of angular deformation between single and double sided fillet weld

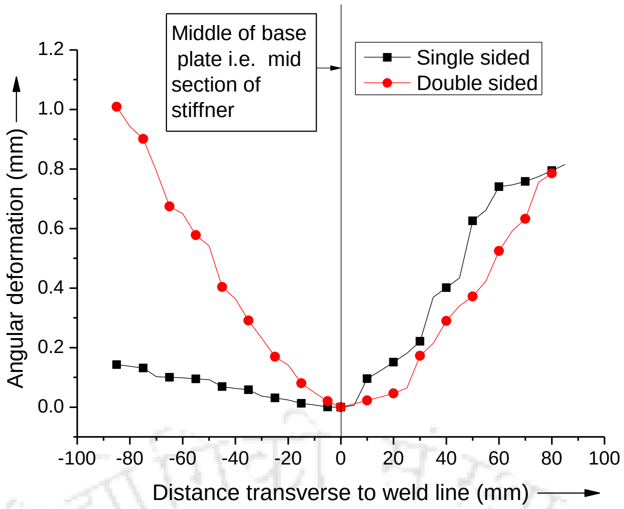

Figure 5.40 Comparison of experimental angular deformation between single and double sided fillet weld

At this present study it was observed that in case of single sided fillet welding the longitudinal residual stress distribution is unbalanced over two sides of the centre of the base plate which is balanced in case of double sided fillet weld. And the maximum value of transverse residual stress is more for single sided fillet weld than the double sided fillet weld. The same pattern can be seen in transverse residual stress also. The maximum value of overall residual stress (von-Misses residual stress) residual stress is more in case of single side fillet welding compare to that of double sided fillet welding. Within and nearer to the welding region, the longitudinal and transverse residual stress is tensile type and away from the weld line it is compressive type.

It was also observed that the peak value of longitudinal residual stress is much higher than the peak value of transverse residual stress in both single and double sided fillet welding. But the maximum value of angular deformation was seen in the double sided fillet welded joint.

5.4.4 Summary

The summary of this study can be stated as below:

- A 3-D finite element model was developed to compare the residual stress and angular deformation in case of single and double-sided fillet welded joints of mild steel plates.

- From the nonlinear transient elasto-plastic thermo-mechanical analysis, it can be seen that in case of single sided fillet welding the residual stress distribution in the left and right side of the stiffener is not uniform i.e. in weld side the stress distribution is tensile in nature near the stiffener and compressive away from the stiffener but it is fully compressive in other side. Double sided fillet welding shows quite common pattern of the residual stress distribution in the left and right side of the stiffener is almost uniform.

- The maximum value of residual stress is more in case of single sided fillet welding compare to that of double sided fillet welding. But the lowest magnitude of angular deformation was seen lower in case of single sided fillet weld. The simulation results reveal that the amount of residual stress present in the single sided fillet weld is more and unbalanced in both side of the center of weld line compared to the double sided fillet weld.

- Both numerical and experimental results indicate that the angular deformation is significantly affected by the choice of fillet welding type (i.e. single and double sided fillet).

- The predicted residual stress from numerical analysis was validated with the published literature whereas the angular deformation was validated with the experiments which provides a sound agreement. Therefore it would be feasible to use this model to predict the angular deformation of single and double sided fillet welds.

5.5 Influence of tacking sequences on residual stresses and distortions

A tacking is a temporary weld which is used to hold the work pieces together at specific locations before the actual welding. Generally manual metal arc welding is used to do the tack welding. A number of tack welds are used in a large structure during the welding process. Hence the positioning of tacking as mechanical boundary constraints may influence the residual stress level and distortion for the whole structure.

At the present study the analysis was carried out to predict the residual stress and distortion of single pass fillet joints with four different tacking sequences. The welding parameters considered for this study is shown in Table 5.10. The dimensions of the stiffened mild steel plate are 200 mm × 200 mm × 6 mm with a web height and thickness of 50 mm and 6 mm respectively.

Table 5.10 Welding parameters

Plate thickness (mm)	Current (A)	Voltage (V)	Welding speed (mm/s)
6	430	22	5

A schematic view of the single sided fillet weld joint along with coordinate system and tack positions is depicted in Figure 5.41 To prevent the rigid body motion, the rigid body boundary condition was incorporated in the FE model and also constraints were applied in weld tack positions.

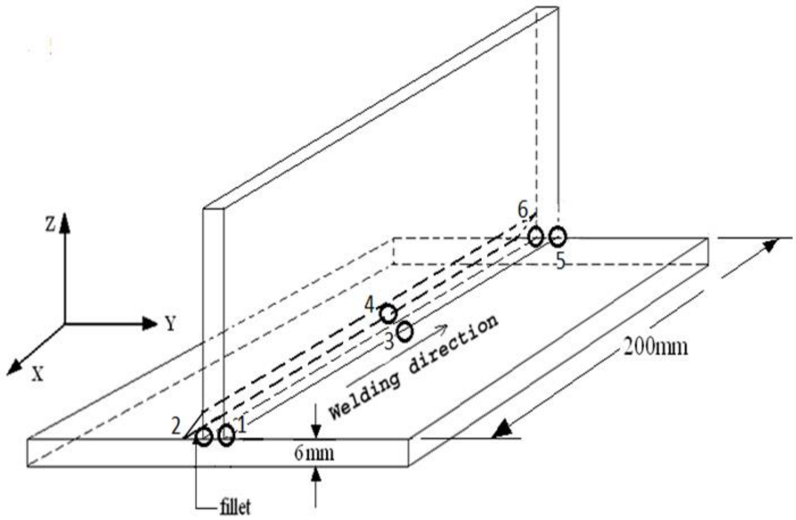

Figure 5.41 Coordinate system and tack positions for single sided fillet welding

At this present study with the existence of six number of tack positions the work piece can be tack welded at least in 57 ways, if we select at least two tacking positions. Therefore, four different tacking sequences were randomly selected from the population of 57, such that there are certain variations in the number of tack positions. Welding was carried out according to different tacking sequences as described in Table 5.11. Tack positions 1, 3 and 5 are opposite to welding side and tack positions 2, 4 and 6 are in the welding side of the single sided fillet joint.

Table 5.11 Tacking sequences and their nomenclatures

Tacking Sequences	Nomenclatures
Tack positions 2 & 6	TS-I
Tack positions 1,3 & 5	TS-II
Tack positions 1, 2, 5 & 6	TS-III
Tack positions 1, 2, 3, 4, 5 & 6	TS-IV

5.5.1 Comparison of distortions

Figure 5.42 illustrates the distortions of the fillet welded plate due to the different tacking sequences i.e. TS-I to TS-IV. The distortions shown in Figure 5.42 are taken perpendicular to the weld line from center of weld to both side of the weld line as shown in Figure 5.42. It is clear from the Figure 5.42 that the angular distortion in the fillet side is more and in the opposite side it is less in all four cases, which means the angular deformation is completely unsymmetrical in nature. The maximum angular deformation in the fillet side can be observed in TS-II (i.e. tack position in 1, 3 and 5) and minimum in TS-IV (i.e. tack position in 1, 2, 3, 4, 5 and 6). Therefore the obtained simulation results clearly indicate the influence of tacking sequences in the present study.

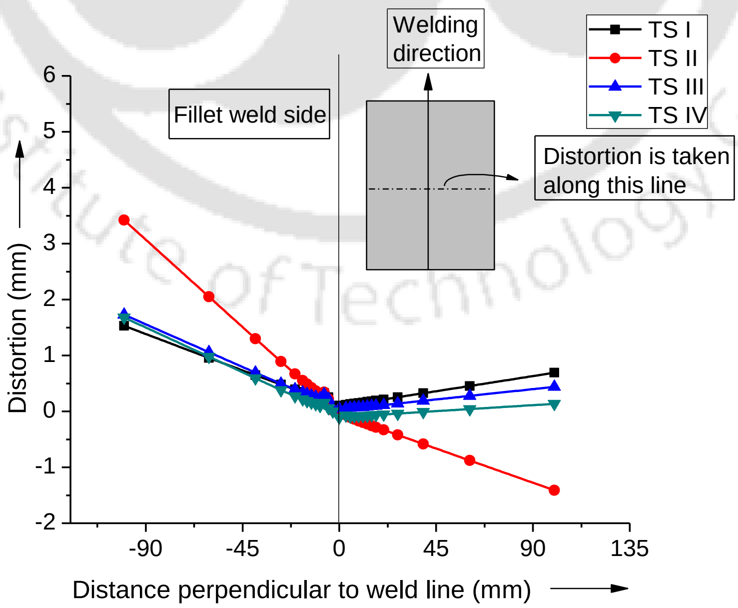

Figure 5.42 Maximum angular distortions perpendicular to the weld line.

A comparison of the predicted angular distortion from FE analysis with the angular distortion from the experimental observation is shown in the Table 5.12.

Table 5.12 Experimental and FE comparison of angular deformation at the middle length

Tacking sequence	FE maximum distortion				Experimental maximum distortion				% of deviations	
	FS		OS		FS		OS		FS	OS
	(mm)	(°)	(mm)	(°)	(mm)	(°)	(mm)	(°)	(%)	(%)
TS-I	2.22	1.27	0.69	0.39	2.32	1.32	0.61	0.34	4.50	12.10
TS-II	3.72	2.13	1.30	0.74	3.17	1.82	1.14	0.65	14.78	12.30
TS-III	2.00	1.14	0.67	0.38	1.73	0.99	0.58	0.33	13.50	13.56
TS-IV	1.78	1.02	0.59	0.33	1.58	0.90	0.51	0.29	11.23	13.55
FS=Fillet Side OS=Opposite side										

The maximum magnitudes of angular deformation are considered both for fillet side and opposite side. For all the tacking sequences the percentage of deviation of the predicted results from the experimental results lays in between 4.55% to 13.55% which is sound enough, thus shows the accuracy of the developed finite element model.

The contour of angular deformations of four different cases is shown in Figure 5.43. As in case of TS-II the restrains are in opposite side of the weld that’s why the angular deformation was enhanced in weld side due to the weld shrinkage force. Similarly, in all other cases as the restrains are in both side of the stiffener (i.e. in weld side and opposite to the weld side), which reduce the angular distortion of the welded structure. This happens because the weld shrinkage force developed in the welded structure is restrained by the weld tacks in both sides.

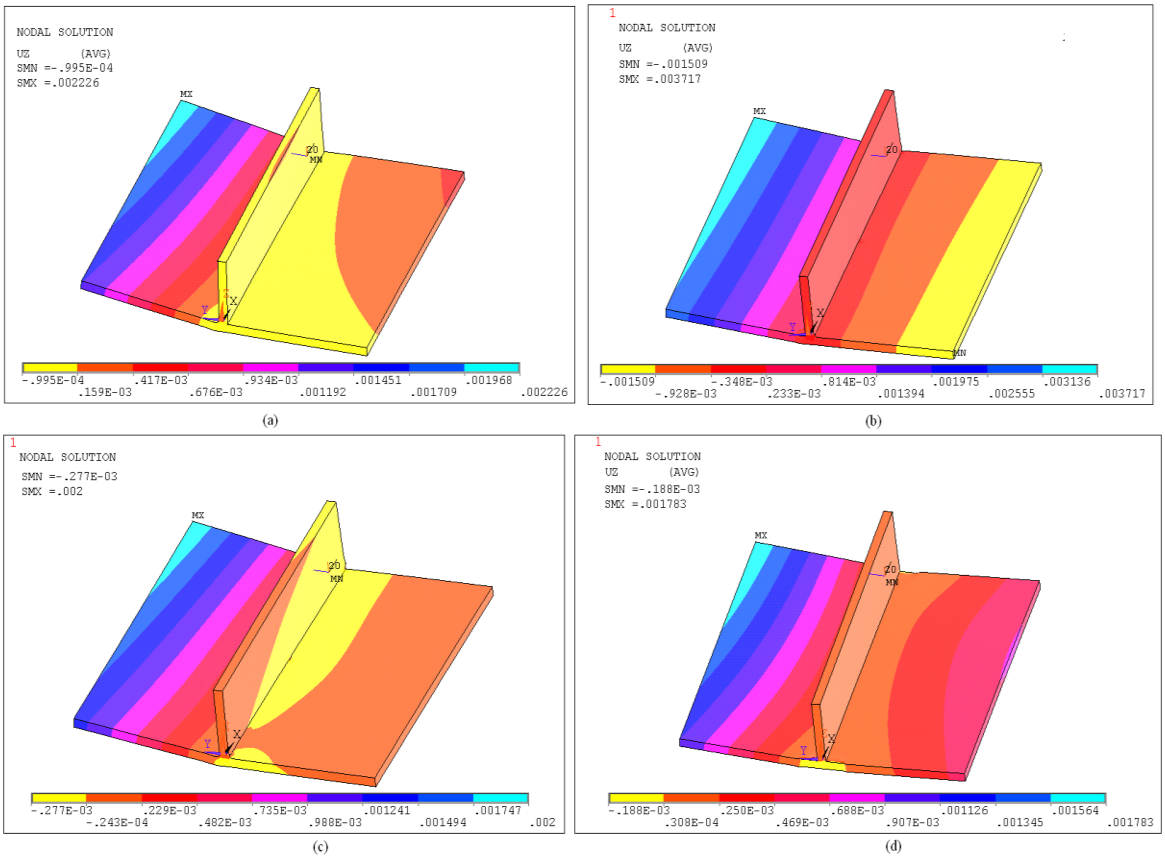

Figure 5.43 Distortions for four different tacking sequences [**(a)** TS-I (**b)** TS-II **(c)** TS-III and **(d)** TS-IV].

5.5.2 Comparison of residual stresses

It was observed that within and closer to the welding region the residual stress is tensile in nature and away from the weld line it is compressive in nature. Figures 5.44 to 5.50 describe the predicted longitudinal, transverse and von-Misses residual stresses distribution along weld line and perpendicular to the weld line for four cases of tacking sequence.

Figure 5.44 represents von-Misses residual stress distribution along the weld line. In all cases the von-misses residual stress distribution can be found uniform throughout the weld line except the tack positions where some non-uniformity can be observed. Figure 5.45 shows the von-Misses residual stress distributions perpendicular to weld line. For TS-II & IV the variation of residual stresses observed at the middle length of welding where tack weld was done.
It was observed that the residual stresses increased due to the tack positions in weld side where as the residual stresses lowered due to the tack positions in opposite side of welding.

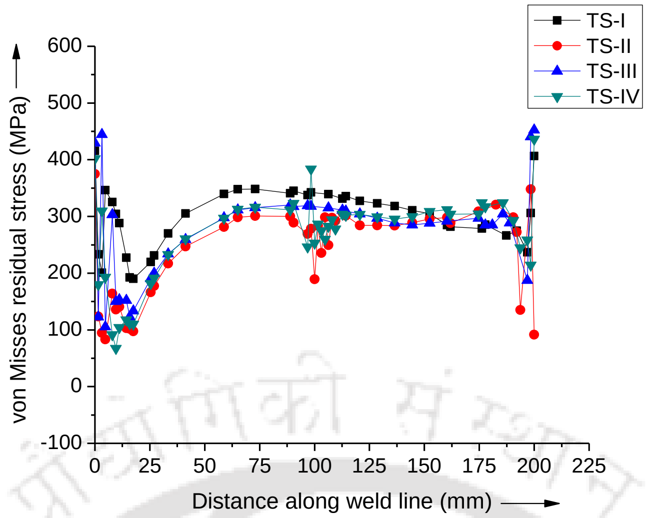

Figure 5.44 von-Misses residual stress distribution along weld line

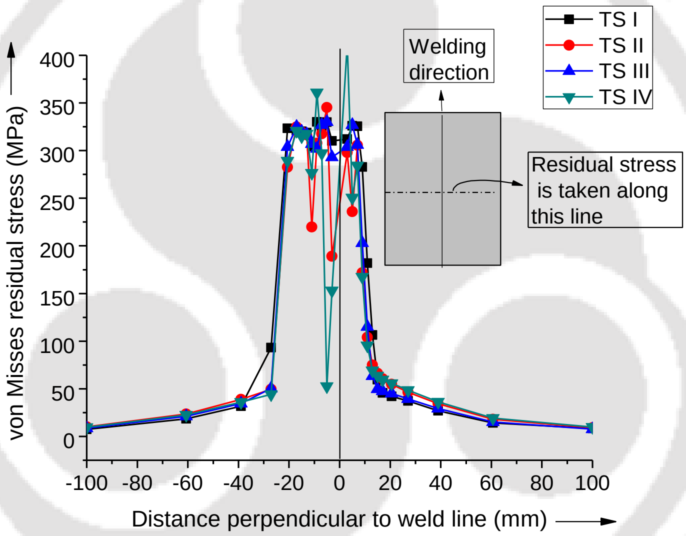

Figure 5.45 von-Misses residual stress distribution perpendicular to weld line

Figure 5.46 represents the longitudinal residual stress distribution along the center line of fillet weld joint. From Figure 5.46 it can be observed that the stress magnitude and distribution patterns are dependent on weld tack sequence. It was observed that except the tack positions the transverse residual stress is uniform through the length and the magnitude of residual stress in tack positions is significantly higher than that of without tack positions. Figure 5.47 represents the longitudinal residual stress distribution perpendicular to the fillet weld line. From this Figure 5.47 it is seen that along the weld line it is tensile and away from the weld line it is compressive in nature. It was observed that though the residual stress distributions near the middle length tack positions (i.e. tack positions 3 & 4) were uneven in nature but the magnitude of residual stresses is reduced for the weld tack positioned opposite to the weld line i.e. for TS-II.

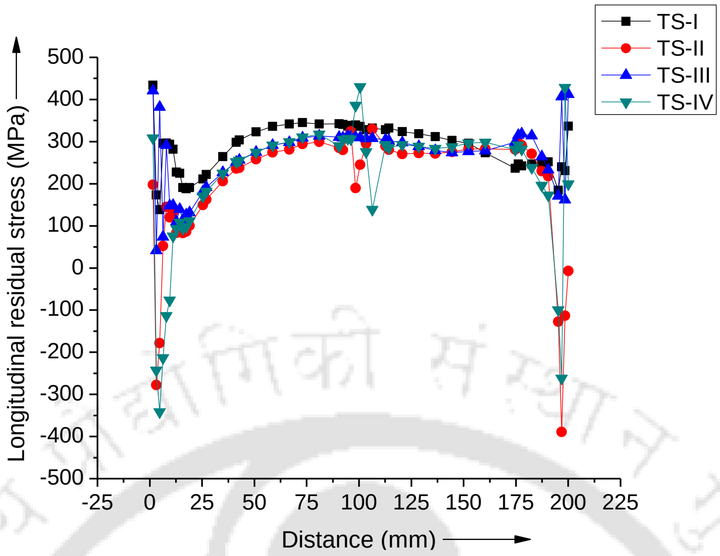

Figure 5.46 Longitudinal residual stress distribution along weld line

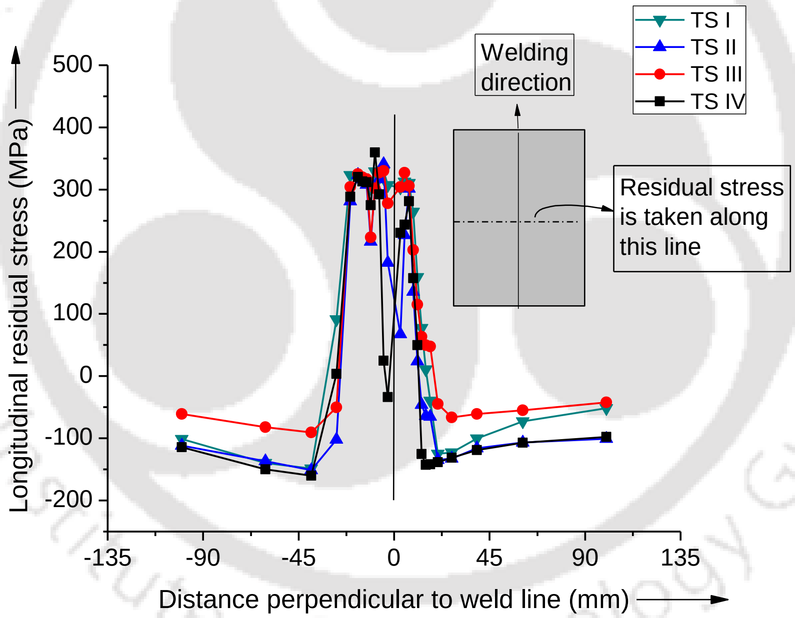

Figure 5.47 Longitudinal residual stress distribution perpendicular to weld line

Figure 5.48 represents the transverse residual stress distribution along the center line of fillet weld. In this case the same pattern as the longitudinal residual stress is observed i.e. in the region of tack position the residual stress is non-uniform but the basic difference is the maximum magnitude of the transverse residual stress is very less than the longitudinal residual stress. The Figure 5.49 represents the transverse residual stress distribution perpendicular to the weld line. It was observed that the residual stress distributions near the middle length tack positions (i.e. tack positions 3 & 4) were uneven in nature.

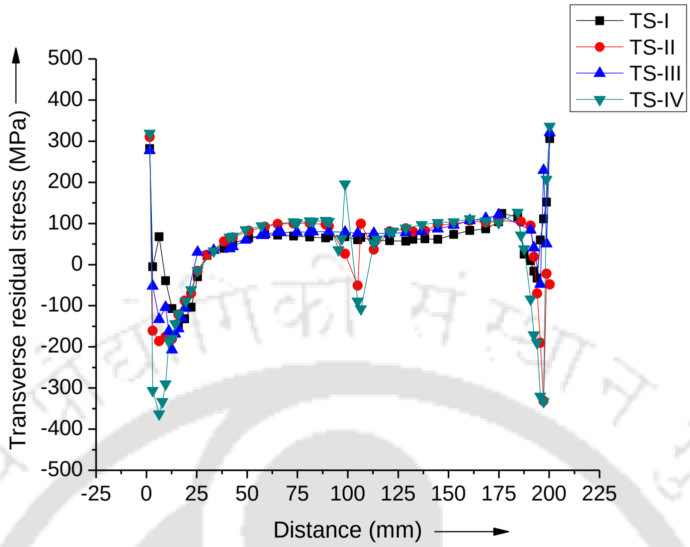

Figure 5.48 Transverse residual stress distribution along weld line

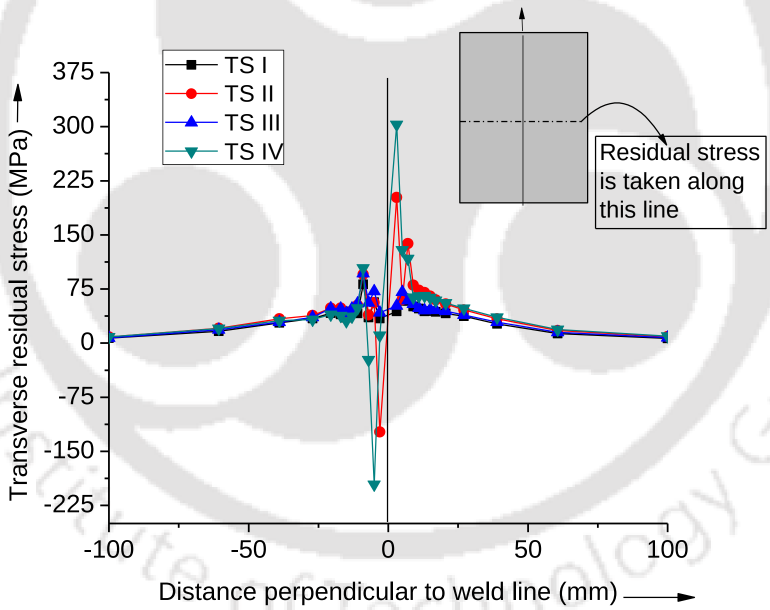

Figure 5.49 Transverse residual stress distribution perpendicular to weld line

5.5.3 Summary

A 3D FE based thermo-mechanical analysis was performed to study the effect of tacking sequences on residual stress and angular distortion of single sided fillet weld. The results reveal that the weld tacking sequences have significant effects on the distribution of residual stresses and angular distortion. The following conclusion can be made from the present study.

- The minimum and maximum magnitude of residual stresses were observed in case of taking sequences TS-II & TS-IV respectively. However, the angular distortion follows opposite trend of residual stress. The minimum value of angular distortion was observed in case of the tacking sequence TS-IV and the maximum for tacking sequence TS-II. It is thus obvious that where the value of residual stress increases there the angular deformation decreases.
- The tacking positions also have a significant effect in residual stress and angular distortion distribution. It is observed that the tacking positions opposite to fillet weld side have almost no effect on residual stress distribution whereas the tacking positions in fillet weld side have significant effect on uneven distribution and increment of residual stresses. It can be concluded from this study that the tack weld position should place opposite to the fillet weld side.

5.6 Effect of welding sequences on thermal history, residual stresses and welding distortions

Large stiffened structures are generally joined by several welding passes which generates thermal stresses and angular deformation and finally premature failure of the structure. The different welding sequences lead to non-uniform heating and cooling which creates complex welding residual stress and angular deformation in the structure. In this present work the effect of four different welding sequences on residual stress, angular deformation of submerged arc welded fillet joint was studied. Thus the developed model presents the convenient welding sequence for enhancing the quality of fabrication process.

5.6.1 Experimental details

The welding parameters used in this study are shown in Table 5.13. In this analysis fillet welding joint was considered which is shown in Figure 5.50. The dimension of mild steel base plate was 200 mm × 200 mm × 8 mm with a stiffener of a web height and thickness of 50 mm & 8 mm respectively.

Table 5.13 Welding parameters used in numerical analysis

Current (A)	Voltage (V)	Welding speed (mm/s)
490	25	5

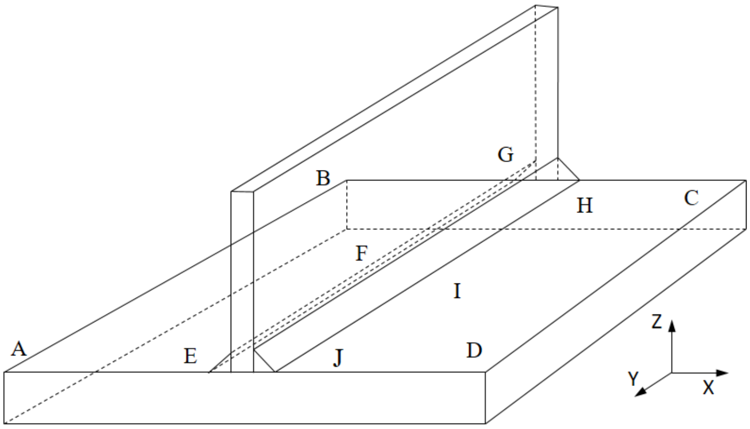

Figure 5.50 Schematic diagram of joint geometry of the fillet joint

To study the effect of welding sequences on residual stress and deformation, four different welding sequences were considered which is given in Table 5.14 as per the Figure 5.50.

Table 5.14 Welding sequences and their nomenclatures

Welding Sequences	Nomenclatures
Point E and J to G and H	WS-I
Point J to H and G to E Point	WS-II
Point F and I to G,H and E,J	WS-III
G,H and E,J to F and I	WS-IV

5.6.2 Thermal history of welding sequences

Numerical and experimental transient thermal and mechanical analysis was performed. Figures 5.51 (a)-(d) show the numerical and experimental comparison of transient thermal history for four different welding sequences i.e. WS-I, WS-II, WS-III and WS-IV respectively. Transient temperature distribution of two different location for each welding sequences were compared. The experimental thermal history of the welded plate for all four welding sequences was captured by K-type thermocouples. From Figures 5.51 (a)-(d) it can be observed that the trends of the predicted thermal history are similar and well matched with the experimental ones.

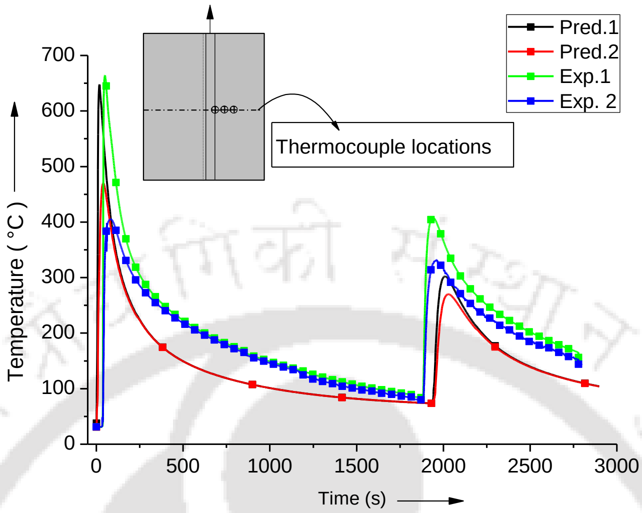

Figure 5.51 (a) Comparison of predicted and experimental time temperature history for WS-I

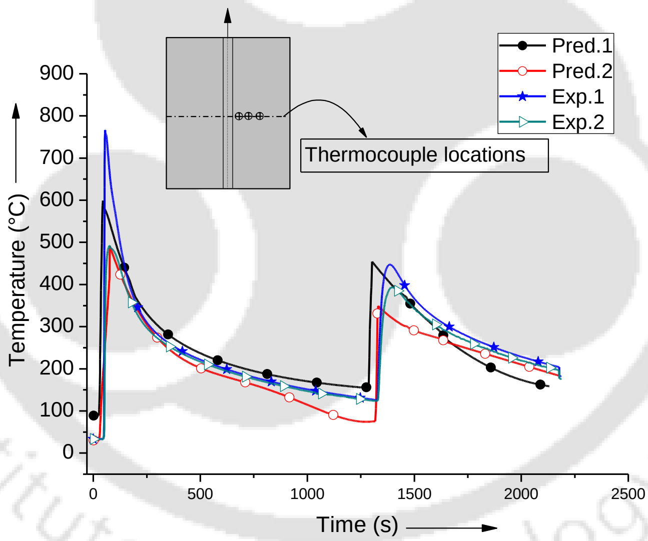

Figure 5.51 (b) Comparison of predicted & experimental time temperature history for WS-II

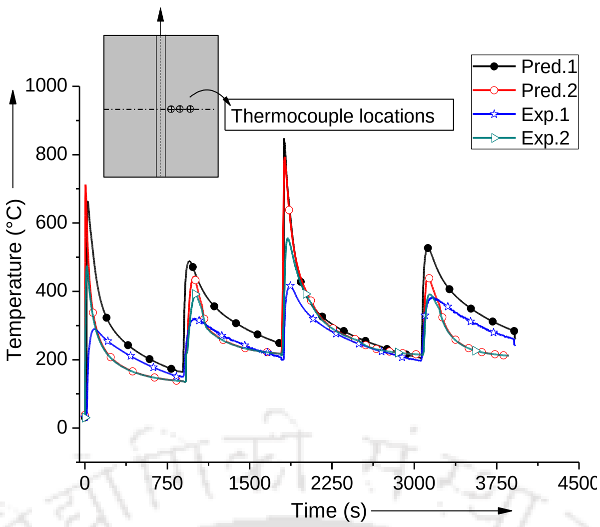

Figure 5.51 (c) Comparison of predicted & experimental time temperature history for WS-III

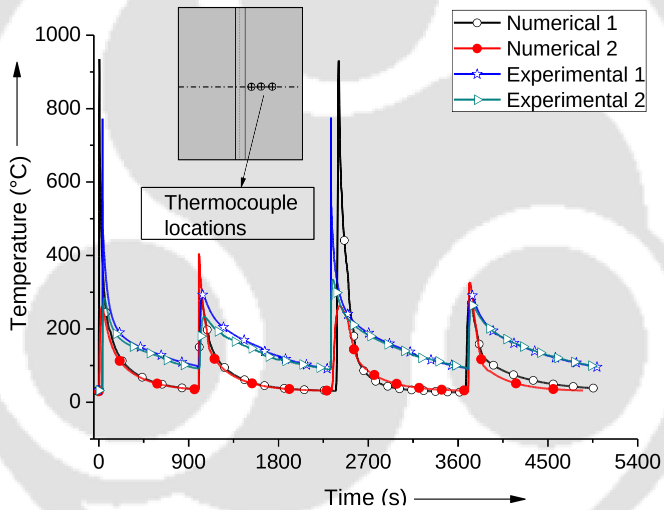

Figure 5.51 (d) Comparison of predicted & experimental time temperature history for WS-IV

Four different welding passes went through the same sample, therefore the temperature raises & cools for four times which depicts the variation of the thermal gradients involves during the welding of a multi-pass sample.

5.6.3 Comparison of the residual stresses

After validation of transient thermal history, the same model was used in structural analysis where the transient thermal history was considered as input load to predict the residual stresses and angular deformation for four different welding sequences. Figures 5.52 and 5.53 show the longitudinal and von-Misses residual stress distribution respectively in the direction perpendicular to the weld line for all cases of welding sequences.

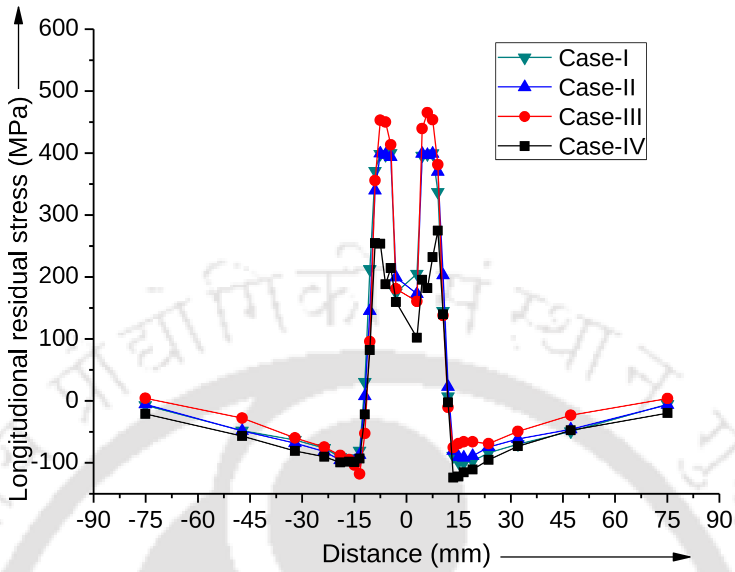

Figure 5.52 Longitudinal residual stress perpendicular to the welding direction for different welding sequences

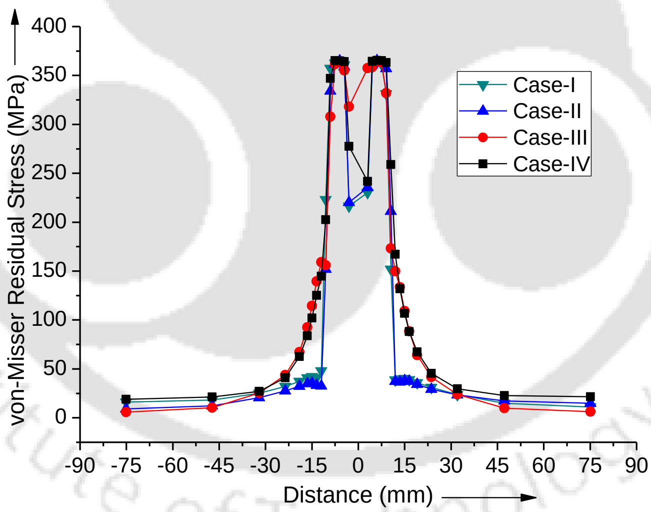

Figure 5.53 von-Misses residual stress distribution

From the above results, it is observed that the welding sequences have significant effect on magnitude and distribution pattern of residual stresses. It can be seen from the Figures 5.52 to 5.53 that all the residual stresses are tensile in nature near the weld line and compressive away from the weld line in WS-I to WS-IV. It is seen that highest magnitude of peak value of von-Misses residual stress found in WS-III and lowest magnitude of peak value of von-Misses residual stress found in WS-IV. Highest magnitude of longitudinal residual stress found in WS-

III and lowest magnitude of peak value of longitudinal residual stress found in WS-IV. It is also observed that by incorporating suitable welding sequence the von-Misses and longitudinal residual stress can be reduced by approximately 5% and 20 % respectively.

5.6.4 Comparison of the angular distortion

The welding sequences induced angular distortion are shown in Figures 5.54 & 5.55. Figure 5.54 shows the angular distortion patterns perpendicular to the weld line at the mid length of the plate for four different welding sequences. The effect of welding sequences is well prominent. Figure 5.55 represents the experimental angular deformation perpendicular to the weld line.

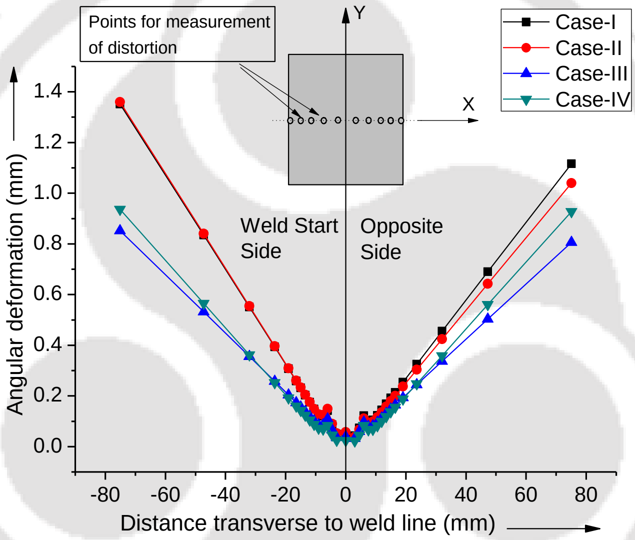

Figure 5.54 Plot of angular deformation perpendicular to the weld line

It can be seen from the above Figure 5.54 that the maximum and minimum value of angular deformations are observed in case of WS-II (1.359 mm) and WS-III (0.805 mm) respectively. Figure 5.55 represents the experimental angular deformations of four different welding sequences.

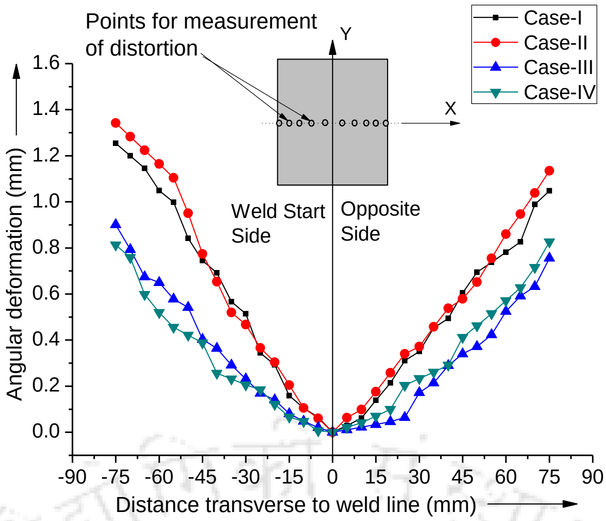

Figure 5.55 Experimental angular deformation perpendicular to the weld line

It can be seen from Figure 5.55 that WS-II (1.342 mm) and WS-III (0.7555 mm) gives the maximum and minimum value of the angular deformation respectively. The trends of the plots are also well matching with the predicted ones as shown in the Figure 5.54. Thus, it can be concluded that the angular deformation in a welded sample can be well controlled and reduced by introducing proper welding sequences.

The comparison among the numerical and experimental maximum value of angular deformation obtained from the four different welding sequences are shown in the Table 5.15. It is observed that the maximum error between the predicted and experimental value of angular deformation is 13.14%.

Table 5.15 Comparison between experimental and predicted maximum angular deformation

	Maximum angular deformation (mm)					
	Welding start side (left)			Opposite side (right)		
	Experimental	Predicted	Error (%)	Experimental	Predicted	Error (%)
WS-I /DS-I	1.254	1.35	7.11	1.047	1.11	6.01
WS-II /DS-II	1.342	1.359	1.25	1.135	1.04	8.37
WS-III /DS-III	0.901	0.851	5.87	0.755	0.8056	6.70
WS-IV/DS-IV	0.813	0.936	13.14	0.825	0.927	12.36

5.6.5 Summary

Based on the observations the following conclusions can be derived from the present investigation:

- A feasible 3-D finite element model for studying the effect of welding sequence in fillet welding was developed utilizing the nonlinear transient elasto-plastic thermo-mechanical analysis.
- Experiments were conducted to measure the thermal history and angular deformation of the different welding sequences. The predicted thermal history and angular deformation profiles are well matching with the experimental ones.
- The residual stress is tensile in nature near and within the weld region and it is compressive in nature away from the weld region. As the distance from the weld line increases the stress reaches towards zero. The magnitude of longitudinal residual stress is much higher than that of transverse residual stress.
- Four different welding sequences were considered to perform the FE analysis of double sided fillet joint. It was observed that welding sequences have prominent effects on both of distortions & residual stresses. The angular deformation can be reduced if the welding is done by proper welding sequences.

5.7 Prediction of weld induced distortion of large structure

Shrinkage and angular distortion in welding are the alarming issues in welded structure, which occur due to change in temperature gradient. This degrades the dimensional quality of a large structure during assembly which leads to rework the products and hence decreases the productivity. Predicting the weld induced residual deformation before the production saves the valuable time and resources for rework. The conventional coupled transient, nonlinear, elasto-plastic thermo-mechanical analysis involves huge computational time. Computing a weld sample of small size with single pass itself takes several hours, which will be a huge amount of time in case of large structures consisting of several welding passes thus there is a real need of an efficient alternative technique to predict the post weld distortions. In the present work an attempt was made to determine the deformation in a submerged arc welded structure using equivalent load technique which reduces the total analysis time drastically of the conventional techniques in case of a small weld structure. In this proposed method, the major time consuming part of analysis i.e. the transient nonlinear elasto-plastic structural analysis part was almost eliminated. So, this method can effectively use to predict the weld induced distortion of very large structure with a computation time almost equal to the time required for transient thermal analysis of a small weld structure only. It is not feasible to analyze such a large welded structure with conventional coupled transient, elasto-plastic, nonlinear thermo-mechanical analysis. The predicted results of distortions were validated with the experimental as well as published results and good agreements were found.

Equivalent load method is based on inherent strains which are a function of the highest temperature and degree of restrain. Nonlinear FE transient thermal analysis was performed to compute the temperature distribution in mild steel plates. Equivalent loads were calculated by using the inherent strain components. An elastic FE analysis of weldment using these equivalent loads was performed to simulate deformation. Predicted distortions show a good agreement with the experimental measurements/published results, and the total computation time was reduced, which proves the reliability of the proposed technique.

5.7.1 Calculation of restraint coefficient

The value of inherent strain depends on the restraint coefficient (β) which further depends on the stiffness of the bar and spring (Equation 5.6). In general the inherent strain is determined experimentally by taking a bar and spring of known stiffness and then heating and cooling the bar. However, in this work an analogy is considered; the weld bead is assumed as the bar as it experiences huge change in temperature during welding. The part of the welded plate adjacent to the weld region is assumed as the spring since this region experiences lesser change in temperature as compared to the weld bead and it acts as a restraint on the weld region. The restraint coefficient is calculated from k (Equation 5.10) and k^* (Equation 5.11).

$$k = AE/L \tag{5.10}$$

$$k^* = AE/L^* \tag{5.11}$$

where k and L are the stiffness and the width of the weld bead, respectively. k^* and L^* are the stiffness and width the weld plate adjacent to weld bead, respectively. The cross section area, A is same for the weld bead as well as of the adjacent plate. Also, the Young's modulus, E is same for weld bead and adjacent plate as both are of same material i.e. mild steel. Thus, the Equation 5.6 can be modified to calculate the restraint co-efficient (β) by using Equations 5.10 & 5.11.

$$\beta = L^{*}/(L + L^{*}) \qquad (5.12)$$

In Equation 5.12, L is the width of the weld bead whose value is known however the value of L^{*} is to be determined. The width of the weld plate (L^{*}) adjacent to the weld bead is considered in such a way that it acts as a spring. In order to determine L^{*} it is required to analyze the temperature distribution at various points (excluding weld bead region) on the plate during welding.

The theoretical background of inherent strain, calculation of restraint co-efficient have been presented in chapter 3 (section 3.7) and the FE thermal analysis details have been given in chapter 5 (section 5.2 & 5.3). Nonlinear FE transient thermal analysis was performed to compute the temperature distribution. Figure 5.56 shows peak temperatures at different locations on the plate from the weld line considering different cases (Table 5.16) by changing welding parameters. From Figure 5.56, it is observed that as the welding parameters like current and voltage are increased, the peak temperature is more. Increasing welding speed, peak temperature decreases and vice versa. Similarly, the peak temperature decreases for thicker plate and vice versa.

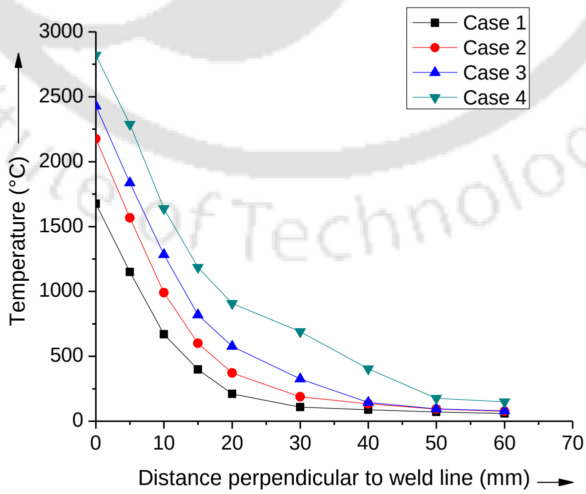

Figure 5.56 Peak temperatures at different distances from the weld line at different welding parameters (Table 5.16)

Table 5.16 Welding parameters for thermal profile

Case	Voltage (V)	Current (A)	Welding speed (mm/s)	Plate thickness (mm)
1	28	510	7	10
2	28	510	6	10
3	30	510	6	10
4	30	550	6	10

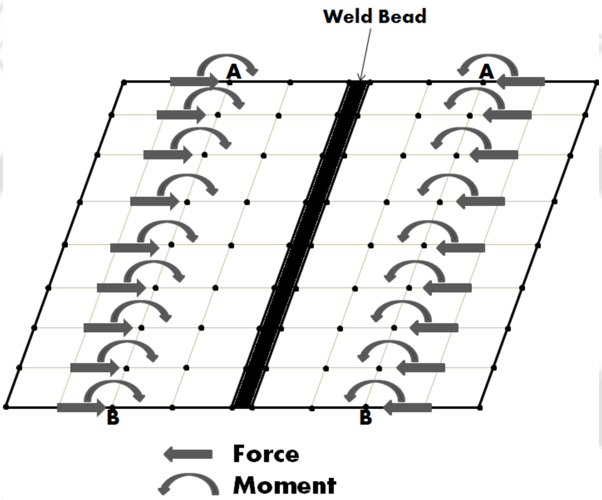

Figure 5.57 Equivalent mechanical loading

Here, the width of the plate (L^*) is considered as the spring length where peak temperature reaches beyond 100 °C. The spring length is around 50 mm in the present study which can be observed in the Figure 5.56. This length varies by changing welding parameters as shown in Figure 5.56. The restraint coefficient can be calculated by using Equation 5.12 with the known value of L and L^*. The force and moment at each node are calculated by using the Equations 3.88 and 3.89, respectively and their value summed up at all the nodes in weld bead region. Further, this total value of force and moment is distributed uniformly among the nodes along the line AB (Figure 5.57) to simulate the distortion in the welded plate considering elastic FE analysis. The distance from the center of the weld line to the line AB is the spring length which was determined from the Figure 5.56. It can be observed from the trial and error experiments that if we consider the spring length as the distance from weld center line to the line where the temperature raises approximately 100 °C provides the best result. It can be seen that the longitudinal shrinkage is very small compared to the transverse shrinkage and which have a very small effect on welding distortion. Therefore, in this present work, for the simplification of the proposed method the longitudinal shrinkage was neglected which further reduces the complexity of the model.

5.7.2 Distortion of butt and fillet welded plates

Figure 5.58 (a-d) shows the distortion patterns obtained using equivalent loading technique in butt welded plates for different welding parameters as in Table 5.16.

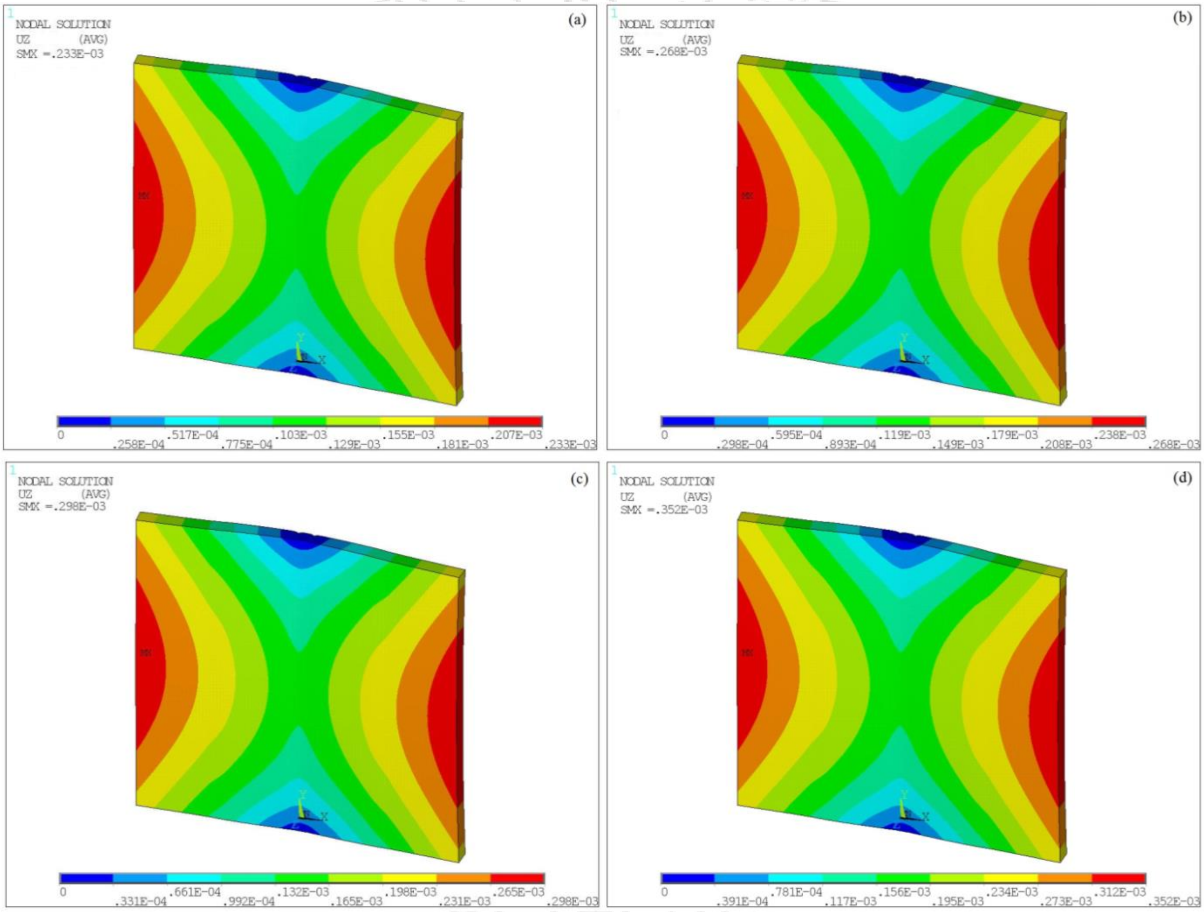

Figure 5.58 Distortion pattern for butt welded plate for four different cases [(a) Case 1; (b) Case 2; (c) Case 3; (d) Case 4].

The variation in distortion pattern for change in parameters like welding current, voltage, speed and thickness of the weld plates can be observed from these figures. Figure 5.58 shows the comparison of distortions along the line AB (parallel to Y axis and close to edge of the plate) considering different cases (Table 5.16) by changing welding parameters. From Figure 5.59, it is observed that as the welding parameters like current and voltage are increased, the distortion is more. Increasing the welding speed decreases the value of distortion and vice versa. Similarly the distortion decreases for thicker plate and vice versa.

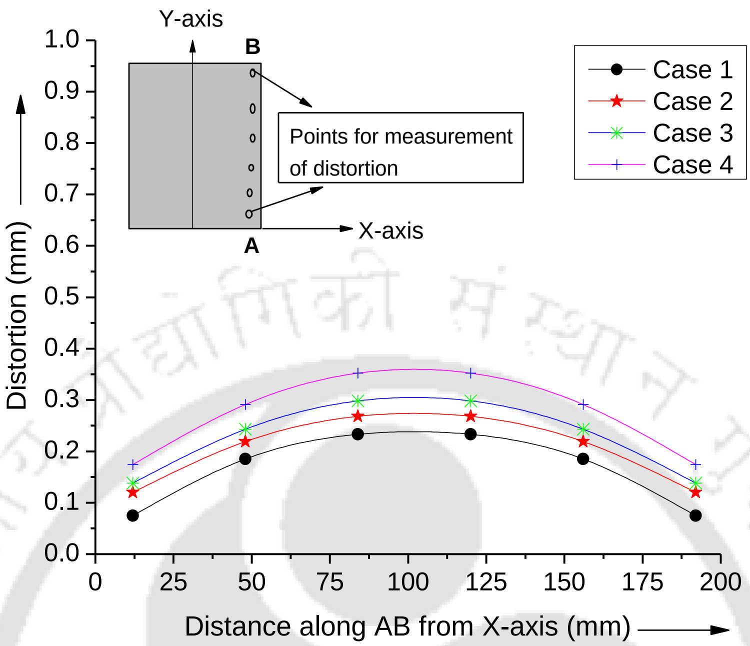

Figure 5.59 Comparison of distortions along the line AB (parallel to Y axis and close to edge of the plate) in butt welded plates considering different cases (Table 5.16)

Figure 5.60 shows the experimental and numerical distortions for a 12 mm thick square butt welded plate along the line AB (parallel to Y axis and close to edge of the plate). The welding parameters are given in Table 5.17. From Figure 5.60, it is observed that the both distortion patterns match well with a variation of 7-10% considering maximum distortion value.

Table 5.17 Welding parameters for butt welding

Plate thickness (mm)	Welding parameters		
	Current (A)	Voltage (V)	Welding speed (mm/s)
10	530	28	6

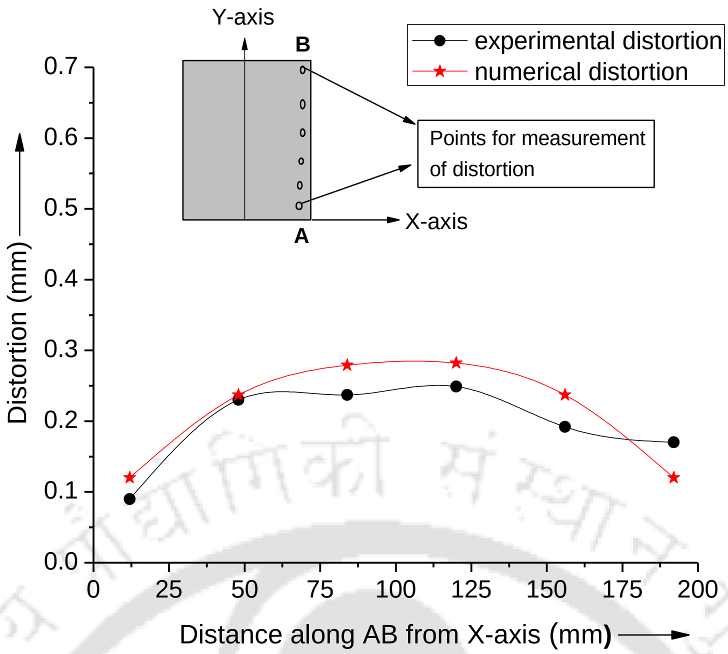

Figure 5.60 Comparison of numerical and experimental distortion along the line AB (parallel to Y axis and close to edge of the plate) for 12 mm thick plate

Figures 5.61 (a-d) show the distortion patterns obtained using equivalent loading technique in fillet welded plates for different welding parameters as in Table 5.16. The dimensions of the base plate and web are 200×200×10 mm and 200×50×10 mm respectively. The variation in distortion pattern for change in parameters like welding current, voltage, speed and thickness of the weld plates can be observed from these figures. Figure 5.62 represents the comparison of distortions along the line AB (parallel to Y axis and close to edge of the plate) in fillet welded plates considering different cases as shown in Table 5.16. From Figure 5.62, it is observed that as the welding parameters like current and voltage are increased, the distortion is more. Increasing the welding speed & plate thickness decreases the value of distortion and vice versa.

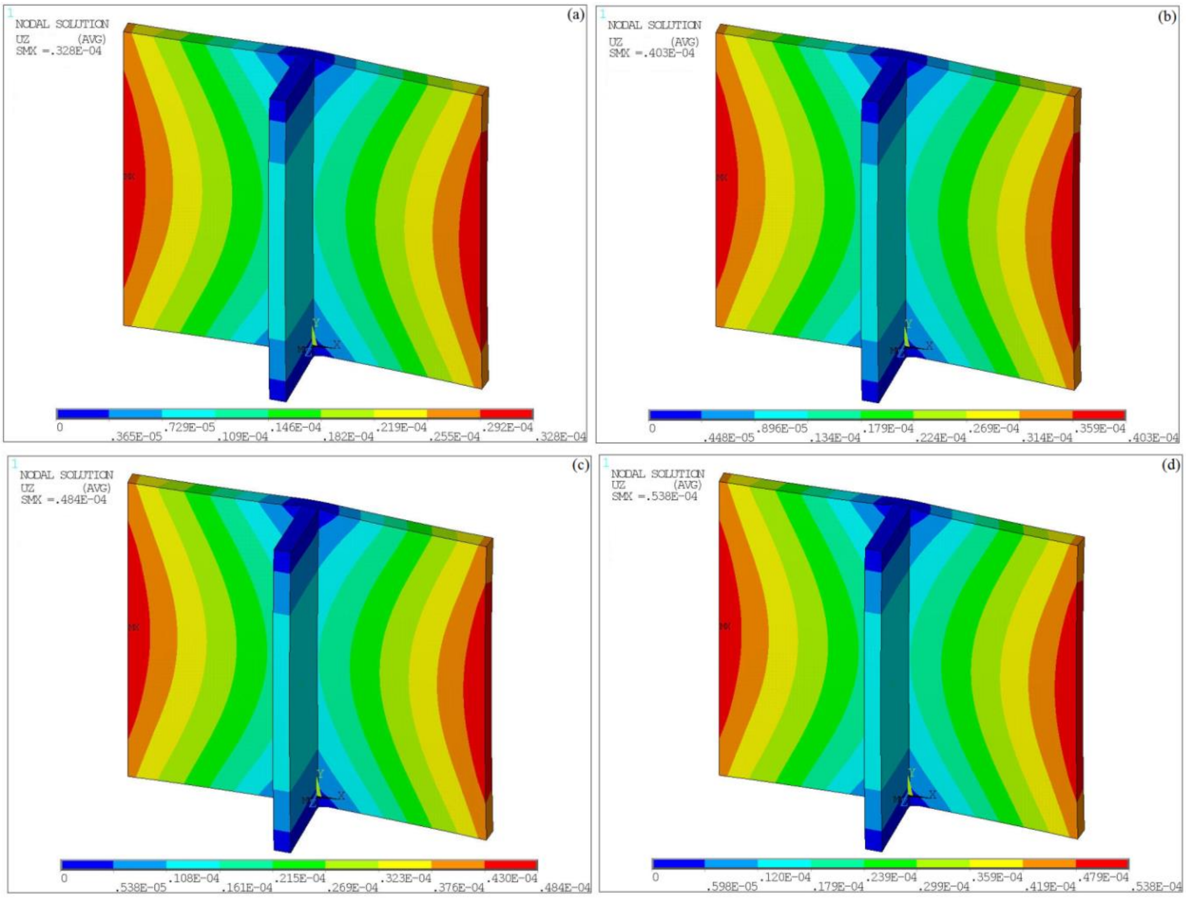

Figure 5.61 Distortion pattern for fillet welded plate for four different cases [(a) Case 1; (b) Case 2; (c) Case 3; (d) Case 4].

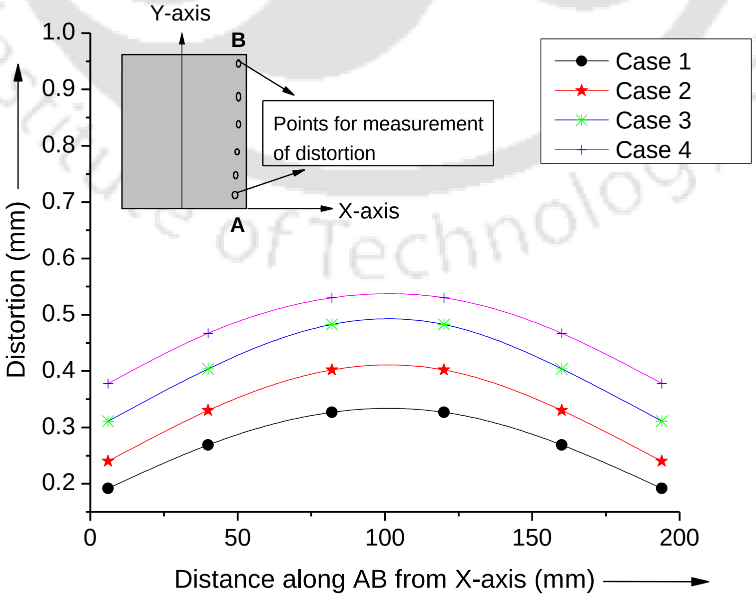

Figure 5.62 Comparison of distortions along the line AB (parallel to Y axis and close to edge of the plate) in fillet welded plates considering different cases (Table 5.16)

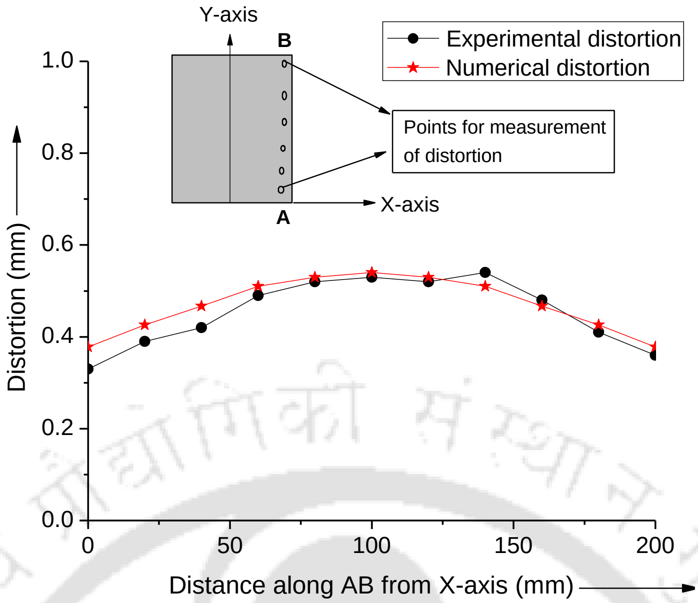

Figure 5.63 Comparison of numerical and experimental distortion along the line AB (parallel to Y axis and close to edge of the plate) for 10 mm thick fillet welded plate

Figure 5.63 shows the experimental and numerical distortions for a 10 mm thick fillet welded plate along the line AB (parallel to Y axis and close to edge of the plate). The welding parameters are given in Table 5.16. From Figure 5.63, it is observed that distortion patterns match well with a variation of 5-9%.

Predicted distortion pattern shows a good agreement with the experimental results, which proves the reliability of the proposed technique. The time consumed for this analysis is just about 30-40 seconds. Thus, this technique is efficient and very less time consuming than the FE thermo-mechanical analysis. Therefore, equivalent loading technique can be used to predict the distortion in a large welded structure.

5.7.3 Large welded structure

The problem of distortion during fabrication process leads to dimensional inaccuracies and misalignments of structural members, which may require corrective tasks or rework if tolerance limit is exceeded. This in turn, lengthens the production cycle leading to increase in the cost of production. Hence, the problem of distortion is always of great concern in fabrication industries. Thus, it is required to assess the extent of possible distortion that may form during fabrication.

Figure 5.64 shows a large welded plate (2000×1400×5 mm) with three longitudinal stiffeners (40×40×6 mm) and two transverse stiffeners (75×50×6 mm). The end nodes at left and right side lugs are constrained with zero DOF. The equivalent loading technique was used to predict the distortion in this large structure.

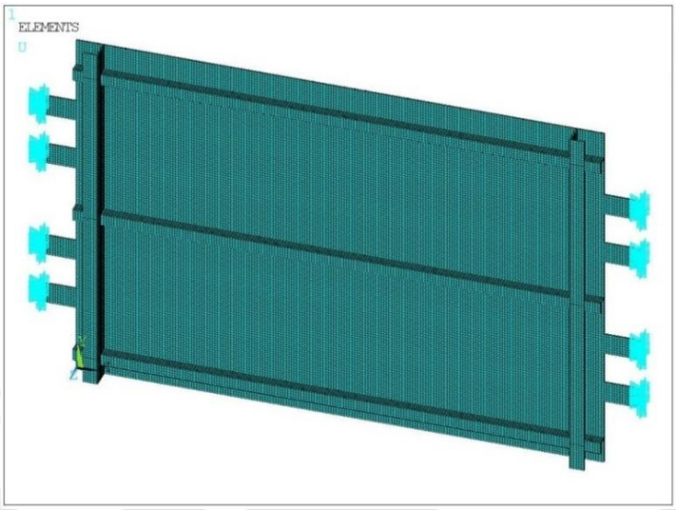

Figure 5.64 Boundary conditions

The loads were first applied on the longitudinal stiffeners and solved, after the solution PSTRES, ON was used and then the loads were applied on the transverse stiffeners and then solved to get the final solution. The result is shown in Figure 5.65. The FE simulation was carried out in a PC having configuration as Intel® Core™ i5 CPU, M460@2.53GHz, 4GB RAM with Windows 7 operating system. The time taken for this analysis or a large structure with plate dimension of 2000 × 1400 × 5 mm by using combined equivalent loading technique and FE elastic analysis is around 2 minutes.

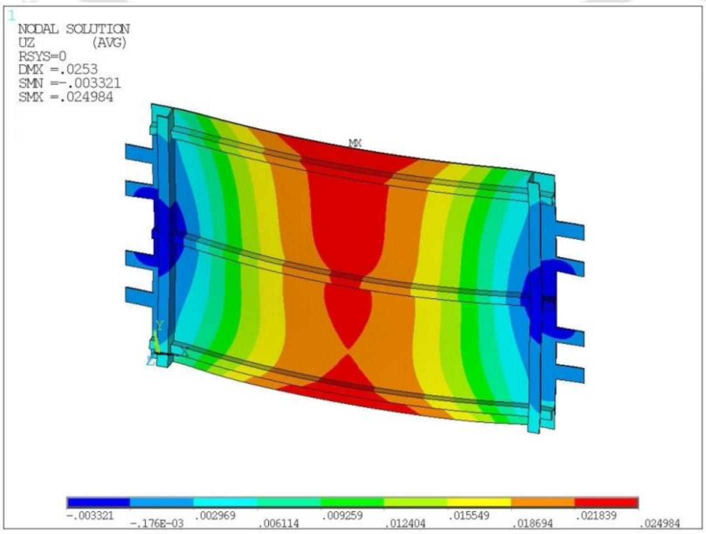

Figure 5.65 Deformation of a large welded plate

Table 5.18 Comparison of analysis time

Analysis Procedure	Time for Thermal Analysis	Time for Structural Analysis
APDL	1.5 hrs	3 hrs
APDL + Equivalent Load Technique	1.5 hrs	40s

Table 5.18 shows the comparison of analysis time between Equivalent load technique and conventional technique. One can observe from Table 5.18 that the structural analysis time is very much less while the equivalent load technique is used hence saves a lot of time as well as resources.

5.7.4 Summary

The preceding study can be summarized as follows:

- In the equivalent loading technique, the bar spring analogy was successfully implemented. The results obtained from the equivalent loading technique are compared with the experimental results and were found to be in reasonable agreement with an error of around 6-10%. Hence, the technique is proved to be efficient.
- The elastic FE analysis using equivalent loading technique involves very less computational time as compared to the 3-D FE nonlinear elasto-plastic thermo-mechanical analysis. Thus, the equivalent loading technique is very useful to predict the distortion in a large welded structure where the simulation time is tremendously greater due to numerous welding passes and sequences.
- This method can be effectively used to predict the weld induced distortion of very large structure with a computation time almost equal to the time required for transient thermal analysis of a small weld structure only.

5.8 Development of an avocado shaped new welding heat source model for the numerical simulation of fusion welding processes

Bead on plate experiments were performed as per the process parameters shows in the Table 5.19. Cross section of the welded samples was taken to measure the weld poll dimensions. Experimentally measured bead width and depth of penetration of the weld pool is shown in the Table 5.20. Figure 5.66 shows the predicted thermal history of three dimensional plate using the proposed heat source model of submerged arc welding.

Table 5.19 Welding process parameters of SAW for different data set

Data set no.	Current	Voltage	Speed(mm/s)	LOS
1	420	27	5.5	2.5
2	425	27.5	6	2.5
3	430	28	6.5	2.5
4	435	28.5	7	2.5
5	415	26	5	2.5
6	420	28	7	2.5
7	430	27	6	2.5
8	425	28.5	5.5	2.5
9	430	27.5	6	2.5

Table 5.20 Weld bead geometry from the experiments

Data set no.	Bead width (mm) b	DOP (mm) c	End crater length (mm) a
1	15.347	5.752	16.512
2	16.453	6.336	17.682
3	16.485	5.915	17.818
4	17.164	6.225	18.324
5	16.853	5.679	18.063
6	16.364	5.788	17.639
7	17.007	6.718	18.189
8	16.859	7.191	18.051
9	15.798	7.007	17.102

5.8.1 Comparison of the thermal profile

The temperature contour of the moving heat source at the beginning , middle and the end of the welding path is shown corresponding to data set no. 3 of Table 5.19. A 3D cross section of the weld plate is shown in the Figure 5.67 where the temperature distribution of SAW can be seen using the proposed heat source configuration.

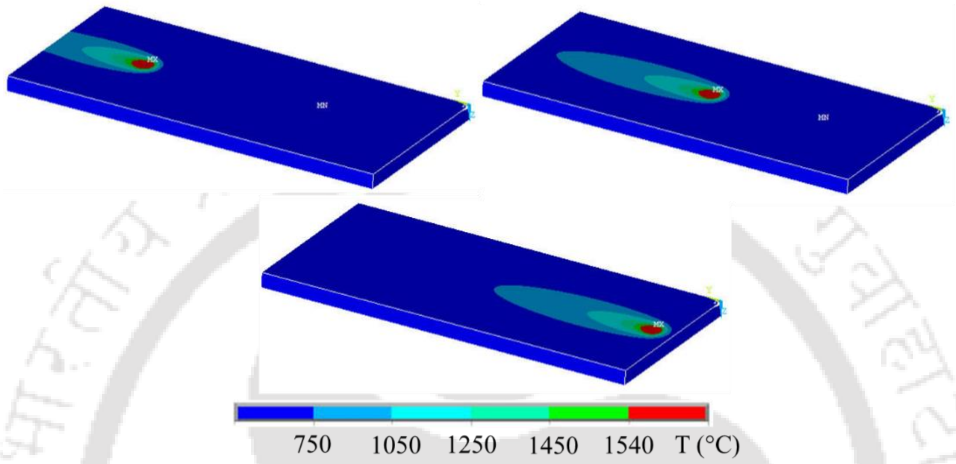

Figure 5.66 Thermal history of the weld heat source at three different locations on 3D plate

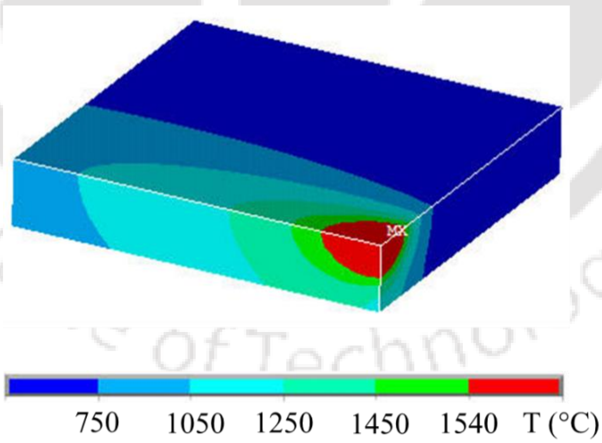

Figure 5.67 3D cross section of the volumetric heat source

K-type thermocouples were used at eight different locations to get the time temperature history of the bead on plate welding, which is plotted in the Figure 5.68. A comparison between the predicted and the experimental thermal history is plotted in the Figure 5.69 where a good agreement can be observed.

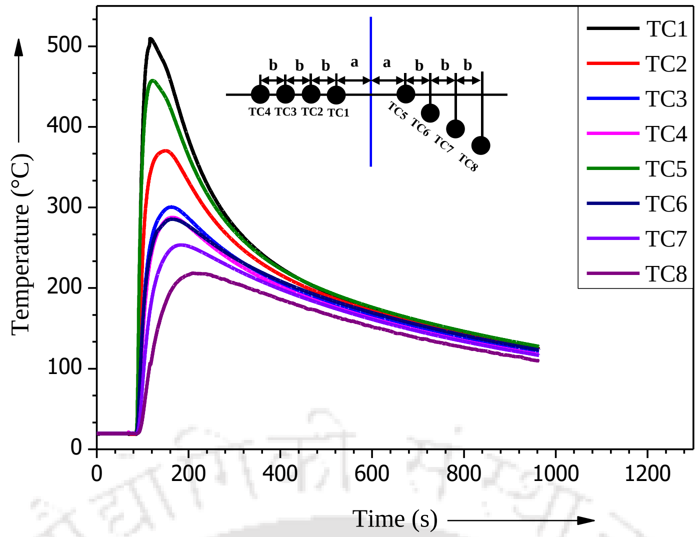

Figure 5.68 Experimental thermal profile (Data set no.3)

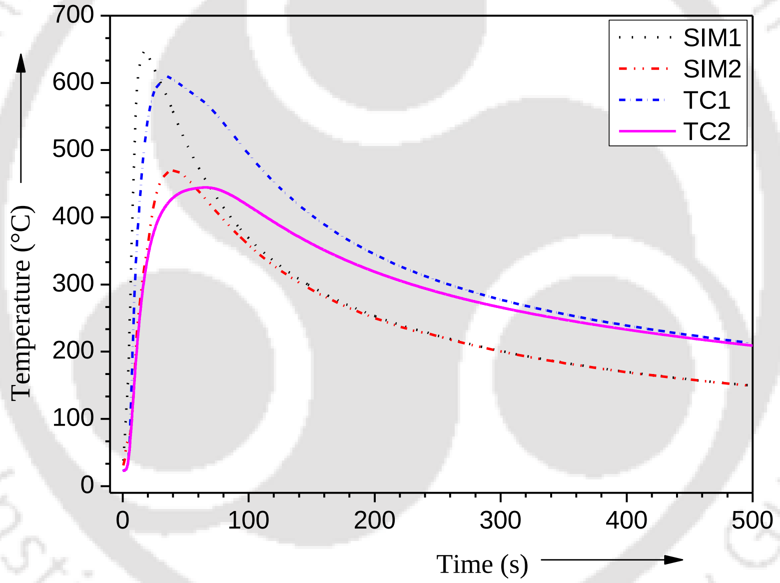

Figure 5.69 Comparison between the predicted and experimental thermal profile (Data set no. 3)

5.8.2 Comparison of the bead geometry

Double ellipsoidal model is a popular model used as the volumetric heat source for fusion welding processes, the simulation results of the present model is compared with the double ellipsoidal model.

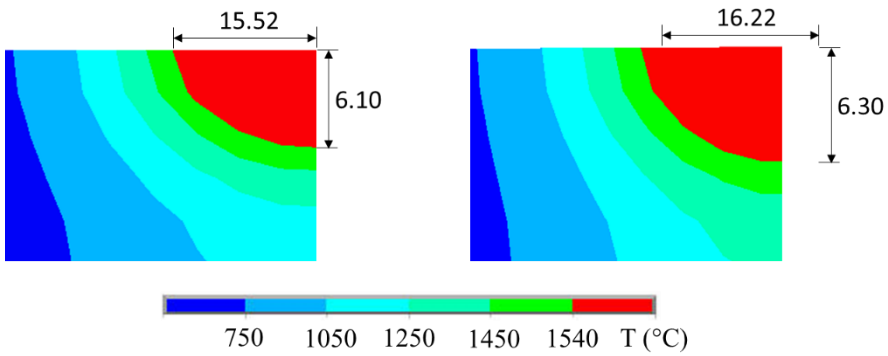

Figure 5.70 Comparison of the cross section of three different heat source (a) double ellipsoidal model, (b) the present model

Figure 5.70 shows the comparison of the computed weld bead shapes of the double ellipsoidal model and the proposed configuration, different weld zones can be seen for both the models. Figure 5.71 shows the comparison of the experimentally measured weld pool shapes (left side) with the predicted one (right side) corresponding to data set 3, 4 and 5 of Table 5.19. A fair agreement between the computed and experimental weld bead cross sections demonstrates the prediction capability of the avocado configuration heat source model.

A comparative study of the predicted weld bead shapes using the proposed avocado configuration model & double ellipsoidal model is shown in the Figure 5.72. The comparison of weld pool dimensions between the predicted and the experimentally measured one as per the weld parameters in Table 5.19 is shown in the Figure 5.73. The numerical value of the percentage error between the predicted and experimentally measured value is given inside the figures. A fair agreement for a wide range of process parameter can be found.

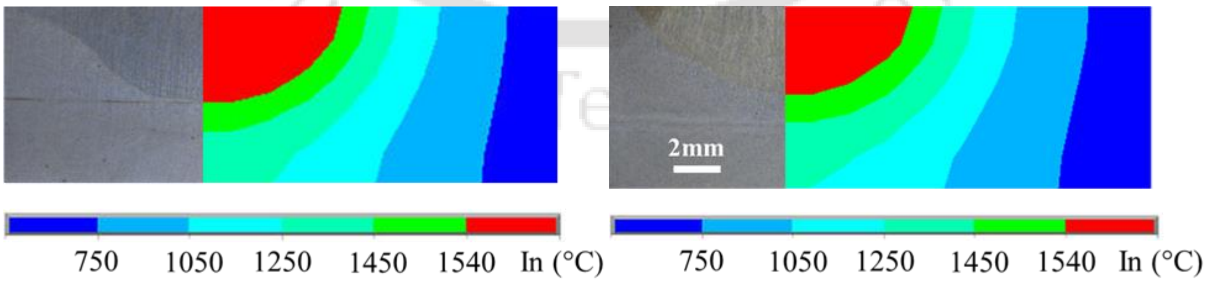

(a) (b)

Figure 5.71 Comparison of experimental weld macrograph (left side) with predicted thermal profile using the proposed heat source model corresponding to (a) data set 3, (b) data set 4, and (c) data set 5 of Table 5.19.

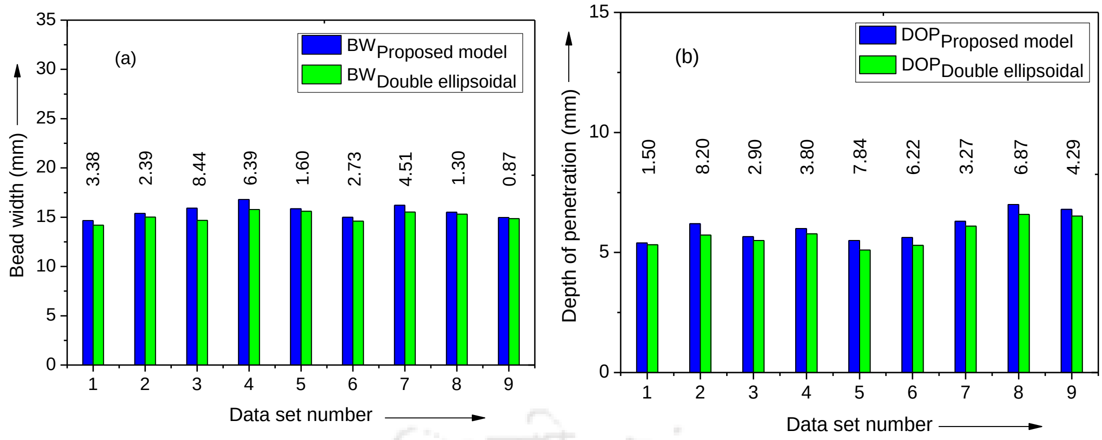

Figure 5.72 Comparison of weld predicted weld bead shapes using the proposed heat source model and the double ellipsoid heat source model of data set #3 of Table 5.19 (a) Weld bead width (b) depth of penetration

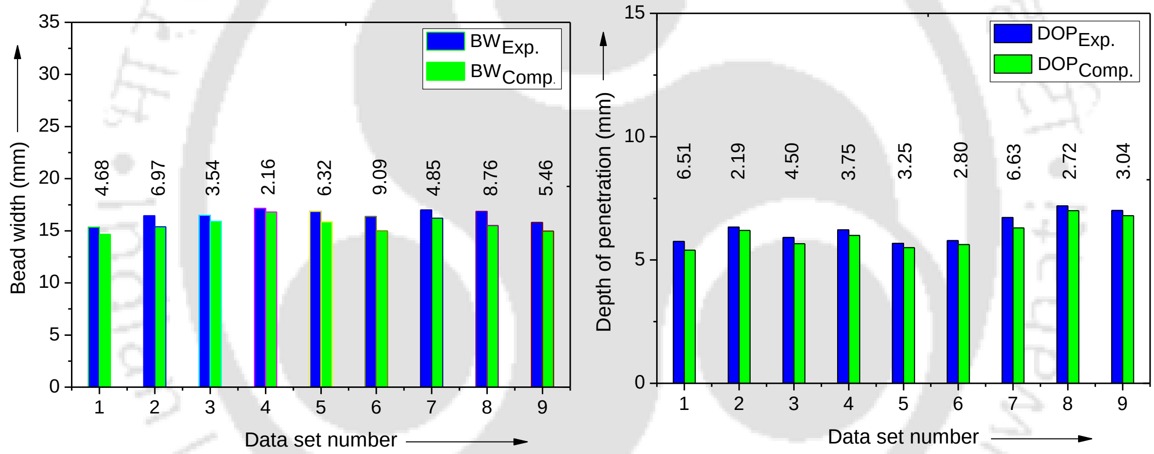

Figure 5.73 Comparison among computed weld pool dimensions using the proposed model and the experimental measurements corresponding to welding parameters of Table 5.19: (a) weld bead width and (b) depth of penetration.

5.8.3 Summary

From the above investigation of development of an avocado shaped new heat source model for the numerical simulation of fusion welding processes, it can be summarized as below:

- A new volumetric heat source is developed to apply in the 3D finite element simulation of the submerged arc welding process. The developed model successfully predicted the transient thermal history of bead on plate welding with a large range of process parameters with error within 12%.

- The generalised form of the avocado-configuration heat source is consists of limited number of model parameters which can provide a true non-uniform shape and it can represent the moving heat source of fusion welding.
- Weld bead shape and dimensions were also predicted using the FE simulation applying the proposed heat source. The predicted weld bead shapes are compared with popular double ellipsoidal heat source model. It is observed that the proposed heat source model is flexible enough for the application in other fusion welding processes provided the proper applicability of the process parameters.

B. Results of experimental investigation

Results of the experimental investigation are presented in this section. The subsequent sub-sections deal with the effect of input welding parameters, joint geometry and surface active elements on weld bead geometry, mechanical and microstructural properties of welded samples as well as optimization of the process parameters.

5.9 Effect of process parameters on microstructure and mechanical properties

Total sixteen numbers of experiments were conducted with different process parameters which were designed based on Taguchi design of experiment (DOE) method. Four different important process parameters of submerged arc welding (SAW) i.e. the welding current, voltage, speed and length of stick out were varied over four different levels. Mechanical properties were tested using Vickers micro-hardness tester and Instron 8801 tensile testing machine. Macrostructure and microstructure were observed using stereo microscope and optical microscope (i.e. Carl Zeiss upright optical microscope) respectively.

The aim of this study is to find out the optimal parameters conditions to achieve the desired welding quality in a single pass single sided welding without any edge preparation of mild steel plates. The design of experiments was done by Taguchi orthogonal array to minimize the huge number experiments thus minimizes time and resources. Four input parameters varied in four different levels as shown in Table 5.21. Square butt joints were prepared using two plates of dimension 200 × 200 × 8 mm. The pates were tack welded using shielded metal arc welding (SMAW) before final welding. The experimental results are shown in Table 5.28.

Table 5.21 Welding parameters and their levels

Variable parameters					Fixed parameters	
Parameters	Values in each level				Parameters	Values
	L1	L2	L3	L4		
Voltage (V)	27	27.5	28	28.5	Root gap (mm)	2.5
Current (A)	470	475	480	485	Wire feed	Automatic
Welding speed (mm/s)	5.5	6	6.5	7	Welding polarity (DCEP)	-
Stick-out (mm)	22	24	26	28	Plate thickness (mm)	8

5.9.1 Micro-hardness

Micro-hardness test were carried out in the Vickers micro-hardness tester. The maximum magnitude of hardness was seen in the fusion zone. The hardness of the heat affected zone is lower than the fusion zone but more than the base metal due to grain refinement. The Figure 5.74 explains the variations of hardness values with the distance perpendicular to the weld line of a welded sample.

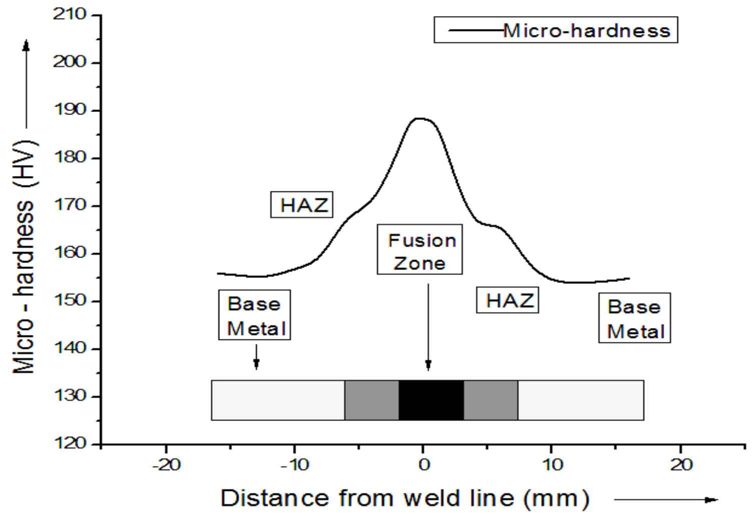

Figure 5.74 Micro-hardness variation with distance

5.9.2 Effect of rate of heat input on tensile properties

Tensile testing was carried out using Instron 8801 universal testing machine with 100 kN load cell at a strain rate of 1.0 mm/min. It was observed that none of the sample failed in the welding zone. The tensile failure occurred between heat affected zone and base metal. Yield strength and ultimate tensile strength of base metal are 388 MPa and 519 MPa respectively. The complete input parameters and results from the tensile and hardness test is given the Table 5.28. The weld quality is highly influenced by the rate of heat input. Rate of heat input can be defined as a measure of the energy transferred per unit length of weld [189]. The thermal efficiency of the SAW process was considered as 95% [156].

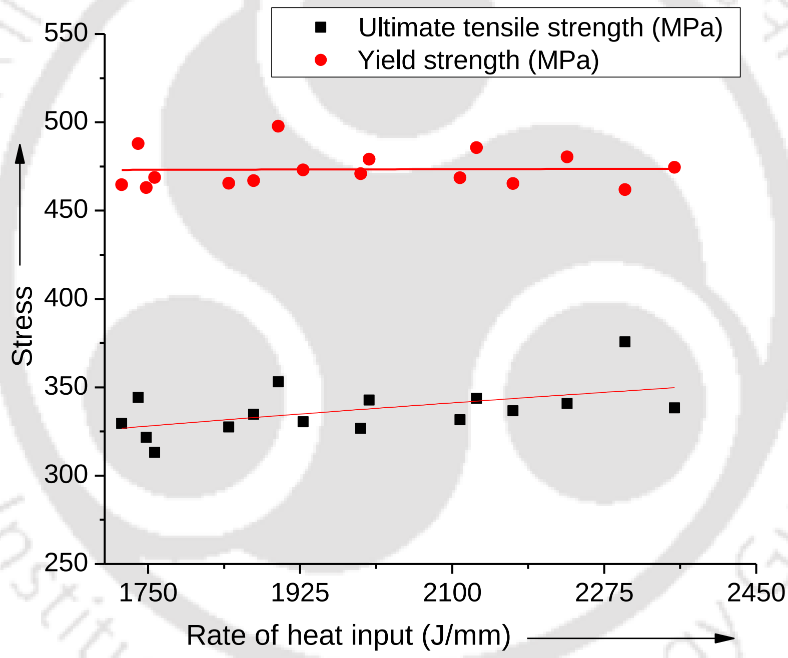

Figure 5.75 Effect of heat input on stresses

To study the combined effect of welding parameters, rate of heat input was considered. It was observed that with increase in rate of heat input the tensile strength of the weld metal increases as the amount of energy to weld more metal increases. It can also be observed that for getting full penetration in the single sided single pass butt welding of 8 mm mild steel plates without edge preparation the rate of heat input can be kept in the range of 1.71-2.35 kJ/mm. Figure 5.75 shows the effect of heat input on yield stress (YS) and ultimate tensile strength (UTS). It can be seen from the figure that the UTS and YS increases with that rate of heat input.

5.9.3 Effect of process parameters on microstructure

The welded samples were polished using emery papers of varying grades from 120 to 2000. Final polishing was done using velvet cloth and alumina paste. Etching was done in 2% Nital solution (i.e. 2% nitric acid and 98% ethyl alcohol). Microstructure was studied in the Carl Zeiss upright optical microscope at various magnifications. METZER-M stereo-microscope was used to capture the macro-graph of welded specimen which showed the different weld zones. Figure 5.76 shows the three different microstructure zones of the welded sample obtained by METZER-M stereo-microscope. Figures 5.77 (a) to (d) show the microstructure of different weld zones of a welded sample.

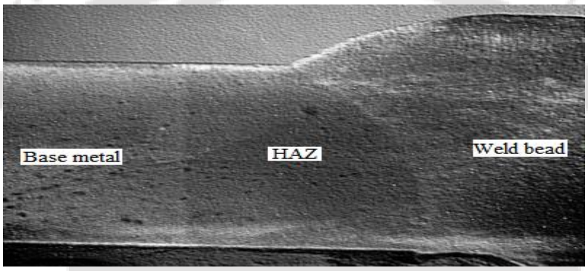

Figure 5.76 Different weld zones (macrograph)

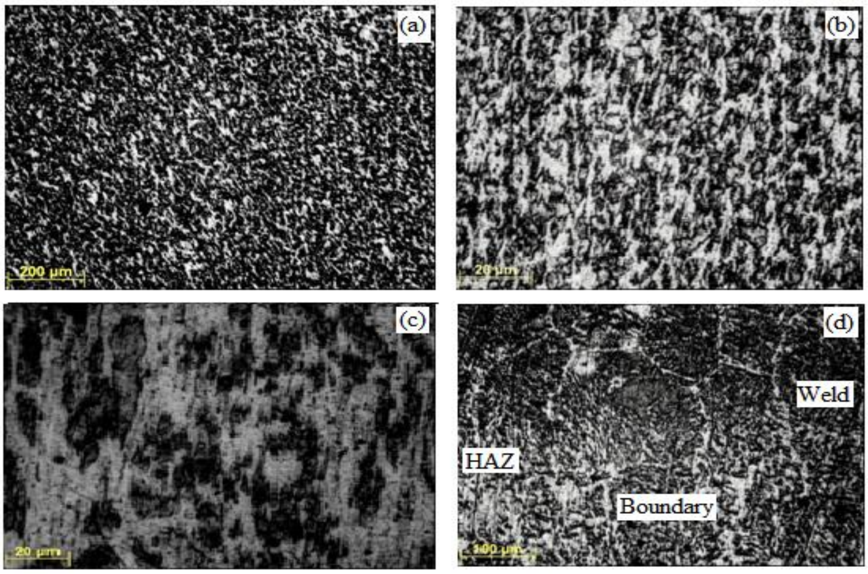

Figure 5.77 Optical micrograph of (a) Base metal (b) HAZ (c) weld zone (d) HAZ-Weld zone

The microstructure of the base metal (Figure 5.77 (a)) contains ferrite (white) and pearlite (black). Fine grain structure was found in the HAZ (Figure 5.77 b) due to grain refinement and grain coarsening was observed in the weld zone. Combination of both fine and coarse grain can be seen in Figure 5.77 d which represents the transition between coarse and find grain structure i.e. this is the intermediate zone between fusion zone and HAZ. As the peak temperature at HAZ region reached above A3 temperature therefore upon cooling austenite decomposes into finer pearlite (black) and ferrite (white). The boundary between HAZ and weld zone is also clearly visible in Figure 5.77 (d). Figure 5.78 shows one of the fractured surface of the tensile samples which was captured by using a FESEM.

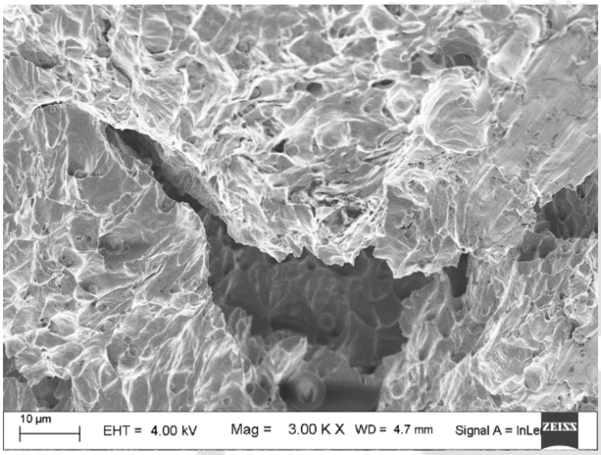

(a)

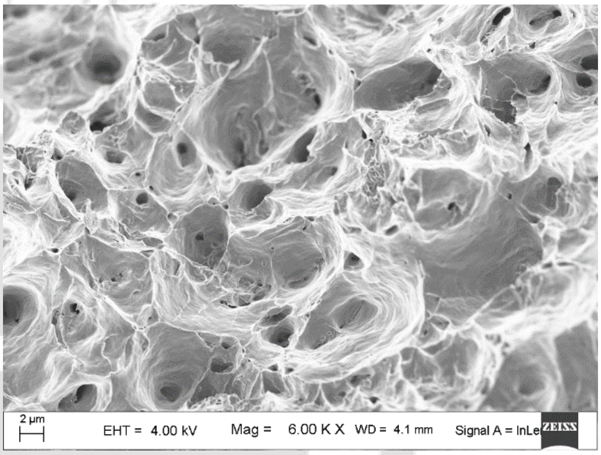

(b)

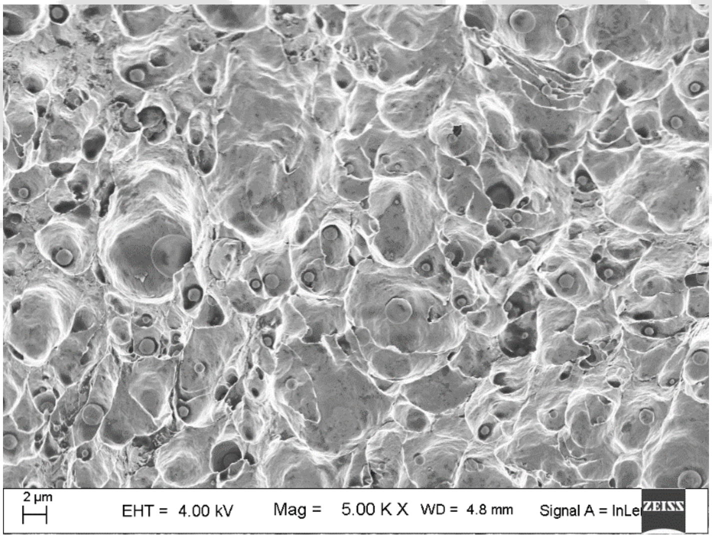

(c)

Figure 5.78 FESEM image of fractured surface of tensile samples

The Figure 5.78 (a) shows FESEM image at the fracture location of the tensile samples. The ball socket shape/dimple shape of the fractured surfaces (Figure 5.78 (b) & (c)) indicates ductile failure. During tensile testing of the welded samples, failure occurred in between base metal and heat affected zone, which was away from the weld line, which indicates a superior weld quality.

5.9.4 Summary

The summary of the preceding study can be stated as below:

- Maximum hardness was observed in the weld zone and which decreases gradually away from the weld line towards base material. The hardness in the weld zone was more due to the greater carbon content in the filler wire.
- None of the tensile samples failed in the weld zone, therefore the strength of the welding was more than the base metal, which confirms a sound welding joint. Based on UTS the maximum joint efficiency was 96%.

5.10 Effect of welding parameters on weld bead geometry & mechanical properties

The weld characteristics of SAW process are greatly influenced by its control parameters. Basic SAW process parameters are welding current, voltage, welding speed, length of stick out, wire diameter, electrode inclination angle, width of welding flux layer, welding feed rate etc. [130]. To obtain a desirable weld quality, selection of the welding process parameters is the most important part. Though the weld quality can be affected by many direct and indirect parameters, the major key process parameters affecting the weld quality as well as bead geometry are welding current, voltage, welding speed and length of stick out. Presence of multiple process parameters and multiple quality characteristics of the weld makes SAW a multi-objective, multi-factor joining technique. In the present study, four levels of four process parameters, i.e., current, voltage, welding speed and length of stick out were considered to study the effect of these parameters on weld bead geometry and mechanical property.

Bead-on-plate experiments were performed on 10 mm thick plates. Figure 5.80 shows polished bead on plate cross section. Table 5.22 presents the input welding process parameters and corresponding weld bead geometries. The effect of welding voltage, current, speed and length of stick out on weld bead width and weld bead reinforcement are discussed in detail below.

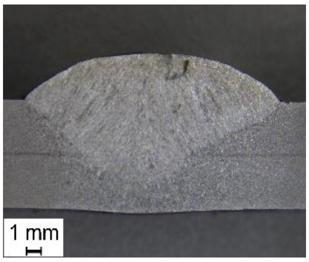

Figure 5.79 Bead on plate weld bead cross section

Table 5.22 Input parameters and corresponding output

Exp. no.	Welding current (A)	Welding voltage (V)	Welding speed (mm/s)	Length of stick out (mm)	Bead width (mm)	Top bead reinforcement (mm)
1	330	28	5.5	23	15.31	2.37
2	340	28	5.5	23	15.8	2.78
3	350	28	5.5	23	16.09	2.94
4	360	28	5.5	23	17.16	3.13
5	330	28	5.5	23	15.31	2.37
6	330	30	5.5	23	16.03	2.45
7	330	32	5.5	23	17.45	3.26
8	330	34	5.5	23	18.25	3.74
9	330	28	5.5	23	15.31	2.37
10	330	28	6	23	15.1	2.22
11	330	28	6.5	23	14.15	1.88
12	330	28	7	23	13.69	1.79
13	330	28	5.5	23	15.31	2.37
14	360	28	5.5	25	15.43	2.46
15	360	28	5.5	27	15.88	3.07
16	360	28	5.5	29	16.28	3.10

5.10.1 Effect of input parameters on bead width

It was observed from Table 5.22 that the welding input parameters have considerable effect on weld bead geometry. It can be observed that current effects on overall weld bead geometry i.e. with increase of current the weld bead width, bead height and penetration increases. However, with the increase of voltage the weld bead becomes wider and flatter but weld penetration remains almost constant. With the increase in welding speed, the overall size of weld geometry decreases but with the increase in length of stick-out, overall size of weld geometry increases.

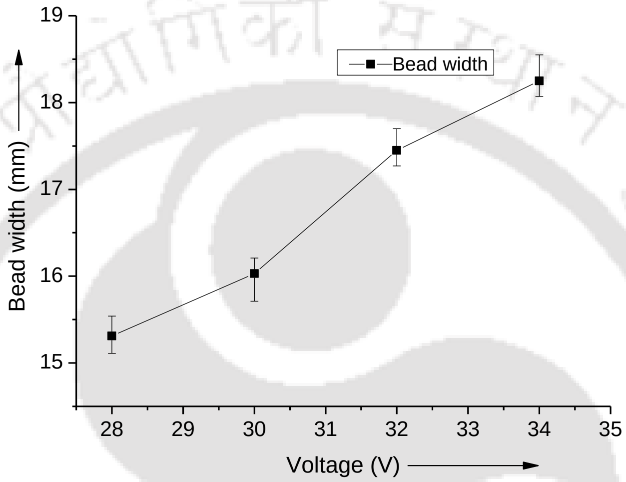

Figure 5.80 Effect of voltage on bead width

Figures 5.80 & 5.81 show the effect of welding voltage, current, speed and length of stick out on weld bead width. From the Table 5.22 & Figure 5.80, it can be understood that with increase in voltage, bead width generally increases. Welding voltage increases arc length i.e. the total area under the welding arc increases thus the bead width increases.

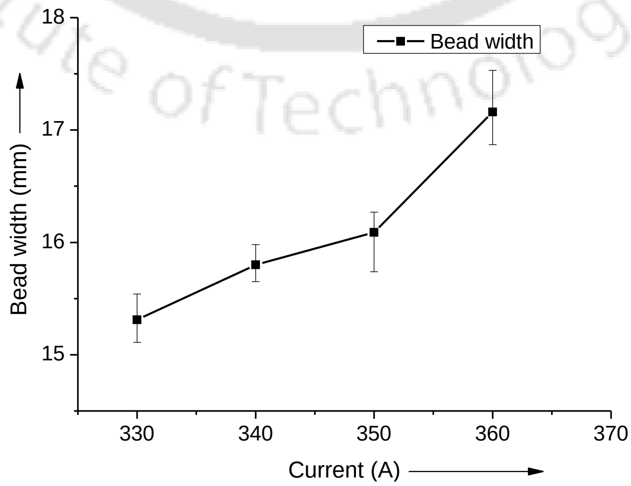

Figure 5.81 Effect of current on bead width

It is observed from Figure 5.81 that current affects the weld bead width significantly. As current level increases bead width increases. Figure 5.82 shows the effect of welding speed on weld bead width.

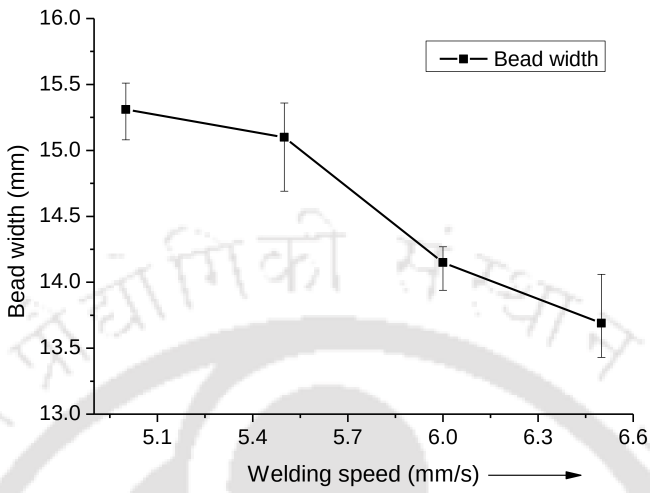

Figure 5.82 Effect of welding speed on bead width

It can be seen from Figure 5.82 that increase of welding speed has a tendency to decrease weld bead width. As heat input per unit length decreases with increase of welding speed, so bead width become narrower. Therefore, it is observed from Figures 5.80 to 5.82 that with increase welding speed the bead width decreases but it almost linearly increases with welding voltage and current. Figure 5.83 shows the effect of electrode stick out on weld bead width.

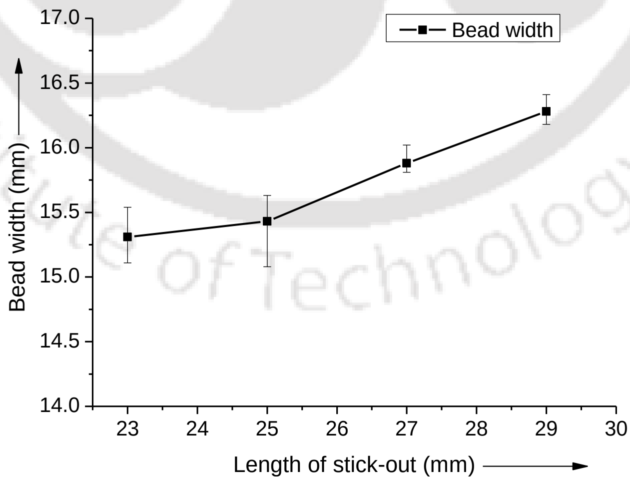

Figure 5.83 Effect of length of stick-out on bead width

It can be seen from the Figure 5.83 that, with the increase in electrode stick out, bead width also increases. For the constant voltage, power source, with increase in stick out length electrode-melting rate increases, due to the resistive heating of the electrode, which in turn results in an increase in weld bead width.

5.10.2 Effect of input parameters on reinforcement

Figures 5.84 to 5.87 show the effect of welding process parameters (welding voltage, current & speed) on weld bead reinforcement. Measured values of weld bead reinforcements of the bead on plate experiments are shown in Table 5.22. Results indicate that the process variables influence weld bead geometry to a significant extent. Welding reinforcement is significantly influenced by welding current and arc voltage.

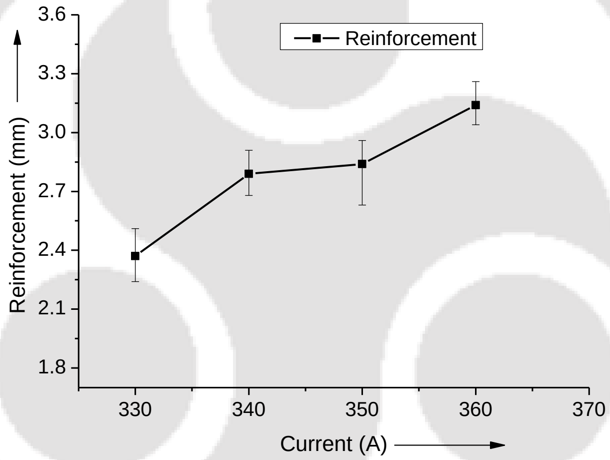

Figure 5.84 Effect of current on weld reinforcement

Figure 5.84 shows the effect of welding current on weld reinforcement. It can be observed from the Figure 5.84 that weld reinforcement increases with the increase of welding current due to the extra melt down of the electrode. Figure 5.86 shows the effect of welding voltage on weld reinforcement.

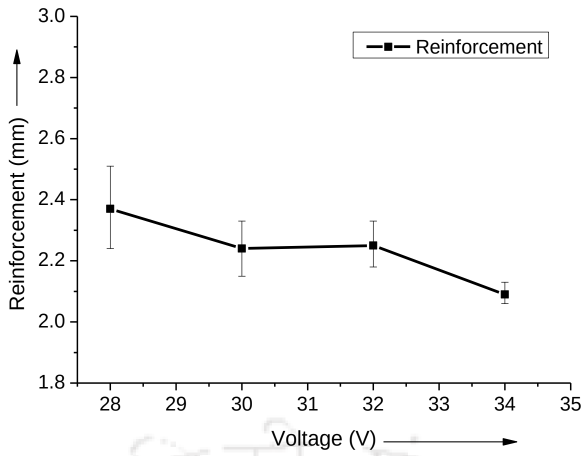

Figure 5.85 Effect of voltage on weld reinforcement

From Figure 5.85, it can be seen that with the increase in voltage reinforcement decreases. With the increase in voltage, flatten upper surface can be seen which reduces the weld reinforcement.

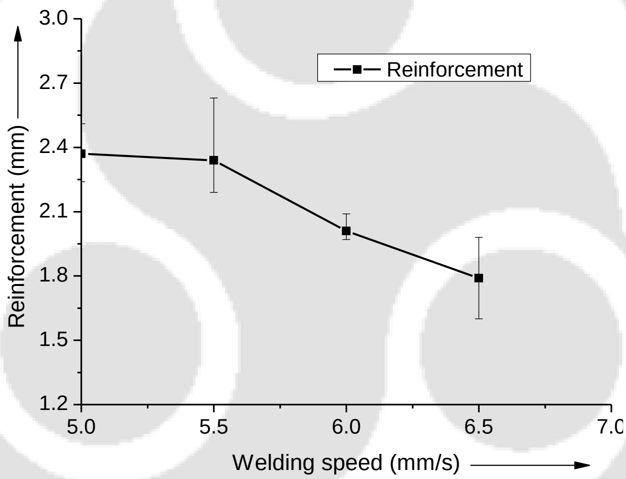

Figure 5.86 Effect of welding speed on weld reinforcement

From Figure 5.86, it is seen that trend of reinforcement with welding speed is decreasing in nature because with higher value of speed, metal deposition rate decreases as well as less amount of heat available per unit time at a particular location, that's why weld bead size decreases.

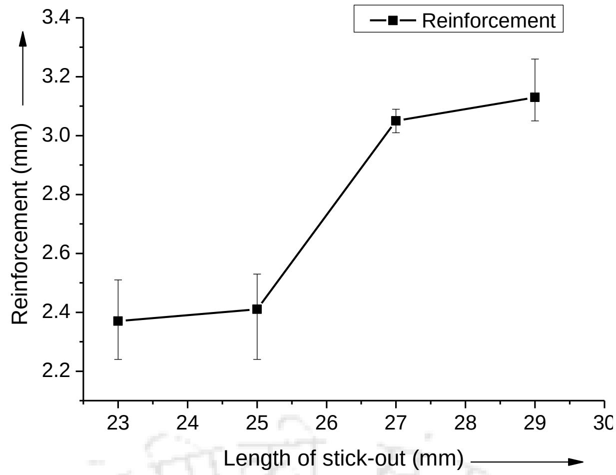

Figure 5.87 Effect of electrode stick-out on weld reinforcement

Figure 5.87 shows the effect of electrode stick out on weld reinforcement. It can be observed from the Figure 5.87 that with the increase in electrode stick out weld reinforcement also increases due to the extra melting of the electrode.

5.10.3 Effect of input parameters on hardness

Hardness test was carried out at different weld zones of all samples as shown in Table 5.23. Hardness ranges are observed from 156-160 HV at base metal, 161-178 HV at HAZ and 162-190 HV at weld region. Results of hardness test are shown graphically in Figures 5.88- 5.91**.** Hardness values in both HAZ and weld metal are found to be higher than base metal, in all the samples due to the grain refinement above recrystallization temperature.

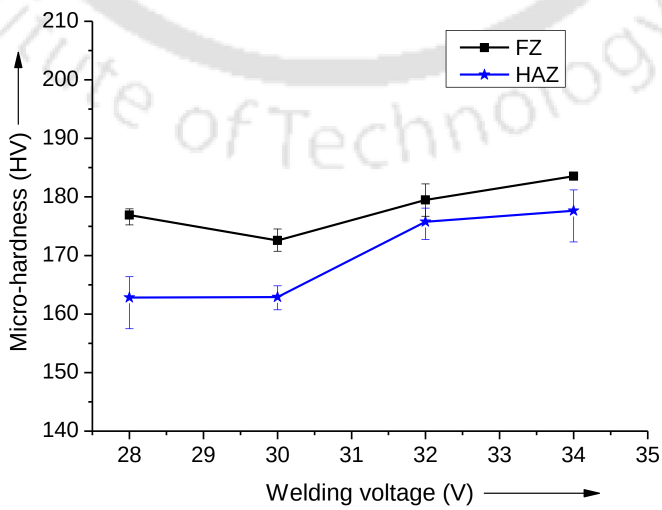

Figure 5.88 Effect of voltage on hardness of weld zone

Table 5.23 Welding input parameters and measured average hardness values

Weld Runs	Current (A)	Voltage (V)	Welding speed (mm/s)	Electrode stick out (mm)	Hardness (HV) Weld Zone	HAZ
1.	330	28	5.5	23	176.9	162.81
2.	340	28	5.5	23	183.55	168.93
3.	350	28	5.5	23	186.89	172.08
4.	360	28	5.5	23	187.18	178.53
5.	330	28	5.5	23	176.9	162.81
6.	330	30	5.5	23	172.56	162.9
7.	330	32	5.5	23	179.48	175.74
8.	330	34	5.5	23	183.55	177.64
9.	330	28	5.5	23	176.9	162.81
10.	330	28	6	23	183.72	165.05
11.	330	28	6.5	23	190.34	171.52
12.	330	28	7	23	182.12	168.17
13.	330	28	5.5	23	176.9	162.81
14.	360	28	5.5	25	172.09	165.04
15.	360	28	5.5	27	170.33	161.01
16.	360	28	5.5	29	179.89	165.89

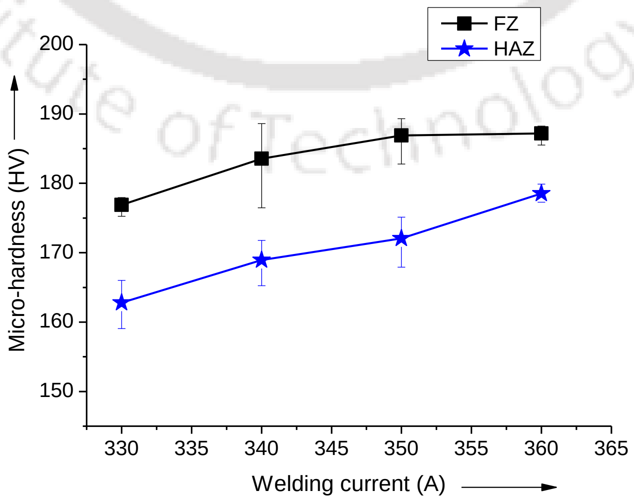

Figure 5.89 Effect of current on micro-hardness

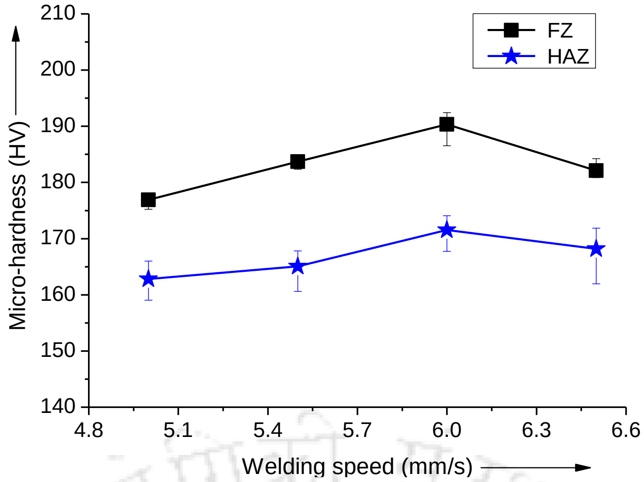

Figure 5.90 Effect of welding speed on micro-hardness

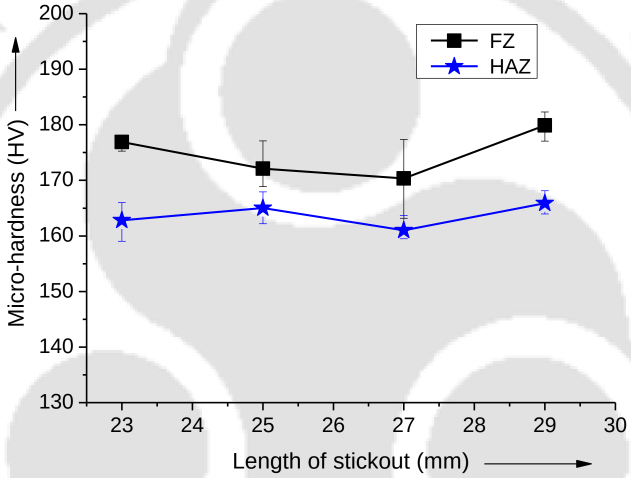

Figure 5.91 Effect of electrode stickout length on hardness

It can be observed from Figure 5.88 & 5.89 that an increase of arc voltage and current produce an increase of amount of carbon precipitation in the weld zone, which results in increase of hardness. From the Figure 5.90, it can be seen that hardness first increases with the increase of welding speed but follows a downward trend at higher welding speed. Length of stick-out have less influence than voltage and current as the increases in hardness is less with compared to other parameters.

5.10.4 Summary

From the above investigation of effect of welding parameters on weld bead geometry & and mechanical properties, it can be summarized as below:

- The submerged arc welding process parameters have significant effect on determination of the bead geometry as well as the mechanical property of the final weldment.
- It can be seen from the results that with the increase in weld voltage, the bead width becomes flatter but top reinforcement decreases. However, with the increase in current both top reinforcement and bead width increases. Hardness shows an increasing trend with current and voltage, as the carbon content increases in the weld zone due to the melting of the electrode.
- Welding speed has negative effect on weld bead dimensions; the overall bead geometry reduces with the reduction in welding speed. Hardness shows less variation with speed. Length of stick out has minor effect on bead as well as micro-hardness.

5.11 Effect of surface active elements on weld bead geometry

Addition of additional oxide elements can alter the weld bed geometry, for that reason effect of different types of surface active fluxes on weld bead geometry was studied. In this present work four different types of elements containing SiO_2, Cr_2O_3, TiO_2, and mixture of all fluxes were used. A comparative study on weld pool geometry, weld penetration, bead width and reinforcement was performed between welding of with and without surface active elements. After the welding, the three output parameters viz. weld bead geometry, penetration and reinforcement were measured. Figure 5.92 shows the cross sectional view of the bead on plate welds with and without surface active element.

(a) (b)

Figure 5.92 Cross sectional view of weld samples (a) with no flux (b) mixture of all three fluxes

5.11.1 Influence of surface active elements on penetration

Weld penetration is defined as the total distance between the top surface of the base plate to the tip of fusion depth. Among the all cases, the mixture of three surface active elements produced most noticeable effect. It increased the penetration more than twice as compared with conventional submerged arc welding. The measured values of weld penetration using different active elements are shown in the Tables 5.23. Total four repetitions were carried out for each measurement.

Table 5.24 Average depth of penetration

	PC1 (300A, 30V, 6 mm/s)	PC2 (325A, 32V, 6 mm/s)	PC3 (350A, 34V, 6 mm/s)
SiO_2	3.632	3.702	4.225
TiO_2	3.635	3.945	4.112
Cr_2O_3	3.852	4.127	4.665
SiO2+ TiO_2+ Cr_2O_3	4.867	5.032	5.42
No SA Elements	2.197	2.76	2.842

PC=Parameter combination

Figure 5.93 depicts the variation of the weld penetration for different surface-active elements at different parameter combinations as per Table 5.24.

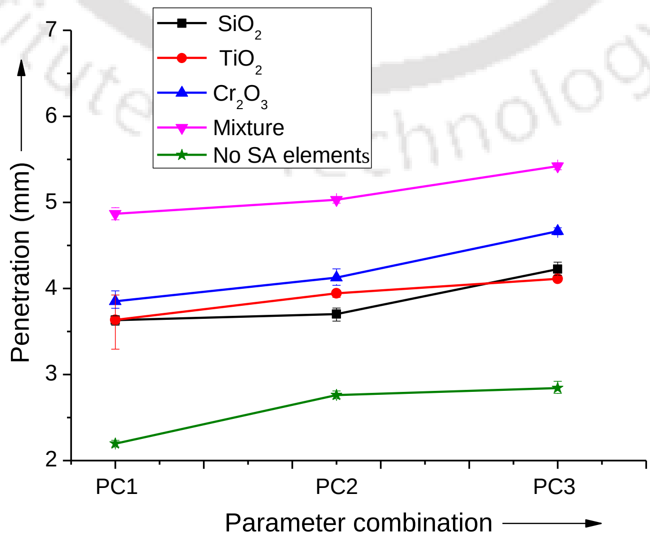

Figure 5.93 Effect of surface-active elements on weld penetration

Welding current has a linear relationship with the penetration i.e. if current is increased then the penetration in all cases increases. SiO_2 flux has shown least amount of penetration. The activating elements increases the transfer of molten metal droplets, this increases the striking and gets more penetration as compare to the welding without activating flux.

5.11.2 Influence of activating flux on bead width

Surface active elements have significant variations in weld bead width. The weld bead widths with surface active elements becomes narrower than those without it. When SiO_2, TiO_2 and Cr_2O_3 flux are used, the surface tension at the center of the weld pool becomes higher than that near the edges. Four repetitions were carried out for each experiments and the average vales of the weld bead width with and without surface active elements are shown in Table 5.25.

Table 5.25 Average weld bead width

Flux type	PC1 (300A, 30V, 6 mm/s)	PC2 (325 A, 32V, 6 mm/s)	PC3 (350A, 34V, 6 mm/s)
SiO_2	15.01	18.05	18.08
TiO_2	18.33	18.42	18.82
Cr_2O_3	12.26	13.48	13.91
SiO_2+ TiO_2+ Cr_2O_3	12.81	16.06	18.18
No Activated elements	16.05	17.25	19.31

PC=Parameter combination

Figure 5.94 illustrates the variation of the weld bead width for different surface active elements at different parameter combinations as per Table 5.25. Least bead width and highest bead width can be seen for Cr_2O_3 and TiO_2 elements respectively.

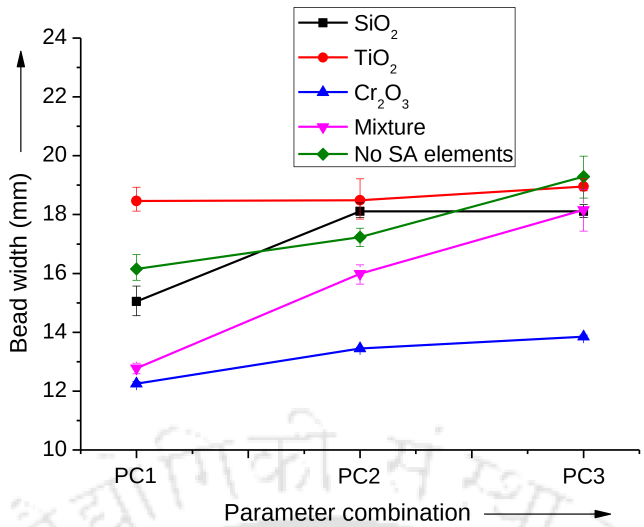

Figure 5.94 Effect of surface-active elements on weld bead width

In conventional SAW, the flow of molten metal takes place from center of the weld to the edges because surface tension at the center is less than that at the welding edges. This results in less penetration and more width of the weld pool. But when surface activating fluxes are used, the reversal of Marangoni effect occurs and due to arc constriction, improvement in depth of penetration and significantly less decrease in bead width are obtained.

5.11.3 Influence of activating flux on weld reinforcement

Reinforcement is the amount of molten metal deposition above the flat surface of the weld base plate. The average values of weld reinforcements are shown in Table 5.26.

Table 5.26 Average weld bead reinforcement

Flux Type	PC1 (300A, 30V, 6 mm/s)	PC2 (320 A, 32V, 6 mm/s)	PC3 (350A, 34v, 6 mm/s)
SiO_2	2.72	2.72	2.63
TiO_2	2.76	2.51	2.53
Cr_2O_3	3.32	3.21	3.13
SiO2+TiO_2+ Cr_2O_3	3.13	2.73	2.72
No Activated Elements	2.47	2.4	2.48

PC=Parameter combination

Figure 5.95 describes the effect of different surface-active element & its mixtures on weld reinforcement at different weld parameter setting as per Table 5.26. From Figure 5.95, it is evident that reinforcement decrease with the increase in voltage & current while keeping other parameters constant. Cr_2O_3 elements shows highest weld reinforcement.

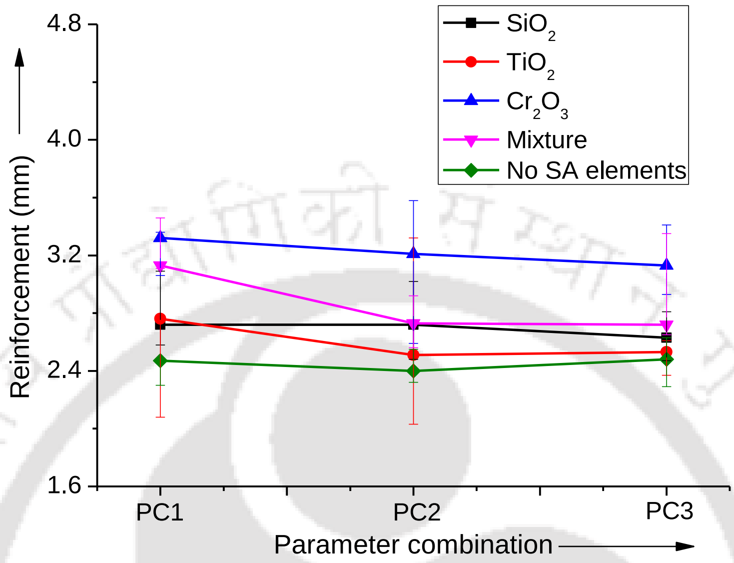

Figure 5.95 Effect of surface-active elements on reinforcement

Without surface activating elements the reinforcement is less than the weld metal using the surface activating elements. Cr_2O_3 has the highest reinforcement and TiO_2 has the lowest reinforcement among all the activating flux. The reinforcement decreases sharply in the weld where the mixture of surface active elements was used.

5.11.4 Summary

The summary from the above investigation of effect surface active elements on weld bead geometry can be summarized as below:

- The mixture of three surface active elements produced most noticeable effect, it was observed that by using surface active elements the penetration can be increased more than twice as compared with conventional submerged arc welding.
- Maximum bead width can be seen in case of TiO_2 flux and maximum penetration was achieved in case of Cr_2O_3 flux.

5.12 Effect of included angle on mechanical properties

For welding thick joints, edge preparation is necessary. Edge preparation takes lots of extra time & effort, amount of weld metal deposit influences the mechanical property of the joint. Thus, weld joint design has significant effect on weld economy as well as the mechanical properties of the welded structure. Experiments were conducted on 10 mm thick plate to study the effect of included angle on mechanical and weld bead properties of single V-butt joints. Included angle were varied for same root opening in single V-groove butt welded joints while all the other welding parameters were kept constant. Table 5.27 shows the experimental measured values of hardness and tensile strength for samples welded with varying weld joint geometry. In this study current and speed were varied while voltage and electrode stick out were kept constant.

Table 5.27 Tensile strength and hardness of welded samples

Weld Runs	Edge preparation	Current (A)	Welding speed (mm/s)	Tensile strength (MPa)	Weld zone hardness (HV)
1.	Square butt joint (0°)	350	5.5	367.37	197.25
2.		400	6	414.84	202.41
3.		450	6.5	484.83	206.62
4.	Included Angle (30°)	350	5.5	376.98	193.1
5.		400	6	471.05	199.79
6.		450	6.5	514.52	202.69
7.	Included Angle (60°)	350	5.5	356.73	194.68
8.		400	6	405.79	191.96
9.		450	6.5	410.5	198.38

5.12.1 Effect of included angle on tensile strength

Figure 5.96 shows the variation of tensile strength for all the joint geometries at three parameter combinations (PC1-3), small included angle (30°) of single-V has maximum ultimate tensile strength of 513 MPa followed by flat butt joint and large included angle of single-V joint having values of 484 MPa and 411 MPa respectively.

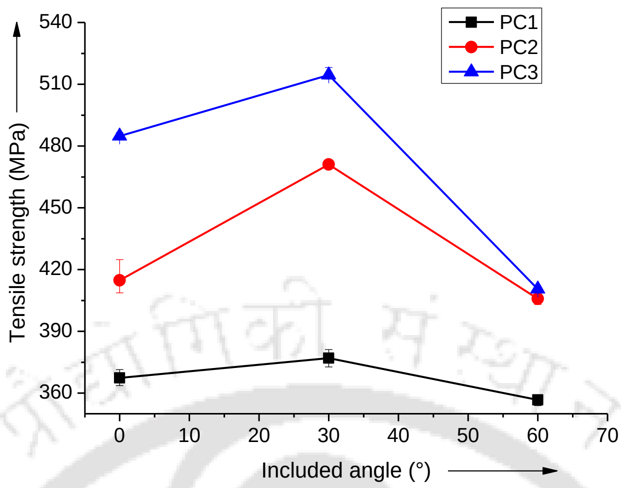

Figure 5.96 Effect of included angle on tensile strength

Smaller included angle shows more tensile strength because groove edge accommodates more metal deposition than flat butt edge and therefore the bonding strength is higher than that of straight flat edge. More the amount of weld metal deposit in higher the expansion and contractions consequently residual stresses increases in the weldment and the heat affected zone. Tensile strength is higher in V-grooved joints over flat edged joints because the bonding strength is dominant over the residual stress due to transfer of heat energy into the weldment.

5.12.2 Effect of included angle on hardness

The hardness value is a measure of the weld metal's resistance to localized plastic deformation or the resistance of a material to any scratch or indentation. Hardness testing is conducted according to Vickers micro-hardness testing method. Hardness of samples were tested starting in the weld bead followed by proceeding in the both leftward and rightward, of the weld bead across the section. Figure 5.97 reveals that the hardness profile of square butt joint is superior to all other weld joints. The increasing trend in the Vickers micro-hardness values are followed by square butt, single-V (small included angle) then single-V (large included angle) weld joints respectively. In all joints the maximum hardness values were observed in the fusion zone area and then heat affected zone (HAZ). The variation in hardness across the weld can be attributed to several factors, mainly due to residual stresses just after welding. However, other factors like grain size, phase composition and metallic inclusion can also contribute to this hardening.

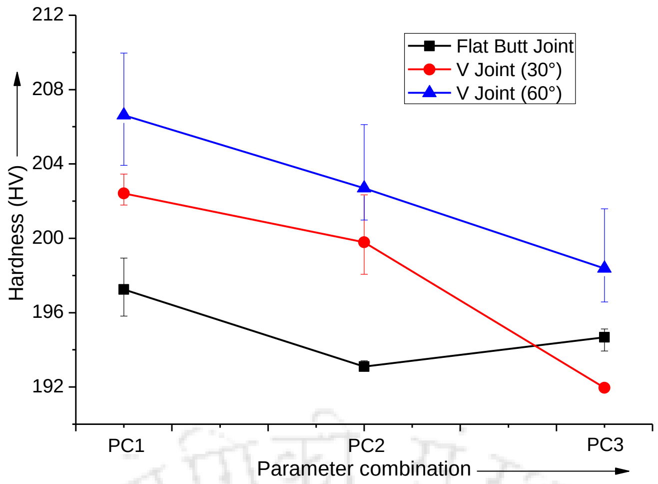

Figure 5.97 Effect of parameter combinations on hardness for different joint geometry

Hardness of the weld bead increases with the increase in the current, while keeping the arc voltage and welding speed constant. Included angels were varied while keeping the other welding parameters like voltage and current constant therefore there was no changes in the heat input into the weldment. The high weld deposit in V-groove joint increases the residual stresses in the weld region and increases the size of heat affected zone too. Residual stresses can significantly affect the engineering properties of the material and this has contributed to reduction in strength and hardness of the weldment and heat affected zone.

5.12.3 Summary

From the above investigation of effect of included angle on mechanical properties, it can be summarized as below:

- Three different joint geometries were taken into consideration; viz. square butt joint, V-butt with 30° included angle, and V-butt with 60° included angle. It can be seen from the results that V-butt joint geometry with 30° included angle produces superior tensile property of the final weldment.
- Maximum micro-hardness was seen in V-butt joint geometry with 60° included angle and flat butt joint shown lowest hardness value.

5.13 Prediction of optimal process parameters using Taguchi Method

Submerged arc welding process consists of multi-input parameters, therefore it is essential to determine the optimal process parameters for achieving desired quality characteristics of the weldment. To determine the range of input parameters, first trial and error method was carried out. One parameter was varied while all other parameters kept constant. After getting the range where full penetration with top and bottom reinforcement was achieved, the range is further subdivided into four levels as shown in Table 5.28 and optimization was carried out to determine optimal parameters setting. The details of optimization processes are discussed in the following subsections.The following Table 5.28 shows the input parameter combinations using the Taguchi L16 orthogonal array and the weld quality characteristics. In this present study voltage, current, speed and length of stick out were considered as the variable parameters. Mechanical characterization was preformed where, micro-hardness and tensile strength were measured.

5.13.1 Signal to noise ratio

To evaluate the optimal parameter settings Taguchi method uses a signal to noise ratio (S/N ratio) which serves the objective function to be optimized within the experimental domain [164]. Depending upon the quality characteristic the S/N ratios are of three types i.e. (i) Lower the better (LB), (ii) Higher the better (HB) and (iii) Nominal is the best (NB).

To achieve optimal parameter setting the output parameters i.e. the yield strength has to be maximized to get a desired weld quality. That is why higher the better S/N ratio was considered in this study. The signal-to-noise ratio (η_{ij}) of higher the better performance characteristic can be expressed as:

$$\eta_{ij} = -10 \log \frac{1}{n} \sum_{k=1}^{n} 1/y_{ijk}^2 \qquad (5.17)$$

where, y_{ijk} is the experimental value of the i^{th} performance characteristic in the j^{th} experiment at the k^{th} observation and n is the no of repetitions.

Table 5.28 Input and output parameters for multi-response optimization

Exp. No.	Voltage (V)	Current (A)	Welding speed (mm/s)	Stick out (mm)	Rate of heat input (η= 95%) (J/mm)	UTS (MPa)	YS (MPa)
1	27.0	470	5.5	2.2	2169.99	465.29	336.73
2	27.0	475	6	2.4	1995	470.87	326.62
3	27.0	480	6.5	2.6	1843	465.43	327.42
4	27.0	485	7	2.8	1719.50	464.63	329.43
5	27.5	470	5.5	2.6	2004.50	479.06	342.73
6	27.5	475	5	2.8	2232.50	480.44	340.78
7	27.5	480	7	2.2	1738.50	487.87	344.29
8	27.5	485	6.5	2.4	1900	497.70	353.07
9	28.0	470	6	2.8	1871.50	466.87	334.75
10	28.0	475	7	2.6	1748	463.07	321.67
11	28.0	480	5.5	2.4	2299	461.80	375.59
12	28.0	485	6	2.2	2109	468.61	331.57
13	28.5	470	7	2.4	1757.50	468.77	313.12
14	28.5	475	6.5	2.2	1928.50	472.95	330.43
15	28.5	480	6	2.8	2128	485.61	343.75
16	28.5	485	5.5	2.6	2356	474.48	338.25

Table 5.29 shows the results of the ANOVA which evaluates the significance of the factors and helps in determining the optimal parameter combination. ANOVA test shows that welding current is having the major effect on yield strength followed by welding speed. The length of stick out and voltage are having almost same contribution on weld quality. The results reveal that all parameters have influence on quality characteristics but ANOVA in the present study does not strongly support this because the P value is not less than 0.05 (95% confidence level) in none of the case. This may be due to the fact that within a narrow experimental domain it was not possible to detect the variations in the process environment (i.e. parameter combination). A fairly broad experimental boundary should be used to conduct experiments in order to fetch desirable results.

Table 5.29 Analysis of Variance of SN ratios for yield strength

Source	DF	Seq SS	Adj SS	Adj MS	F	P	% C
Voltage (V)	3	0.4243	0.4243	0.14142	1.19	0.444	21.82
Current (A)	3	0.4944	0.4944	0.1648	1.39	0.396	25.42
Welding speed (mm/s)	3	0.5628	0.5628	0.18759	1.58	0.358	28.94
Length of stick out (mm)	3	0.1072	0.1072	0.03572	0.3	0.825	5.51
Residual Error	3	0.3556	0.3556	0.11852			18.29
Total	15	1.9442					100

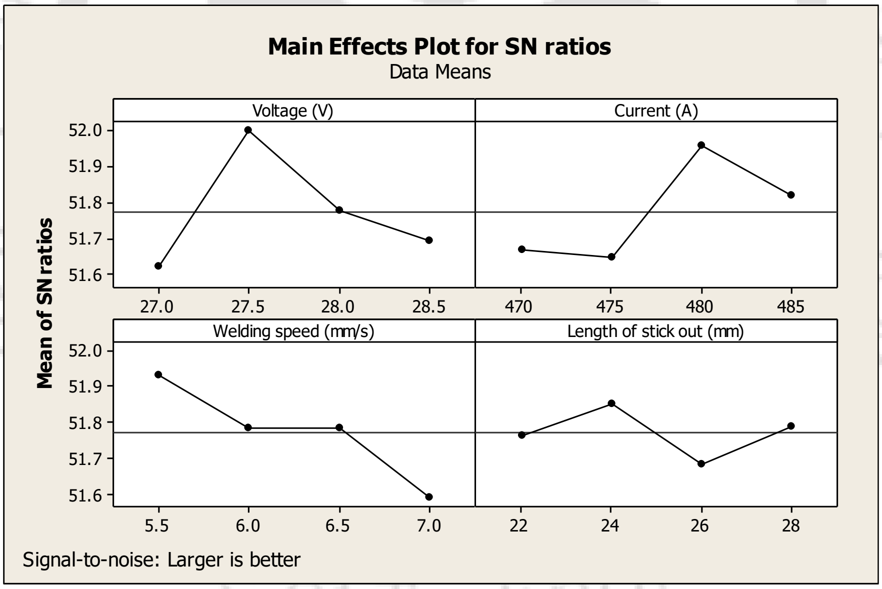

Figure 5.98 Main effect plot for yield strength

Minitab 15.0 [185] was used to generate the main effect plots. The main effect plots in the Figure 5.98 shows the optimal parameter combination for getting maximum yield strength which is V2-A3-S1-LOS2 i.e voltage 27.5 V, current 480 A, welding speed 5.5 mm/s and length of stick out should be 24 mm. Similarly for ultimate tensile strength, the main effect plots in the Figure 5.99 shows the optimal parameter combination for getting maximum ultimate tensile strength which is V2-A4-S2-LOS2 i.e voltage 27.5 V, current 485 A, welding speed 6 mm/s and length of stick out should be 24 mm.

Table 5.30 Analysis of Variance of SN ratios for ultimate tensile strength

Source	DF	Seq SS	Adj SS	Adj MS	F	P	% C
Voltage (V)	3	0.37951	0.37951	0.126503	6.64	0.077	73.06
Current (A)	3	0.03331	0.03331	0.011103	0.58	0.666	6.41
Welding speed (mm/s)	3	0.03486	0.03486	0.01162	0.61	0.653	6.71
Length of stick out (mm)	3	0.0146	0.0146	0.004865	0.26	0.854	2.81
Residual Error	3	0.05712	0.05712	0.019042			10.99
Total	15	0.5194					100

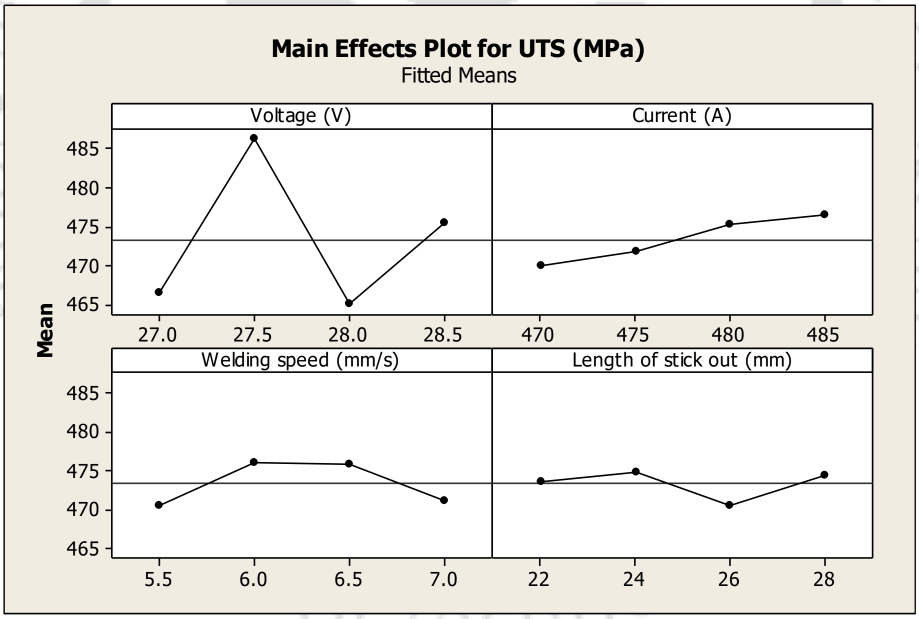

Figure 5.99 Main effect plot for ultimate tensile strength

5.13.2 Confirmation test

It was observed that the optimized parameters does not fall into the domain of Taguchi L16 orthogonal array, therefore confirmation test was done using the optimized parameters with three repetitions and the ultimate tensile strength and yield strength were found to be 510.24

MPa and 377.26 MPa respectively. Which confirmed the optimum parameter setting. To predict the optimal process parameters for individual responses, Taguchi optimization have to be performed for the individual responses accordingly. To predict optimal process parameters for all the responses together multi-objective optimization process is essential. Multi-response optimization of the all the responses together was carried out using Grey relational analysis along with Taguchi method, which is given in the next section.

5.13.3 Summary

The summary of the present study is given as follows:

- For getting a quality weld with adequate top and bottom reinforcement for 8 mm thick plate, the variable parameters can be varied for getting maximum yield strength as: voltage 27.5 V, current 480 A, welding speed 5.5 mm/s and length of stick out 24mm with a fixed root gap of 2.5 mm and using the power source as direct current reverse polarity.
- Percentage of contribution shows that welding speed, current and voltage are having the major effect on yield strength but length of stick out have very minor contribution. In case of ultimate tensile strength, welding voltage is having the major contribution and rest of the parameters are having minor contribution.
- The results reveal that all parameters have influence on quality characteristics but ANOVA in the present case does not strongly support this. This may be due to the fact that within a narrow experimental domain it was not possible to detect the variations in the process environment (parameter combination). A fairly broad experimental limit should be used to conduct experiments in order to fetch desirable results

5.14 Multi-response optimization based on Grey Taguchi method

To determine the optimal parameter settings, S/N ratio was utilized to find the optimal parameter settings in Taguchi method. But it was not possible to find out optimal parameter setting using Taguchi method alone. Grey relational analysis was used to convert the multi-response to a single response and Taguchi method was further used to find out the optimal parameter settings.

The S/N ratio depends on the type of the quality characteristics. In the present study total seven output parameters are considered viz. top bead height, top bead width, bottom bead height, bottom bead height, angular deformation, ultimate tensile strength, yield strength and percentage of elongation. Smaller-the-better criteria was chosen for angular deformation, since it is always desirable to have lower angular deformation, rest of the responses were analyzed using higher-the better criteria. The input process parameters and the responses are shown in **Table 5.31**. The stepwise procedure for transforming experimental data into Grey relational grade is shown in Figure 5.100. The detailed steps and results obtained from this analysis are discussed below.

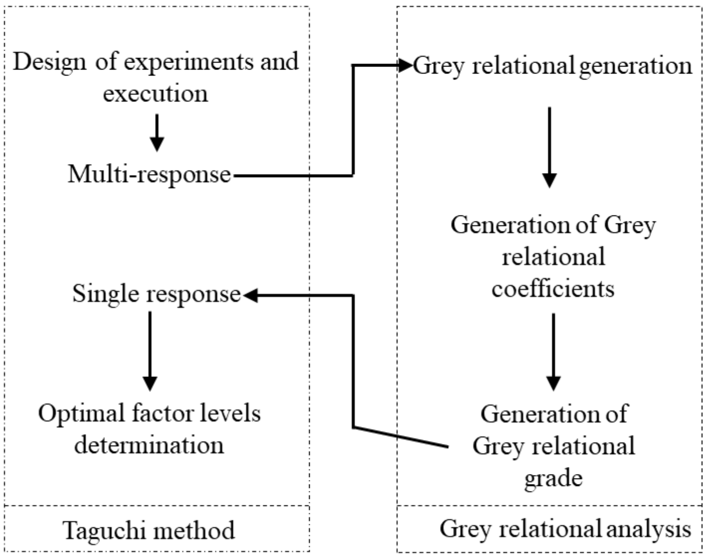

Figure 5.100 Methodology for multi-response optimization by Grey Taguchi method

Table 5.31 Input process parameters and the responses

Sl. No.	Voltage (V)	Current (A)	Welding speed (mm/s)	LOS (mm)	TBH (mm)	TBW (mm)	BBH (mm)	AD (mm)	UTS (MPa)	YS (MPa)	Elongation (%)
1	27	470	5	22	2.42	15.57	0.30	1.60	465.29	336.73	10.31
2	27	475	5.5	24	2.63	14.55	0.46	1.09	470.87	326.62	12.69
3	27	480	6	26	2.22	13.08	0.45	2.20	465.43	327.42	7.64
4	27	485	6.5	28	0.88	11.52	2.25	1.02	464.63	329.43	9.88
5	27.5	470	5.5	26	2.41	14.86	0.18	1.38	479.06	342.73	11.64
6	27.5	475	5	28	2.29	16.15	0.87	1.59	480.44	340.78	14.33
7	27.5	480	6.5	22	1.70	12.59	0.57	1.86	487.87	344.29	10.75
8	27.5	485	6	24	2.19	13.81	0.84	1.56	497.70	353.07	13.91
9	28	470	6	28	1.97	14.37	0.79	2.47	466.87	334.75	10.32
10	28	475	6.5	26	1.83	13.47	0.42	0.35	463.07	321.67	12.70
11	28	480	5	24	1.77	14.82	1.66	2.38	461.80	375.59	11.57
12	28	485	5.5	22	1.37	14.38	1.88	2.22	468.61	331.57	18.78
13	28.5	470	6.6	24	1.85	13.39	0.31	1.74	468.77	313.12	18.61
14	28.5	475	6	22	2.19	15.47	0.35	0.97	472.95	330.43	12.10
15	28.5	480	5.5	28	1.45	14.59	1.89	1.04	485.61	343.75	13.31
16	28.5	485	5	26	2.22	16.11	1.72	0.822	474.48	338.25	13.67

where WS=welding speed, LOS=length of electrode stick out, TBH=Top bead height, TBW= Top bead width, BBH=Bottom bead height, AD=Angular deformation, UTS=Ultimate tensile strength, YS=Yield strength

At the initial step the output responses were normalized to find out the Grey relational generation (GRG) i.e. all the measured experimental output characteristics were normalized between 0 to 1. Angular deformation were normalized corresponding to smaller the better criterion as shown in Equation 3.97, all other parameters were normalized as per higher the better criterion as shown in Equation 3.98. Table 5.32 shows the normalized output data.

Table 5.32 Normalization of output data (Grey relational generation)

YS_HB	UTS_HB	%E_HB	AD_LB	TBH_HB	TBW_HB	BBW_HB
0.622059	0.903016	0.760597	0.5891178	0.121876	0.124695	0.518642
0.783896	0.747328	0.546565	0.34702	0	0.345134	0.791395
0.77109	0.898995	1	0.8743828	0.232399	0.66277	0.624464
0.738915	0.921224	0.798887	0.3165592	1	1	0.192367
0.526012	0.519248	0.640895	0.483944	0.126844	0.279021	0.77384
0.557227	0.480805	0.399507	0.5840855	0.195908	0	0.589661
0.50104	0.273806	0.721042	0.7142632	0.535213	0.767443	0.651175
0.360493	0	0.437388	0.5688159	0.252432	0.504872	0.58203
0.653754	0.858819	0.759443	1	0.378279	0.383393	1
0.863134	0.964847	0.545648	0	0.456064	0.579204	0.75303
0	1	0.647241	0.9565969	0.490928	0.286043	0
0.704658	0.810473	0	0.8804372	0.720327	0.382728	0.246311
1	0.805985	0.015356	0.6558578	0.448777	0.594617	0.940312
0.722907	0.689456	0.59953	0.2913823	0.250071	0.146867	0.901599
0.509685	0.336692	0.490885	0.3256801	0.67382	0.336156	0.325116
0.597727	0.646964	0.458915	0.2204592	0.233784	0.008951	0.442444

After normalization Grey relational coefficient is calculated as shown in Equation 3.99. To calculate Grey relational coefficient Δ_{oi} has to be calculated, which is shown in Table 5.33. The calculated Grey relational coefficients are shown in Table 5.34. The GRCs represents the correlation between the desired and actual experimental output data.

Table 5.33 Δ_{oi} for each responses

YS	UTS	%E	AD	TBH	TBW	BBW
0.377941	0.096984	0.239403	0.410882	0.878124	0.875305	0.481358
0.216104	0.252672	0.453435	0.65298	1	0.654866	0.208605
0.22891	0.101005	0	0.125617	0.767601	0.33723	0.375536
0.261085	0.078776	0.201113	0.683441	0	0	0.807633
0.473988	0.480752	0.359105	0.516056	0.873156	0.720979	0.22616
0.442773	0.519195	0.600493	0.415914	0.804092	1	0.410339
0.49896	0.726194	0.278958	0.285737	0.464787	0.232557	0.348825
0.639507	1	0.562612	0.431184	0.747568	0.495128	0.41797
0.346246	0.141181	0.240557	0	0.621721	0.616607	0
0.136866	0.035153	0.454352	1	0.543936	0.420796	0.24697
1	0	0.352759	0.043403	0.509072	0.713957	1
0.295342	0.189527	1	0.119563	0.279673	0.617272	0.753689
0	0.194015	0.984644	0.344142	0.551223	0.405383	0.059688
0.277093	0.310544	0.40047	0.708618	0.749929	0.853133	0.098401
0.490315	0.663308	0.509115	0.67432	0.32618	0.663844	0.674884
0.402273	0.353036	0.541085	0.779541	0.766216	0.991049	0.557556

Table 5.34 Grey relational coefficients

GRC_YS	GRC_UTS	GRC_%E	GRC_AD	GRC_TBH	GRC_TBW	GRC_BBW
0.569514	0.837543	0.676221	0.548918392	0.362812142	0.363555775	0.509497817
0.698223	0.6643	0.52442	0.433658856	0.333333333	0.432950704	0.705612043
0.685956	0.83194	1	0.799210718	0.394445832	0.597207275	0.571078887
0.656957	0.863893	0.713152	0.422496844	1	1	0.382370295
0.513354	0.509813	0.582001	0.492098869	0.364124591	0.409507438	0.688553619
0.530351	0.490583	0.454342	0.545902512	0.383408607	0.333333333	0.549245712
0.500521	0.407766	0.641884	0.636345442	0.518249249	0.682540435	0.589049515
0.438786	0.333333	0.470539	0.536950721	0.400779691	0.502447699	0.544679832
0.590845	0.779811	0.675167	1	0.445743733	0.44778498	1
0.785095	0.934312	0.523915	0.333333333	0.478956533	0.543008342	0.669370498
0.333333	1	0.586332	0.920127333	0.495504706	0.411876128	0.333333333
0.628661	0.725135	0.333333	0.807020661	0.641294645	0.447518544	0.398822843
1	0.720446	0.336781	0.592317294	0.475636352	0.552252544	0.893354258
0.643424	0.616869	0.555266	0.413695743	0.400022709	0.369512738	0.835560182
0.50489	0.429809	0.495484	0.425778373	0.605195088	0.42961076	0.425574
0.554156	0.586142	0.480268	0.390765184	0.394877316	0.335334361	0.472788289

Table 5.35 Grey relational grades

GRG
0.670214713
0.576089898
0.704951996
0.617594999
0.586174617
0.572083832
0.546510823
0.46979776
0.669535111
0.618668779
0.62613229
0.582899711
0.638624718
0.608736459
0.49088277
0.541509082

The average of the Grey relational coefficients gives the Grey relational grade as shown in Table 5.35 The Grey relational grades renovates the multi response problem into a single response optimization problem, which is further optimized using Taguchi method.

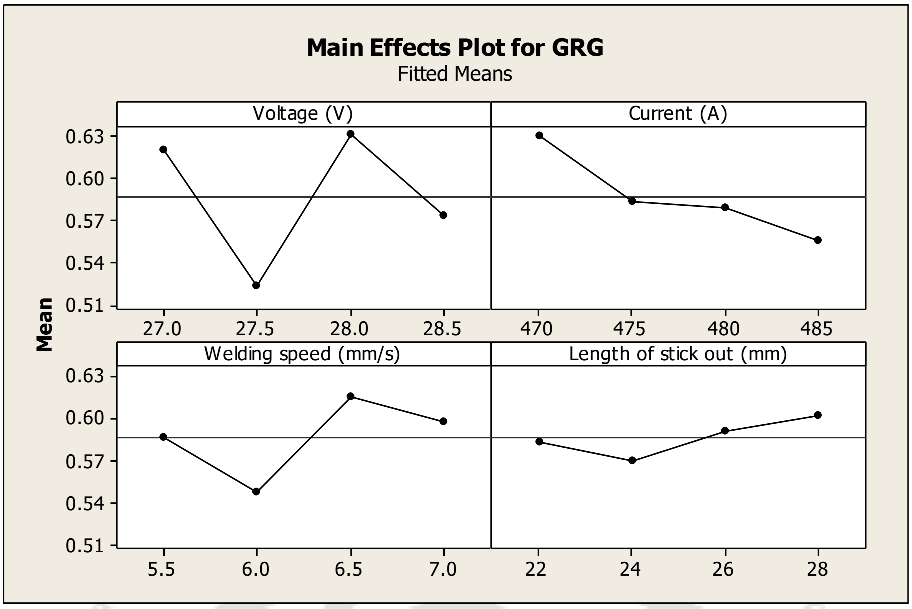

Figure 5.101 Main effect plots of SN ratios for grey relational grade

Table 5.36 Analysis of Variance of SN ratios for Grey relational grades

Source	DF	Seq SS	Adj SS	Adj MS	F	P	% Contribution
Voltage (V)	3	0.028591	0.028591	0.00953	2.47	0.238	44.75
Current (A)	3	0.011573	0.011573	0.003858	1	0.499	18.11
Welding speed (mm/s)	3	0.009904	0.009904	0.003301	0.86	0.549	15.50
Length of stick out (mm)	3	0.002265	0.002265	0.000755	0.2	0.893	3.54
Error	3	0.011554	0.011554	0.003851			18.08
Total	15	0.063887					

Figure 5.101 shows the main effect plots for overall GRG. For the main effect plots it can be seen that welding voltage of 28 V, current of 470 A, welding speed of 6.5 mm/s and length of stick out of 28 mm are the optimal parameter settings for this multi response problem. Table 5.36 represents the analysis of variance suing the adjusted SS for tests. It is observed that P-value of none of the parameters is less than 0.05, therefore no parameter is significant, which may be due to experimental errors involved in this study. It can also be observed fro Table 5.36 that welding voltage have the highest percentage of contribution on the output data and length of stick out has the lowest percentage of contribution on the welding quality for this multi-response problem.

5.14.1 Confirmation experiment

For confirmation of experimental results, three experiments were performed at same process parameters (optimal settings) as suggested by Taguchi analysis of utility data. The observed values of various response characteristics are given in Table 5.37.

Table 5.37 Results of the confirmation experiments

Sl. No.	TBH (mm)	TBW (mm)	BBH (mm)	AD (mm)	UTS (MPa)	YS (MPa)	% Elongation
Experiment 1	2.65	16.87	2.30	0.36	505.82	435.93	13.68
Experiment 2	2.73	16.55	2.26	0.30	502.17	433.18	14.52
Experiment 3	2.70	16.78	2.45	0.32	498.33	429.92	14.79

5.14.2 Summary

The summary of the preceding study is as follows:

- For getting a quality weld with adequate top and bottom reinforcement the variable parameters can be as voltage 28 V, current 470 A, welding speed 6.5 mm/s and length of stick out 28 mm with a fixed root gap of 2.5 mm and using the power source as direct current reverse polarity.
- Within the specified range of parameters, the predicted results by the multi-characteristic optimization model agree with the experimental results.

CHAPTER 6

Conclusions and future works

6.1 Conclusions

In this present study, numerical analysis and experimental investigation of submerged arc welded mild steel plates have been carried out extensively. Welding of thick metal plates needs edge preparation; one of the aim of this study was to do welding without any edge preparation. Butt as well as fillet welds were performed by using submerged arc welding. As welding is one of the most complex manufacturing process involving multi-physics, numerical modelling considering all the physical phenomena is an extremely difficult task. However with the help of suitable assumptions and few other methodologies developed by the earlier researchers made this process easier. Here, 3D FE models were developed to estimate the temperature profile of the welded plates and estimate the residual stress and distribution. Effect of tacking and welding sequences were studied for the development of sustainable mitigation techniques. Angular distortion in large structures also estimated by using an equivalent technic. A new volumetric heat source model was developed which can be used in the simulations of fusion welding. Effect of weld parameters, joint geometry on weld bead geometry as well as mechanical property was studied. The addition of surface active elements enhances the weld penetration, effect of the same was studied. Optimizations were carried out to determine the best parameter combination.

From the preceding investigations the following conclusions arrived which can be summarized as below:

- 3D FE nonlinear elasto-plastic transient thermo-mechanical model was successfully developed for both butt and fillet welding joints which were validated with experimental results and published literature. A good agreement between the predicted and experimental results was observed with an error of 5 to 10%.

- From the comparative study of residual stresses and angular deformations between single and double-sided fillet welded mild steel joints it was observed that single sided fillet welding shows non-uniform pattern of the residual stress distribution in the left and right side of the stiffener whereas it is almost uniform for double sided fillet welding. The peak magnitude of residual stress is more in case of single side fillet welding compare to that of double sided fillet welding. However, higher magnitude of angular deformation is observed in case of double sided fillet welding.

- The tacking positions also have a significant effect in residual stresses and angular distortion distribution. It was observed that the tacking positions opposite to fillet weld side have negligible effect on residual stress distribution whereas the tacking positions in fillet weld side have significant effect on uneven distribution and increment of residual stresses. So, the number of tack welds should be as minimum as possible if not avoidable and it should be placed opposite to the fillet weld side.

- It was observed that welding sequences have prominent effects on both distortion & residual stresses. The angular deformation can be reduced significantly by choosing proper welding sequences.

- Prediction of distortion of large welded structure with multiple welding passes is a very difficult task due to limitation of computation resource. An equivalent loading technique with the bar-spring analogy was successfully implemented to predict the weld induced distortion of large welded structure. The elastic FE analysis using equivalent loading technique involves very less computational time as compared to the 3-D FE nonlinear elasto-plastic thermo-mechanical analysis.

- Based on experimental study, an avocado shaped volumetric heat source was developed. The generalised form of the avocado-configuration heat source consists of limited number of model parameters, which can provide a real non-uniform shape of moving heat source of fusion welding. The developed heat source model was validated with experimental results. A good agreement between the predicted and experimental results was observed with an error of 8 to 10%.

- Single pass single sided experimental square butt joints were successfully made on 8 mm to 12 mm thick plates. Through thickness fusion along with adequate top and bottom reinforcements were achieved using flux-filled reusable backing bar.

- From mechanical characterization, it was observed that the maximum hardness was observed in the weld zone and which decreases gradually away from the weld line towards base material. The increment of hardness in the weld zone was more for lower welding speed, higher voltage and higher current. Maximum hardness at weld zone and HAZ were around 20 % and 12% more than the base material respectively.

- Hardness shows an increasing trend with increasing of current and voltage. Hardness shows less variation with speed. Length of stick out has minor effect on bead as well as micro-hardness.

- None of the tensile samples failed in the weld zone, failure was seen in between the base metal and heat affected zone. Based on UTS the maximum joint efficiency was 96%.

- It was seen that with the increase in weld voltage, the bead width becomes flatter but top reinforcement decreases. However, with the increase in current both top reinforcement and bead width increases. Welding speed has negative effect on weld bead dimensions; the overall bead geometry reduces with the increase in welding speed.

- Surface active elements play a significant role for welding of thicker plates. It was found that by choosing appropriate activated flux weld bead penetration can be increased by more than two times i.e. 221%.

- It was seen from the results of three different joint geometries that V-butt joint geometry with 30° included angle produces superior mechanical property than the other joint geometries. Maximum ultimate strength and hardness were obtained at 30° included angle which were 99 % and 129 % to that of the base material respectively.

- To get optimal process parameters for desired weld quality, Taguchi optimization technique was used for single output problem. To determine the optimal process parameters for multiple output problem, Grey relational analysis in combination with Taguchi method was used. From ANOVA it was observed that welding voltage was having highest contribution, followed by welding current & welding speed and length of stick had the least contribution on the weld quality characteristics.

6.2 Scope of future works

Various aspects of fusion welding were investigated in the present study. It included the prediction of thermal profile and distortion patterns of weldments, study of the effect of tacking sequence & welding sequence on residual stress and angular deformation. Prediction of distortion in large structure, generalized heat source modelling, effect of process parameters on weld quality and optimization of welding parameters. Based on these studies scope of further study are presented as follows:

- The present study was limited to single pass welds only therefore it can be extended to the thermo-mechanical analysis of multi-pass welding of thick plates.

- Residual stress and distortion in weld structures is a matter of serious concern, further work is required for developing different mitigation technics for controlling residual stresses and angular deformations.

- Development of an equivalent loading technique for finding out the welding sequence induced deformation in large structures.

- The developed avocado shaped heat source was used to predict the thermal history of submerged arc welding, this type of heat source models also needs to be used for thermo-mechanical analysis of other fusion welding processes like GTAW, GMAW etc..

Appendix I

The Gaussian distribution of the power density in a proposed 'configuration' heat source model at centre and semi-axes a, b, c parallel to coordinate axes x, y, z can be stated as:

$$q_{(x,y,z)} = q_m \times e^{\left\{-\left[By^2+\left(Ax^2+Cz^2\right)\times t(y)\right]\right\}} \quad \text{(i)}$$

$$where, t(y) = \frac{1}{e^{my}} \quad \text{(ii)}$$

q_m is the maximum value of the power density at the centre of a proposed avocado shape and *A*, *B*, *C* and m are the distribution parameters. Conservation of energy requires the intensity of heat distributed inside the half of the avocado shape and is expressed as

$$2Q = 4\int_0^\infty\int_0^\infty\int_0^\infty q_m \times e^{\left\{-\left[By^2+\left(Ax^2+Cz^2\right)\times\left(\frac{1}{e^{my}}\right)\right]\right\}} dxdydz + 4\int_0^\infty\int_0^\infty\int_0^\infty q_m \times e^{\left\{-\left[By^2+\left(Ax^2+Cz^2\right)\times\left(\frac{1}{e^{-my}}\right)\right]\right\}} dxdydz$$

(iii)

$$= I + J(let) \quad \text{(iv)}$$

I is valid if *y*= +*y* and *J* is valid if *y*= -*y*

The distribution is different in +ve and –ve side of y-axis.

After simplifying the above equation, the q_m can be estimated as per the following procedure given below

$$\therefore I = 4\int_0^\infty\int_0^\infty\int_0^\infty q_m \times e^{\left\{-\left[By^2+\left(Ax^2+Cz^2\right)\times\left(\frac{1}{e^{my}}\right)\right]\right\}} dxdydz \quad \text{(v)}$$

$$= 4q_m \int_0^\infty\int_0^\infty e^{-\left[By^2+Ax^2\left(e^{-my}\right)\right]} \times [\frac{\sqrt{\pi}}{2}(\frac{1}{\sqrt{Ce^{-my}}})]dxdy$$

$$(As, \int_0^{\infty} e^{-Ax^2}\, dx = \frac{\sqrt{\pi}}{2}.\frac{1}{\sqrt{A}}) \text{ for A>0}$$

$$= 4q_m \int_0^{\infty} e^{-\left[By^2\right]} \times [\frac{\sqrt{\pi}}{2}(\frac{1}{\sqrt{Ae^{-my}}})] \times [\frac{\sqrt{\pi}}{2}(\frac{1}{\sqrt{Ce^{-my}}})]dy$$

$$= \frac{\pi q_m}{\sqrt{AC}} \int_0^{\infty} e^{\left[-By^2\right]} \times e^{my} dy$$

$$= \frac{\pi q_m}{\sqrt{AC}} \int_0^{\infty} e^{\left[my-By^2\right]} dy$$

$$= \frac{\pi q_0}{\sqrt{AC}} \int_0^{\infty} e^{-B\left[y^2-\frac{m}{B}y\right]} dy$$

$$\because [y^2 - \frac{m}{B}y = y^2 - 2y.\frac{m}{2B} + (\frac{m}{2B})^2 - (\frac{m}{2B})^2$$

$$= (y - \frac{m}{2B})^2 - \frac{m^2}{4B^2}]$$

$$\therefore I = \frac{\pi q_m}{\sqrt{AC}} e^{\frac{m^2}{4B}} \int_0^{\infty} e^{-B(y-\frac{m}{2B})^2} dy = \frac{\pi q_m}{\sqrt{AC}}.e^{\frac{m^2}{4B}}.\frac{\sqrt{\pi}}{2}.\frac{1}{\sqrt{B}} = \frac{\pi\sqrt{\pi} q_m\, e^{\frac{m^2}{4B}}}{2\sqrt{ABC}}$$

As $\frac{m}{2B}$ is very small, neglecting the same.

$$(As, \int_0^{\infty} e^{-Ax^2}\, dx = \frac{\sqrt{\pi}}{2}.\frac{1}{\sqrt{A}})$$

for A>0

$$\Rightarrow I = \frac{\pi\sqrt{\pi} q_m\, e^{\frac{m^2}{4B}}}{2\sqrt{ABC}} \qquad \text{(vi)}$$

Similarly,

$$J = 4\int_0^{\infty}\int_0^{\infty}\int_0^{\infty} q_m \times e^{\left\{-\left[By^2 + \left(Ax^2 + Cz^2\right)\times\left(\frac{1}{e^{-my}}\right)\right]\right\}} dxdydz \qquad \text{(vii)}$$

$$= 4q_m \int_0^{\infty}\int_0^{\infty} e^{-\left[By^2 + Ax^2\left(e^{my}\right)\right]} \times [\frac{\sqrt{\pi}}{2}(\frac{1}{\sqrt{Ce^{my}}})]dxdy$$

$$(As, \int_0^{\infty} e^{Ax^2}\, dx = \frac{\sqrt{\pi}}{2}.\frac{1}{\sqrt{A}})$$

$$= 4q_m \int_0^{\infty} e^{-\left[By^2\right]} \times [\frac{\sqrt{\pi}}{2}(\frac{1}{\sqrt{Ae^{my}}})] \times [\frac{\sqrt{\pi}}{2}(\frac{1}{\sqrt{Ce^{my}}})] dy$$

$$= \frac{\pi q_m}{\sqrt{AC}} \int_0^{\infty} e^{\left[-By^2\right]} \times e^{-my} dy$$

$$= \frac{\pi q_m}{\sqrt{AC}} \int_0^{\infty} e^{\left[-my-By^2\right]} dy$$

$$= \frac{\pi q_m}{\sqrt{AC}} \int_0^{\infty} e^{-B\left[y^2+\frac{m}{B}y\right]} dy$$

$$\because [y^2 + \frac{m}{B} y = y^2 + 2y.\frac{m}{2B} + (\frac{m}{2B})^2 - (\frac{m}{2B})^2$$

$$= (y + \frac{m}{2B})^2 - \frac{m^2}{4B^2}]$$

$$\therefore J = \frac{\pi q_m}{\sqrt{AC}} e^{\frac{m^2}{4B}} \int_0^{\infty} e^{-B(y+\frac{m}{2B})^2} dy = \frac{\pi q_m}{\sqrt{AC}}.e^{\frac{m^2}{4B}}.\frac{\sqrt{\pi}}{2}.\frac{1}{\sqrt{B}} = \frac{\pi\sqrt{\pi} q_m e^{\frac{m^2}{4B}}}{2\sqrt{ABC}} \qquad \text{(viii)}$$

$$\therefore 2Q = I + J = \frac{\pi\sqrt{\pi} q_m e^{\frac{m^2}{4B}}}{2\sqrt{ABC}} + \frac{\pi\sqrt{\pi} q_m e^{\frac{m^2}{4B}}}{2\sqrt{ABC}} = \frac{\pi\sqrt{\pi} q_m e^{\frac{m^2}{4B}}}{\sqrt{ABC}} \qquad \text{(ix)}$$

Optimum point Calculation for shifting the ellipse centre:

$$\frac{y^2}{b^2} + (\frac{x^2}{a^2} + \frac{z^2}{c^2}) e^{-my} = 1$$

This equation defines the geometric shape of the avocado.

In 2-D plate, the equation becomes as following

$$\frac{y^2}{b^2} + \frac{x^2}{a^2}.e^{-my} = 1 \qquad \text{(x)}$$

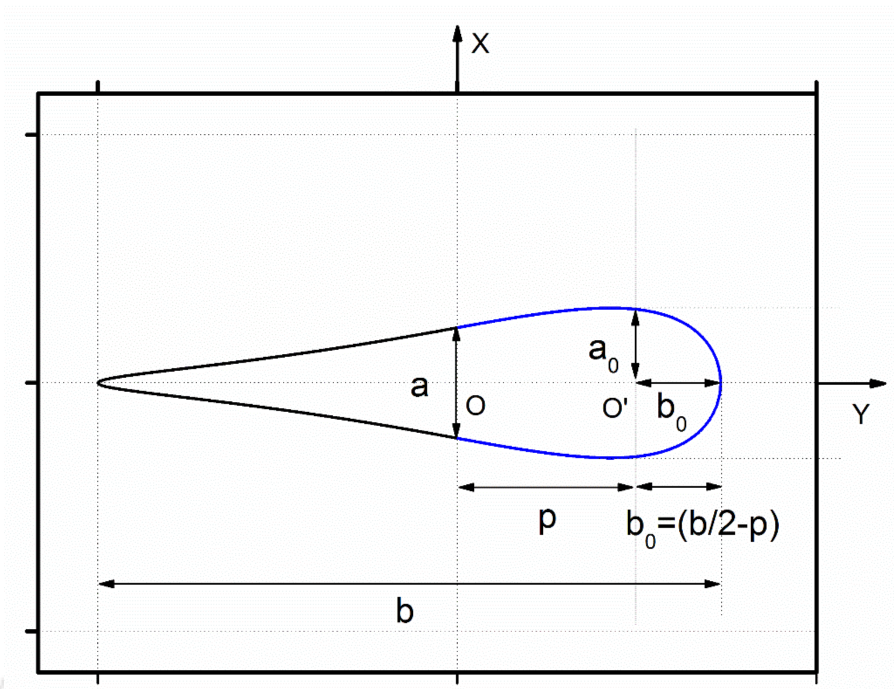

Figure 1 Parameters of the avocado shape

After derivating as following

For optimum value (slope X-Y plane)

$$\frac{dx}{dy}=\frac{\{(m\frac{x^2}{a^2}e^{-my})-\frac{2y}{b^2}\}}{(\frac{2xe^{-my}}{a^2})}=0$$

$$\Rightarrow \frac{2y}{b^2}-\frac{mx^2e^{-my}}{a^2}=0$$

$$\therefore \frac{2y}{b^2}=\frac{mx^2e^{-my}}{a^2}$$

$$\Rightarrow \frac{x^2e^{-my}}{a^2}=\frac{2y}{mb^2} \qquad \text{(xi)}$$

From eq. (x) and (xi) we get

$$\frac{y^2}{b^2}+\frac{2y}{mb^2}=1$$

$$\Rightarrow y^2+\frac{2y}{m}=b^2$$

$$\Rightarrow my^2+2y-mb^2=0$$

$$\frac{y^2}{b^2}+\frac{x^2}{a^2}.e^{-my}=1 \ \ (Assuming\ \ 2D)$$

$$\Rightarrow \frac{2y}{b^2}+[\frac{2.x.e^{-my}}{a^2}.\frac{dx}{dy}]-\frac{m.x^2.e^{-my}}{a^2}=0$$

$$\Rightarrow \frac{mx^2e^{-my}}{a^2}-\frac{2y}{b^2}=\frac{2xe^{-my}}{a^2}.\frac{dx}{dy}$$

$$\Rightarrow \frac{dx}{dy}=\frac{\{(m\frac{x}{a^2}{}^2e^{-my})-\frac{2y}{b^2}\}}{(\frac{2xe^{-my}}{a^2})}$$

$$\therefore y = \frac{-2 \pm \sqrt{4 + 4.m.b^2.m}}{2.m}$$

$$= \frac{-2 \pm 2\sqrt{1 + m^2 b^2}}{2.m}$$

$$= \frac{-1 \pm \sqrt{1 + m^2 b^2}}{m}$$

Lets consider $y = \frac{-1 + \sqrt{1 + m^2 b^2}}{m} = p$ Where $y > 0$ (xii)

$\therefore$ Optimum slope at $y = p$

$$\sqrt{1 + m^2 b^2} > 1$$
$$\Rightarrow (1 + m^2 b^2) > 1$$
$$\Rightarrow m^2 b^2 > 0$$
$$i.e.\ mb > 0 \text{ is possible if } m \text{ is} +ve \text{ since } b \text{ is} +ve$$

Similarly if we consider Y-Z plane, we find the optimum point at y=p

From eq. (x) and (xi) we also get

At optimal point

$$\frac{x^2}{a^2}.e^{-my} = \frac{2y}{mb^2}$$

$\therefore$ *at* $y = p$

$$x^2 = a^2.e^{mp}.\frac{2p}{mb^2}$$

$$x = \sqrt{\frac{2a^2}{mb^2} pe^{mp}} = a_0$$

$$\Rightarrow a^2 = a_0^{\ 2}.m.b^2.\frac{1}{2p}.e^{-mp}$$

(xiii)

Similarly

$$z = \sqrt{\frac{2c^2}{mb^2} pe^{mp}} = c_0$$

$$\Rightarrow c^2 = c_0^{\ 2}.m.b^2.\frac{1}{2p}.e^{-mp}$$

(xiv)

where $c_0 = depth\ (desired)$

$a_0 = Half\ width$

$c_0 = depth\ of\ penetration$

The dimension of m should be $\frac{1}{L}$, then the above equation will be dimensionally balanced.

a_0, c_0 can be defined from experiment. However, b is not defined. We need another condition to find the value of b.

Therefore, the strategy is considered such that at least a small part of the arc is circular or symmetrical for a moving heat source.

Let's assume $b_0 = (\frac{b}{2} - p)$ (From Fig. 1)

Assume that $a_0 = b_0$

$$\therefore \frac{b}{2} - p = b_0$$

$$\Rightarrow b - 2p = 2b_0$$

$$\Rightarrow b - 2b_0 = 2p = \frac{-2 + 2\sqrt{1 + m^2b^2}}{m}$$

$$\Rightarrow mb + 2 - 2.m.b_0 = 2\sqrt{1 + m^2b^2}$$

$$\Rightarrow (mb + 2 - 2m.b_0)^2 = 4(1 + m^2b^2)$$

$$\Rightarrow m^2b^2 + 4 + 4mb + 4.m^2.b_0^{\ 2} - 4mb.mb_0 - 8.mb_0 = 4 + 4m^2b^2$$

$$\Rightarrow m^2b^2 + 4 + 4mb + 4.m^2.b_0^{\ 2} - 4mb.mb_0 - 8.mb_0 - 4 - 4m^2b^2 = 0$$

$$\Rightarrow -4mb + 4m^2b.b_0 + 8.mb_0 - 4.m^2.b_0^{\ 2} + 3m^2b^2 = 0$$

$$\Rightarrow 3m^2b^2 + b(4m^2b_0 - 4m) + 8mb_0 - 4m^2.b_0^{\ 2} = 0$$

$$\therefore b = \frac{-(4m^2b_0 - 4m) \pm \sqrt{(4m^2b_0 - 4m)^2 - 4.3.m^2(8mb_0 - 4m^2b_0^{\ 2})}}{2.3.m^2}$$

$$\Rightarrow b = \frac{2}{3m} - \frac{2b_0}{3} + \frac{\pm\sqrt{(4m^2b_0 - 4m)^2 - 4.3.m^2(8mb_0 - 4m^2b_0^{\ 2})}}{6m^2}$$

By considering only positive value

$$b = \frac{2}{3m} - \frac{2b_0}{3} + \frac{\sqrt{(4m^2b_0 - 4m)^2 - 4.3.m^2(8mb_0 - 4m^2b_0^{\ 2})}}{6m^2} \qquad \text{(xv)}$$

$$Now,\ p = \frac{-1 + 1\sqrt{1 + b^2m^2}}{m};\ \text{where}\ b = \frac{2}{3m} - \frac{2b_0}{3} + \frac{\sqrt{(4m^2b_0 - 4m)^2 - 4.3.m^2(8mb_0 - 4m^2b_0^{\ 2})}}{6m^2}$$

and b_0 will be taken from experimental measurements.

Therefore a_0 , b_0 , c_o can be calculated from experimental data.

Accordingly the heat source parameters *a, b c* are easily defined.

$$a = a_0 b\sqrt{\frac{m}{2p}e^{-mp}} \quad ; \quad c = c_0 b\sqrt{\frac{m}{2p}e^{-mp}}$$

Therefore the modified equation for –ve side is:

$$\frac{(y-p)^2}{b^2} + (\frac{x^2}{a^2} + \frac{z^2}{c^2}).e^{-m(y-p)} = 1 \qquad \text{(xvi)}$$

Therefore the modified equation for +ve side is:

$$\frac{(y-p)^2}{b^2} + (\frac{x^2}{a^2} + \frac{z^2}{c^2}).e^{+m(y-p)} = 1 \qquad \text{(xvii)}$$

Let's consider A, B, C are the distribution parameters for the front part and A', B', C' are the distribution parameters for rear part.

Validation:

Replacing y=y-p in the distribution equation we get

$$2Q = 4\int_0^{\infty}\int_0^{\infty}\int_0^{\infty} \mathrm{q_m} \times \mathrm{e}^{\left\{-\left[\mathrm{B(y\text{-}p)^2} + \left(\mathrm{Ax^2+Cz^2}\right)\times\left(\frac{1}{e^{m(y-p)}}\right)\right]\right\}} \mathrm{dxdydz}$$

$$+4\int_0^{\infty}\int_0^{\infty}\int_0^{\infty} \mathrm{q_m} \times \mathrm{e}^{\left\{-\left[\mathrm{B(y+p)^2} + \left(\mathrm{Ax^2+Cz^2}\right)\times\left(\frac{1}{e^{-m(p-y)}}\right)\right]\right\}} \mathrm{dxdydz} \qquad \text{(xviii)}$$

$$= M + N(let)$$

$$Now, M = 4\int_0^{\infty}\int_0^{\infty}\int_0^{\infty} \mathrm{q_m} \times \mathrm{e}^{\left\{-\left[\mathrm{B(y\text{-}p)^2} + \left(\mathrm{Ax^2+Cz^2}\right)\times\left(\frac{1}{e^{m(y-p)}}\right)\right]\right\}} \mathrm{dxdydz} \qquad \text{(xix)}$$

$$= 4\int_0^\infty\int_0^\infty q_m . \mathrm{e}^{-\left[\mathrm{B(y\text{-}p)}^2+\left(\mathrm{Ax}^2\right)\times\left(e^{-m(y-p)}\right)\right]} . \frac{\pi}{2} . \frac{1}{\sqrt{Ce^{-m(y-p)}}} dxdy$$

$$\because \left[\int_0^\infty e^{-Ax^2} = \frac{\pi}{2} . \frac{1}{\sqrt{A}}\right]$$

$$= 4\int_0^\infty q_m . \mathrm{e}^{-\left[\mathrm{B(y\text{-}p)}^2\right]} . \frac{\pi}{2} . \frac{1}{\sqrt{Ce^{-m(y-p)}}} . \frac{\pi}{2} . \frac{1}{\sqrt{Ae^{-m(y-p)}}} dy$$

$$= \frac{\pi q_m}{\sqrt{AC}} \int_0^\infty \mathrm{e}^{-B(y-p)^2} . \frac{1}{e^{-m(y-p)}} dy$$

$$= \frac{\pi q_m}{\sqrt{AC}} \int_0^\infty \mathrm{e}^{m(y-p)} . \mathrm{e}^{-B(y-p)^2} dy$$

$$let, y - p = z$$
$$\therefore dy = dz$$

y	0	∞
z	-p	∞

$$\therefore M = \frac{\pi q_m}{\sqrt{AC}} \int_{-p}^\infty \mathrm{e}^{mz} . \mathrm{e}^{-Bz^2} dz = \frac{\pi q_m}{\sqrt{AC}} \int_{-p}^0 \mathrm{e}^{mz} . \mathrm{e}^{-Bz^2} dz + \frac{\pi q_m}{\sqrt{AC}} \int_0^\infty \mathrm{e}^{mz} . \mathrm{e}^{-Bz^2} dz] = R + S(let) \quad \text{(xx)}$$

Now,

$$R = \frac{\pi q_m}{\sqrt{AC}} \int_{-p}^0 \mathrm{e}^{mz} . \mathrm{e}^{-Bz^2} dz = \frac{\pi q_m e^{\frac{m^2}{4B}}}{\sqrt{AC}} \int_{-p}^0 \mathrm{e}^{-B(z-\frac{m}{2B})^2} dz \quad \text{(xxi)}$$

$$let, z = -y$$
$$\therefore dz = -dy$$

z	-p	0
y	p	0

$$\therefore R = \frac{\pi q_m \mathrm{e}^{\frac{m^2}{4B}}}{\sqrt{AC}} \int_p^0 \mathrm{e}^{-B(-y-\frac{m}{2B})^2} (-dy) = \frac{\pi q_m \mathrm{e}^{\frac{m^2}{4B}}}{\sqrt{AC}} \int_0^p \mathrm{e}^{-B(y+\frac{m}{2B})^2} dy \quad \text{(xxii)}$$

Applying Simpson's 1/3 rule,

$$R = \frac{\pi q_m e^{\frac{m^2}{4B}}}{\sqrt{AC}} \cdot \frac{p}{6}[e^{-\frac{m^2}{4B}} + 4e^{-B(\frac{p}{2}+\frac{m}{2B})^2} + e^{-B(p+\frac{m}{2B})^2}]$$

$$= \frac{\pi q_m e^{\frac{m^2}{4B}}}{\sqrt{AC}} \cdot \frac{p}{6}[e^{-\frac{m^2}{4B}} + 4e^{-\frac{B}{4}(p+\frac{m}{B})^2} + e^{-B(p+\frac{m}{2B})^2}] \quad \text{(xxiii)}$$

Now,

$$S = \frac{\pi q_m}{\sqrt{AC}} \int_0^\infty e^{mz} . e^{-Bz^2}\, dz$$

$$= \frac{\pi q_m e^{\frac{m^2}{4B}}}{\sqrt{AC}} \int_0^\infty e^{-B(z-\frac{m}{2B})^2}\, dz$$

$$= \frac{\pi q_m e^{\frac{m^2}{4B}}}{\sqrt{AC}} \cdot \frac{\sqrt{\pi}}{2} \cdot \frac{1}{\sqrt{B}}$$

$$\Rightarrow S = \frac{\pi\sqrt{\pi}.q_m e^{\frac{m^2}{4B}}}{2\sqrt{ABC}} \quad \text{(xxiv)}$$

Limit of integration

$$let,\ z - \frac{m}{2B} = x$$

$$\therefore dz = dx$$

z	0	∞
x	$-\frac{m}{2B}$	∞

$$\therefore M = R + S$$

$$= \frac{\pi q_m e^{\frac{m^2}{4B}}}{\sqrt{AC}} \cdot \frac{p}{6}[e^{-\frac{m^2}{4B}} + 4e^{-\frac{B}{4}(p+\frac{m}{B})^2} + e^{-B(p+\frac{m}{2B})^2}] + \frac{\pi\sqrt{\pi}.q_m e^{\frac{m^2}{4B}}}{2\sqrt{ABC}} = q_m.k(let) \quad \text{(xxv)}$$

where $k = \left[\frac{\pi e^{\frac{m^2}{4B}}}{\sqrt{AC}} \cdot \frac{p}{6}\left\{e^{-\frac{m^2}{4B}} + 4e^{-\frac{B}{4}(p+\frac{m}{B})^2} + e^{-B(p+\frac{m}{2B})^2}\right\} + \frac{\pi\sqrt{\pi}\, e^{\frac{m^2}{4B}}}{2\sqrt{ABC}}\right]$

Let us consider the distribution parameters for the rear part are A', B' & C' , therefore for N we can find

$$\therefore N = L + T$$

$$= \frac{-\pi p q_m e^{\frac{m^2}{4B'}}}{6\sqrt{A'C'}}[e^{-B'(p+\frac{m}{2B'})^2} + 4e^{-\frac{B'}{4}(p+\frac{m}{B'})^2} + e^{-B'(\frac{m}{2B'})^2}] + \frac{\pi\sqrt{\pi}.q_m e^{\frac{m^2}{4B'}}}{2\sqrt{A'B'C'}} = q_m.l(let) \quad \text{(xxvi)}$$

$$\text{where } l=\left[\frac{-\pi p\, e^{\frac{m^2}{4B}}}{6\sqrt{AC}}\left\{e^{-B(p+\frac{m}{2B})^2}+4e^{-\frac{B}{4}(p+\frac{m}{B})^2}+e^{-B(\frac{m}{2B})^2}\right\}+\frac{\pi\sqrt{\pi}\, e^{\frac{m^2}{4B}}}{2\sqrt{ABC}}\right]$$

To estimate A, B, C, the semi-axes of a proposed avocado shape a, b, c in the x, y, z axes directions respectively, are defined such that the heat density falls to $0.05q_m$ at the surface of proposed avocado shape. In x-direction;

$$q(a_0,0,0)=q_m\times e^{(-Aa^2)}=0.05\times q_m \qquad \text{(xxix)}$$

$$\Rightarrow e^{-Aa^2}=0.05$$

$$\therefore A\approx\frac{3}{a_0^{\,2}}$$

$$Similarly,\ B\approx\frac{3}{b_0^{\,2}}\ \ ;C\approx\frac{3}{c_0^{\,2}}$$

$$\text{Also, } A'\approx\frac{3}{a_0^{\,2}}\ \ ;B'\approx\frac{3}{(b-b_0)^2}\ \ ;C'\approx\frac{3}{c_0^{\,2}}$$

$$\therefore A=A';B\neq B';C=C'$$

The heat density distribution for the front and rear part are expressed as

$$q_f=q_m\, e^{-\frac{3(y-p)^2}{b_o^2}+(\frac{3x^2}{a_0^2}+\frac{3z^2}{c_0^2})e^{-m(y-p)}} \quad \text{and } q_r=q_m\, e^{-\frac{3(y-p)^2}{(b-b_o^2)}+(\frac{3x^2}{a_0^2}+\frac{3z^2}{c_0^2})e^{+m(y-p)}} \quad \text{respectively}$$

We found that *A=A', C=C'* but $B\neq B'$

$$\therefore 2Q=M+N$$

$$=q_m.k+q_m.l$$

$$=q_m.(\frac{\pi\, e^{\frac{m^2}{4B}}}{\sqrt{AC}}.\frac{p}{6}[e^{-\frac{m^2}{4B}}+4e^{-\frac{B}{4}(p+\frac{m}{B})^2}+e^{-B(p+\frac{m}{2B})^2}]+\frac{\pi\sqrt{\pi}\, e^{\frac{m^2}{4B}}}{2\sqrt{ABC}})+q_m.(\frac{-\pi p\, e^{\frac{m^2}{4B'}}}{6\sqrt{AC}}[e^{-B(p+\frac{m}{2B'})^2}+4e^{-\frac{B}{4}(p+\frac{m}{B'})^2}+e^{-B(\frac{m}{2B'})^2}]+\frac{\pi\sqrt{\pi}.e^{\frac{m^2}{4B'}}}{2\sqrt{AB'C}})$$

$$=q_m.w(let) \qquad \text{(xxvii)}$$

where

$$w=\left[\frac{\pi\,\mathrm{e}^{\frac{m^2}{4B}}}{\sqrt{AC}}.\frac{p}{6}\left\{\mathrm{e}^{-\frac{m^2}{4B}}+4\,\mathrm{e}^{-\frac{B}{4}(p+\frac{m}{B})^2}+\mathrm{e}^{-B(p+\frac{m}{2B})^2}\right\}+\frac{\pi\sqrt{\pi}\,\mathrm{e}^{\frac{m^2}{4B}}}{2\sqrt{ABC}}\right]+\left[\frac{-\pi\,p\,\mathrm{e}^{\frac{m^2}{4B'}}}{6\sqrt{AC}}\left\{\mathrm{e}^{-B(p+\frac{m}{2B'})^2}+4\,\mathrm{e}^{-\frac{B}{4}(p+\frac{m}{B'})^2}+\mathrm{e}^{-B(\frac{m}{2B'})^2}\right\}+\frac{\pi\sqrt{\pi}.\mathrm{e}^{\frac{m^2}{4B'}}}{2\sqrt{AB'C}}\right]$$

$$\therefore q_m=\frac{2Q}{w}=\frac{2Q}{\left(\frac{\pi\,\mathrm{e}^{\frac{m^2}{4B}}}{\sqrt{AC}}.\frac{p}{6}[\mathrm{e}^{-\frac{m^2}{4B}}+4\,\mathrm{e}^{-\frac{B}{4}(p+\frac{m}{B})^2}+\mathrm{e}^{-B(p+\frac{m}{2B})^2}]+\frac{\pi\sqrt{\pi}\,\mathrm{e}^{\frac{m^2}{4B}}}{2\sqrt{ABC}}\right)+\left(\frac{-\pi\,p\,\mathrm{e}^{\frac{m^2}{4B'}}}{6\sqrt{AC}}[\mathrm{e}^{-B'(p+\frac{m}{2B'})^2}+4\,\mathrm{e}^{-\frac{B'}{4}(p+\frac{m}{B'})^2}+\mathrm{e}^{-B'(\frac{m}{2B'})^2}]+\frac{\pi\sqrt{\pi}\,\mathrm{e}^{\frac{m^2}{4B'}}}{2\sqrt{AB'C}}\right)}$$

(xxviii)

Calculation of M_f and M_r

The heat density distribution inside the front part and rear part of the proposed avocado shape configuration can be expressed as:

$$2\int_0^\infty\int_0^\infty\int_0^\infty q_{f(x,y,z)}\,dxdydz=\frac{1}{2}M_f.Q \qquad \text{(xxx)}$$

$$\Rightarrow\frac{q_m.k}{2}=\frac{1}{2}M_f.Q$$

$$\therefore M_f=\frac{q_m.k}{Q} \qquad \text{(xxxi)}$$

Similarly for the rear part

$$2\int_0^\infty\int_0^\infty\int_0^\infty q_{r(x,y,z)}\,dxdydz=\frac{1}{2}M_r.Q \qquad \text{(xxxii)}$$

$$\Rightarrow\frac{q_m.l}{2}=\frac{1}{2}M_r.Q$$

$$\Rightarrow M_r=\frac{q_m.l}{Q} \qquad \text{(xxxiii)}$$

It is known that,

$$\mathrm{q}_{(x,y,z)}=\mathrm{q_m}\times\mathrm{e}^{\left\{-\left[\mathrm{By}^2+\left(\mathrm{Ax}^2+\mathrm{Cz}^2\right)\times t(y)\right]\right\}} \quad \text{where } t(y)=\frac{1}{e^{my}}$$

The heat density distribution inside the front part and rear part of the proposed avocado shape configuration can be expressed as:

$$2\int_0^{\infty}\int_0^{\infty}\int_0^{\infty} q_{(x,y,z)} dxdydz = \frac{1}{2} M_f .Q \qquad \text{(xxxiii)}$$

$$\Rightarrow 2\int_0^{\infty}\int_0^{\infty}\int_0^{\infty} \mathrm{q_m} \times \mathrm{e}^{\left\{-\left[\mathrm{B(y-p)^2} + \left(\mathrm{Ax^2+Cz^2}\right) \times \frac{1}{e^{m(y-p)}}\right]\right\}} dxdydz = \tfrac{1}{2} A_f .Q$$

$$\Rightarrow \frac{2Q}{\left(\frac{\pi\sqrt{\pi}\,\mathrm{e}^{\frac{m^2}{4B}}}{\sqrt{ABC}}\right)} \times 2 \times \int_0^{\infty}\int_0^{\infty}\int_0^{\infty} \mathrm{e}^{\left\{-\left[\mathrm{B(y-p)^2} + \left(\mathrm{Ax^2+Cz^2}\right) \times \frac{1}{e^{m(y-p)}}\right]\right\}} = \frac{1}{2} M_f .Q$$

$$\Rightarrow \frac{2Q}{\left(\frac{\pi\sqrt{\pi}\,\mathrm{e}^{\frac{m^2}{4B}}}{\sqrt{ABC}}\right)} \times 2 \times \frac{1}{4}\left(\frac{\pi\,\mathrm{e}^{\frac{m^2}{4B}}}{2\sqrt{AC}} . \frac{p}{6}[\mathrm{e}^{-\frac{m^2}{4B}} + 4\mathrm{e}^{-\frac{B}{4}(p+\frac{m}{B})^2} + \mathrm{e}^{-B(p+\frac{m}{2B})^2}] + \frac{\pi\sqrt{\pi}.\mathrm{e}^{\frac{m^2}{4B}}}{2\sqrt{ABC}}\right) = \frac{1}{2} M_f .Q$$

$$\Rightarrow M_f = \frac{4}{\left(\frac{\pi\sqrt{\pi}\,\mathrm{e}^{\frac{m^2}{4B}}}{\sqrt{ABC}}\right)} \times 2 \times \frac{1}{4}\left(\frac{\pi\,\mathrm{e}^{\frac{m^2}{4B}}}{2\sqrt{AC}} . \frac{p}{6}[\mathrm{e}^{-\frac{m^2}{4B}} + 4\mathrm{e}^{-\frac{B}{4}(p+\frac{m}{B})^2} + \mathrm{e}^{-B(p+\frac{m}{2B})^2}] + \frac{\pi\sqrt{\pi}.\mathrm{e}^{\frac{m^2}{4B}}}{2\sqrt{ABC}}\right)$$

$$\therefore M_f = \frac{2}{\left(\frac{\pi\sqrt{\pi}\,\mathrm{e}^{\frac{m^2}{4B}}}{\sqrt{ABC}}\right)} \times \left(\frac{\pi\,\mathrm{e}^{\frac{m^2}{4B}}}{2\sqrt{AC}} . \frac{p}{6}[\mathrm{e}^{-\frac{m^2}{4B}} + 4\mathrm{e}^{-\frac{B}{4}(p+\frac{m}{B})^2} + \mathrm{e}^{-B(p+\frac{m}{2B})^2}] + \frac{\pi\sqrt{\pi}.\mathrm{e}^{\frac{m^2}{4B}}}{2\sqrt{ABC}}\right) \qquad \text{(xxxiv)}$$

Similarly for the rear part considering $A=A'$, $C=C'$ but $B \neq B'$

$$M_r = \frac{2}{\left(\frac{\pi\sqrt{\pi}\,\mathrm{e}^{\frac{m^2}{4B'}}}{\sqrt{AB'C}}\right)} \times \left(\frac{-\pi p q_m\,\mathrm{e}^{\frac{m^2}{4B'}}}{6\sqrt{AC}}[\mathrm{e}^{-B(p+\frac{m}{2B'})^2} + 4\mathrm{e}^{-\frac{B}{4}(p+\frac{m}{B'})^2} + \mathrm{e}^{-B(\frac{m}{2B'})^2}] + \frac{\pi\sqrt{\pi}.q_m\,\mathrm{e}^{\frac{m^2}{4B'}}}{2\sqrt{AB'C}}\right)$$

$$\therefore M_f + M_r = \frac{q_m.k}{Q} + \frac{q_m.l}{Q} = \frac{q_m}{Q}(k+l) = \frac{2Q}{Q.w}(k+l) = 2 \qquad \text{(xxxiv)}$$

References

1. Yapp, D., (2007), “Management of weld quality”, Lecture Notes on Topic MAN1.5, Welding Engineering Research Centre, Cranfield University, Bedford, UK.
2. Qureshi, M. E., (2008), “Analysis of residual stresses and distortions in circumferentially welded thin-walled cylinders”, Doctoral dissertation, Mechanical Engineering, College of Electrical and Mechanical Engineering, National University of Sciences and Technology, Rawalpindi, Pakistan.
3. Blodgett, O.W., (1984), “Distortion: how to minimize it with sound design practices and controlled welding procedures plus proven methods for straightening distorted members”, The Lincoln Electric Company, Cleveland, Ohio, pp. 1-19.
4. Hibbitt H. D. and Marcal, P.V., (1973) “A numerical thermo-mechanical model for the welding and subsequent loading of a fabricated structure”, Journal of Computers and Structures, vol. 3, pp. 1153-1174.
5. Feng Z. and Ridge O., (2005), “Processes and mechanisms of welding residual stress and distortion”, Woodhead Publishing Limited, Cambridge, UK.
6. Standard Welding Terms and Definitions, 12th Edition, (2009), American Welding Society.
7. Datta, S., Bandyopadhyay, A. and Pal, P. K., (2008), Solving multi-criteria optimization problem in submerged arc welding consuming a mixture of fresh flux and fused slag, The International Journal of Advanced Manufacturing Technology, vol. 35 (9), pp. 935-942.
8. ANSYS, Theory reference for the mechanical APDL and mechanical applications, Release 15.0, Ed. Kohnke, P., ANSYS Inc., Southpointe, Canonsburg, Pennsylvania.
9. Cary, H B, “Submerged arc welding”, (1986), Pergamon Press, Encyclopedia of Materials Science and Engineering. vol. 6, pp. 4721-4722.
10. Xiuzhi, Y., Qinghua, X., Niandong, Y. and Xinhua, X., (2011), “Twin-wire submerged arc welding process of a high-strength low-alloy steel”, Journal of Wuhan University of Technology-Mater. Sci. Ed., vol. 26 (1), pp. 114-117.
11. Gulenc, B. and Kahraman, N., (2003), “Wear behaviour of bulldozer rollers welded using a submerged arc welding process”, Materials and Design, vol. 24, pp. 537-542.
12. Ramakrishnan M. and Muthupandi V., (2013), “Application of submerged arc welding technology with cold wire addition for drum shell long seam butt welds of pressure vessel components”, International Journal of Advanced Manufacturing Technology, Springer-Verlag, vol. 65, pp. 945-956.

13. Deng D., Luo Y., Serizawa H., Sibahara M. and Murakawa H., (2003), "Numerical simulation of residual stress and deformation considering phase transformation effect", Transactions of the Japan Welding Research Institutetute, vol. 32 (2), pp. 325-333.
14. Withers, P. J. and Bhadeshia, H. K. D. H., (2001), "Residual stress Part 1-Measurement techniques", Materials Science and Technology, vol. 17, pp. 355-365.
15. Withers, P. J. and Bhadeshia, H. K. D. H. (2001). "Residual stress Part 2- Nature and origins", Materials Science and Technology, vol. 17, pp. 366-375.
16. Asim, K., Lee, J. and Pan, J., (2011), "Failure mode of laser welds in lap-shear specimens of high strength low alloy (HSLA) steel sheets", Fatigue and Fracture of Engineering Materials and Structures, vol. 35, pp. 219-236.
17. Kong, F. and Kovacevic, R., (2012), "Development of a comprehensive process model for hybrid laser-arc welding", "Welding Processes", Edited by Radovan, K., Intech, New York, pp.165-190.
18. Lucas, B., Verhaeghe, G. and Leggatt, R., "Distortion-Types and causes", http://www.twi-global.com/technical-knowledge/job-knowledge/distortion-types-and-causes-033/, ac on 15-10-2014.
19. Arai, Y., Kikuchi, M., Watanabe, T. and Nakagaki, M., (1995), "Residual stress due to welding and its effect on the assessment of cracks near the weld interface", International Journal of Pressure Vessels and Piping, vol. 63(3), pp. 237-248.
20. Weisman, C. (1976), "Welding Handbook: Fundamentals of welding", American Welding Society, Seventh Ed., vol. 1.
21. Pilipenko, A., (2001), "Computer simulation of residual stress and distortion of thick plates in multi electrode submerged arc welding: Their mitigation techniques" Doctoral thesis, Norwegian University of Science and Technology, Trondheim, Norway.
22. Ivetic, G., Lanciotti, A., Polese, C., (2008), "Electric strain gauge measurement of residual stress in welded panels", Journal of Strain Analysis, vol. 44, pp.117-126.
23. Bhatti A. A., (2015) "Computational weld mechanics: Towards simplified and cost effective FE simulations", Ph.D. Thesis, KTH Department of Aeronautical and Vehicle Engineering, Stockholm, Sweden.
24. Fourier, J. B. J., (1822), "Théorie analytique de la chaleur", Firmin Didot, Paris.
25. Rosenthal, D., (1946), "The theory of moving sources of heat and its application to metal treatments", Trans. ASME, vol. 43 (11), pp. 849-865.
26. Eager, T. W. and Tsai, N. S., (1983), "Temperature fields produced by travelling distributed heat sources", Weld. J. vol. 62 (12) pp. 346-355.

27. Rybicki, E. F., Schmueser, D. W., Stonesifer, R. W., Groom, J. J., and Mishler, H.W., (1978), "A finite element model for residual stresses and deflections in girth butt welded pipes", Journal of Pressure Vessel Technology, vol. 100, pp. 256-262.
28. Debiccari, A., (1986), "Control of distortion and residual stresses in girth welded pipes", Ph.D. Thesis, Massachusetts Institute of Technology, USA.
29. Seo, S. I., Yang, Y. H. and Jang C. D., (2001), "Development of new finite element method to analyze deformation of plate due to line heating", Journal of Ship Production, vol. 17, pp.1-7.
30. Friedman, E., (1975), "Thermomechanical analysis of the welding process using the finite element method", Trans. A.S.M.E. Journal of Pressure Vessel Technology, vol. 973(3), pp. 206-213.
31. Bai-Qiao Chen, (2011), "Prediction of heating induced temperature fields and distortions in steel plates", Dissertation of Master in Naval Architecture and Marine Engineering, Instituto Superior Técnico, Universidade Técnica de Lisboa ,Portugal.
32. Goldak, J,, Chakravarti, A. and Bibby, M., (1984), "A new finite element model for heat sources", Metallurgical Transactions B, vol. 15 B, pp. 299-305.
33. Goldak, J,, Bibby, M, Moore, J., House, R. and Patel, B., (1986), "Computer modeling of heat flow in welds", Metallurgical Transactions B, vol. 17 B, pp. 587-600.
34. Michaleris, P. and DeBiccari, A., (1997), "Prediction of welding distortion", Research Supplement, vol. 76, pp. 172-181.
35. Wahab, M. A., Painter, M. J. and Davies, M. H., (1998), "The prediction of the temperature distribution and weld pool geometry in the gas metal arc welding process", The Journal of Materials Processing Technology, VOL. 77, PP.233-239.
36. Gery, D., Long, H. and Maropoulos, P., (2005), "Effects of welding speed, energy input and heat source distribution on temperature variations in butt joint welding", Journal of Materials Processing Technology, vol.167, pp. 393-401.
37. Sabapathy, P. N., Wahab, M. A. and Painter, M. J., (2001), "Numerical Models of in service welding of gas pipeline", Journal of Materials Processing Technology, vol. 118, pp. 14-21.
38. Ravichandran, G., Raghupathy, V. P. and Ganesan, N., (1996), "Analysis of temperature distribution during circumferential welding of cylindrical and spherical components using the finite element method", Journal of Computer and Structures, vol. 59 (2), pp. 225-255.

39. Ueda, Y., and Yamakawa, T., (1971) "Analysis of thermal-elastic stress and strain during welding by finite element method", Japan Welding Research Institute (JWRI) of Osaka University, vol. 2 (2), pp. 90-100.
40. Radaj, D., "Heat effects of welding: Temperature field residual stress distortion", Springer-Verlag, 1992.
41. Andersson, B. A. B., (1978), "Thermal stresses in submerged arc welded joint considering phase transformations", ASME Journal of Engineering Material and Technology, vol. 100, pp. 356-362.
42. Zhang, W., Roy, G. G., Elmer, J. W. and DebRoy, T., (2003), "Modeling of heat transfer and fluid flow during gas tungsten arc spot welding of low carbon steel", Journal of Applied Physics, vol. 93(5), , pp. 3022-3033.
43. Rai, R., Roy, G. G. and DebRoy, T., (2007), "A computationally efficient model of convective heat transfer and solidification characteristics during keyhole mode laser welding", Journal of Applied Physics, vol. 101, pp. 054909-1 to 054909-11.
44. Wang, Y., Fu, P., Guan, Y., Lu, Z. and Wei, Y., (2013), "Research on modeling of heat source for electron beam welding fusion-solidification zone", Chinese Journal of Aeronautics, vol. 26 (1), pp. 217-223.
45. He1, X., Fuerschbach, P. W. and DebRoy, T., (2003), "Heat transfer and fluid flow during laser spot welding of 304 stainless steel", Journal of Physics D: Applied Physics, vol. 36, pp. 1388-1398.
46. Bag, S. and De, A., (2008), "Development of a three-dimensional heat-transfer model for the gas tungsten arc welding process using the finite element method coupled with a genetic algorithm-based identification of uncertain input parameters", Metallurgical and Materials Transactions A, vol. 39A, pp. 2698-2710.
47. Bag, S., Trivedi, A. and De, A., (2009), "Development of a finite element based heat transfer model for conduction mode laser spot welding process using an adaptive volumetric heat source", International Journal of Thermal Sciences, vol. 48, pp.1923-1931).
48. Trivedi, A, Bag, S. and De, A., (2007), "Three-dimensional transient heat conduction and thermomechanical analysis for laser spot welding using adaptive heat source", Science and Technology of Welding and Joining, vol. 12(1), pp. 24-31.
49. Bag, S. and De, A., (2010), "Computational modelling of conduction mode laser welding process", Edited by Xiaodong Na in Laser Welding, ch. 6, pp. 133-160,

50. Perez, T. E., Radovltzky, R. A., and Ovorkln, E. N., (1993), “On a thermal model for saw multipass butt weldments”, Proceedings Third International Conference on Trends in Welding Research, Gatlinburg, Tennessee, June 1992, (Ed. David, S. A. and Vitek, J. M.), ASM International,. pp. 69-73.
51. Ghosh, A. and Chattopadhyaya, S., (2011) “Transient heat conduction of submerged arc welded plates”, Journal on Manufacturing and Industrial Engineering’, Technical University in Košice, Faculty of Manufacturing Technologies, vol. 4, pp. 10-12.
52. Nguyen, N. T., Ohta, A., Suzuki, N., Maeda, Y., (1999), “Analytical solutions for transient temperature of semi-infinite body subjected to 3-d moving heat source, Welding Journal, vol. 78, pp. 265-s - 274-s.
53. Ghosh, A., Chattopadhyaya, S., (2011), Prediction of weld bead penetration, transient temperature distribution and HAZ width of submerged arc welded structural steel plates. Defect Diffusion Forum, vols. 316-317, pp. 135-152.
54. Ghosh, A., Chattopadhyaya, S., (2010), Analytical solution for transient temperature distribution of semi-infinite body subjected to 3-D moving heat source of submerged arc welding process, International Conference on Mechanical and Electrical Technology, Singapore.
55. Yadaiah, N., and Bag, S., (2012), Effect of heat source parameters in thermal and mechanical analysis of linear GTA welding process, Journal of the Iron and Steel Institute of Japan, vol. 52(11), pp. 2069-2075.
56. Wu, C. S., Hu, Q. X., and Gao, J. Q., (2009), An adaptive heat source model for finite-element analysis of keyhole plasma arc welding, Computational Materials Science, vol. 46 pp. 167-172.
57. Luo, Y., You, G., Ye, H., and Liu, J., (2010), Simulation on welding thermal effect of AZ61 magnesium alloy based on three-dimensional modeling of vacuum electron beam welding heat source, Vacuum, vol. 84, pp. 890-895.
58. Li, P., and H. Lu., (2012), Hybrid heat source model designing and parameter prediction on tandem submerged arc welding, The International Journal of Advanced Manufacturing Technology, vol. 62, pp. 577-585.
59. Li, Y., Feng, Y. H., Zhang, X. X., Wu, C. S., (2013), An improved simulation of heat transfer and fluid flow in plasma arc welding with modified heat source model, International Journal of Thermal Sciences, vol. 64 pp. 93-104.
60. Amin, S. A., Sigmund, K., Akselsen, O. M., (2012), Determination of welding heat source parameters from actual bead shape, Computational Materials Science, vol. 54 pp. 176-182.

61. Podder, D., Mandal, N. R. and Das, S., (2014), Heat Source Modelling and Analysis of Submerged Arc Welding, Welding Journal, vol. 93 pp. 183-192.
62. Yadaiah N. and Bag, S., (2014), Development of egg-configuration heat source model in numerical simulation of autogenous fusion welding process, International Journal of Thermal Sciences, vol. 86, pp. 125-138.
63. Lindgren, L. E., (2001), "Finite element modelling and simulation of welding part 1: Increased complexity", Journal of Thermal Stresses, vol. 24, pp. 141-192.
64. Lindgren, L. E., (2001), "Finite element modelling and simulation of welding part 2: Improved material modelling", Journal of Thermal Stresses, vol. 24, pp. 195-231.
65. Lindgren, L. E., (2001), "Finite element modelling and simulation of welding part 3: Efficiency and integration", Journal of Thermal Stresses, vol. 24, pp. 305-334.
66. Watanabe, M., and Satoh, K., (1961), "Effect of welding conditions on the shrinkage and distortion in welded structures," Welding Journal, vol. 40 (8), pp. 377-384.
67. Luo, Y., (1997), "Description of inherent strain and its application to prediction of welding deformation and residual stress under multi-pass welding" Doctoral Thesis, Osaka University.
68. Hong, J. K., Tsai, C. L. and Dong, P., (1998), "Assessment of numerical procedures for residual stress analysis of multipass weld", Welding Journal, pp. 372s-382s.
69. Dong, P., (2001), "Residual stress analyses of a multi-pass girth weld: 3-D special shell versus axisymmetric models", Journal of Pressure Vessels Technology, vol. 123, pp. 207-213.
70. Lindgren, L. E., (2006), "Numerical modeling of welding", Computer methods in applied mechanical and engineering, vol. 195, pp. 6710-6736.
71. Tekriwal, P. and Mazumdar, J., (1988), "Finite element analysis of three dimensional heat transfer in gas manual arc welding," Welding Research Supplement, Welding Journal, pp. 150-156.
72. Bonifaz, E., (2000), "Finite element analysis of heat flow in single-pass arc welds," Welding Research Supplements, 121-125.
73. Brown, S. and Song, H., (1992), "Implication of three-dimensional numerical simulation of welding of large structures," Welding Journal, pp. 55-62.
74. Murugan, S., Kumar, P. V., Raj, B. and Bose, M. S. C., (1998), "Temperature distribution during multipass welding of plates, International Journal of Pressure Vessels and Piping, vol. 75, pp. 891-905.

75. Murugan, S., Rai, S. Kumar, K., Jayakumar, P. V., Raj, T., and Bose, M.S.C., (2001), “Temperature distribution and residual stresses due to multipass welding in type 304 stainless steel and low carbon steel weld pads”, International Journal of Pressure Vessels and Piping, vol. 78, pp. 307-317.
76. Malik, A. M., Qureshi, M. E., and Dar, N. E., (2007), Numerical simulation of arc welding investigation of various process and heat source parameters”, Failure of Engineering Materials and Structures, UET Taxila Mechnical Engineering Department, pp.127-142.
77. Englund, R., Sweeney, S., and Johnson, D. (2005), “A demonstration of heat affected zone from welding”. Proceedings of the 2005 American Society for Engineering Education Annual Conference and Exposition.
78. Mandal, N., and Sundar, C., (1997), “Analysis of welding shrinkage,” Welding Research Supplement, Welding Journal, pp. 233-238.
79. Puchaicela, J., (1998), “Control of distortion of welded steel structures,” Welding Journal, pp. 49-52.
80. Tsai, C. L., Park, S. C. and Cheng, W. T., (1999), “Welding distortion of a thin-plate panel structure”, Welding Journal, vol. 78, pp. 156s -165s.
81. Tsai, C., Park, S., and Cheng, W., (2001), “design analysis for welding of heavy W-shapes,” Welding Research Supplement, Welding Journal, pp. 35-41.
82. Jang, G., Kim, H., and Kam, S., (2001), “The effect of root opening on mechanical properties, Deformation and Residual Stress of weldments,” Welding Research Supplement, Welding Journal, pp. 80-89.
83. Mahapatra, M. M., Datta, G. L., Pradhan, B., and Mandal, N. R., (2006), “Three-dimensional finite element analysis to predict the effects of SAW process parameters on temperature distribution and angular distortions in single-pass butt joints with top and bottom reinforcements,” International Journal of Pressure Vessels and Piping, vol. 83, pp. 721-729.
84. Teng, T. L., Fung, C. P., Chang, P. H., and Yang, W. C. (2001), Analysis of residual stresses and distortions in T-joint fillet welds. International Journal of Pressure Vessels and Piping, vol. 78, pp.523-538.
85. Tsai, C. L., and Jung, G. H. (2004), Plasticity-based distortion analysis for fillet welded thin- plate T-joints, Welding Journal, vol. 83, pp. 177s-187s.
86. Mahapatra, M. M., Datta, G. L., Pradhan, B., and Mandal, N. R., (2007), Modelling the effects of constraints and single axis welding process parameters on angular distortions in

one-sided fillet welds, Proceedings of the Institution of Mechanical Engineers, Part B: Journal of Engineering Manufacture, vol. 221 (B3), pp. 397-407.

87. Mahapatra, M. M., Datta, G. L., Pradhan, B. and Mandal, N. R. (2007), “Modelling of angular distortion of double-pass butt-welded plate”, Proceedings of the Institution of Mechanical Engineers, Part B, Journal of Engineering Manufacture, vol. 222, pp. 391-402.
88. Biswas, P., Kumar, D. A., Mandal, N. R., and Mahapatra, M. M., (2011), “A study on the effect of welding sequence in fabrication of large stiffened plate panels”, Journal of Marine Science and Application, vol. 10, pp. 429-436.
89. Souloumiac, B., Boitout, F., and Bergheau, J. M., (2002), A new local global approach for the modelling of welded steel component distortions’, London, Maney Publishing.
90. Ueda, Y., Kim, Y. C., and Umekuni, A., (1985), “Measuring theory of three-dimensional residual stresses using a thinly sliced plate perpendicular to welded line,” Transactions of Joining and Welding Research Institute Osaka University, vol. 14 (2), pp. 151-157.
91. Murakawa, H., Luo, Y., and Ueda, Y., (1997), “Prediction of welding deformation and residual stress by elastic FEM based on inherent strain (in Japanese),” Journal of the Society of Naval architects of Japan, vol. 180, pp. 739-751.
92. Jang, C. D., Lee, C. H., and Ko, D. E., (2002), “Prediction of welding deformations of stiffened panels,” Proceedings of the Institution of Mechanical Engineers, Part M, Journal of Engineering for the Maritime Environment, vol. 216 (2), pp. 133-143.
93. Ha, Y. S., (2008), “Development of thermal distortion analysis method on large shell structure using inherent strain as boundary condition (in Korean),” Journal of the Society of Naval Architects of Korea, vol. 45 (1), pp. 93-100.
94. Ha, Y. S., Cho, S.H., and Jang, T. W., (2008), “Development of welding distortion analysis method using residual strain as boundary condition,” Materials Science Forum, vols. 580-582, pp. 649-654.
95. Zienkiewicz, O. C., (2001), “The finite element method”, 3rd ed., Tata McGraw-Hill Pub. Co. Ltd., New Delhi.
96. Reddy, J. N., (2003), “An introduction to the finite element methods”, Second edition", Tata McGraw-Hill Pub. Co. Ltd., New Delhi.
97. Chandrupatla, T. R. and Belegundu, A. D., (2002), “Introduction to finite element in engineering”, Prentice-Hall of India Private Ltd., New Delhi.
98. Valentin, R. T., Sérgio, M. O. T., Pedro, M. G. P. M., Miguel A. V. de F., Paulo M. S. T. de C., (2008), “Residual stress measurement using the contour and the sectioning methods

in a MIG weld : effects on the stress intensity factor”, Ciência e Tecnologia dos Materiais, vol. 20, pp. 114-119.

99. Roy, A. K., Venkatesh, A., Marthandam, V., Dronavalli, S. B., Wells, D., and Rogge, R, (2005), Residual stress characterization in structural materials by destructive and nondestructive techniques, Journal of Materials Engineering and Performance, vol. 14, pp. 203-211.

100. Sariel, J., Dahan, I., Reuven, R., Szanto, M., and Stern, A., (2006), “Residual stress distributions in GTA spot welded Ti6Al4V disks”, JCPDS-International Centre for Diffraction Data, pp. 195-200.

101. Allen, A. J., Hutchings, M. T., Windsor, C. G. and Andreani, C., (1985), “Neutron diffraction methods for the study of residual stress fields”, Advances in Physics, vol. 34 (4), pp. 445-443.

102. Smith, D. J., Bouchard, P. J. and George, D., (2000), “Measurement and prediction of residual stresses in thick-section steel welds”, Journal of Strain Analysis for Engineering Design, vol. 35 (4), pp. 287-305.

103. Bouchard, P. J., George, D., Santisteban, J. R., Bruno, G., and Dutta, M., (2005), Measurement of the residual stresses in a stainless steel pipe girth weld containing long and short repairs, International Journal of Pressure Vessels and Piping, vol. 82, pp. 299-310.

104. Suzuki, T., (2011), “Residual stress measurement of welding area by neutron diffraction method”, Nippon Steel Technical Report, no. 100, pp. 47-50.

105. Ripley, M. I., (2006), “Residual stress measurement using neutrons”, Materials and Testing Conference, 2005, Materials Forum, vol. 30, pp. 219-224.

106. Colegrove, P., Ikeagu, C., Thistlethwaite, A., Williams, S., Suder, W., Steuwer, A., and Pirling, T., (2009), “The welding process impact on residual stress and distortion”, Science and Technology of Welding and Joining, vol. 14 (8), pp. 717-725.

107. Bray, D. E., Kim, S. J. and Fernandes, M., (1999), “Ultra-sonic evaluation of residual stresses in rolled aluminum plate”, Proceedings of the Ninth International Symposium on Nondestructive characterization of materials, Robert E. Green, Ed., Sydney, Australia,. American Institute of Physics, Melville, New York, vol. 497, pp. 443-448.

108. Uzun, F., and Bilge, A. N., (2011), “Investigation of total welding residual stress by using ultrasonic wave velocity variations”, Gazi University Journal of Science (GU J Sci), vol. 24 (1), pp. 135-141.

109. Cho, J. R., Lee, B. Y., Moon, Y. H., and Tyne, C. J. Van., (2004), "Investigation of residual stress and post weld heat treatment of multi-pass welds by finite element method and experiments", Journal of Materials Processing Technology, vol. 155-156, pp.1690-1695.
110. ASTM E 837-01, "Standard test method for deter-mining residual stresses by the hole drilling strain-gauge method", (2001), American Society for Testing and Materials, West Conshohocker, Philadelphia.
111. Leggatt, R. H., Smith, D. J., Smith, S. D. and Faure, F., (1996), "Development and experimental validation of the deep hole method for residual stress measurement", Journal of Strain Analysis for Engineering Design, vol. 31, pp.177-186.
112. Smith, D. J. and Bonner, N. W., (1994), "Measurement of residual stresses in a thick section steel welds", Engineering Integrity Assessment (Eds. J.H. Edwards, J. Kerr and P. Stanley), Engineering Materials Advisory Services, Chameleon Press, Birmingham, pp. 259-274.
113. Bonner, N. W. and Smith, D. J., (1996), "Measurement of residual stresses using the deep hole method", Residual Stresses in Design, Fabrication, Assessment and Repair, American Society of Mechanical Engineers, New York, vol. 327, pp. 53-65.
114. Bonner, N. W., (1996), "Measurement of residual stresses in thick section steel welds", PhD thesis, University of Bristol.
115. Ueda, Y., Fukuda, K. and Endo, S., (1989), "New measuring method of three-dimensional residual stresses in long welded joints using inherent strains as parameters-Lz method", Transaction of ASME, Journal of Engineering Materials and Technology, vol. 11, pp.1-8.
116. Leggatt, R. H., (1986), "Residual stresses and distortion in multi- pass butt welded joints in type 316 stainless steel", Proceedings of the International Conference on Residual Stresses, Garmisch-Partenkirchen, Germany, vol. 1, pp. 997-1004.
117. Faure, F. and Leggatt, R. H., (1996), "Residual stresses in austenitic stainless steel primary coolant pipes and welds of pressurised water reactors", International Journal of Pressure Vessels and Piping, vol. 65, pp. 265-275.
118. Smith, D. J. and Garwood, S. J., (1992), "Influence of post weld heat treatment on the variation of residual stresses in 50 mm thick welded ferritic steel plates". International Journal of Pressure Vessels and Piping, vol. 51, pp. 241-256.
119. Hodgson, D. Z. L., Smith, D. J. and Shterenlikht, A., (2009), "Residual stress measurement in steel beams using the incremental slitting technique", Advances in X-ray Analysis, JCPDS-International Centre for Diffraction Data, vol. 52, pp. 659-666.

120.Hosseinzadeh, F. and Bouchard, P., (2011), "Application of the contour method to validate residual stress predictions" Second International Conference on Advances in Nuclear Materials (ANM-2011), Mumbai, India.

121.Adak, M. and Mandal, N. R., 2010, "Numerical and experimental study of mitigation of welding distortion", Applied Mathematical Modelling, vol. 34, pp. 146-158.

122.Deng, D., Liang, W. and Murakawa, H., (2007), "Determination of welding deformation in fillet-welded joint by means of numerical simulation and comparison with experimental measurements", Journal of Materials Processing Technology, vol. 183, pp. 219-225.

123.Park, J. U., Lee, H. W. and Bang, H. S., (2002), "Effects of mechanical constraints on angular distortion of welding joints", Science and Technology of Welding and Joining, vol. 7:4, pp. 232-239.

124.Deng, D., and Murakawa, H., (2008), "Prediction of welding distortion and residual stress in a thin plate butt-welded joint", Computational Materials Science, vol. 43, pp. 353-365.

125.Camilleri, D., Comlekci, T., and Gray, T. G. F., "Computational prediction of out-of-plane welding distortion and experimental investigation", Journal of Strain Analysis, vol. 40 (2), pp. 161-176.

126.Tong, X. C., (2011), Advanced materials for thermal management of electronic packaging, Springer.

127.Biswas, P. and Mandal N. R., (2010), "Thermomechanical finite element analysis and experimental investigation of single-pass single-sided submerged arc welding of C-Mn steel plates", Proceedings of Institute of Mechanical Engineers, Part B: Journal of Engineering Manufacture, vol. 224, pp. 627-639.

128.Biswas, P., Mahapatra, M. M. and Mandal, N. R., (2009), "Numerical and experimental study on prediction of thermal history and residual deformation of double-sided fillet welding", Proceedings of the Institution of Mechanical Engineers, Part B, Journal of Engineering Manufacture, vol. 224, pp. 125-134.

129.Biswas, P., Mandal, N. R. and Sha, O. M., (2010), "Numerical and Dimensional Analysis for Prediction of Line Heating Residual Deformations", Journal of Marine Science and Application, vol. 9, pp. 14-21.

130.Satheesh, M. and Dhas, J. E. R., (2014), Multi objective optimization of weld parameters of boiler steel using fuzzy based desirability function, Journal of Engineering Science and Technology Review, vol. 7 (1), pp, 29-36.

131. Matsuoka, S., Okamoto, Y. and Okada, A., (2013), "Influence of weld bead geometry on thermal deformation in laser micro-welding", The Seventeenth CIRP Conference on Electro Physical and Chemical Machining (ISEM), Procedia CIRP, vol. 6, pp. 492- 497.

132. Kim, M., Kang. M. and Chung, H., (2015), Simplified welding distortion analysis for fillet welding using composite shell elements, "International Journal of Naval Architecture and Ocean Engineering, vol. 7, pp. 452-465.

133. Taban, E., Deleu, E., Dhooge, A. and Kaluc, E., (2008), Submerged arc welding of thick ferritic martensitic 12Cr stainless steel with a variety of consumables, Science and Technology of Welding and Joining, vol. 13 (4), pp. 327-334.

134. Zhang, X. P. and Dorn, L., (1999), "Investigation on the possibility of using the microshear test as a surveillance method to estimate the mechanical properties and fracture toughness of nuclear pressure vessel steel, A508CL3, and its joints welded by narrow-gap submerged-arc welding", International Journal of Pressure Vessels and Piping, vol. 76, pp. 35-41.

135. Shi, Y. W., Han, Z. X. and Zhou, N. N., (1996), "Estimates of local tensile strength of welded joints, International Journal of Pressure Vessels and Piping, vol. 65, pp. 41-45.

136. Luo, J., Yuan, Y., Wang, X. and Yao, Z., (2013), "Double-Sided Single-Pass Submerged Arc Welding for 2205 Duplex Stainless Steel", Journal of Materials Engineering and Performance, vol. 22 (9), pp. 2477-2486.

137. Ramakrishnan, M., Padmanaban, K. and Muthupandi, V., (2013), "Studies on fracture toughness of cold wire addition in narrow groove submerged arc welding process", International Journal of Advanced Manufacturing Technology, vol. 68, pp. 293-316.

138. Kolhe, K. P. and Datta, C. K., (2007), "Prediction of microstructure and mechanical properties of multipass SAW", Journal of Materials Processing Technology, vol. 197, pp. 241-249.

139. Lu, S., Kwon, O., Kim, T., and Kim, K., (2004), "Microstructure and wear property of Fe-Mn-Cr-Mo-V alloy cladding by submerged arc welding", Journal of Materials Processing Technology, vol. 147, pp. 191-196.

140. Prasad, K., and Dwivedi, D. K., (2008), Some investigations on microstructure and mechanical properties of submerged arc welded HSLA steel joints, International Journal of Advanced Manufacturing Technology, vol. 36, pp. 475-483.

141. Paniagua-mercado, A. M., Lopez-hirata, V. M., and Dorantes-rosales, H. J., (2008), "Effect of TiO_2-containing fluxes on the mechanical properties and microstructure in submerged-arc weld steels", Materials Characterization, vol. 60 (1), pp. 36-39.

142.Lan, L., Qiu, C., Zhao, D., Gao, X., and Du, L., (2012), "Analysis of microstructural variation and mechanical behaviors in submerged arc welded joint of high strength low carbon bainitic steel", Materials Science and Engineering A, vol. 558, pp. 592-601.

143.DuPont, J. N., (2005), "Influence of surface active flux on the microstructure and properties of SASS welds", Naval Surface Warfare Center, Carderock Division Lehigh University, Bethlehem, PA, www.lehigh.edu/~inemg/Framset/Research_Activities/JLP/SASS/SASS_7.htm, as on 28-12-2012.

144.Tseng, K. H., Chuang, K. J., (2012), "Application of iron-based powders in tungsten inert gas welding for 17Cr-10Ni-2Mo alloys", Powder Technology, vol. 228, pp. 36-46.

145.Tseng, K. H., (2013), "Development and application of oxide-based flux powder for tungsten inert gas welding of austenitic stainless steels", Powder Technology, vol. 233, pp. 72-79.

146.Huang, H. Y., (2009), "Effects of shielding gas composition and activating flux on GTAW weldments", Materials and Design, vol. 30, pp. 2404-2409.

147.Huang, H. Y., (2010), "Effects of activating flux on the welded joint characteristics in gas metal arc welding", Materials and Design, vol. 31, pp. 2488-2495.

148.Modenesi, P. J., ApolinaÂrio, E. R., and Pereira, I. M., (2000), "TIG welding with single-component fluxes", Journal of Materials Processing Technology, vol. 99, pp. 260-265.

149.Li, Q., Wang, X., Zou, Z. and Wu, J., (2007), "Effect of activating flux on arc shape and arc voltage in tungsten inert gas welding", The Transactions of Nonferrous Metals Society of China, vol. 17 (3), pp. 486-490.

150.Liu, L. M., Caiand D. H. and Zhang, Z. D., (2007), "Gas tungsten arc welding of magnesium alloy using activated flux-coated wire", Scripta Materialia, vol. 57, pp. 695-698.

151.Lowke, J. J., Tanaka, M., Ushio, M. and Lowke, J. J., (2005), "Mechanisms giving increased weld depth due to a flux", Journal of Physics D: Applied Physics, vol. 38(18), pp. 3438.

152.Snow, H. M. M., (2002), "Investigation of the effect of a surface active flux on the microstructure and properties of gas tungsten arc welds made on a superaustenitic stainless steel" Theses and Dissertations, Paper 753.

153.Bag S. and Yadaiah, N., (2011), "Possible role of surface active elements in weld pool modelling of fusion welding process", Proceedings of International Conference on Computational Methods in Manufacturing, Indian Institute of Technology Guwahati, 2011.

154.Bag, S., and Trivedi, A., (2008), "Use of a multivariate optimization algorithm to develop a self-consistent numerical heat transfer model for laser spot welding", International Journal of Advanced Manufacturing Technology, vol. 38, pp. 575-585.

155.Raja, J. E., and Kumanan, S., (2011), "Optimization of parameters of submerged arc weld using non conventional techniques" Applied Soft Computing Journal, vol. 11 (8), pp. 5198-5204.

156.Kumanan, S., Dhas, J. E. R., and Gowthaman, K., (2007), "Determination of submerged arc welding process parameters using Taguchi method and regression analysis", Indian Journal of Engineering and Materials Sciences, vol. 14, pp. 177-183.

157.Singh, A., Datta, S., Sankar, S., Singha, T., and Majumdar, G., (2011), "Optimization of bead geometry of submerged arc weld using fuzzy based desirability function approach", Journal of Intelligent Manufacturing, vol. 24 (35), pp. 1-10.

158.Tsai, H. L., Tarng, Y. S., and Tseng, C. M., (1996), "Optimisation of Submerged Arc Welding Process Parameters in Hardfacing", International Journal of Advanced Manufacturing Technology, vol. 12, pp. 402-406.

159.Nagesh, D. S. and Datta, G. L., (2002), "Prediction of weld bead geometry and penetration in shielded metal-arc welding using artificial neural networks", Journal of Materials Processing Technology, vol. 123, pp. 303-312.

160.Tarng, Y. S., Yang, W. H. and Juang, S. C., (2000), "The use of fuzzy logic in the taguchi method for the optimisation of the submerged arc welding process", International Journal of Advanced Manufacturing Technology, vol. 16, pp. 688-694.

161.Tarng, Y. S., Juang, S. C. and Chang, C. H., (2002), "The use of grey-based Taguchi methods to determine submerged arc welding process parameters in hardfacing", Journal of Materials Processing Technology, vol. 128, pp. 1-6.

162.Bag, S., (2009), "Error analysis of forward and reverse heat conduction and convection calculations considering uncertainties in welding", Science and Technology of Welding and Joining, vol. 14 (7), pp. 662-668.

163.Bag, S., (2009), "Development of efficient numerical heat transfer model coupled with genetic algorithm based optimisation for prediction of process variables in GTA spot welding", Science and Technology of Welding and Joining, vol. 14 (4), pp. 333-345.

164.Datta, S., Bandyopadhyay, A. and Pal, P. K., (2008), "Application of Taguchi philosophy for parametric optimization of bead geometry and HAZ width in submerged arc welding using a mixture of fresh flux and fused flux", International Journal of Advanced Manufacturing Technology, vol. 36, pp. 689-698.

165. Datta, S., and Bandyopadhyay, A., (2008), “Grey-based Taguchi method for optimization of bead geometry in submerged arc bead-on-plate welding”, International Journal of Advanced Manufacturing Technology, vol. 39, pp. 1136-1143.

166. Datta, S., and Bandyopadhyay, A., (2008), “Solving multi-criteria optimization problem in submerged arc welding consuming a mixture of fresh flux and fused slag”, International Journal of Advanced Manufacturing Technology, vol.35, pp. 935-942.

167. Karaoglu, S., and Secgin, A., (2008), “Sensitivity analysis of submerged arc welding process parameters”, Journal of Materials Processing Technology, vol. 202, pp. 500-507.

168. Datta, S., Nandi, G., Bandyopadhyay, A., and Pal, P. K., (2009), “Application of PCA-based hybrid Taguchi method for correlated multicriteria optimization of submerged arc weld: a case study”, The International Journal of Advanced Manufacturing Technology, vol. 45 (3-4), pp. 276-286.

169. Sudhakaran, R., Murugan, V. V. and Sakthivel, S. P. S., (2010), “Optimization of process parameters to minimize angular distortion in gas tungsten arc welded stainless steel 202 grade plates using genetic algorithms”, International Journal of Engineering Science and Technology, vol. 2 (5), 731-748.

170. Njiraini, B. N., Ikua, B. W. and Maranga, S. M., (2012), “Experimental investigations on welding deformation control methods of a butt-weld in a manual arc welding operation”, Proceedings of the 2012 Mechanical Engineering Conference on Sustainable Research and Innovation, vol. 4, pp. 305-309.

171. Pavelic, V., Tanbakuchi, R., Uyehara, O. A. and Myers, P. S., (1969), Experimental and computed temperature histories in gas tungsten-arc welding of thin plates, Welding Journal vol. 48 (7) pp. 295-305.

172. Friedman, E., (1978), Analysis of weld puddle distortion and its effect on penetration, Welding Journal Research Supplement, vol. 57, pp. 161-166.

173. Bezuhov, N. L., (1968), “Basics theory of elasticity, plasticity and creep”, Visshaya Shkola, Moscow.

174. Rao, P. N., (1998), “Manufacturing technology”, Tata McGraw-Hill Pub. Co. Ltd., New Delhi.

175. Chakrabarty, J., 1965, “Theory of plasticity”, McGraw-Hill publications, Singapore.

176. Mandal, N. R., (2004), “Welding and distortion control”, Narosa Publishing House, New Delhi.

177. Cheng, W., (2005), “In-plane shrinkage strains and their effects on welding distortion in thin-wall structures”, PhD thesis, The Ohio State University, USA.

178. Alberg, H., (2005), "Simulation of welding and heat treatment modelling and validation", PhD thesis, Luleå University of Technology, Sweden.
179. Tsai, N. S. and Eagar, T. W., (1983), "Temperature fields produced by traveling distributed heat sources", Welding Journal, vol. 62, pp. 346s-355s.
180. Guedes Soares, C., Gordo, J. M. and Teixeira, A. P., (1998), "Elasto-plastic behavior of plates subjected to heat loads", Journal of Constructional Steel Research, vol. 45(2), pp. 179-198.
181. Biswas, P., Mandal, N. R. and Sha, O. P., (2007), "Three dimensional finite element prediction of transient thermal history and residual deformation due to line heating", Journal of Engineering for the Maritime Environment, Part M, vol. 221 (1), pp. 17-30.
182. Nishikawa, H., 2004, "Inherent strains in welding," Proceedings of the Annual International Offshore and Polar Engineering Conference, France, pp. 126-132.
183. Serizawa, H., Nishikawa, H., and Murakawa, H., 2007, "Distortion in welding using inherent strains," Science and Technology of Welding and Joining, vol. 1282, pp. 147-152.
184. Khurram, A., and Khurram, S., 2012, "FE simulation of welding distortion and residual stresses in butt joint using inherent strain," International Journal of Applied Physics and Mathematics, vol. 2 (6), pp. 3-9.
185. Minitab 17 Statistical Software (2010), Minitab, Inc., State College, Pennsylvania.
186. Ma, N. X., Ueda, Y. and Murakawa. H., (1995). FEM Analysis of 3D welding residual stresses and angular distortion in T-type fillet welds. Transaction of Joining and Welding Research Institute, vol. 24 (2), pp. 115-122.
187. Ross, P. J., (1996), Taguchi Techniques for Quality Engineering, McGraw-Hill, New York.
188. Mandal, N. R. and Adak, M., (2001), "Fusion Zone and HAZ prediction through 3-D simulation of welding thermal cycle", Journal of the Mechanical Behaviour of Materials, vol. 12 (6), pp. 401-414.
189. Boob, A. N. and Gattani, G. K., (2013), "Study on effect of manual metal arc welding process parameters on width of heat affected zone (HAZ) for MS 1005 steel", International Journal of Modern Engineering Research (IJMER), Vol. 3, pp. 1493-1500.
190. Masubuchi, K., (1980), Analysis of welded structures: residual stress, distortion, and their concequences, Pergamon Press Ltd, London.

191.Deng, D., Ma, N., and Murakawa, H., (2011), Finite element analysis of welding distortion in a large thin-plate panel structure, Trans of Joining and Welding Research Institute Osaka University, vol. 40 (1), pp. 89-100.

192.Pathak, A. K. and Datta, G. L., (2004), 'Three-dimensional finite element analysis to predict the different zones of microstructures in submerged arc welding' Proceedings of the Institution of Mechanical Engineers, vol. 218 (B3), pp. 2690-280.

List of Publications

Journals

1. Arpan Kumar Mondal, Pankaj Biswas & Swarup Bag, "Influence of tacking sequence on residual stress and distortion of single sided fillet submerged arc welded joint", Journal of Marine Science and Application, Springer, Vol. 14, Issue 3 (2015), pp. 250-260, ISSN: 1671-9433, DOI: 10.1007/s11804-015-1320-z.
2. Arpan Kumar Mondal, Pankaj Biswas & Swarup Bag, "Prediction of Weld Induced Distortion of Large Structure Using Equivalent Load Technique", Proceedings of the Institution of Mechanical Engineers, Part B: Journal of Engineering Manufacture, SAGE Publications, pp. 1-14, DOI: 10.1177/0954405416646309 (13th most viewed article for the month of June 2016)
3. Arpan Kumar Mondal, Pankaj Biswas & Swarup Bag, "Prediction and comparative study of submerged arc weld induced residual stress and angular deformation of single and double sided fillet welded joint using Finite element analysis" International Journal of Steel Structures, Springer, Vol. 17, Issue 1, pp 9-18 , DOI: 10.1007/s13296-016-0093-9.
4. Arpan Kumar Mondal, Pankaj Biswas & Swarup Bag, "Effect of Welding Sequence on Submerged Arc Welded Fillet Joint", Welding in the World, Springer, Vol. 61, Issue 4, pp. 711–721, DOI: 10.1007/s40194-017-0468-3
5. Arpan Kumar Mondal, Nirsanametla Yadaiah, Pankaj Biswas & Swarup Bag, "Development of a new heat source model for prediction of thermal properties of submerged arc welding" (Communicated).
6. Arpan Kumar Mondal, Pankaj Biswas & Swarup Bag, "A comparative study of the effect of groove angles on mechanical properties of submerged arc welded butt joints" (Under preparation)
7. Arpan Kumar Mondal, Pankaj Biswas & Swarup Bag, "Multi-objective optimization of the process parameters of submerged arc welded mild steel plates" (Under preparation)

Book Chapter

8. Arpan Kumar Mondal, Pankaj Biswas, Swarup Bag & M. M. Mahapatra "Prediction of weld induced angular distortion of single sided and double sided fillet joint by

SAW process", Advances in Material Forming and Joining, Springer, pp. 203-220, ISBN: 978-81-322-2354-2, 2015.

Conference Proceedings

9. Arpan Kumar Mondal, Pankaj Biswas, Swarup Bag &M.M. Mahapatra, "Finite Element Analysis of weld induced residual stress of double sided fillet welded joint", International Symposium on Processing and Fabrication of Advanced Materials XXI (PFAM – XXI), Indian Institute of Technology Guwahati , December 10-13, 2012.
10. Arpan Kumar Mondal, Pankaj Biswas & Swarup Bag, "Effect of process parameters on residual stress distribution of submerged arc welded butt joint" 7th Asia Pacific IIW International Congress on "Recent Development in Welding and Joining Technologies" , July 8-10, 2013, Singapore Management University (SMU), Singapore.
11. Arpan Kumar Mondal, Pankaj Biswas & Swarup Bag, "Effect of process parameters on microstructure and mechanical properties of single pass single sided square butt joint by submerged arc welding" IIW International Congress 2014 on "Advancement In Welding, Cutting And Surfacing Technologies For Improved Economy And Sustainable Environment" , April 9-11, 2014, Pragati Maidan, Delhi, India.
12. Arpan Kumar Mondal, Pankaj Biswas & Swarup Bag, "Prediction of Weld Induced Angular Distortion of Single Sided and Double Sided Fillet Joint by SAW Process", 5th International and 26th All India Manufacturing Technology, Design and Research Conference AIMTDR 2014, Department of Mechanical Engineering, IIT Guwahati, Guwahati, India, December 12-14, 2014.
13. Arpan Kr. Mondal, Nirupam Mondal, Dipankar Bose, Pankaj Biswas and Swarup Bag "Development of a new heat source model and thermo-mechanical analysis of submerged arc welding", National Welding Seminar, NWS 2016, 15-17 December 2016, Kolkata
14. Arpan Kr. Mondal, Chandan Kr. Mondal, Dipankar Bose, Pankaj Biswas and Swarup Bag, "Effect of surface activating elements on weld bead geometry of mild steel welds by submerged arc welding" National Welding Seminar, NWS 2016, 15-17 December 2016, Kolkata